# Launching Jets and Outflows from Magnetized Accretion Disks

## Advection, Diffusion, Dynamo

**Deniss Stepanovs**
Max-Planck-Institut für Astronomie

**Heidelberg 2014**

*Dissertation in Astronomy*
**submitted to the**
**Combined Faculties of the Natural Sciences and Mathematics**
**of the Ruperto-Carola-University of Heidelberg, Germany,**
**for the degree of**
*Doctor of Natural Sciences*

**Put forward by**
**M.Sc. *Deniss Stepanovs***
**born in Riga, Latvia**

**Oral examination: 10.12.14**

# Launching Jets and Outflows from Magnetized Accretion Disks

## Advection, Diffusion, Dynamo

**Deniss Stepanovs**
Max-Planck-Institut für Astronomie

**Referees:** **Priv. Doz. Dr. Christian Fendt**
**Prof. Dr. Cornelis Dullemond**

# Abstract

The results of three-dimensional, axisymmetric, magnetohydrodynamic simulations are presented, investigating the launching of jets and outflows from a magnetically diffusive accretion disk. The time evolution of the disk structure is self–consistently taken into account. In contrast to previous works, spherical coordinates for the numerical grid were applied. The new setup made it possible to run simulations for more than 150,000 dynamical times on a domain extending 1500 inner disk radii with a resolution of up to 24 cells per disk height in the inner disk. This, in fact, is the longest and resolved simulation performed so far.

A novel approach to the analysis of disk-jet system was developed and interrelations between the properties of the jet and the underlying disk were derived. Using this method, it was shown that it is the actual disk magnetization that best describes the disk–jet evolution. The actual disk magnetization at the jet foot point is the main parameter that governs the properties of the jet, namely all jet steady-state MHD integrals. Depending on the disk magnetization, jet launching occurs in two different but complementary regimes - jets driven predominantly by centrifugal or magnetic forces. These regimes differ in the ejection efficiency concerning mass, energy, angular momentum, and all jet integrals.

The self-generation of the magnetic field by a $\alpha^2\Omega$ mean-field dynamo was also addressed. In this setup, the magnetic flux is continuously generated, diffuses outwards the disk, and fills the entire disk. A magnetic field of the inner disk is similar to open field structure, favoring magneto-centrifugal launching. The outer disk field is highly inclined and predominantly radial. The differential rotation induces a strong toroidal component that plays the key role in the outflow launching. These outflows from the outer disk are slower, denser, and less collimated. A toy–model triggering a time-dependent mean-field dynamo was invented. The general result is that the episodic ejection and *large-scale jet knots* can be steered by a time-dependent *disk dynamo* that regenerates the jet-launching magnetic field.

# Zusammenfassung

In der vorliegenden Arbeit werden die Ergebnisse von drei-dimensionalen, achsensymmetrischen, magnetohydrodynamischen Simulationen vorgestellt und die Erzeugung von Jets und Ausströmungen einer magnetisch diffusen Akkretionsscheibe untersucht. Hierbei wurde die zeitliche Entwicklung der Scheibenstruktur beachtet. Im Gegensatz zu vorherigen Arbeiten wurden hier Kugelkoordinaten verwendet. Ein neues Setup ermöglicht es Simulationen für einen Zeitraum von mehr als 150.000 dynamische Zeitschritte laufen zu lassen, in einem Bereich welcher über 1500 mal so großist wie der Scheibenradius. Für die innere Scheibe beträgt die Auflösung bis zu 24 Zellen pro Scheibenhöhe. Dies ist somit die zeitlich längste als auch räumlich höchst aufgelöste Simulation die jemals durchgeführt wurde.

Für die Analyse von Jets aus Akkretionsscheiben wurde eine neue Methode entwickelt und Zusammenhänge zwischen den Eigenschaften des Jets und der zugrundeliegenden Akkretionsscheibe konnten abgeleitet werden. Mit dieser Methode konnte gezeigt werden, dass die Scheiben-Jet-Entwicklung am besten durch die Magnetisierung der Scheibe beschrieben werden kann. Die Magnetisierung der Scheibe am Austrittspunkt des Jets ist der Hauptparameter der die Eigenschaften des Jets bestimmt, nämlich alle ”steady state” MHD Integrale. In Abhängigkeit von der Scheibenmagnetisierung kann ein Jet auf zwei verschiedene aber dennoch komplementäre Weisen erzeugt werden, und entweder hauptsächlich von Zentrifugalkräften oder Magnetfeldern getrieben werden. Beide Szenarien unterscheiden hinsichtliche der Effizienz der ausgeworfenen Masse, Energie, des Drehimpulses und aller Jet Integrale.

Es wurde ebenfalls ein Dynamo mit einem selbsterzeugenden $\alpha^2\Omega$ Feld untersucht. In diesem Setup wird der magnetische Fluss kontinuierlich erzeugt, diffundiert nach außen und füllt schließlich die gesamte Scheibe. Das Magnetfeld der inneren Scheibe ist strukturell ähnlich zu offenen Feldlinien, was für eine magnetisch-zentrifugale Erzeugung spricht. Das Magnetfeld der äußeren Scheibe hate eine Schrägstellung und ist hauptsächlich radial. Differentiale Rotation induziert eine große torodiale Komponente, welche die Schlüsselrolle beim Erzeugen von Ausströmungen spielt. Diese ”Outflows” der äußeren Scheibe sind langsamer, dichter und nicht sehr stark gebündelt. Es wurde ein Modell entwickelt, welches einen Dynamo mit einem gewöhnlichen zeitabhängigen Feld auslöst. Das Hauptergebnis ist das episodische Auswürfe und großräumige Jet-Knoten durch einen zeitabhängigen Scheibendynamo beeinflusst werden können, welcher das Magnetfeld für die Jet-Erzeugung regeneriert.

*To everyone interested*

# Contents


1 Introduction **1**

1.1 Jets in a nutshell . . . 1

1.2 From Nebulae to Outflows . . . 3

1.3 From Outflows to Disks . . . 6

1.4 The Magneto-centrifugal Mechanism . . . 7

1.5 Aims and motivation . . . 12

1.6 Thesis outline . . . 13

2 Theoretical Background **15**

2.1 MHD Equations . . . 15

2.2 Modeling Turbulence . . . 16

2.3 Mean-field Induction Equation . . . 18

2.4 The Magnetic Diffusivity Model . . . 19

2.5 Jet integrals . . . 20

3 Numerical approach **23**

3.1 Initial Conditions . . . 23

3.1.1 Initial Conditions: Dynamo Case . . . 27

3.2 Boundary Conditions . . . 28
3.2.1 Boundary Conditions: Dynamo Case . . . 30
3.3 Numerical Grid and Normalization . . . 31
3.4 Numerical Code PLUTO . . . 34

4 Modeling Disks and Jets **37**
4.1 Introduction . . . 37
4.2 The Magnetic Diffusivity Model . . . 39
4.2.1 Anisotropic Diffusivity . . . 40
4.3 A Reference Simulation . . . 42
4.3.1 Comparison to Previous Simulations . . . 46
4.3.2 Disk Structure and Disk Surface . . . 46
4.3.3 Launching Mechanism . . . 47
4.3.4 Control Volume . . . 50
4.3.5 Mass Flux Evolution . . . 50
4.3.6 Magnetic Field Bending Parameter Study . . . 53
4.3.7 Resolution Study . . . 53
4.4 Magnetization Analysis . . . 58
4.4.1 Transport of Angular Momentum and Energy . . . 60
4.4.2 Analysis of Magnetization, Diffusivity and Fluxes . . . 63
4.4.2.1 Accretion Mach Number . . . 65
4.4.2.2 Magnetic Shear . . . 65
4.4.2.3 Mass and Energy Flux . . . 67
4.5 A Stable Long-term Evolution . . . 70
4.5.1 Constraints on the Diffusivity Parameters . . . 71

4.5.2 The Accretion Instability . . . 73
4.5.3 A Proper Magnetization Profile . . . 73
4.5.4 A Modified Diffusivity Model . . . 74
4.5.5 The Long-term Disk-outflow Evolution . . . 75
4.5.6 Results of the Strong Diffusivity Model . . . 76
4.5.7 Dynamical Profiles of a Steady State Accretion Disk . . . 78
4.5.8 Discussion of the New Diffusivity Model . . . 82
4.6 Conclusions . . . 83

5 Connecting Jet to the Disk **85**
5.1 Introduction . . . 85
5.2 Model Setup . . . 87
5.3 General Disk-jet Evolution . . . 87
5.3.1 Disk and Jet Characteristic Quantities . . . 88
5.4 Steady-state Jet MHD Integrals . . . 89
5.4.1 Conserved Quantities Along the Jet . . . 93
5.4.2 Asymptotic Jet Velocity . . . 96
5.5 The Disk-jet Connection . . . 100
5.5.1 "Stability" Check . . . 100
5.5.2 Jet Energy and Angular Momentum Relation . . . 100
5.5.3 Jet Energy and Disk Magnetization . . . 101
5.5.4 Alfvén Lever Arm . . . 101
5.5.5 The Accretion-Ejection Process . . . 106
5.5.6 Different Launching Mechanisms . . . 114
5.6 From Jet Observables to Disk Properties . . . 114

5.7 Conclusions . . . 116

6 Launching Jets from $\alpha\Omega$-Dynamo Disk **119**

6.1 Introduction . . . 119

6.2 Modelling Large Scale Turbulence . . . 122

6.2.1 The Magnetic Diffusivity Model . . . 122

6.2.2 The Dynamo Model . . . 123

6.3 A Reference Dynamo Simulation . . . 124

6.3.1 Dynamo Effect versus Magnetic Diffusion . . . 126

6.3.2 Disk Structure and Disk Surface . . . 126

6.3.3 Outflow Launching: Accretion-Ejection . . . 127

6.3.4 Dynamical Profiles of a Dynamo Disk Driving Jets . . . 130

6.3.5 Dynamo versus Non-Dynamo Simulations . . . 132

6.3.6 Resolution Study . . . 133

6.4 Episodic Jet Ejection Triggered by a Time-variable Disk Dynamo . . . 135

6.4.1 Structure and Evolution of the Episodic Jets . . . 140

6.4.2 Self-induced Magnetic Field Regeneration . . . 141

6.5 Conclusions . . . 144

7 Summary and Outlook **147**

7.1 Summary . . . 147

7.2 Outlook . . . 149

Acknowledgements **151**

Bibliography **153**

# 1 Introduction

Astrophysical jets as highly collimated, supersonic beams of plasma and outflows of lower speed are observed to emerge from a wide variety of astrophysical objects. Over last decades it has become clear that the magnetic field plays a crucial role in launching, acceleration and collimation of the jet and outflows. However, many fundamental questions remain outstanding such as following. *What is the main agent of jet-launching that controls this phenomenon? What kind of disk drives what kind of jets? What is the origin of the magnetic field in outflow launching processes?* This work addresses exactly these questions, revealing the great role of the disk magnetization in jet-launching process.

## 1.1 Jets in a nutshell

Since people had started to discover Cosmos until modern times, it was believed that the cosmos objects are perfect spheres. Continuous observations, however, showed another picture. Nevertheless, many celestial bodies could be approximated by ellipsoids. In the beginning of 20th century, very peculiar objects were discovered - that are better approximated by a stick. These sticks, now known as jets, appear to be fast moving flows, usually collimated, that can propagate very far from their origin. The first relativistic jet (Figure 1.1) was found by Curtis (1918). This

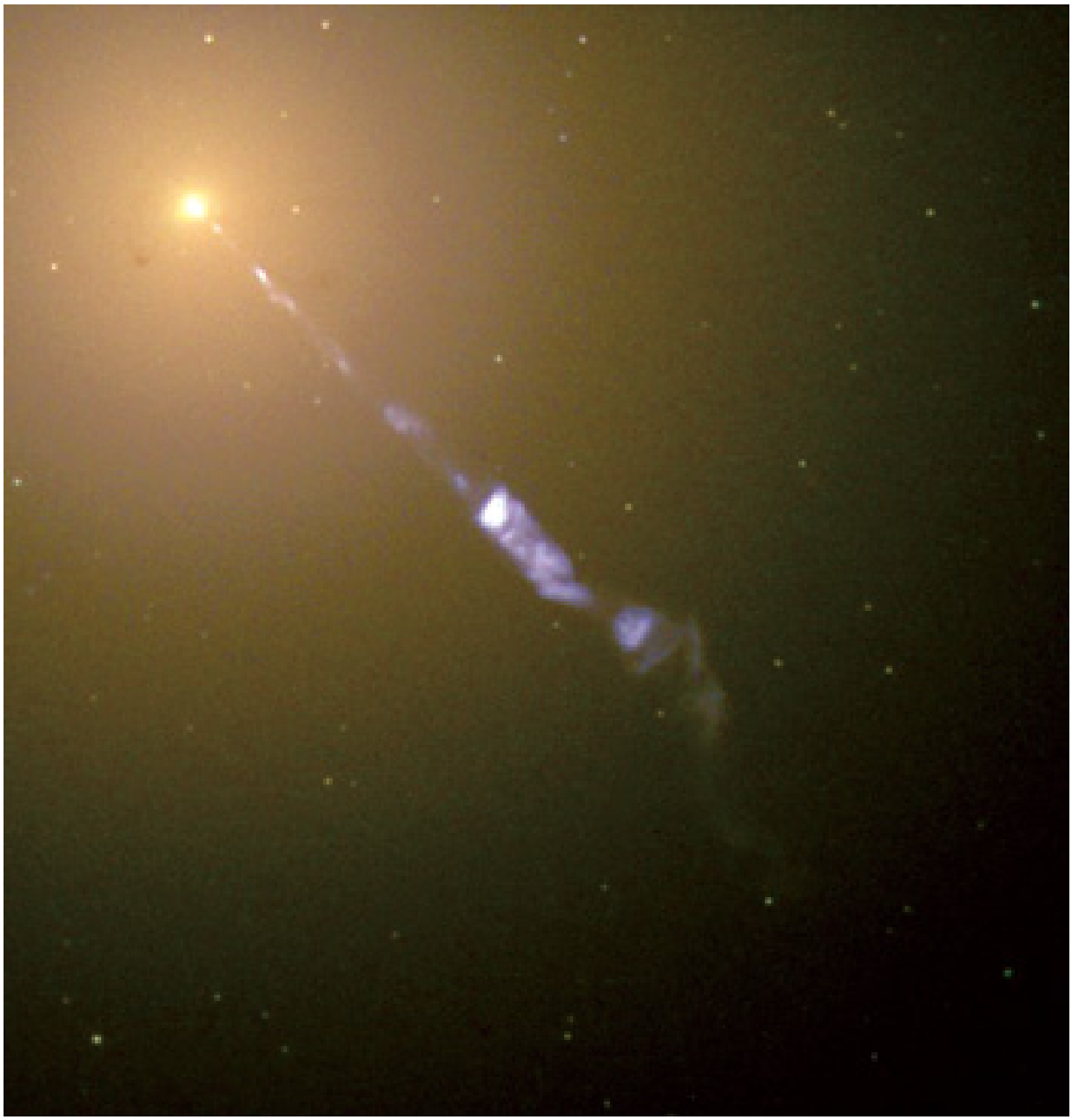

**Figure 1.1:** Hubble Space Telescope image of the jet emanating from galaxy M87.

jet, emanating from the M87 galaxy, is an example of so-called AGN (active galactic nuclei) jets. They originate from the center of galaxies - the place occupied by the black holes and propagate far into the intergalactic media. In early 80th, the jets from young stellar objects (YSOs) were discovered (see below). These are also stick-like structures that originate from the vicinity of new forming stars, however, they are much slower than AGN jets and extend in space only on a parsec scales. Later, with the advance of technologies, it became possible to probe even brown dwarfs (BD) for the presence of the outflows. There is certain evidence that outflows from BD really exist (Monin et al. 2013).

Observationally, AGN jets are very different from YSO or BD outflows. The light from AGN jets is found to be highly polarized with continuous spectrum that can be approximated by multiple power-laws. This is a direct evidence for the synchrotron radiation, that highlights the importance of the magnetic field in launching process. In contrast, outflows from YSOs are mostly observed in forbidden molecular lines (see below) of the shock-heated gas. Nevertheless, the presence of the magnetic field in the molecular outflows was also established (Akeson & Carlstrom 1997; Vlemmings et al. 2006).

Whatever mechanism is responsible for the jet formation, the great importance of the magnetic field is well acknowledged. Moreover, one may argue that the magnetic field is the only source that can extract the matter from a deep potential well into fast moving, collimated structures. It is still an open question what is the jet-launching mechanism, however, there is a general, so-called magneto-centrifugal launching mechanism, that can be, in principle, shared by all systems: AGN, YSO, and BD. The magneto-centrifugal mechanism is the main framework used in this study (see below). The main idea of the magneto-centrifugal launching mechanism is that a presence of the magnetic field in the disk enhances the angular momentum transport. This happens much faster if the magnetic field is ordered and large-scale. The outflows can be seen then simply as a byproduct of the star formation process.

The results of this study are more applicable to outflows from YSOs since there are much more details known about these systems rather than AGNs or BDs. In the next sections, a historical overview of molecular outflows from YSOs is presented and the general physics of the jet-launching is discussed.

## 1.2 FROM NEBULAE TO OUTFLOWS

The story of outflows from YSOs begins

from late 19th century, when Burnham (1890, 1894) observed a small emission nebula near the *T Tauri* star. However, at that time, this nebula, now known as Burnham's Nebula, was not

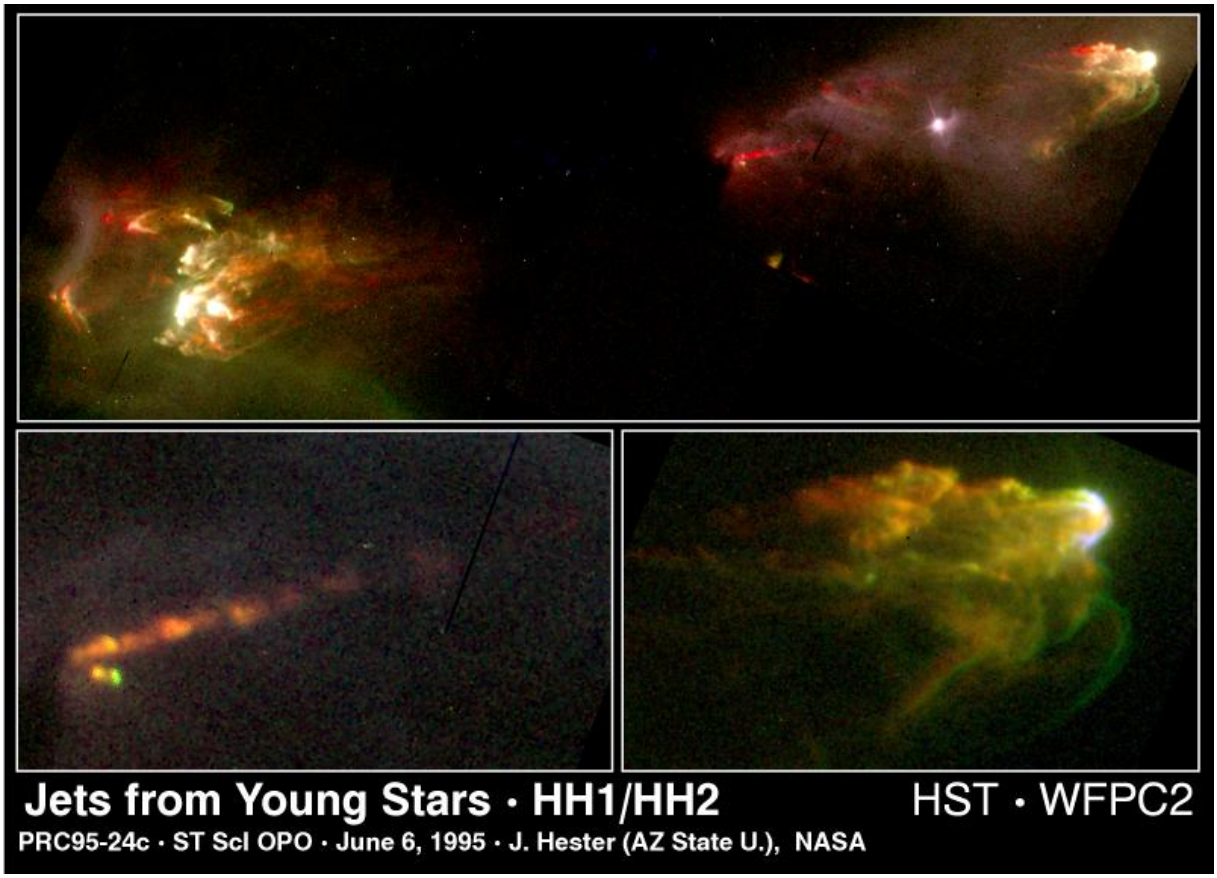


**Figure 1.2:** Herbig-Haro objects imaged by the Hubble Space Telescope's WFPC2. Credit J. Hester (ASU), WFPC2 Team, NASA.

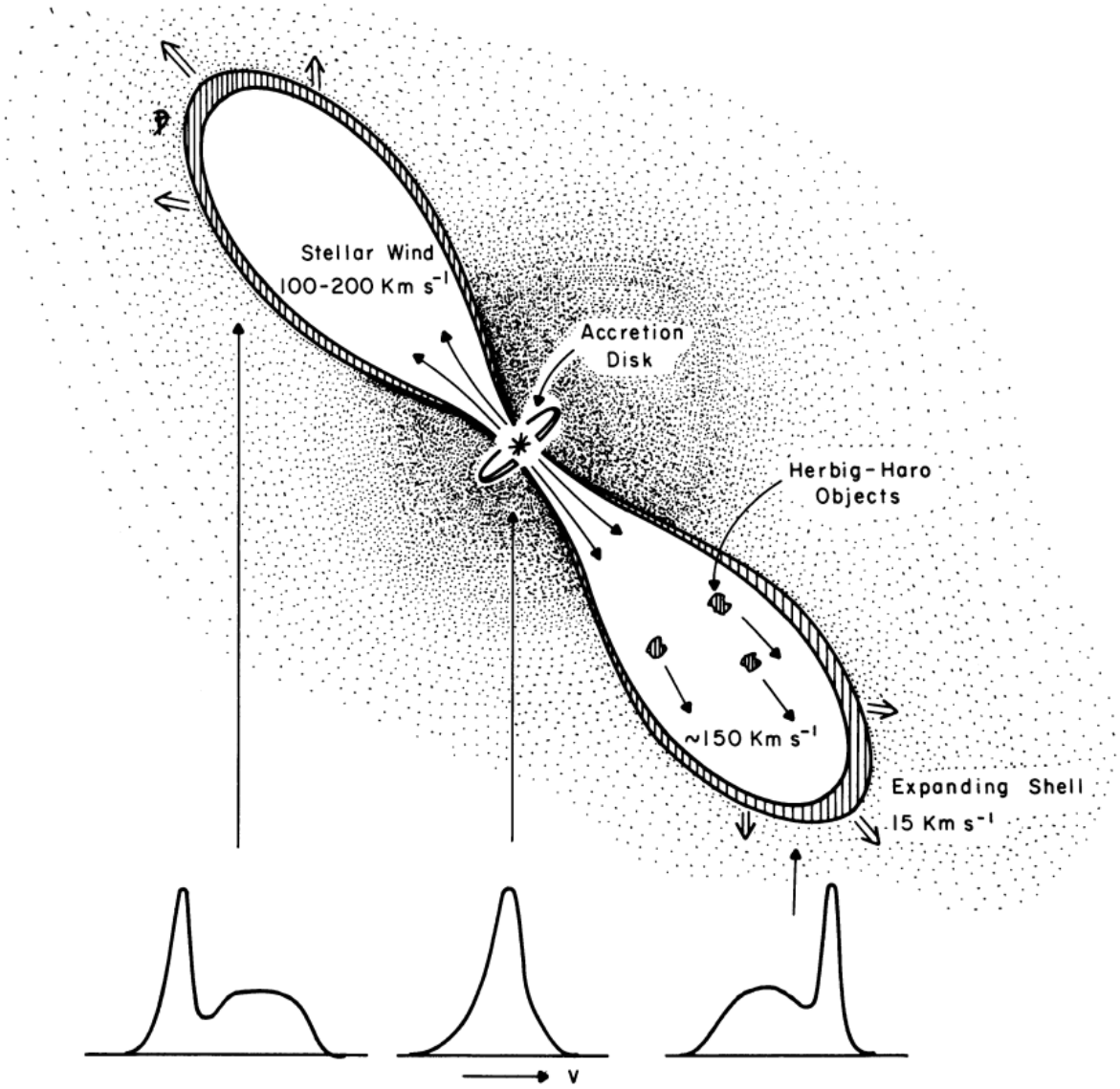


**Figure 1.3:** A schematic picture of the stellar wind driven shock model for L1551, indicating the CO line profiles which would be expected at different positions across the source. The HH-objects are not necessarily located inside the shell; because of their high velocities, they may have been ejected through the shell and into the surrounding medium. Credit Snell et al. (1980).

recognized as a distinct class of objects. Only sixty years later, Herbig (1950, 1951, 1952) and Haro (1952, 1953) independently showed that the emission line spectra of Burnham's Nebula can be attributed to a broad class of objects, later called Herbig-Haro (HH) objects. Figure 1.2 presents the Hubble images of the nebulae around a variable star (V380 Ori) in Orion Nebula, that were studied by both authors. These objects, now known as HH1 and HH2, show strong hydrogen recombination lines ($H_\alpha$, $H_\beta$) as well as a variety of atomic forbidden lines (e.g., [OI] at $\lambda = 6300$ and $\lambda = 6363$, [SII] at $\lambda = 6717$ and $\lambda = 4608$). What is remarkable about these objects is that they show a striking dissimilarity to the spectrum of an ordinary T Tauri star, that is always present in the nebulae. The origin and nature of these nebulae remained a puzzle, unless Schwartz (1975) proposed that the observed spectral lines may be excited by the shocks of the supersonic winds that originates from the young stars. However, these winds has to be much stronger than a typical T Tauri star can produce.

The puzzle became partly solved in early 80th. Snell et al. (1980) discovered the bipolar nature of CO outflow in the L1551 outflow, presenting a schematic picture of the stellar wind driven shock (Figure 1.3). Later Dopita et al. (1982) presented a model wherein the HH-objects were produced by bipolar ejection from a T Tauri star that is surrounded by an accretion disk. Only one year later, Mundt & Fried (1983) reported on the discovery of four jet-like structures that are highly collimated - at least close to their stars. These observations directly indicated that most HH-objects were not independent entities. Instead, they appear as shocks between the interstellar medium and collimated jets originating from YSOs.

However, it was not clear yet what is the origin of molecular outflows.

## 1.3 FROM OUTFLOWS TO DISKS

The widespread occurrence of bipolar CO outflows in early 80s led to realization that outflows are a fundamental feature of the star formation. Various physical parameters for CO outflows have the following ranges: length $D_{\rm max} = 0.04 - 4$ pc, maximal velocity $V_{\rm max} = 3 - 150$ km s$^{-1}$, dynamical age = $0.01 - 2\ 10^5$ yr, molecular mass = $0.1 - 170\ M_\odot$, outflow momentum = $0.1 - 1000\ M_\odot$kms$^{-1}$, kinetic energy = $10^{43} - 10^{47}$ erg, mechanical luminosity = $0.001 - 2600\ L_\odot$, roughly 85% of CO outflows are bipolar (Fukui et al. 1993).

It became obvious that these outflows could not be driven by the radiative pressure provided by the central star (Bally & Lada 1983). Another problem of driving jets by means of the central object was to explain the collimation of the outflow that is present already very close to the central star (Takano et al. 1984).

Molecular outflows were found to be more frequent in embedded sources than in visible stars,

thus the more massive circumstellar structure is the more powerful is the outflow (Lada 1985; Cabrit & Andre 1991).

Nowadays, there are clear evidences that YSO outflows are linked to the accretion disk around the star (Konigl & Pudritz 2000). Standard analytical models (Ferreira & Pelletier 1993, 1995; Ferreira 1997) also confirmed a tight relation between the accretion and the ejection. The presence of accretion disks around low, intermediate mass (Watson et al. 2007) and massive (Davies et al. 2010) pre-main-sequence stars has been firmly established. However, not all pre-main-sequence stars have disks. Previous studies on stellar clusters Haisch et al. (2001) showed that the disk fraction decreases with time, indicating that a lifetime of the disks are about few million years. Such a decline was also found in the outflow activity (Gomez et al. 1997).

Stellar jets are believed to be powered by the gravitational energy liberated during accretion, and, in fact, such correlation was found (Cabrit et al. 1990; Li 1995). Besides the relation between accretion and ejection activities, there is a distinct geometrical relation: jets and outflows are typically observed to be perpendicular to the disk planes. The exact details of the accretion disks, namely, their structure, the magnetic field distribution, instabilities and turbulence present is the disks, are still not fully understood. Nevertheless, the theoretical models together with the numerical experiments become more and more developed, that assures that at some point the convergence of the theory will be met.

The theory of accretion disks and outflows bring several hot fields of research together: i) accretion disk turbulence ii) accretion-ejection processes iii) interstellar turbulence. It it believed that accretion disks are highly turbulent, especially with the presence of the magnetic field. The disk turbulence enhances the angular momentum transport in the disk and also can lead to the dynamo effect, thus to the generation of the magnetic field. However, it is still not feasible to self-consistently treat both the turbulence and large-scale dynamics of the outflow. Therefore, the $\alpha$-prescription of Shakura & Sunyaev (1973) is used for the magnetic diffusivity modeling (Chapter 2). The accretion-ejection processes are, in fact, very important in the general theory of star formation. As jets and outflows propagate into space, they help to sustain the interstellar turbulence that otherwise would decay on much shorter timescales. How much mass can be accreted onto the star and ejected into the space and by what means is a very important issue.

Summarizing, the observations suggest that jets and outflows are intimately connected to the accretion disks. In the next section, the mechanism by which jets and outflows are launched from the accretion disks is discussed.

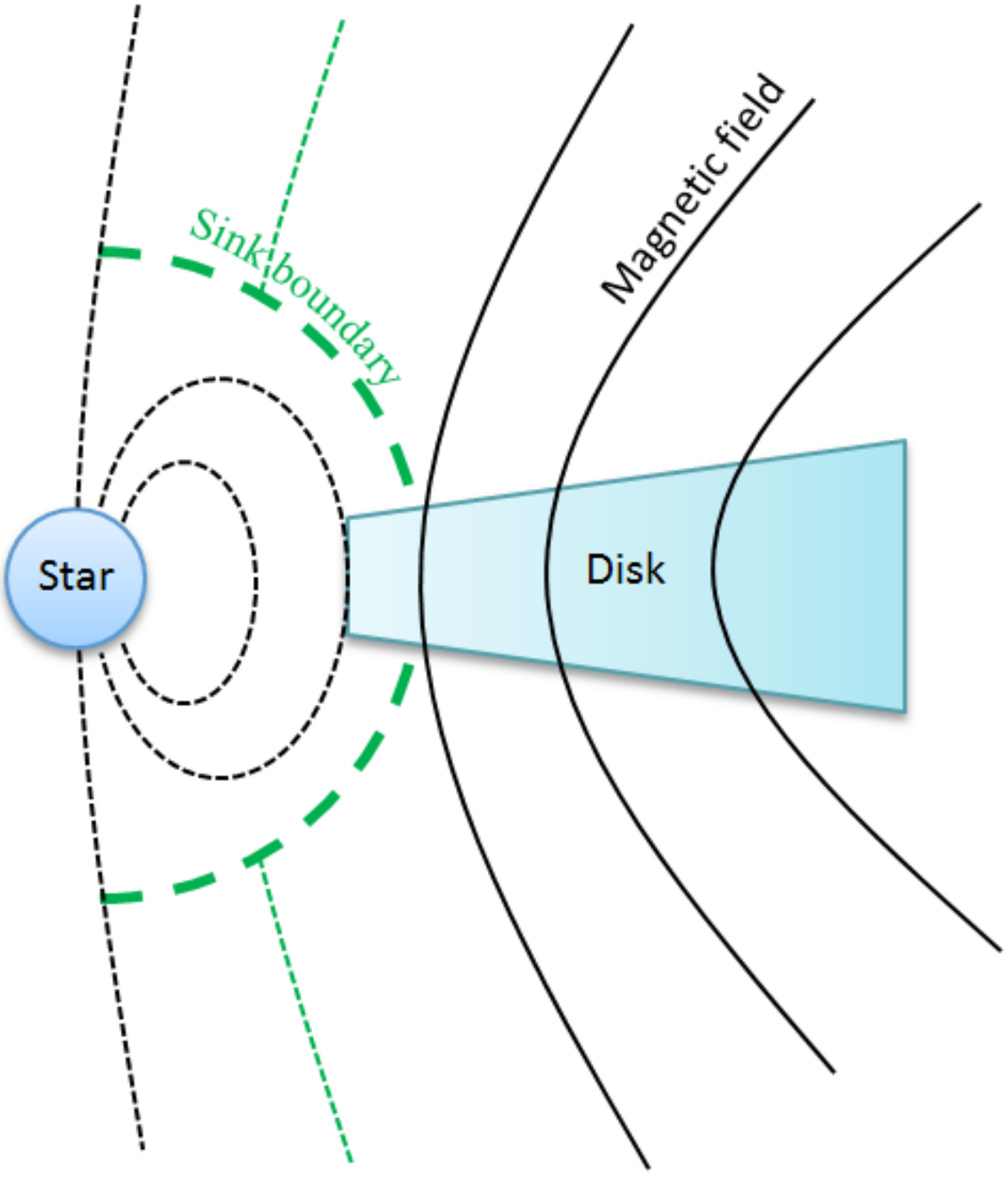


**Figure 1.4:** Sketch of the outflow launching process. The main ingredients are the star, the accretion disk, gap between them, and the magnetic field.

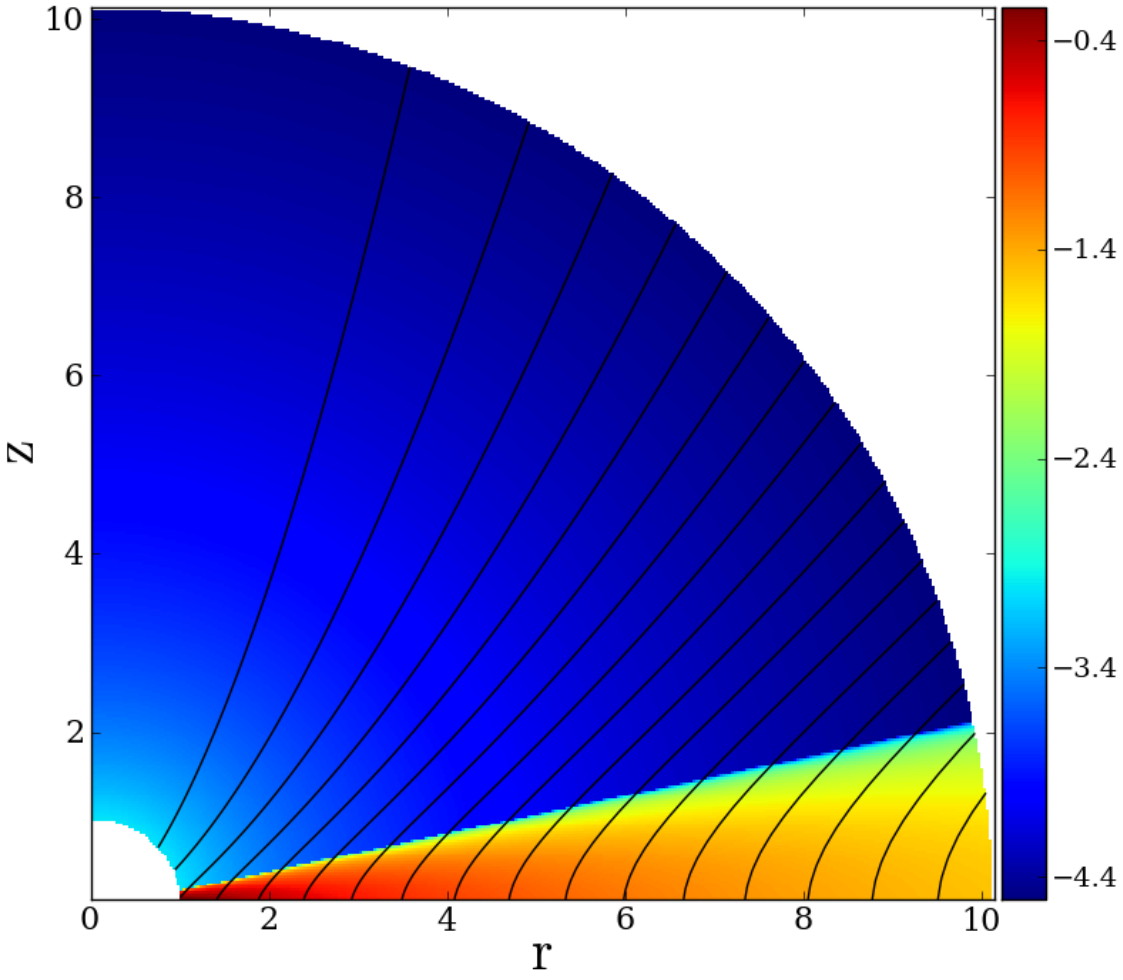


**Figure 1.5:** Initial state of the simulations. The mass density is shown by colors, in logarithmic scale. The black lines mark the initial magnetic field lines.

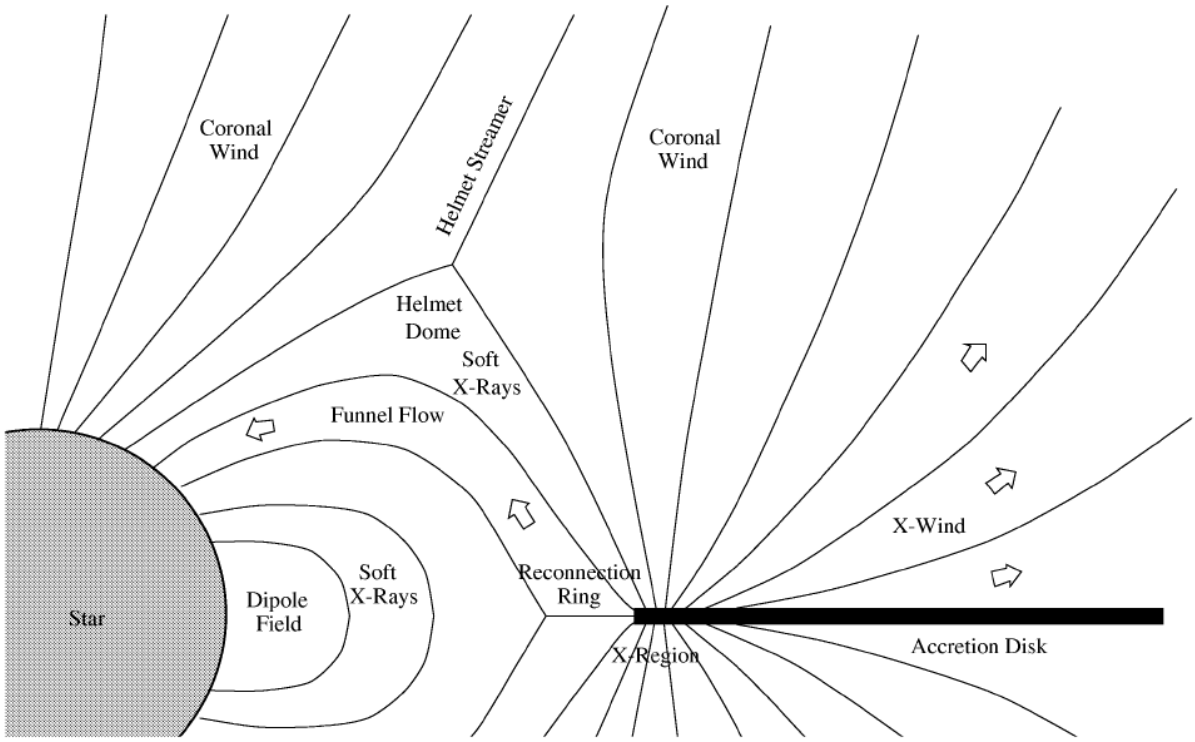


**Figure 1.6:** Illustration of the X-wind configuration. Credit (Shu & Shang 1997)

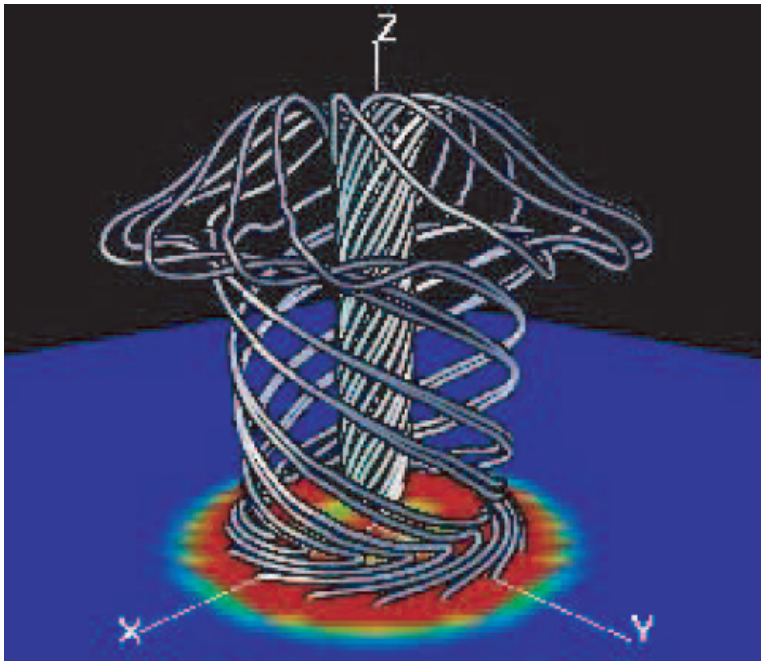


**Figure 1.7:** Illustration of the tower jet. Note the structure of the magnetic field lines. Credit (Kato et al. 2004)

## 1.4 THE MAGNETO-CENTRIFUGAL MECHANISM

This section discusses the general physics of the jet-launching process. It also discusses different flavors (models) of the problem, namely X-winds and tower jets.

A typical picture of jet-launching consists of four main ingredients (Figure 1.4): the central object, the accretion disk around it, the gap between the disk and the central object, and a certain structure of a large-scale magnetic field imposed. Instead of the latter, a disk dynamo can be prescribed, that in the end will self-consistently generate the magnetic field. Usually a point-like mass of the order of a solar mass is assumed in the center and a self-similar, Keplerian, accretion disk around. Typically, a hydrostatic corona is prescribed above the disk. Depending on the goals, the certain structure of the magnetic field is imposed. If the main concern is the disk-star interaction, typically dipolar field is declared to be in the centre. If the jet itself is the main object of a study, like in this work, the innermost area is usually modeled as a sink. Note the thick, dashed, green line in Figure 1.4. The sink conditions simply allow the matter go in, toward the star, but not out, thus the star is out of the scope. Figure 1.5 shows the initial setup of the non-dynamo simulation presented in this work. Note the similarity between the sketch of the physical system (Figure 1.4) and the initial state of the simulation (Figure 1.5). In what follows, the disk-star interaction is not considered and sink conditions are assumed.

Depending on the structure of the magnetic field that is initially imposed or kept during simulations, different launching scenarios can be studied. Nevertheless, as shown in this work, all of them can be formally understood from the magneto-centrifugal perspective.

Three main processes that can be distinguished in the jet formation are the following: i) launching or lifting ii) acceleration iii) collimation of the matter, however, all of them continuously flow one into another. It is the magnetic field that makes all these processes viable. According to the magneto-centrifugal launching scenario, the large-scale magnetic field exerts a torque on the disk. It breaks the matter and allows a part of it to be accreted onto the central object. The excess of the angular momentum is transported out to the disk corona by means of the magnetic field. As it is discussed in detail in this work, it is always buoyant forces of the magnetic field in the disk that really pushes the matter upward, since the only positive force in vertical direction is, in fact, the thermal pressure gradient.

Starting from the disk surface, the excess of the angular momentum leads to the centrifugal force that pushes the matter outward in radial direction. On the other hand, the magnetic pressure is now positive in vertical direction (it changes sign at the disk surface) and plays a key role in the acceleration of the outflow. Also, starting only from the disk surface, the radial component of the the Lorentz force becomes negative, thus responsible for the collimation of the flow. To summarize, the established large-scale magnetic field extracts the angular momentum (as well as

mass and energy) from the accretion disk, accelerates and collimated the matter into the outflows.

The magneto-centrifugal launching mechanism was first proposed by Blandford & Payne (1982); Pudritz & Norman (1983) and later studied by many authors (see below). However, certain flavors of the launching mechanism exist. One of them is so-called X-wind model that was proposed by Shu & Shang (1997). According to this model, the inner disk region is of a main interest. This is the region in which the star and the disk magnetic field meet together in a rather small area. The star and disk dynamics leads to a specific X-like structure of the magnetic field and fast moving X-winds (see Figure 1.6). However, if the dynamics of the disk-star is not considered, and the inner area is modeled as a sink, the disk-jet dynamics can be nicely understood under the magneto-centrifugal framework. The X-region is, basically, the region where the magnetic field is much stronger than in the rest of the disk. Chapter 4 and Chapter 5 explore the structures in which the inner magnetic field is much stronger than the rest disk. It comes naturally under certain conditions in the accretion disk, namely, when the disk is subject to the strong accretion instability.

Another launching mechanism, so-called tower jets, was proposed by Lynden-Bell & Boily (1994); Lovelace et al. (1995). In this scenario, there is a magnetic loop-like structure present in the disk and the strong toroidal field is constantly amplified from it by the differential in the disk. This results in the development of a strong magnetic pressure, that further accelerates the outflow in the vertical direction, building up a, so-called, tower jet. Again, this can be understood in terms of the magneto-centrifugal mechanism. The difference here is that it is the magnetic, but not the centrifugal forces that drive, accelerate outflows. As can be seen in Chapter 4 and Chapter 5, if the poloidal field that penetrates the disk is weak, the outflows are predominantly driven by the magnetic pressure gradient. In Chapter 6, tower jets are discussed as a result of dynamo generated magnetic field.

To summarize, the jet-launching mechanism can be described under the magneto-centrifugal framework, that is used throughout this work.

## 1.5 AIMS AND MOTIVATION

So far, the general mechanism of jet launching from magnetized disks has been studied by a number of authors. However, due to the complexity of the problem, the combined action of the various processes engaged could not be easily disentangled. Another problem arises if only a short-term evolution of the system is considered, as the initial evolution is mainly governed by the initial conditions.

One of the major aims of this thesis is to find what is the main agent that governs jet-launching

process. For this purpose a very robust setup for jet-launching is provided. It can be evolved up to, previously unimaginable timescales with a high resolution. Using this setup, the subtle analysis of the actual disk variables was developed. It allowed to disentangle two physically different processes in the disk: advection and diffusion of the magnetic flux, and find the main physical quantity that governs the disk–jet evolution.

The jet launching and collimation problem is usually addressed numerically applying a large-scale initial poloidal magnetic field. This holds in particular for simulations in which only the acceleration and collimation processes are studied, assuming the underlying disk as a boundary condition (Ustyugova et al. 1995; Ouyed & Pudritz 1997; Krasnopolsky et al. 1999; Fendt & Čemeljić 2002; Fendt 2006; Pudritz et al. 2006; Fendt 2009; Vaidya et al. 2009; Porth & Fendt 2010).

Also simulations treating the launching mechanism, i.e. simulations of the accretion-ejection process, that include the time evolution of the disk dynamics, so far have assumed a global large-scale magnetic field as initial condition (Shibata & Uchida 1985; Casse & Keppens 2002, 2004; Meliani et al. 2006; Zanni et al. 2007; Tzeferacos et al. 2009; Murphy et al. 2010; Sheikhnezami et al. 2012; Fendt & Sheikhnezami 2013).

These studies are also aimed to understand the interconnection between the jet and underlying disk properties. Unfortunately, the numerical studies remained rather fragmented, studying only a small subset of the highly dimensional problem of the jet launching. To determine the inter-relation between the jet and the underlying disk is one of the main objectives of this research. One of the major questions this study addresses can be simply stated: what kind of disks drive what kind of jets? The current setup, used throughout this work, allows to probe both the disk and the jet in a very broad parameter space, providing valuable dependencies between disk and jet properties.

As was mentioned above, there is a set of studies that uses the initially imposed magnetic field. However, it is still an open issue what is the exact structure and the strength of the magnetic field in the accretion disks, and where it comes from. Besides a central stellar magnetic field or advection of magnetic field from the ambient medium, a turbulent dynamo can be a major source of the disk magnetic field (Pudritz 1981b,a; Brandenburg et al. 1995). In order to study the disk dynamo in the context of outflow launching, only a few numerical experiments were performed in which the magnetic field was generated *ab initio* (Bardou et al. 2001; von Rekowski et al. 2003; von Rekowski & Brandenburg 2004). These authors were first to show how accretion disks start producing the outflows when the magnetic field is amplified by the dynamo to about its equipartition value.

A further motivation for considering a disk dynamo for jet launching is the time-dependent ejection of the jet material. For protostellar jets the typical timescale for ejection, derived from the

observed knot separation and jet velocity, are in the range of 10-100 years. The typical timescale of the jet launching area is, however, about 10-20 days, that is the Keplerian period of the inner disk. A time-variable dynamo can be responsible for changing the jet launching conditions on longer timescales.

Therefore, another objective of this thesis is to understand the origin of the magnetic field and the structural and temporal features the magnetic field possesses. The temporal variations of the dynamo can, in fact, lead to regeneration and reestablishing of the magnetic field in the disk and thus the outflow launched.

## 1.6 THESIS OUTLINE

This research investigates the interrelation between jet and underlying accretion disk and the generation of the disk magnetic field by the disk dynamo.

**CHAPTER 2** presents the basic equations used in this work. These are equations of resistive magnetohydrodynamics adapted for studying the dynamo related problem. The induction equation is modified to address the dynamo problem under the $\alpha\Omega$-dynamo framework. This chapter discusses the subtlety of the large-scale modeling of turbulence. Finally, the jet integrals – the conserved quantities along the jet – are provided.

**CHAPTER 3** describes the numerical approach used in this work to address the jet launching problem. First, the initial and boundary conditions are discussed, stressing the difference between the dynamo and non-dynamo simulations. Units and normalization are given in this chapter, that allows to scale the simulations onto the astrophysical objects. The chapter closes with the comments on the code that was used for all simulations performed in this work.

**CHAPTER 4** presents the so-called reference simulation of the disk-jet system. Using this high resolution setup, a very long evolution of the system has been studied and valuable results obtained. Among them, a crucial role of the disk magnetization has been disclosed, two main processes in the disk, namely, diffusion and advection, has been disentangled, and two different regimes of jet launching have been distinguished. This chapter follows from a publication Stepanovs & Fendt (2014a).

**CHAPTER 5** investigates what kind of jets are launched by what kind of disks. This chapter further studies the great importance of the disk magnetization, moving from the disk to the jet space. A striking interrelation between the jet properties, in terms of the jet integrals, and the degree of the underlying disk magnetization has been firmly established. This chapter also discusses how from the jet observables the magnetization of the underlying disk can be inferred. The corresponding example is also provided. This chapter follows from a paper submitted to the Astrophysical Journal Stepanovs & Fendt (2014b).

**CHAPTER 6** presents simulations of the disk-jet system in which the magnetic field is generated by the disk dynamo. It begins from exploring the dynamo setup and its difference from a non-dynamo one. Later, a toy-model that is aimed to model the episodic jet events, known as knots, is introduced. The main objective of this chapter is to explore the structure of the generated by the dynamo magnetic field. This chapter follows from the paper, accepted to publication Stepanovs et al. (2014).

**CHAPTER 7** summarizes the final results of the thesis and provides an outlook to the future research.

# 2

# Theoretical Background

This chapter describes the basic theoretical insights to the physical phenomena studied in this work. It begins with the equations of magnetohydrodynamics, that are used throughout the work (Section 1). The approach to model a turbulent diffusivity in large scale simulations is reviewed in Section 2. The induction equation examined in Section 3, where its adaptation for treating the dynamo problem is discussed. Finally, the steady state, axisymmetric MHD theory is discussed in the context of jet integrals (Section 4).

## 2.1 MHD Equations

In current work, the time-dependent, resistive MHD equations are solved on a spherical grid $(R, \Theta)$. $(r, z)$ are referred as cylindrical coordinates. The dynamics of a magnetized fluid is governed by the mass conservation,

$$\frac{\partial \rho}{\partial t} + \nabla \cdot (\rho \boldsymbol{V}) = 0, \tag{2.1}$$

with the plasma density $\rho$ and flow velocity $\boldsymbol{V}$, the momentum conservation,

$$\frac{\partial \rho \boldsymbol{V}}{\partial t} + \nabla \cdot \left[ \rho \boldsymbol{V}\boldsymbol{V} + \left( P + \frac{\boldsymbol{B} \cdot \boldsymbol{B}}{2} \right) I - \boldsymbol{B}\boldsymbol{B} \right] + \rho \nabla \Phi_{\mathrm{g}} = 0 \tag{2.2}$$

with the thermal pressure $P$ and the magnetic field $\boldsymbol{B}$. The central object of point mass $M$ has a gravitational potential $\Phi_g = -G\,M/R$. Note that equations are written in non-dimensional form, and, as usual, the factor $4\pi$ is neglected. The polytropic equation of state is applied, $P \propto \rho^\gamma$, with the polytropic index $\gamma = 5/3$.

The conservation of energy,

$$\frac{\partial e}{\partial t} + \nabla \cdot \left[ \left( e + P + \frac{\boldsymbol{B} \cdot \boldsymbol{B}}{2} \right) \boldsymbol{V} - (\boldsymbol{V} \cdot \boldsymbol{B})\boldsymbol{B} + \overline{\overline{\eta}} \boldsymbol{J} \times \boldsymbol{B} \right] = -\Lambda_{\rm cool}, \tag{2.3}$$

with the total energy density,

$$e = \frac{P}{\gamma - 1} + \frac{\rho \boldsymbol{V} \cdot \boldsymbol{V}}{2} + \frac{\boldsymbol{B} \cdot \boldsymbol{B}}{2} + \rho \Phi_g, \tag{2.4}$$

given by the sum of thermal, kinetic, magnetic, and gravitational energy, respectively. The electric current density is denoted by $\boldsymbol{J} = \nabla \times \boldsymbol{B}$. As shown by Tzeferacos et al. (2013), cooling may indeed play a role for jet launching, influencing both jet density and velocity. For the sake of simplicity, the cooling term is set equal to Ohmic heating, $\Lambda_{\rm cool} = -\overline{\overline{\eta}} \boldsymbol{J} \cdot \boldsymbol{J}$. Thus, all generated heat is instantly radiated away.

The evolution of the magnetic field is governed by the induction equation,

$$\frac{\partial \boldsymbol{B}}{\partial t} = \nabla \times (\boldsymbol{V} \times \boldsymbol{B} - \overline{\overline{\eta}} \boldsymbol{J}), \tag{2.5}$$

where the tensor $\overline{\overline{\eta}}$ is the magnetic diffusivity.

The system of MHD equations is closed by the solenoidal condition for the magnetic field

$$\nabla \cdot \boldsymbol{B} = 0. \tag{2.6}$$

The above mentioned induction equation (Equation 2.5) is used for the non-dynamo simulations. In order to properly treat the generation of the magnetic field by a dynamo, the induction equation has be be accordingly modified. This will be discussed later in this chapter.

## 2.2 MODELING TURBULENCE

Accretion disks are considered to be highly turbulent for any degree of the disk magnetization. The source of the turbulence is still debated, however, a great variety of unstable modes in magnetized accretion disks exists (Keppens et al. 2002). In the case of moderately magnetized disks,

the main candidate is the magneto-rotational instability (MRI; Balbus & Hawley 1991; Fromang 2013). Highly magnetized disks are subject to the Parker instability (Gressel 2010; Johansen & Levin 2008) and the trans-slow Alfvén continuum modes (Goedbloed et al. 2004).

Although, each year brings us closer in understanding of the turbulence, we are still far from the final theory. In principle, there are two approaches to treat the turbulence related problems. First, the small-scale simulations address the turbulence itself. For example, shearing box simulations of the accretion disks tries to address the issues of the angular momentum transport, or effective (turbulent) diffusivity as well as viscosity coefficients. Second, the large-scale simulations take the parameters of turbulence for granted. This approach allows studying astrophysical phenomena as a whole. The small-scale turbulence is not considered, though the large-scale effects are modeled by the effective coefficients of the diffusivity and dynamo. The simulations of this work belong to this category.

The puzzling question is the following: what is the effective diffusivity and viscosity the disk turbulence provides, and how can these effects be properly implemented under the mean field approach?

Though, extrapolating the results from a self-consistent, local treatment of turbulence to the mean field approach is not straightforward. In the local treatment, for example, the extraction of angular momentum is due to both turbulence – operating on small scales – and torques by the mean magnetic field on large scales. Thus, the removal of angular momentum goes hand in hand with destroying the turbulent magnetic field or the effective magnetic diffusivity. In case of the mean field approach, there is no small-scale turbulence and, thus, no angular momentum removal by local turbulent motions. Here, the diffusivity plays only a role for leveling the magnetic field gradient, thus setting the overall structure of the magnetic field. Unfortunately, we lack complete knowledge of the disk turbulence, thus the connection between the mean magnetic field and the fluctuating part, or, in other words, the relation between the mean magnetic field and the effective torques, and the diffusivity and viscosity that turbulence provides. When moving from a local turbulence approach to the mean field approach, the relevance of the model should be approved by the relevance of the magnetic field distribution itself, and not by the diffusivity model. However, one should keep in mind that the magnetic field strength and structure of real accretion disks are also not known. Therefore, when considering any simulation results, the diffusivity model applied should always be taken into account.

When the dynamo is included in the simulations, the picture becomes even more complicated. Now, the magnetic field can be amplified not only by the motion of the plasma, but also by a dynamo.

## 2.3 MEAN-FIELD INDUCTION EQUATION

The dynamo mechanism provides a means of converting kinetic energy into magnetic energy. In astrophysical context, by a dynamo one usually consider the generation of the magnetic field from a turbulent media. Turbulent dynamos have to be tackled via direct numerical simulations or by stochastic methods (Brandenburg & Subramanian 2005; Brandenburg et al. 2012).

However, large-scale dynamos can be treated if small-scale turbulence is averaged out. Parker (1955) was first who proposed the idea to incorporate the dynamo-effect by adding an extra term $\alpha \boldsymbol{B}$ into the induction equation. Later the rigorous theory for the $\alpha$-effect was developed by Krause & Rädler (1980). In the mean field theory one solves the Reynolds averaged equations, decomposing the velocity and magnetic fields into their mean and fluctuating parts,

$$\boldsymbol{V} = \bar{\boldsymbol{V}} + \boldsymbol{v} \qquad \boldsymbol{B} = \bar{\boldsymbol{B}} + \boldsymbol{b}, \tag{2.7}$$

where $\bar{\boldsymbol{V}}$ and $\bar{\boldsymbol{B}}$ are the mean velocity and magnetic fields, while $\boldsymbol{v}$ and $\boldsymbol{b}$ are their fluctuating parts. Substituting Equation 2.7 into the induction equation and averaging it yields the mean field induction equation,

$$\frac{\partial \boldsymbol{B}}{\partial t} = \nabla \times (\boldsymbol{V} \times \boldsymbol{B} + \bar{\mathcal{E}} - \overline{\overline{\eta}} \boldsymbol{J}), \tag{2.8}$$

where

$$\bar{\mathcal{E}} = \overline{\boldsymbol{v} \times \boldsymbol{b}} \tag{2.9}$$

is the mean electromotive force (EMF). In isotropic turbulence $\bar{\mathcal{E}} = 0$, however, in the presence of rotation and stratification $\bar{\mathcal{E}}$ can be finite (Krause & Rädler 1980).

In particular, mean field theory suggests that EMF has a components parallel to the magnetic field and currents

$$\bar{\mathcal{E}} = \alpha_{\mathrm{T}} \boldsymbol{B} - \eta_{\mathrm{T}} \boldsymbol{J}, \tag{2.10}$$

where subscript T reminds of the turbulent nature of the physical quantities.

Substitution of Equation 2.10 into the mean field induction equation (Equation 2.8) yields

$$\frac{\partial \boldsymbol{B}}{\partial t} = \nabla \times (\boldsymbol{V} \times \boldsymbol{B} + \overline{\overline{\alpha}}_{\mathrm{dyn}} \boldsymbol{B} - \overline{\overline{\eta}} \boldsymbol{J}), \tag{2.11}$$

where the tensor $\overline{\overline{\alpha}}_{\mathrm{dyn}}$ describes the $\alpha$-effect of the mean-field dynamo, and the tensor $\overline{\overline{\eta}}$ the magnetic diffusivity and both are of a turbulent nature.

There are, however, other non-linear processes that can, in principle, be incorporated into the model of the diffusivity and dynamo-effect. It is believed that when the magnetic field becomes sufficiently strong, the MRI modes become suppressed (Fromang 2013). On the other hand, a strong magnetic field may become buoyant, leading to the Parker instability. While the MRI is confined within the disk, the Parker instability operates closer to the surface of the disk where the toroidal magnetic field is stronger.

## 2.4 THE MAGNETIC DIFFUSIVITY MODEL

As mentioned above, a self-consistent study of the origin of the turbulence is beyond the scope of this study. Therefore, the $\alpha$-prescription (Shakura & Sunyaev 1973) for the magnetic diffusivity is applied, implicitly assuming that the diffusivity has a turbulent origin. The diffusivity profile can be extended up to one disk height above the disk surface (Figure 3.1).

In this study, the diffusivity tensor is composed by diagonal non-zero components,

$$\eta_{\phi\phi} \equiv \eta_{\rm P} \quad \eta_{\rm RR} = \eta_{\theta\theta} \equiv \eta_{\rm T}, \tag{2.12}$$

where $\eta_{\rm P}$ denote the poloidal magnetic diffusivity, and $\eta_{\rm T}$ the toroidal magnetic diffusivity, respectively [1].

In this work, different diffusivity models are examined, nevertheless, all of them can be represented in a following form,

$$\eta_{\rm P} = \alpha_{\rm ssm}(\mu) C_{\rm s} \cdot H \cdot F_\eta(z), \tag{2.13}$$

where the vertical profile of the diffusivity is described by a function

$$F_\eta(z) = \begin{cases} 1 & z \le H \\ \exp(-2(\frac{z-H}{H})^2) & z > H, \end{cases}$$

confining the diffusivity to the disk region.

Although this parameterization of diffusivity is commonly used (except the profile function $F_\eta(z)$), there are no clear constraints upon the value $\alpha_{\rm ssm}$ may take. As an example, King et al. (2007) discuss a magnitude of the turbulent $\alpha$-parameter derived from observations and simulations, indicating observational values $\alpha_{\rm ssm} \simeq 0.1..0.4$. Numerical models with zero net magnetic

[1] Note that the notation of toroidal and poloidal diffusivity follows the actual use in axisymmetric jet formation simulations. A more general notation, applicable also in three dimensions, would be that of azimuthal and meridional diffusivity

field usually provide low numerical values $\alpha_{\rm ssm} \simeq 0.01$, reaching at most $\alpha_{\rm ssm} \simeq 0.03$ (Stone et al. 1996; Beckwith et al. 2011; Simon et al. 2012; Parkin & Bicknell 2013). On the other hand, numerical modeling of the MRI applying a non-zero net magnetic field (Bai & Stone 2013) indicates substantially higher values, $\alpha_{\rm ssm} \simeq 0.08 - 1.0$, with a corresponding magnetization $\mu = 10^{-4}, 10^{-2}$.

Obviously, different functions of $\alpha_{\rm ssm}(\mu)$ will lead to different evolution. First, the well-known model for magnetic diffusivity used by many authors previously (Casse & Keppens 2004; Zanni et al. 2007; Sheikhnezami et al. 2012) is applied,

$$\eta_{\rm P} = \alpha_{\rm m} V_{\rm A} \cdot H \cdot F_{\eta}(z) \tag{2.14}$$

by setting $\alpha_{\rm ssm} = \alpha_{\rm m}\sqrt{2\mu}$, where $V_{\rm A} = B_{\rm P}/\sqrt{\rho}$ is the Alfvén speed, and $\mu$, $C_{\rm s}$, and $H$ are the magnetization, the adiabatic sound speed and the local disk height, respectively, measured at the disk midplane. $C_{\rm s}$ and $\alpha_{\rm ssm}$ are evolved in time, but for the sake of simplicity, $H$ ad $F_{\eta}(z)$ are kept constant in time, thus equal to the initial distribution. In Chapter 4, the revised model of the diffusivity – strong model – is examined, with $\alpha_{\rm ssm} \propto \mu^2$. However, as the dynamo simulations start from zero poloidal magnetic field, the diffusivity model has to be revised. In the case of dynamo simulations, the disk magnetization is estimated not only from the poloidal magnetic field component, but from the mean magnetic field in the entire disk.

In general, all components of the diffusivity tensor can be different from zero. In order to simplify the problem, it is common to set all non-diagonal components to zero. On the other hand, diagonal components can be different. As discussed later in Chapter 4, the anisotropy parameter $\chi \equiv \eta_{\rm T}/\eta_{\rm P}$ is prescribed to model anisotropy of the diffusivity in poloidal and toroidal directions.

It will be shown in Section 4, that there is not only upper limit for the anisotropy parameter, but also the lower limit. The anisotropy parameter is set to $\chi = 0.5$ for both non-dynamo and dynamo simulations.

## 2.5 JET INTEGRALS

The ability to express conserved quantities of the dynamical system not only simplifies the solution process, but brings a deeper understanding in the studied phenomenon. Astrophysical jets are not an exception. In axisymmetric, stationary, ideal MHD there are four conserved quantities along the jet or, more specifically, the magnetic flux surface $\Psi \equiv \int \vec{B}_{\rm p} \cdot d\vec{A}$. The conservation of the mass, results in the first conserved quantity, namely the mass load per flux surface

$$K(\Psi) = \frac{\rho V_{\rm P}}{B_{\rm P}}, \tag{2.15}$$

The so-called angular velocity of the field lines follows from the poloidal component of the induction equation

$$\Omega_{\rm F}(\Psi) = \frac{V_\phi}{r} - \frac{kB_\phi}{\rho r}, \tag{2.16}$$

Conservation of the angular momentum leads to the conservation of the specific angular momentum along the flux surface,

$$L(\Psi) = L_{\rm V} + L_{\rm B} = rV_\phi - \frac{rB_\phi}{K} \tag{2.17}$$

Finally, the conservation of the specific energy follows from the conservation of the energy along the flux surface,

$$E(\Psi) = \frac{V_\phi^2 + V_{\rm P}^2}{2} + \Phi_{\rm g} + h + (L - rV_\phi)\Omega_{\rm F} \tag{2.18}$$

There are two more derived integrals that are commonly used, namely

$$J(\Psi) = E - \Omega_{\rm F} L, \tag{2.19}$$

that contains only mechanical quantities and the maximum jet speed

$$V_{\rm inf} = \sqrt{2E}, \tag{2.20}$$

that may serve as an estimate for the maximum energy of jet propagation.

One should however keep in mind that these integrals are conserved starting only from the disk corona, where the magnetic diffusivity is negligible. Nevertheless, it is possible to predict the jet integrals by knowing what happens in the disk. In Chapter 5 the deep interrelation between the jet, namely the above-mentioned jet integrals, and the underlying disk magnetization is established.

# 3

# Numerical approach

This chapter describes the numerical approach to the jet launching problem. First, the initial and boundary conditions are discussed. Though, the numerical setup for dynamo and non-dynamo simulations is rather similar, the differences between these setups are particularly stressed. The corresponding units and normalization, that allow to scale the simulations for astrophysical application, are also provided. Finally, the details of the code and its specification used for all the simulations are provided.

## 3.1 Initial Conditions

The initial conditions follow from a standard setup, which has been applied in a number of previous publications (Zanni et al. 2007; Sheikhnezami et al. 2012; Fendt & Sheikhnezami 2013). The initial structure of the accretion disk is calculated as the solution of the steady state force equilibrium,

$$\nabla P + \rho \nabla \Phi_{\rm g} - \boldsymbol{J} \times \boldsymbol{B} - \frac{1}{R} \rho V_\phi^2 (\boldsymbol{e}_R \sin\theta + \boldsymbol{e}_\theta \cos\theta) = 0. \tag{3.1}$$

This equation is solved assuming radial self-similarity, i.e., assuming that all physical quantities $X$ scale as a product of a power law in $R$ with some function $F(\theta)$,

$$X \equiv X_0 R^{\beta_X} F(\theta). \tag{3.2}$$

Self-similarity requires in particular that the sound speed and the Alfvén speed scales as the Keplerian velocity, $V_\mathrm{K} \propto r^{-1/2}$, along the disk midplane. As a consequence, the power–law coefficients $\beta_X$ are determined as follows, $\beta_{V_\phi} = -1/2, \beta_\mathrm{P} = -5/2, \beta_\rho = -3/2$, and $\beta_{B_\mathrm{R}} = \beta_{B_\theta} = \beta_{B_\phi} = -5/4$.

An essential non-dimensional parameter governing the initial disk structure is the ratio $\epsilon$ between the isothermal sound speed $C_\mathrm{s}^\mathrm{T} = \sqrt{P/\rho}$ and the Keplerian velocity $V_\mathrm{K} = \sqrt{GM/r}$, evaluated at the disk midplane, $\epsilon = \left[C_\mathrm{s}^\mathrm{T}/V_\mathrm{K}\right]_{\theta=\pi/2}$. This quantity determines the disk thermal scale height $H_\mathrm{T} = \epsilon r$. It is generally initially assumed a thin disk with $\epsilon = 0.1$. Note that for the remainder of the thesis, when discussing the dynamical properties of disk and outflow, the *adiabatic sound speed* $C_\mathrm{s} = \sqrt{\gamma P/\rho}$ is considered. The geometrical disk height, namely the region where the density and rotation significantly decrease, is about $2\epsilon$ (see Figure 3.1). Therefore the geometrical disk height is defined as $H \equiv 2\epsilon r$.

Following Zanni et al. (2007), the simulation is initialized only with a poloidal magnetic field, defined via the vector potential $\boldsymbol{B} = \nabla \times A\boldsymbol{e}_\phi$, with

$$A = \frac{4}{3} B_{\mathrm{p},0} r^{-1/4} \frac{m^{5/4}}{(m^2 + ctg^2\theta)^{5/8}}. \tag{3.3}$$

The parameter $B_{\mathrm{p},0} = \epsilon\sqrt{2\mu_0}$ determines the strength of the initial magnetic field, while the parameter $m$ determines the degree of bending of the magnetic field lines. For $m \to \infty$, the magnetic field is purely vertical. As will be shown below, the long-term evolution of the disk–jet structure is insensitive to this parameter, since, due to advection and diffusion processes and the jet outflow, the magnetic field structure changes substantially over time. Therefore, in general, the bending parameter $m = 0.5$ .

The strength of the magnetic field is governed by the magnetization parameter

$$\mu = \left.\frac{B_\mathrm{P}^2}{2P}\right|_{\theta=\frac{\pi}{2}}, \tag{3.4}$$

the ratio between the poloidal magnetic field pressure and the thermal pressure, evaluated at the midplane, and is set to be constant with radius. As will be shown in Chapter 4, the magnetic field distribution substantially changes over time, while the disk–jet dynamics is governed by the actual disk magnetization. Typically, the initial magnetization is $\mu_0 \approx 0.01$ in this simulations.

Outside the disk, the gas and pressure distribution is defined as hydrostatic "corona,"

$$\rho_\mathrm{cor} = \rho_{\mathrm{cor},0} R^{-1/(\gamma-1)}, \qquad P_\mathrm{cor} = \frac{\gamma-1}{\gamma}\rho_{\mathrm{cor},0} R^{-\gamma/(\gamma-1)}, \tag{3.5}$$

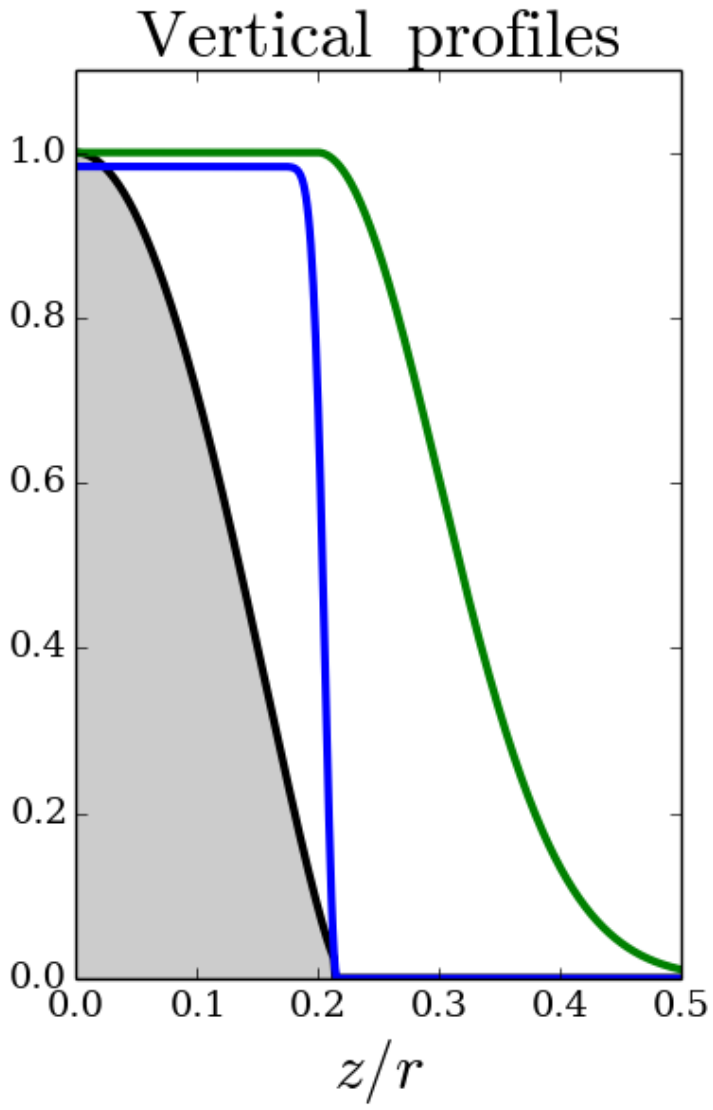


**Figure 3.1:** Initial vertical profiles of the disk quantities: density (black, blue shaded), rotational velocity (blue), and magnetic diffusivity $F_\eta$ (green). The magnetic diffusivity profile is set constant in time.

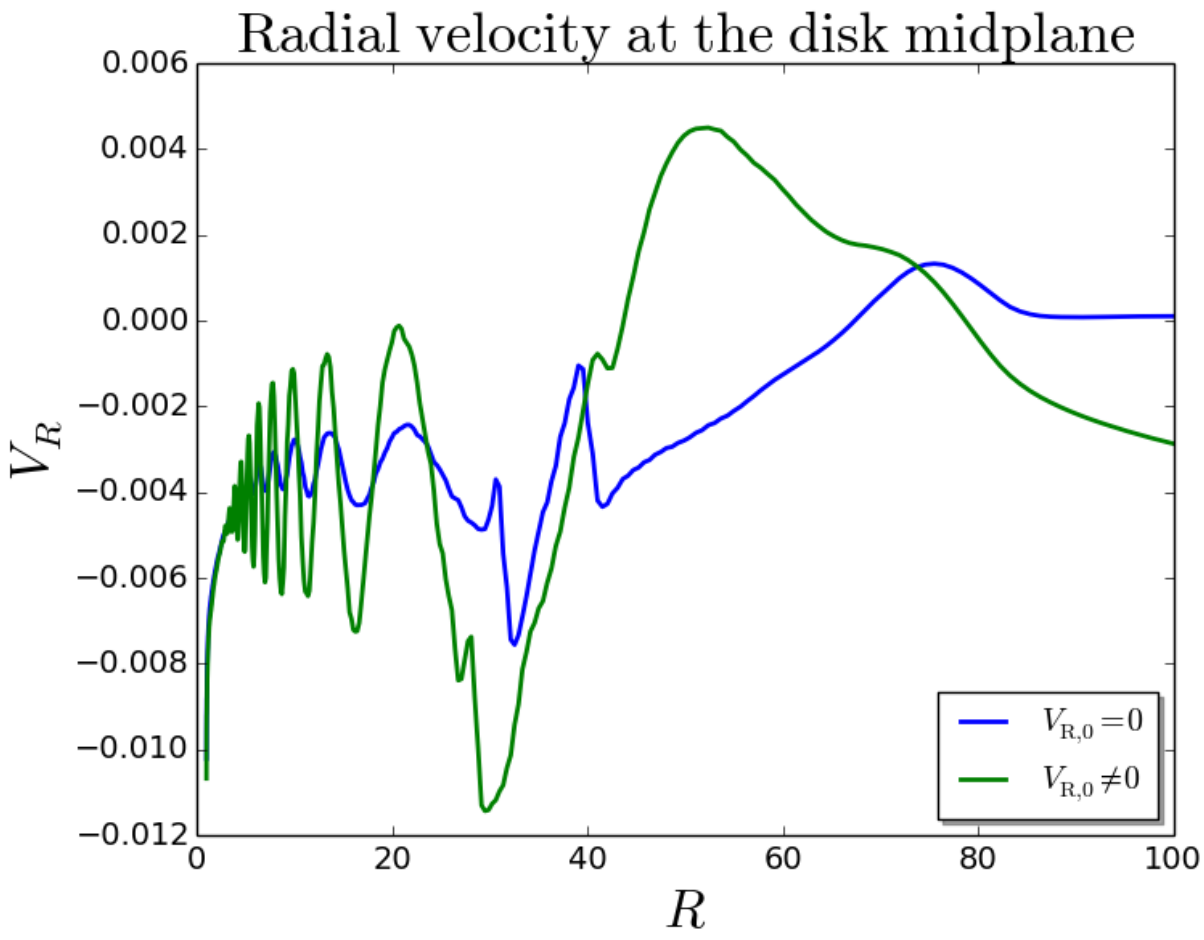


**Figure 3.2:** Accretion velocity profile along the disk midplane at $T = 1000$ and $T = 10000$ for the cases of zero and non-zero initial radial velocity.

where $\rho_{\rm cor,0} = \delta\rho_{\rm disk}(R = 1, \theta = \pi/2)$ with $\delta = 10^{-3}$.

Although it is common to define the initial accretion velocity, balancing the imposed diffusivity $V_R = \eta J_\phi / B_\theta$, it is not necessary for the chosen set of parameters. It can even disturb the initial evolution of the disk accretion. Accretion requires corresponding torques to be sustained and since there is no initial poloidal current defined, $B_\phi = 0$ (which takes time to build up from a weak poloidal field), a non-zero initial velocity will only lead to extra oscillations. Figure 3.2 illustrates this issue, showing two identical simulations with zero and non-zero accretion velocity. The origin of the oscillations for both cases is the inner boundary. The first wave of accretion is somehow bounced outward by the inner boundary and results in an oscillatory pattern. That the bouncing at the inner disk boundary is most likely caused by small inconsistencies between the boundary conditions and the intrinsic disk physics, a problem that may be present in other studies. Although they both result in the same final profile (a steady state has been reached only for small disk radii), the simulations with zero velocity profiles show fewer oscillations.

### 3.1.1 INITIAL CONDITIONS: DYNAMO CASE

Here the initial conditions in case of the dynamo simulations are briefly discussed. All dynamo simulations performed start from a very weak initial magnetization $\mu_{\rm init} = 10^{-5}$. Therefore the initial structure of the accretion disk can be obtained as the solution to the steady-state force equilibrium equation (Equation 3.1), neglecting the contribution by the Lorentz force ($\mu = 0$).

Assuming a self-similar disk structure this equation can be solved analytically.

All the simulations are initialized with a purely radial magnetic field, confined within the disk and defined via the vector potential $\vec{B} = \nabla \times A\vec{e_\phi}$, and

$$A = B_{\rm p,0} r^{-1} e^{-8z/H^2}. \tag{3.6}$$

The parameter $B_{\rm p,0} = \epsilon\sqrt{2\mu_{\rm init}}$ denotes the strength of the initial magnetic field, while $\epsilon = 0.1$ is ratio of isothermal sound[1] to Keplerian speed. Although this magnetic field distribution may be considered as somewhat artificial, it provides a smooth evolution during the initial phase. Simulations starting from a purely toroidal magnetic field as the initial condition showed very similar results.

In contrast, purely vertical magnetic field would generate strong currents at the disk surface region because of the strong initial shear between the rotating disk and the non-rotating corona. This would greatly impact the initial evolution of the accretion-ejection structure. As long as the

[1] Note however, that the adiabatic equation of state is used

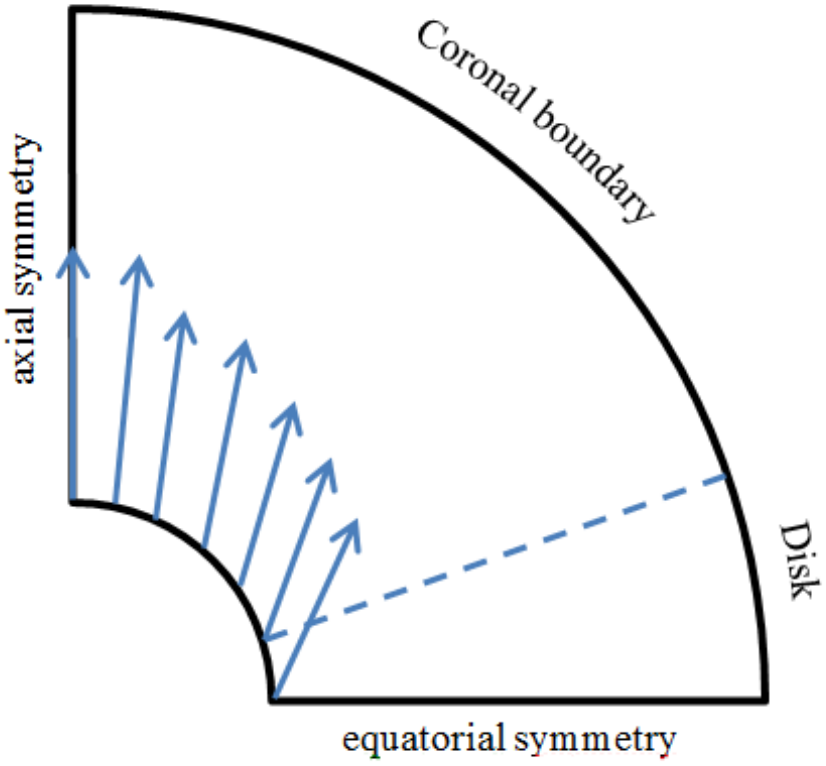


**Figure 3.3:** Illustration of the boundary conditions. Along the inner and outer radial boundaries, two zones – the corona and the disk region – are distinguished. Arrows represent the magnetic field distribution along the inner boundary, which is preserved by the boundary condition.

*initial* magnetization $\mu_{\rm init}$ is low, it does not play a substantial role for the initial disk evolution. This is the result of the exponential evolution of the magnetic field amplification by the dynamo.

## 3.2 BOUNDARY CONDITIONS

The standard symmetry conditions along the rotational axis and the equatorial plane has been applied. Along the radial boundaries of the domain, two different areas are distinguished. That is (1) a disk boundary for $\theta > \frac{\pi}{2} - 2\epsilon$,[2] and (2) a coronal boundary for $\theta < \frac{\pi}{2} - 2\epsilon$, and consider different conditions along them (see Figure 3.3).

Along the inner radial boundary for all simulations, a constant slope for the poloidal component

[2]Note, $2\epsilon \approx \text{arctg}(2\epsilon)$

**Table 3.1:** Inner and Outer Boundary Conditions.

| | $\rho$ | P | $V_R$ | $V_\theta$ | $V_\phi$ | $B_\mathrm{R}$ | $B_\theta$ | $B_\phi$ |
|---|---|---|---|---|---|---|---|---|
| Inner disk | $\sim r^{-3/2}$ | $\sim r^{-5/2}$ | $\sim r^{-1/2}, \leq 0$ | 0 | $\sim r^{-1/2}$ | Slope | Slope | $\sim r^{-1}$ |
| Inner corona | $\sim r^{-3/2}$ | $\sim r^{-5/2}$ | $0.2cos(\varphi)$ | $0.2sin(\varphi)$ | $\sim r^{-1/2}$ | Slope | Slope | 0 |
| Outer disk | $\sim r^{-3/2}$ | $\sim r^{-5/2}$ | Outflow, $\leq 0$ | Outflow | Outflow | div B =0 | Outflow | $\sim r^{-1}$ |
| Outer corona | $\sim r^{-3/2}$ | $\sim r^{-5/2}$ | Outflow, $\geq 0$ | Outflow | Outflow | div B =0 | Outflow | $\sim r^{-1}$ |
| Axis | Sym | Sym | Sym | Anti | Anti | Sym | Anti | Anti |
| Equator | Sym | Sym | Sym | Anti | Sym | Anti | Sym | Anti |

**Note.** Outflow is the zero gradient condition and the constant slope conditions are marked by "slope". Symmetric and anti-symmetric boundary conditions are marked by "Sym" and "Anti", respectively

of the magnetic field

$$\varphi = 70^\circ \left(1 + \exp(-\frac{\theta - 45^\circ}{15^\circ}\right)^{-1} \tag{3.7}$$

was imposed, where $\varphi$ is the angle with respect to the unit vector $\boldsymbol{e}_R$. The magnetic field direction is axial near the axis, $\theta = 0$, while at the inner disk radius the inclination is 70° with respect to the disk surface. A smooth variation of the magnetic field direction is prescribed along the inner radial boundary. This is in concordance with Pelletier & Pudritz (1992), who showed that for a warm plasma the maximum angle with respect to the disk surface necessary to launch outflows is about 70°, and slightly larger than for a cold plasma (Blandford & Payne 1982).

The method of constraint transport requires the definition of only a tangential component, thus to prescribe $B_\theta$ along the innermost boundary, while the normal component $B_\mathrm{R}$ follows from solving $\nabla \cdot \boldsymbol{B} = 0$. In order to implement the prescription of a constant magnetic field angle, $\nabla \cdot \boldsymbol{B} = 0$ is solved, taking into account the ratio of the cell-centered magnetic field components $B_\theta / B_\mathrm{R} = -\tan(\varphi)$. The integration is started from the axis ($\theta = 0$), where $B_\theta = 0$. Thus, by fixing the slope of the magnetic lines, the magnetic field strength is allowed to vary.

Along the inner coronal boundary, a weak inflow into the domain with $V_\mathrm{P} = 0.2$ is prescribed. This is applied to stabilize the inner coronal region between the rotational axis and the disk jet, since the interaction between the current carrying, magnetized jet and zero-$B_\phi$ coronal region may lead to some extra acceleration of the coronal gas. As shown by Meliani et al. (2006) the pressure of such an inflow (e.g., a stellar wind) may influence the collimation of the jet, changing the shape of the innermost magnetic field lines.

In order to keep the influence of the dynamical pressure of the inflow similar during the whole evaluation (and also for different simulations), the density of this inflow is set with respect to the disk density at the inner disk radius. The density of the inflow corresponds to a hydrostatic corona $\rho_{\rm infl} = \rho_{\rm cor} = \rho_{\rm disk}|_{\rm midplane}(t) \cdot \delta$, where $\delta = 10^{-3}$. The inflow direction is aligned with the magnetic field direction. By choosing a denser inflow the time step of the simulations is also increased by approximately three times, as the Alfvén speed in the coronal region lowers.

By varying the slope of the magnetic field $\varphi$ along this inner corona in the range of 60–80 deg, it showed that it only slightly affects the slope of the innermost magnetic field lines. The global structure of the magnetic field is instead mainly governed by the diffusivity model. Since the inner boundary by design models the magnetic barrier of the star, a rather steep slope was chosen in order to avoid the disk magnetic flux entering the coronal region.

Across the inner disk boundary (that is the accretion boundary), density and pressure are both extrapolated by power laws, applying $\rho R^{-3/2} = const$ and $PR^{-5/2} = const$, respectively. Both the toroidal magnetic field as well as the toroidal velocity components are set to vanish at the inner coronal boundary, $B_\phi = 0$, $V_\phi = 0$. For the inner disk boundary, the condition $B_\phi \sim 1/r$ ($J_\theta = 0$) are applied, and the radial and the toroidal velocities are extrapolated by power laws, $V_R R^{-1/2} = const$, and $V_\phi R^{-1/2} = const$, respectively, while $V_\theta = 0$.

For the inner disk boundary, only negative radial velocities are allowed, making the boundary to behave as a "sink," thus absorbing all material that is delivered by the accretion disk at the inner disk radius.

As the application of spherical coordinates provides an opportunity to use a much larger simulation domain compared to cylindrical coordinates, the outer boundary conditions have little influence on the evolution of the jet launched from the very inner disk. Therefore $\rho$ and $P$ are extrapolated with the initial power laws and apply the standard PLUTO outflow conditions for $V_R$, $V_\theta$, and $V_\phi$ at the outer boundary, thus, zero gradient conditions. $B_\phi \sim 1/r$ ($J_\theta = 0$) are further required for the toroidal magnetic field component, while a simple outflow condition is set for $B_\theta$. Again, $B_{\rm R}$ is obtained from the $\nabla \cdot \boldsymbol{B} = 0$.

For the radial velocity component, the coronal region, where positive velocities $V_R \geq 0$ are required, is distinguished from the disk region, where negative velocities $V_R \leq 0$ are enforced.

As the application of a spherical geometry is new in this context, the boundary conditions are summarized in the Table 3.1.

### 3.2.1 BOUNDARY CONDITIONS: DYNAMO CASE

In this subsection, the boundary conditions in case of the dynamo simulations are briefly discussed.

In case of the dynamo simulations, the only change is made for the coronal region of the inner boundary. Here, the magnetic flux is not allowed to penetrate the inner coronal region, thus not only $B_\phi = 0$, but also $B_R = 0$. Since the magnetic field vanishes in that area, a purely radial profile of the inflow into the corona is prescribed (in contrast to an inflow aligned to the magnetic field considered previously), keeping the same inflow velocity $V_R = 0.2$.

Since the magnetic field is suppressed in the inner coronal region, the shear in the area between the coronal region and the disk boundary can develop strong electric currents. This makes the region between the axis and the jet subject to small-scale perturbations, especially in the runs with high resolution. On the other hand, the jet launching area of the inner disk always shows a smooth, stable, and non-fluctuating evolution.

## 3.3 NUMERICAL GRID AND NORMALIZATION

No physical scales are introduced in the equations above. The results of the simulations will be presented in non-dimensional units. All variables, namely $P, \rho, \boldsymbol{V}$, and $\boldsymbol{B}$, are normalized to their values at the inner disk radius $R_0$. Lengths are given in units of $R_0$, corresponding to the inner disk radius. Velocities are given in units of $V_{\mathrm{K},0}$, corresponding to the Keplerian speed at $R_0$. Thus, $2\pi T$ corresponds to one revolution at the inner disk radius. Densities are given in units of $\rho_0$, corresponding to $R_0$. Pressure is measured in $P_0 = \epsilon^2 \rho_0 V_0^2$.

Thus the scale-free simulations may apply to a variety of jet sources. In the following, the physical scaling concerning three different object classes – brown dwarfs (BDs), YSOs, and AGNs is provided. In order to properly scale the simulations, the following masses for the central object are varied, $M = 0.05 M_\odot$ (BD; Whelan et al. 2011), $M = 1 M_\odot$ (YSO; Ray et al. 2007), $M = 10^8 M_\odot$ (AGN,Kormendy & Richstone 1995). The typical scales for the inner disk radius are

$$\begin{aligned} R_0 &= 0.1\,\mathrm{AU} \quad \text{(YSO)} \\ &= 0.01\,\mathrm{AU} \quad \text{(BD)} \\ &= 20\,\mathrm{AU}\left(\frac{R_0}{10 R_\mathrm{S}}\right)\left(\frac{M}{10^8 M_\odot}\right) \quad \text{(AGN)}, \end{aligned} \tag{3.8}$$

**Table 3.2:** Typical Parameter Scales for Different Sources. Simulation results will be given in code units and can be scaled for astrophysical application.

| | YSOs | BDs | AGNs | Unit |
|---|---|---|---|---|
| $R_0$ | 0.1 | 0.01 | 20 | AU |
| $M_0$ | 1 | 0.05 | $10^8$ | $M_\odot$ |
| $\rho_0$ | $10^{-10}$ | $10^{-13}$ | $10^{-12}$ | g cm$^{-3}$ |
| $V_0$ | 94 | 66 | $6.7 \times 10^4$ | km s$^{-1}$ |
| $B_0$ | 15 | 0.5 | 1000 | G |
| $T_0$ | 1.7 | 0.25 | 0.5 | days |
| $\dot{M}_0$ | $3 \times 10^{-5}$ | $2 \times 10^{-10}$ | 10 | M$_\odot$ yr$^{-1}$ |
| $\dot{J}_0$ | $3.0 \times 10^{36}$ | $1.5 \times 10^{30}$ | $3 \times 10^{51}$ | dyne cm |
| $\dot{E}_0$ | $1.9 \times 10^{35}$ | $6.7 \times 10^{29}$ | $2.6 \times 10^{46}$ | erg s$^{-1}$ |

where $R_S = 2GM/c^2$ is the Schwarzschild radius of the central black hole. For consistency with the non-relativistic approach, $R_0 > 10R_S$ is required, implying that highly relativistic outflows cannot be properly treated. In the case of YSOs, the choice of $R_0$ is supported by the observations (Pinte et al. 2008), however the inner structure of the BDs and AGNs is still under debate.

The Keplerian speed at the inner disk radius is normalized by,

$$\begin{aligned} V_{K0} &= 94\,\mathrm{km\,s^{-1}} \left(\frac{M}{M_\odot}\right)^{1/2} \left(\frac{R_0}{0.1\mathrm{AU}}\right)^{-1/2} \quad \text{(YSO)} \\ &= 66\,\mathrm{km\,s^{-1}} \left(\frac{M}{0.05M_\odot}\right)^{1/2} \left(\frac{R_0}{0.01\mathrm{AU}}\right)^{-1/2} \quad \text{(BD)} \\ &= 6.7 \times 10^4\,\mathrm{km\,s^{-1}} \left(\frac{R_0}{10R_S}\right)^{-1/2} \quad \text{(AGN)} \end{aligned} \tag{3.9}$$

the time unit which is expressed in units of $T_0 \equiv R_0/V_{K0}$,

$$\begin{aligned} T_0 &= 1.7\,\mathrm{days} \left(\frac{M}{M_\odot}\right)^{-1/2} \left(\frac{R_0}{0.1\mathrm{AU}}\right)^{3/2} \quad \text{(YSO)} \\ &= 0.24\,\mathrm{days} \left(\frac{M}{0.05M_\odot}\right)^{-1/2} \left(\frac{R_0}{0.01\mathrm{AU}}\right)^{3/2} \quad \text{(BD)} \\ &= 0.5\,\mathrm{days} \left(\frac{R_0}{10R_S}\right)^{3/2} \quad \text{(AGN)} \end{aligned} \tag{3.10}$$

The mass accretion rate is a parameter which is, in principle, accessible by observation. Thus, the normalization of density $\rho_0$ can be chosen by setting suitable accretion rates $\dot{M}_0 = R_0^2 \rho_0 V_{\mathrm{K0}}$. Assuming Assuming $\dot{M}_{\mathrm{acc}} \simeq 10^{-7}\,\mathrm{M}_\odot\,\mathrm{yr}^{-1}$ (YSO) $\dot{M}_{\mathrm{acc}} \simeq 10^{-12}\,\mathrm{M}_\odot\,\mathrm{yr}^{-1}$ (BD) $\dot{M}_{\mathrm{acc}} \simeq 10\,\mathrm{M}_\odot\,\mathrm{yr}^{-1}$ (AGN) and taking into account that the typical accretion rates the simulations provide are of the order of $\dot{M}_{\mathrm{acc}} \simeq 0.01$ (in code units), one gets

$$\begin{aligned}
\dot{M}_0 &= 3\times 10^{-5}\mathrm{M}_\odot\,\mathrm{yr}^{-1}\left(\frac{\rho_0}{10^{-10}\frac{\mathrm{g}}{\mathrm{cm}^3}}\right)\left(\frac{M}{M_\odot}\right)^{1/2}\left(\frac{R_0}{0.1\mathrm{AU}}\right)^{3/2} \qquad \text{(YSO)}\\
&= 2\times 10^{-10}\mathrm{M}_\odot\,\mathrm{yr}^{-1}\left(\frac{\rho_0}{10^{-13}\frac{\mathrm{g}}{\mathrm{cm}^3}}\right)\left(\frac{M}{0.05M_\odot}\right)^{1/2}\left(\frac{R_0}{0.01\mathrm{AU}}\right)^{3/2} \qquad \text{(BD)}\\
&= 10\,\mathrm{M}_\odot\,\mathrm{yr}^{-1}\left(\frac{\rho_0}{10^{-12}\frac{\mathrm{g}}{\mathrm{cm}^3}}\right)\left(\frac{M}{10^8 M_\odot}\right)^{1/2}\left(\frac{R_0}{10R_{\mathrm{S}}}\right)^{3/2} \qquad \text{(AGN)}
\end{aligned} \tag{3.11}$$

The torques and powers are given in units of $\dot{J}_0 = R_0^3 \rho_0 V_{\mathrm{K0}}^2$ and $\dot{E}_0 = R_0^2 \rho_0 V_{\mathrm{K0}}^3$ respectively:

$$\begin{aligned}
\dot{J}_0 &= 3.0\times 10^{36}\mathrm{dyne\,cm}\left(\frac{\rho_0}{10^{-10}\frac{\mathrm{g}}{\mathrm{cm}^3}}\right)\left(\frac{M}{M_\odot}\right)\left(\frac{R_0}{0.1\mathrm{AU}}\right)^{2} \qquad \text{(YSO)}\\
&= 1.5\times 10^{30}\mathrm{dyne\,cm}\left(\frac{\rho_0}{10^{-13}\frac{\mathrm{g}}{\mathrm{cm}^3}}\right)\left(\frac{M}{0.05M_\odot}\right)\left(\frac{R_0}{0.01\mathrm{AU}}\right)^{2} \qquad \text{(BD)}\\
&= 1.2\times 10^{51}\mathrm{dyne\,cm}\left(\frac{\rho_0}{10^{-12}\frac{\mathrm{g}}{\mathrm{cm}^3}}\right)\left(\frac{M}{10^8 M_\odot}\right)^{3}\left(\frac{R_0}{10R_{\mathrm{S}}}\right)^{2} \qquad \text{(AGN)}
\end{aligned} \tag{3.12}$$

$$\begin{aligned}
\dot{E}_0 &= 1.9\times 10^{35}\mathrm{erg\,s}^{-1}\left(\frac{\rho_0}{10^{-10}\frac{\mathrm{g}}{\mathrm{cm}^3}}\right)\left(\frac{M}{M_\odot}\right)^{3/2}\left(\frac{R_0}{0.1\mathrm{AU}}\right)^{1/2} \qquad \text{(YSO)}\\
&= 6.7\times 10^{29}\mathrm{erg\,s}^{-1}\left(\frac{\rho_0}{10^{-13}\frac{\mathrm{g}}{\mathrm{cm}^3}}\right)\left(\frac{M}{0.05M_\odot}\right)^{3/2}\left(\frac{R_0}{0.01\mathrm{AU}}\right)^{1/2} \qquad \text{(BD)}\\
&= 2.6\times 10^{46}\mathrm{erg\,s}^{-1}\left(\frac{\rho_0}{10^{-12}\frac{\mathrm{g}}{\mathrm{cm}^3}}\right)\left(\frac{M}{10^8 M_\odot}\right)^{2}\left(\frac{R_0}{10R_{\mathrm{S}}}\right)^{1/2} \qquad \text{(AGN)}
\end{aligned} \tag{3.13}$$

The magnetic field is normalized to its midplane values $B_0 = \sqrt{8\pi P_0 \mu}$,

$$\begin{aligned} B_0 &= 15\mathrm{G}\left(\frac{\mu}{0.1}\right)^{1/2}\left(\frac{\epsilon}{0.1}\right)\left(\frac{\rho_0}{10^{-10}\frac{\mathrm{g}}{\mathrm{cm}^3}}\right)^{1/2}\left(\frac{M}{M_\odot}\right)^{1/2}\left(\frac{R_0}{0.1\mathrm{AU}}\right)^{-1/2} \quad \text{(YSO)} \\ &= 0.5\mathrm{G}\left(\frac{\mu}{0.1}\right)^{1/2}\left(\frac{\epsilon}{0.1}\right)\left(\frac{\rho_0}{10^{-13}\frac{\mathrm{g}}{\mathrm{cm}^3}}\right)^{1/2}\left(\frac{M}{0.05M_\odot}\right)^{1/2}\left(\frac{R_0}{0.01\mathrm{AU}}\right)^{-1/2} \text{(BD)} \\ &= 1\mathrm{kG}\left(\frac{\mu}{0.1}\right)^{1/2}\left(\frac{\epsilon}{0.1}\right)\left(\frac{\rho_0}{10^{-12}\frac{\mathrm{g}}{\mathrm{cm}^3}}\right)^{1/2}\left(\frac{M}{10^8 M_\odot}\right)^{1/2}\left(\frac{R_0}{10R_\mathrm{S}}\right)^{-1/2} \text{(AGN)} \end{aligned} \tag{3.14}$$

Table 3.2 summarizes the typical scales for leading physical variables.

Numerical grid was chosen to have equidistant spacing in the $\theta$ direction, but stretched cell sizes in the radial direction, considering $\Delta R = R\Delta\theta$. The computational domain of a size $R = [1, 1500R_0], \theta = [0, \pi/2]$ is discretized with $(N_R \times N_\theta)$ grid cells. A general resolution of $N_\theta = 128$ is used. In order to cover a factor 1500 in radius, $N_R = 600$ is applied. This gives a resolution of 16 cells per disk height ($2\epsilon$) in the general case. However, a resolution study was also performed, applying a resolution two times as high (or low), thus using $256 \times 1200$ (or $64 \times 300$) cells for the whole domain, or 35 (9) cells per disk height.

## 3.4 NUMERICAL CODE PLUTO

All numerical calculations performed in this work are carried out with astrophysical code PLUTO (Mignone et al. 2007), version 4.0, PLUTO is a finite-volume/finite-difference, shock-capturing code designed to integrate a system of conservation laws

$$\frac{\partial \boldsymbol{U}}{\partial t} = -\nabla \cdot T(\boldsymbol{U}) + S(\boldsymbol{U}), \tag{3.15}$$

where $\boldsymbol{U}$ represents a set of conservative quantities, $T(\boldsymbol{U})$ is the tensor "flux" and $S(\boldsymbol{U})$ defines the source terms. The explicit form of $\boldsymbol{U}$, $T(\boldsymbol{U})$ and $S(\boldsymbol{U})$ depends on the particular physics module selected. Among them are classical hydrodynamics, special relativistic hydrodynamics, ideal/resistive magnetohydrodynamics, special (ideal) relativistic magnetohydrodynamics. PLUTO comes in two flavors: static and adaptive grids.

In this work, the resistive MHD equations are solved on a static spherical grid.

Numerical integration of the conservation law (Equation 3.15) is performed through shock-capturing schemes using the finite volume formalism. In general, Equation 3.15 is solved in four steps. First, conservative variables $\boldsymbol{U}$ are transferred into primitive variables $\boldsymbol{V}$. On the second step, cell-centered primitive variables $\boldsymbol{V}$ are interpolated onto cell faces. The code provides different methods of interpolation. The piecewise parabolic method of Colella & Woodward (1984) is applied for all simulations. On the next step, a Riemann problem at zone edges is solved. Again, the code provides a number of different solvers, characterized by different numerical diffusivity. The Harten–Lax–van Leer Riemann solver (Toro et al. 1994) is used for all simulations presented. On the last step, the conservative law is further evolved in time. For this purpose, a third-order order Runge–Kutta scheme is applied.

Such a general scheme does not necessarily preserve the solenoidal condition of the magnetic field. For this purposes, the code allows choosing different methods that properly keep the divergence-free condition. Since the generation of the magnetic field by its own is the purpose of current work, the method Constrained Transport (Londrillo & del Zanna 2004), that directly evolves the magnetic field potential using Stoke's theorem. This method by definition ensures the magnetic field being divergence-free.

The Courant–Friedrichs–Lewy condition is satisfied by using a CFL number of 0.4.

As the PLUTO code is a open-source software written in C, it allows further modification of the code. The code has been modified for treating a dynamo related problem. For this purpose, the extra dynamo-term was added into the induction equation (see Chapter 6).

# 4

# Modeling Disks and Jets: from the launching area to propagation scales*

This chapter presents the reference simulation of the disk-jet system. Using this high resolution setup, a very long evolution of the system has been studied and valuable results obtained. Among them, a crucial role of the disk magnetization has been disclosed, two main processes in the disk, namely, diffusion and advection, has been disentangled, and two different regimes of jet launching has bet distinguished.

## 4.1 Introduction

Astrophysical jets as highly collimated beams of high–velocity material and outflows of a small degree of collimation and a lower speed are a ubiquitous phenomenon in a variety of astrophysical sources. The role of magnetic fields in the realm of jets and accretion disks cannot be

*This chapter is based on a paper published in the Astrophysical Journal by Deniss Stepanovs and Christian Fendt; titled: Modeling MHD Accretion-Ejection – from the Launching Area to Propagation Scales (Stepanovs & Fendt 2014a). All the simulations, the figures and most of the scientific discussion and interpretation presented in this chapter were done by the author of the thesis.

underestimated. It is crucial for the launching, acceleration, and collimation of jets (see, e.g., Blandford & Payne 1982; Pudritz & Norman 1983; Uchida & Shibata 1985; Camenzind 1990; Pelletier & Pudritz 1992; Sauty & Tsinganos 1994; Ustyugova et al. 1995; Fendt & Camenzind 1996; Ouyed & Pudritz 1997; Pudritz et al. 2007; Fendt 2009) . However, due to the complexity of the physical problem, the exact time evolution and geometry of these processes is still under debate.

Jets and outflows from young stellar objects (YSOs) and active galactic nuclei (AGNs) clearly affect their environment, and, thus, at the same time the formation process of the objects that are launching them (see, e.g., Banerjee et al. 2007; Gaibler et al. 2012). However, in order to quantify the feedback phenomenon – namely, to specify how much mass, angular momentum, and energy is being ejected into the surrounding via the outflow channel – it is essential to model the physics in the innermost launching area of the disk–jet system with a high resolution. It is commonly accepted that ejection and accretion are tightly connected to each other (Li 1995; Ferreira & Pelletier 1995). The study of these phenomena is also motivated by the observed correlation between accretion and ejection signatures (Cabrit et al. 1990).

This chapter discusses these topics, and will provide a relation between actual magnetization within the disk and the ejection to the accretion ratio for mass and energy.

The first numerical simulations of this kind were presented by Casse & Keppens (2002, 2004), who demonstrated how an outflow can be self-consistently launched out of the accretion disk, accelerated to high velocity and collimated in a narrow beam. Later, Meliani et al. (2006) studied in particular the impact of a central stellar wind on the accretion disk magnetic field inclination. The work by Zanni et al. (2007) revealed the great importance of the underlying disk diffusivity, namely, the strength of diffusivity and its directional anisotropy. Studying two limits of rather high and low diffusivity, and keeping the same (about equipartition) magnetic field strength and field structure, the authors found that a steady state of the simulation could not be reached for an arbitrary combination of these parameters. Tzeferacos et al. (2009) in particular found that the efficiency of the launching mechanism is strongly dependent on the disk magnetization.

A common assumption was that in order to launch jets, the magnetic field should be rather strong, about the equipartition value. This question was investigated in detail by Murphy et al. (2010), demonstrating that jets could be driven even with a weak magnetization of $\mu \approx 0.002$.

So far, the general mechanism of jet launching from magnetized disks has been studied by a number of authors. However, due to the complexity of the problem, the combined action of the various processes engaged could not be easily disentangled. Another problem arises if only a short-term evolution of the system is considered, as this will be strongly dependent on the initial conditions. What is somewhat complicating the interpretation of simulations in the literature is that the model setup is usually categorized by the initial parameters, and not by the actual

quantities such as the actual disk magnetization, accretion velocity, etc. at a certain evolutionary time. The latter was first discussed by Sheikhnezami et al. (2012), however, the parameter space applied in those simulations was rather limited. The present study will show that it is the actual disk properties, in particular, the disk magnetization, that govern the accretion and ejection.

As shown by Hawley et al. (1995) and later adapted by Casse & Keppens (2004); Meliani et al. (2006), the turbulent energy and angular momentum flux is dominated by the magnetic stress rather than the Reynolds stress. Thus, in the presence of a moderately strong magnetic field the Reynolds stress becomes less important. In order to disentangle the complex behavior and keep the simulations simple, only non-viscous disks are examined.

Considering the accretion–ejection scenario, before any general relation between physical quantities can be claimed, it is essential that the system itself has dynamically evolved over a sufficiently extended period of time. Therefore the simulations were evolved for at least 10.000 dynamical times. It will be shown that such a long simulation requires that the advective and diffusive processes must be well in balance.

The following approach was applied. First, the standard diffusivity model (see, e.g., Zanni et al. 2007) was considered. After having obtained a near equilibrium solution with advection and diffusion in balance, the state of the system was closely examined. Essentially, it is the balance between diffusion and advection that governs the strength of the actual disk magnetization. The latter appears to be the key ingredient for the evolution of the entire system. Exploring a wide range of the actual disk magnetization allows to derive a general correlation between the actual disk magnetization and major quantities of the disk–jet system, such as the mass and energy ejection efficiencies.

A model setup that is well suited for a long-term evolution study of the jet launching problem is also presented. The use of spherical geometry provides a high resolution in the inner region of the disk – the site of jet launching – and a low resolution for the outer regions, where the physical processes typically evolve on much longer timescales.

This chapter is organized as follows. Section 2 describes the diffusivity model that is used in the simulations. Section 3 discusses the reference simulation, which is characterized by the balance between advection and diffusion, and uses the standard diffusivity model. Section 4 presents a detailed analysis of jet launching disks, revealing the major role of the disk magnetization in the disk–jet evolution. Section 5 discusses the simulations applying a new diffusivity model that essentially overcomes the accretion instability observed in the previous simulations. This allows to follow the evolution of the disk–jet system substantially longer. Finally, Section 6 summarizes the results.

## 4.2 THE MAGNETIC DIFFUSIVITY MODEL

Accretion disks are considered to be highly turbulent, subject to the MRI in moderately magnetized disks (Balbus & Hawley 1991; Fromang 2013), and the Parker instability (Gressel 2010; Johansen & Levin 2008) for stronger magnetized disks. It is believed that when the magnetic field becomes sufficiently strong, the MRI modes become suppressed (Fromang 2013). On the other hand, a strong magnetic field may become buoyant, leading to the Parker instability. While the MRI is confined within the disk, the Parker instability operates closer to the surface of the disk where the toroidal magnetic field is stronger.

As a self-consistent study of the origin of the turbulence is beyond the scope of this study, a $\alpha$-prescription (Shakura & Sunyaev (1973)) for the magnetic diffusivity is applied. It is implicitly assumed that the diffusivity arises from the turbulence of the underlying disk.

The reference simulation, extensively presented in current chapter, uses a commonly used prescription of the diffusivity $\eta_{\rm P} = \alpha_{\rm m} V_{\rm A} \cdot H \cdot F_\eta(z)$. This can be seen as a particular case of more general parametrization of $\eta_{\rm P} = \alpha_{\rm ssm}(\mu) C_{\rm s} \cdot H \cdot F_\eta(z)$, by applying $\alpha_{\rm ssm} = \alpha_{\rm m}\sqrt{2\mu}$. $C_{\rm s}$ and $\alpha_{\rm ssm}$ are evolved in time, but for the sake of simplicity, $H$ and $F_\eta(z)$ are kept constant in time, thus equal to the initial distribution. The main reason is to avoid additional feedback, which favors the accretion instability (see below, or, e.g., Campbell 2009). The test simulations evolving the disk height in time in fact indicate the rise of such instability earlier than in the case of a fixed-in-time disk diffusivity aspect ratio.

In order to overcome the accretion instability, the strong diffusivity model is introduced, that is discussed in later sections of this chapter.

### 4.2.1 ANISOTROPIC DIFFUSIVITY

The anisotropy parameter $\chi \equiv \eta_{\rm T}/\eta_{\rm P}$ quantifies the different strength of diffusivity in poloidal and toroidal directions. In the literature it is common to assume $\chi$ of the order of unity. Considering viscous disks, Casse & Ferreira (2000) showed that there is a theoretical limit for $\eta_{\rm T}$, namely $\eta_{\rm T} > \eta_{\rm P}$. Highly resolved disk simulations indeed suggest $\chi \simeq 2...4$ (Lesur & Longaretti 2009), implying that the toroidal field component is typically diffusing faster than the poloidal component.

The majority of simulations in the literature consider a magnetic field strength in equipartition with the gas pressure. However, also studying weakly magnetized disks, it was shown that there is also an upper limit for the anisotropy parameter, above which the simulations show irregular behavior. On the other hand, it was pointed out by several authors (see, e.g., Zanni et al. 2007)

that in case of a very low anisotropy parameter (thus, a weak toroidal diffusivity), the simulations might suffer from instabilities caused by strong pinching forces. Nonetheless, the existence of an upper limit for the anisotropy parameter was so far obscured by other processes.

Assuming a steady state and combining the poloidal component of the diffusion equation, $M_R = \alpha_{\rm ssm} H J_\phi / B_{\rm P}$, with the relation for the Mach number $M_R = 2/\sqrt{\gamma} H J_R / B_{\rm P} \mu_{\rm act}$ (see below, Königl & Salmeron 2011), an interrelation between the toroidal and poloidal electric currents can be derived,

$$\frac{J_\phi}{J_R} = \frac{\sqrt{2\mu}}{\sqrt{\gamma}\alpha_{\rm m}}. \tag{4.1}$$

This relation has been proven to approximately hold for all of the simulations performed, thus indicating that a steady state has indeed been reached. Since the only free parameter in this relation is $\alpha_{\rm m}$, the choice of $\alpha_{\rm m}$ governs the ratio of the electric current components.

As shown previously (Ferreira & Pelletier 1995; Ferreira 1997; Ferreira & Casse 2013) the toroidal component of the induction equation can be written as

$$\eta_{\rm T} J_R|_{\rm mid} = -R^2 \int_0^{2\epsilon} \mathbf{B}_{\rm P} \cdot \nabla \mathbf{\Omega} d\varphi - V_\theta B_\phi \tag{4.2}$$

(here expressed for spherical coordinates), where $J_R$ is computed at the disk midplane. This equation essentially states that the induction of the toroidal magnetic field component (from twisting the poloidal component) is balanced by the diffusion through the disk midplane and by the flux escaping through the disk surface. The $V_\theta B_\phi$ terms are not neglected, considering the assumption of a thin disk (Ferreira & Casse 2013), as it is of key importance in the simulations, in particular in the regime of a moderately strong magnetic field, $\mu \geq 0.1$.

Assuming that the induction of the magnetic field is primarily due to radial gradients, the radial component of the magnetic field can be approximated by a power law, $B_{\rm R} \propto R^{-5/4}$, and Equation 4.2 may be transformed into $\eta_{\rm T} J_R|_{\rm mid} \simeq B_{\rm R} C_{\rm s} - V_\theta B_\phi$, or

$$(\alpha_{\rm ssm}\chi - M_\theta) J_R \simeq \frac{B_{\rm R}}{H}, \tag{4.3}$$

where

$$M_\theta = -V_\theta^+ / C_{\rm s} \tag{4.4}$$

is denoted as the ejection Mach number, where $V_\theta^+$ is measured at the disk surface.

Using relation 4.1 between the poloidal and toroidal electric currents and defining the curvature part of the toroidal current $J_\phi^{\rm curv} \equiv B_{\rm R}/H$, one may derive a constraint for the anisotropy

parameter,

$$\frac{J_\phi^{\rm curv}}{J_\phi} \simeq \left(\alpha_{\rm m}\chi - \frac{M_\theta}{\sqrt{2\mu}}\right)\alpha_{\rm m} \leq 1. \tag{4.5}$$

Any magnetic field geometry that is outwardly bent and has a decreasing field strength in the outward direction has to satisfy this relation, as $J_\phi$ consists of two positive terms, the gradient and the curvature. In cases where the vertical velocity term can be neglected (e.g., for a very weak magnetic field with $\mu \leq 0.02$), the anisotropy parameter is $\chi < 1/\alpha_{\rm m}^2$, which, for the choice of $\alpha_{\rm m}$, is about 0.4. By probing the $\chi$ parameter space, it was found that in order to obtain a stable accretion-outflow configuration for weakly magnetized disks, the $\chi$ should be in the range $0.3 - -0.7$. Therefore $\chi = 0.5$ was set for all of the simulations. Note that in simulations applying an anisotropy parameter $\chi \geq 0.7$, there is a problem that the poloidal magnetic field lines were "moving" rapidly, such that the bending of the field lines along the disk midplane was actually inverted. This is a result of the combined effects of a strong outward diffusion and low torques at the midplane. On the other hand, in case of a rather low anisotropy parameter, the accretion is rapid and the jet does establish a steady behavior.

The reason why the commonly chosen anisotropy $\chi > 1$ leads to a steady behavior is rather simple. As the disk magnetization grows during advection, the ejection Mach number grows as well ($M_\theta \propto 6\mu$ saturating at a level of 0.8; see below). Thus, in the case of a high disk magnetization – usually assumed in the literature – the above mentioned upper limit for the anisotropy parameter is satisfied. In the case of weak magnetic field simulations, performed, for example, by Murphy et al. (2010), this limit is most likely satisfied by additional viscous torques.

## 4.3 A REFERENCE SIMULATION

In this section, the reference simulation is presented. The aims were two-fold. First, with the new setup it was possible to increase both the period of time evolution and the spatial extension of jet-launching conditions considerably compared to previous works. Second, with the long-term evolution simulations, it was possible to investigate the interrelation between the actual disk properties such as magnetization, the ejection to accretion ratios of mass and energy, jet velocity, and others. This has not been done in the past, as most papers have compared the initial parameters of the simulations. As shown by Sheikhnezami et al. (2012), both the magnetization and diffusivity may substantially change during the disk evolution, and the parameters for the initial setup $\mu_0$ or $\alpha_{\rm ssm}$ are not sufficient to characterize the disk–jet system.

In order to uniquely specify the initial conditions for the simulation, a number of non-dimensional characteristic parameters is prescribed. The initial disk height is set by $\epsilon$. For all simulations,

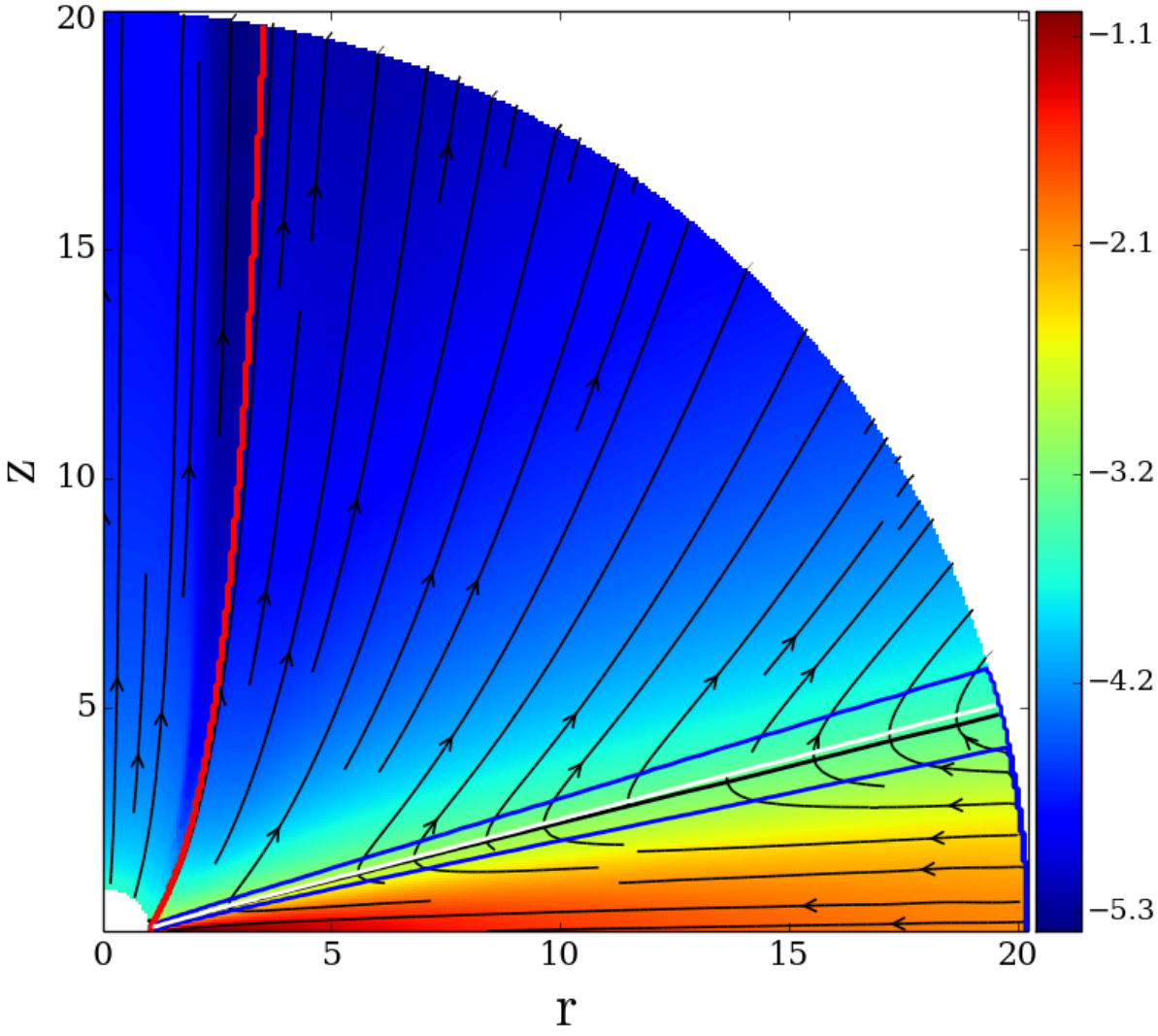


**Figure 4.1:** Physically different regions of the disk–jet structure at $t = 10,000$. Shown is the mass density (in logarithmic scale) and streamlines of the poloidal velocity (black lines with arrows). The red line marks the magnetic field line rooted at in innermost area of the midplane. The upper blue line separates an area where $V_p \| B_p$ from the disk. The accretion and ejection areas are separated with white ($V_r = 0$) and black ($F_\phi = 0$) lines, respectively. The lower blue line separates the accretion area where $V_r >> V_\theta$ from the rest of the structure.

**Table 4.1:** Comparison of The Simulations with Simulations Performed by Other Authors

| Reference | Cell/2$\epsilon$ | $\epsilon$ | $m$ | $\alpha_{\rm m}$ | $\chi$ | $\mu_0$ | $\mu_{\rm act}$ |
|---|---|---|---|---|---|---|---|
| Casse & Keppens (2004) | 0.5 | 0.1 | | $< 1$ | 1 | $\simeq 1$ | $\cdots$ |
| Zanni et al. (2007) | 2.5 | 0.1 | 0.35 | 0.1 ... 1.0 | 1, 3 | 0.3 | $\cdots$ |
| Tzeferacos et al. (2009) | 2.5 | 0.1 | 0.4 | 0.1 ... 1.0 | 3, 100 | 0.1–3.0 | $\cdots$ |
| Sheikhnezami et al. (2012) | 8.0 | 0.1 | 0.4 | 1.0 | 1/3, 3 | 0.002–0.1 | $\cdots$ |
| This work, ref. simulation | 16 | 0.1 | 0.2–0.9 | 1.1–1.9 | 0.5 | 0.003–0.03 | 0.001–0.5 |
| This work, resolution study | 24.5 | 0.1 | 0.2–0.9 | 1.1–1.9 | 0.5 | 0.003–0.03 | 0.001–0.5 |

**Note.** The resolution is estimated for the *inner* disk ($R = 1$)

$\epsilon = 0.1$ was applied. The initial strength and structure of the magnetic field is set by $\mu_0$ and $m$, respectively. In all simulations, $m = 0.5$ was chosen.

As it will shown below, the initial disk magnetization can fail to characterize the jet-launching process, but it is responsible for the overall disk torques. The main reason is that the magnetization in the inner disk, from which the main jet is being launched, changes very quickly. However, the magnetic field in the overall disk is primarily set by the initial magnetization.

In these simulations $\mu_0 = (0.003, 0.01, 0.03)$ are examined.

The model for diffusivity is chosen by selecting the distribution $\alpha_{\rm ssm}(\mu)$ and the anisotropy parameter $\chi$. The anisotropy parameter $\chi = 0.5$ is set for all simulations. A standard diffusivity model (Equation 2.14) is applied, thus the diffusivity is set only by the $\alpha_{\rm m}$ parameter. As will be shown later, the simulations are very sensitive to this parameter. If not stated otherwise, $\alpha_{\rm m} = 1.65$.

The reference simulation is referred as to the setup with $\epsilon = 0.1, m = 0.5, \mu_0 = 0.01, \alpha_{\rm m} = 1.65, \chi = 0.5$. Usually, the simulations run until $t = 10,000$, corresponding to about 1600 orbits at the inner disk radius.

Figure 4.2 shows the time evolution of the disk–jet structure of the reference simulation. Note that here only a small cylindrical part of a much larger, spherical domain is presented. Although a broad parameter space is explored, the evolution for this simulation can be seen as typical.

The first snapshot shows the initial state – a hydrodynamic disk in force-balance, the non-rotating hydrostatic corona in pressure equilibrium with the disk, and the initial non-force-free magnetic field. After some 1000 revolutions, the inner parts of the disk-outflow reaches a quasi-steady

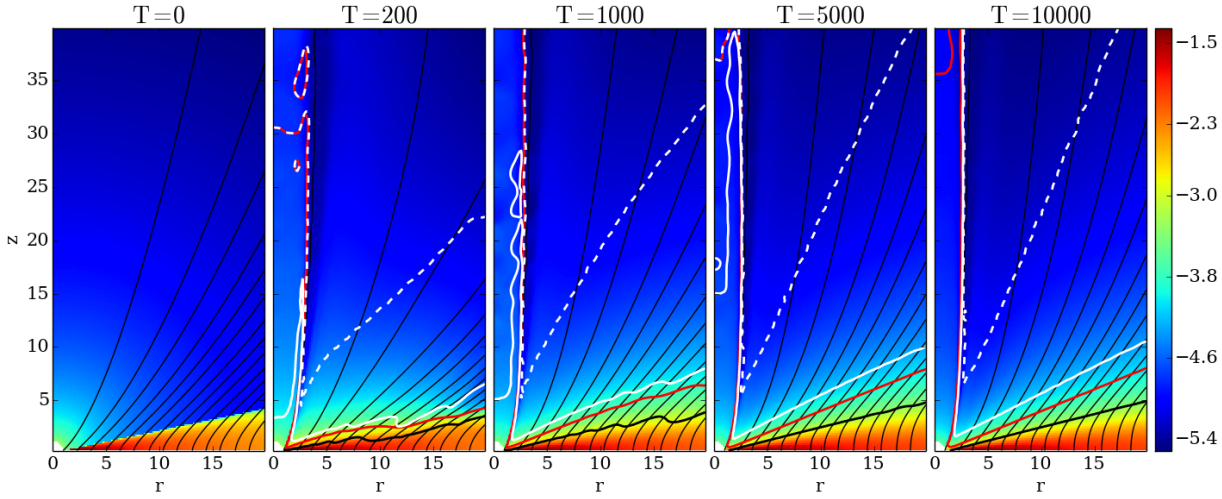


**Figure 4.2:** Time evolution of the disk–jet structure for the reference simulation. Shown is the evolution of the density (by colors, in logarithmic scale), the poloidal magnetic field lines (thin black lines), the disk surface (thick black line) the sonic (red line), the Alfvén (white line), and the fast Alfvén (white dashed line) surfaces.

state. However, it takes a much longer time for the outer parts to reach such a state. The outflow, initiated at early times and constantly accelerated, finally reaches a super-fast magnetosonic speed. The outflow-launching area along the disk surface grows with time. However, the parts of the outflow being launched from larger disk radii are less powerful.

This reference simulation applying typical parameters from the literature can be re-established very well by the presented approach. Using a spherical setup, the resolution in the inner part of the disk is higher than in the literature, and the simulations run substantially longer than any other simulation published previously. The presented simulations behave very robustly. There are two main reasons for that. First, the spherical geometry does well resolve the inner part of the disk, from which the dominant part of the jet is launched, but smooths out the small-scale perturbations in the outer disk. By that, perturbations arising throughout the disk are diminished. Second, the choice for the diffusivity parameter $\alpha_{\rm m}$ allows the simulations to evolve into a quasi-steady state in which advection is balanced by diffusion. However, even with such an optimized numerical setup (the reference setup), the simulations show some irregular behavior typically at about 30,000 time units. The reason is that since the current diffusivity model is prone to the accretion instability (see Lubow et al. 1994, and section below), the simulations are always in a state of marginal stability. As a consequence, the simulations evolve into a state of either high or low magnetization. In case of high magnetization the structure of the inner disk is being drastically changed and the current model of diffusivity cannot be applied. In the opposite case of weak magnetization, stable jets cannot be sustained.

In the following, different components of the disk–jet system and the jet-launching and acceleration mechanism will be discussed. It will be shown how certain disk properties, such as the location of the disk surface or the mass fluxes in the physically different areas are measured. The role of the diffusivity, the strength, and geometry of the magnetic field is explored in respect to the outflow and accretion rates.

### 4.3.1 COMPARISON TO PREVIOUS SIMULATIONS

In the Introduction, the literature of accretion–ejection simulations was already discussed. In this section, specific details in which presented simulations differ from previous works are explicitly emphasized.

- A spherical grid has been applied, offering the opportunity of a much larger domain size as well as much higher resolution *in the inner part* of the disk. A new set of boundary conditions is used which is adapted to the spherical grid.
- A continuous range of simulation parameters was explored. In particular, the interrelations between the *actual* flow parameters, rather than an interrelation to the *initial* values are discussed.
- Altogether, the presented model setup allows very long-term simulations on a large grid – so far the simulations run for approximately 30,000 time units for a standard diffusivity model, and more than 150,000 time units for the modified strong diffusivity model.
- The inflow (into the coronal region) density is allowed to vary in time, thus keeping the ratio between the inflow and the disk densities $\delta$ the same as initially.

A vast range of the parameter space that covers the majority of simulations performed in the literature (see Table 4.1) was explored. Similar to all these papers, a thin disk with $\epsilon = 0.1$ is assumed. It is common to assume a magnetic diffusivity parameter $\alpha_{\rm m}$ of about unity. In current case, values $\alpha_{\rm m} = 1.1...1.9$ were applied. For the magnetic field bending parameter, $m = 0.5$ was chosen, which is slightly higher than the values usually adapted, $m = 0.35...0.4$. Although it is finally shown that $m$ plays only a minor role, the current choice is motivated by the fact that this value is more consistent with the inner boundary condition. The magnetic diffusivity anisotropy parameter $\chi$ is chosen to be smaller than unity, since it helps to keep sufficiently strong torques at the midplane and the bending of the magnetic field that supports launching.

Although the simulation are started from a moderately weak initial magnetic field, the actual field strength in the inner disk at a certain radius may vary substantially over time. This allows to

study the interrelation between disk accretion and ejection physics and the actual magnetic field strength (thus the actual disk magnetization).

### 4.3.2 Disk Structure and Disk Surface

The disk surface is defined as a surface where the *radial velocity changes sign*. In a steady state, the area where the radial velocity and the magnetic torque changes sign is almost identical.

Figure 4.1 shows the typical structure of the disk–jet system. Several, physically different regions can be distinguished – the inflow area, the jet acceleration area, the launching area, and the accretion domain. These are separated by colored lines. The white and black lines mark the disk surface that separates disk and corona regions. Two other lines separate the accretion, launching, and acceleration areas. The accretion region is defined as the area where velocity is mainly radial, $V_\theta < 0.1 V_R$, and the acceleration region as the area where the flow velocity is parallel to the magnetic field, $\sin(\text{angle}(\boldsymbol{B}, \boldsymbol{V})) < 0.1$. The region in between is characterized as the launching area.

In the simulations, the position of the disk surface as defined above remains about constant in time. This confirms the choice of the control volume (see below) and our choice to fix the diffusive scale height during the simulation.

According to the boundary conditions, a weak inflow into the region between the inner disk radius and the rotational axis, is prescribed. This inflow provides the matter content as well as the pressure balance along the rotational axis. The astrophysical motivation can be the presence of a central stellar magnetic field or a stellar wind. In Figure 4.1, the inflow area is the area between the rotational axis and the red line that marks the magnetic field line rooted in the inner disk radius at the midplane. In all figures below, the magnetic field line closest to the axis always corresponds to the magnetic field line anchored at the inner disk radius.[1]

### 4.3.3 Launching Mechanism

Here the jet-launching mechanism in the reference simulation is discussed, that is – as in previous simulations – the Blandford–Payne magneto-centrifugal driving.

[1] Note that there are magnetic field lines that still penetrate the disk, but are not rooted at the disk midplane. These lines originate from inside the inner disk radius and are considered as intermediate between the axial coronal region and the main disk outflow. The pure inflow, which is prescribed from the coronal region along the inner boundary, is moving with the injection speed, and thus is not accelerated.

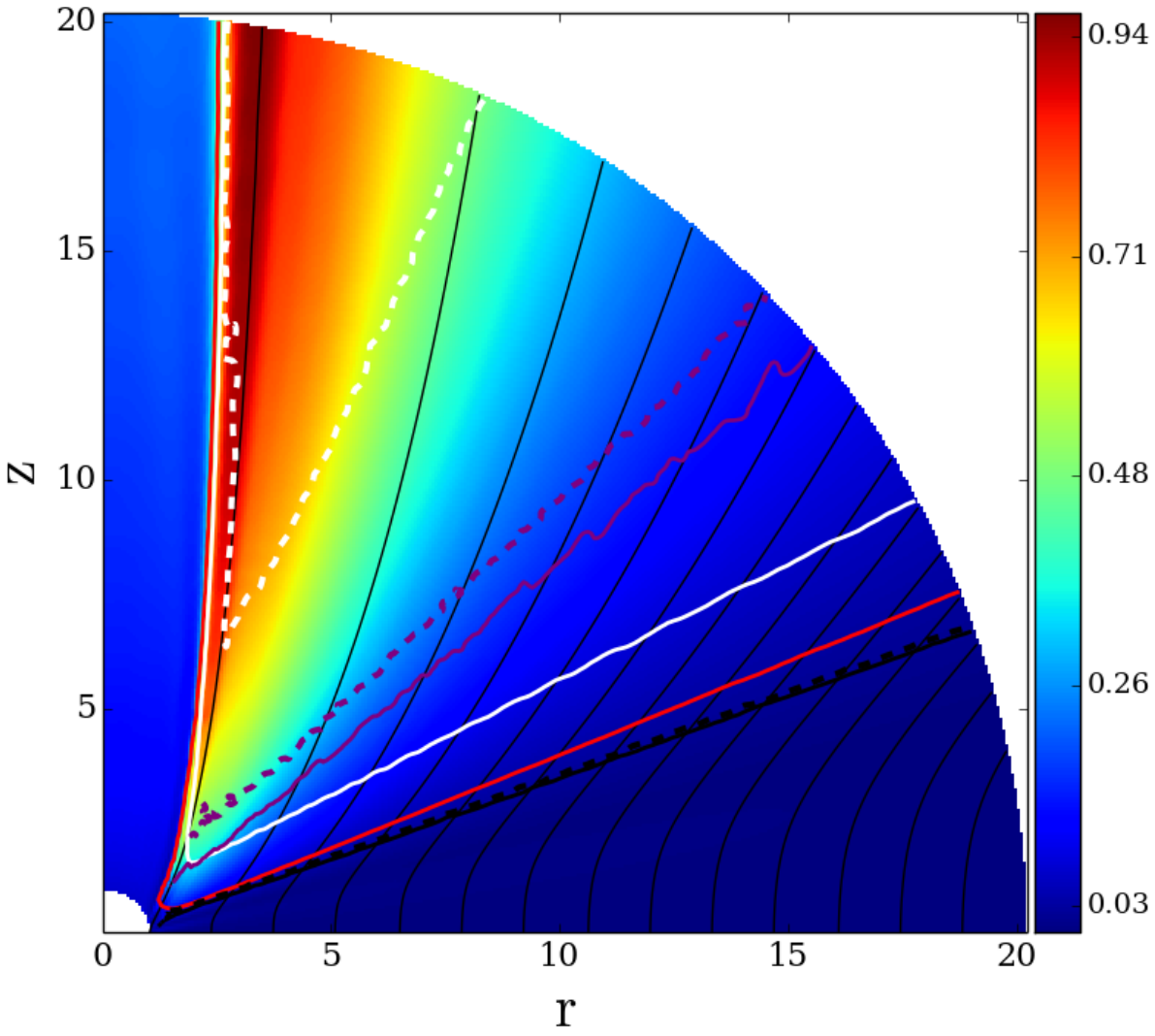


**Figure 4.3:** Importance of the Lorentz force with respect to the pressure and centrifugal forces for the reference simulation at $T = 10,000$. Shown are the poloidal speed (different colors), the poloidal magnetic field (black thin lines), Alfvén (white), fast-magnetosonic (dashed white), sonic (red) surfaces. The thick black lines denote the surface where the Lorentz force is equal to the pressure force components: parallel (dashed) and perpendicular (solid) to the magnetic field. The thick purple lines denote the surface where the Lorentz force is equal to the centrifugal force components: parallel (dashed) and perpendicular (solid) to the magnetic field. The thick black lines denote the ratios of the Lorentz to the pressure forces components: parallel (left) and perpendicular (right) to magnetic field.

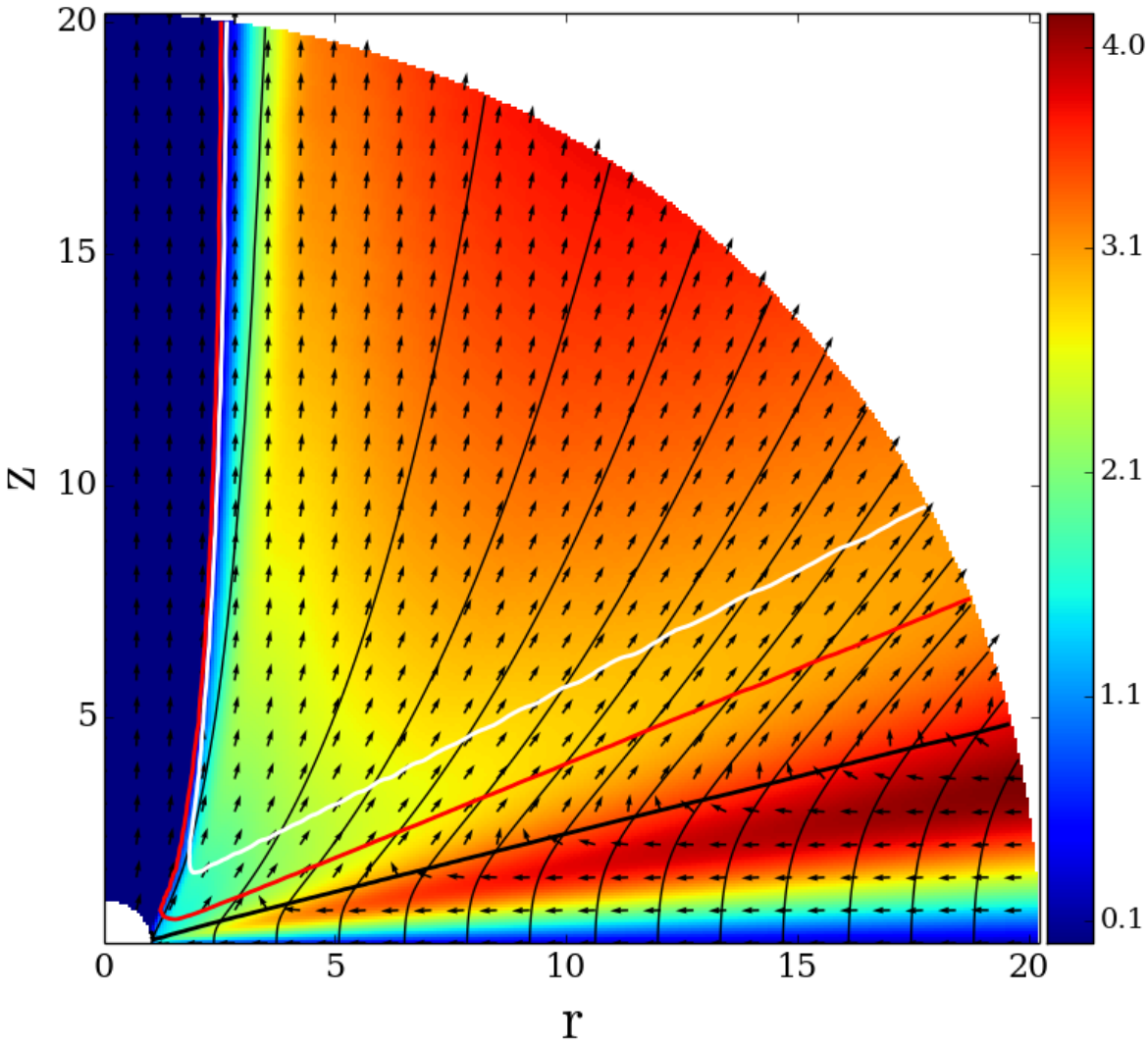


**Figure 4.4:** Ratio of the toroidal to the poloidal magnetic field for the reference simulation at $T = 10,000$. The lines represent the disk (thick black line) the sonic (red line), the Alfvén (white line) surfaces. Arrows show the normalized velocity vectors.

As demonstrated above (see Figure 4.1), the magnetic torque $rF_\phi$ changes sign on the disk surface. It is negative in the disk and positive in the corona. Thus, the magnetic field configuration established extracts angular momentum from the disk. The angular momentum extraction relies on the induced toroidal magnetic field component, which plays a key role in transferring the angular momentum $\sim B_r B_\phi$. Gaining angular momentum, the material that is loaded to the field lines from the accretion disk is pushed outward by the centrifugal force.

In order to illustrate the acceleration process, the magnitude of Lorentz force with respect to the thermal pressure and centrifugal forces are shown. Figure 4.3 shows the contours where the perpendicular and parallel components of the Lorentz force are equal to the perpendicular and parallel components of the pressure and centrifugal forces, respectively. In the accretion disk, both the pressure and the centrifugal forces dominate the poloidal component of the Lorentz force. Below the disk surface, the Lorentz force (toroidal component) extracts the angular momentum from the disk.

Since the Lorentz force increases along the outflow, it is worth checking the decomposed Lorentz force components $F = \nabla \times B \times B$ in the directions parallel and perpendicular to the magnetic field (Ferreira 1997). The ratio between the toroidal and parallel components of the magnetic field,

$$\frac{F_\parallel}{F_\phi} = -\frac{B_\phi}{B_\mathrm{P}}, \tag{4.6}$$

is shown in Figure 4.4. The centrifugal force is stronger in the inner area of the disk rather than in the outer parts of the disk.

At the sonic surface, the Lorentz force overcomes the pressure forces. From this point on, the main acceleration force is the centrifugal force. Further along the outflow – between the Alfvén surface and the fast surface – the Lorentz force becomes the main accelerating force.

### 4.3.4 CONTROL VOLUME

In this section, the control volume for calculating fluxes is described. In the $\theta$ direction the control volume is enclosed by the disk surface (as defined above), $S_S$, and the disk midplane. The two other surfaces that enclose the control volume are marked by $S_1$ and $S_R$, and correspond to the vertical arcs at the innermost disk radius ($R = 1$) and at any other radius $R$. The control volume defined by these surfaces is denoted by $V(R)$.

The flux of a physical quantity is defined as being positive if it increases this quantity in the control volume. The flux of a physical quantity is defined as being positive if it decreases this quantity of the control volume. The factor of two in front of the integrals takes into account the fact that only one hemisphere is treated. Note also a minus sign in front of the integrals.

### 4.3.5 Mass Flux Evolution

Here the mass flux evolution, namely the accretion and ejection rates, is explored.

The disk mass enclosed by a radius $R$ of the control volume (Section 4.3.4) follows from

$$M(R) = 2 \int_{V(R)} \rho dV, \tag{4.7}$$

while the mass accretion rate at a certain radius $R$ is

$$\dot{M}_{\rm acc}(R) = -2 \int_{S_1}^{S_R} \rho \boldsymbol{V}_p \cdot d\boldsymbol{S}, \tag{4.8}$$

and the mass ejection rate is integrated along the disk surface,

$$\dot{M}_{\rm ej}(R) = -2 \int_{S_S} \rho \boldsymbol{V}_p \cdot d\boldsymbol{S}. \tag{4.9}$$

It is common to introduce the ejection index $\xi$, which is based on the mass conservation law for a steady solution (Ferreira & Pelletier 1995). It basically measures the steepness of the radial profile of the accretion rate along the midplane. Setting the outer radius to $r$ and the inner radius to unity, the ejection index interrelates ejection and accretion,

$$\frac{\dot{M}_{\rm ej}}{\dot{M}_{\rm acc}} = 1 - r^{-\xi}. \tag{4.10}$$

The ejection index is obtained by a linear approximation of $\xi = -\log(1 - \dot{M}_{\rm ej}/\dot{M}_{\rm acc})/\log(r)$ within $r = [2, 10]$ The higher the ejection index, the higher the fraction of accreted matter being ejected within a given radius, and the less matter reaches the inner boundary. For the reference simulation $\xi \simeq 0.3$ at $T \simeq 10.000$.

Although the disk continuously loses mass (Figure 4.5), after dynamical times 1000–2000 the disk mass loss is much smaller that the corresponding ejection and accretion rates. Therefore the simulation is considered as evolving through a series of quasi-steady states. A continuous disk mass loss is a typical feature of a simulation like the reference simulation. This is because the mass accretion from outside some outer disk radius is not able to sustain the mass that is lost by accretion and ejection within this radius. It was also found that the standard diffusivity model typically leads to a magnetic field distribution in the disk that is almost constant in time (not in space). These two facts result in an increase of the disk magnetization in the inner disk, which in turn leads to more rapid accretion in the inner disk.

Figure 4.5 shows the time evolution of the mass accretion and ejection rates. Note also the general decrease of the mass fluxes over time, which is a direct consequence of the decrease of

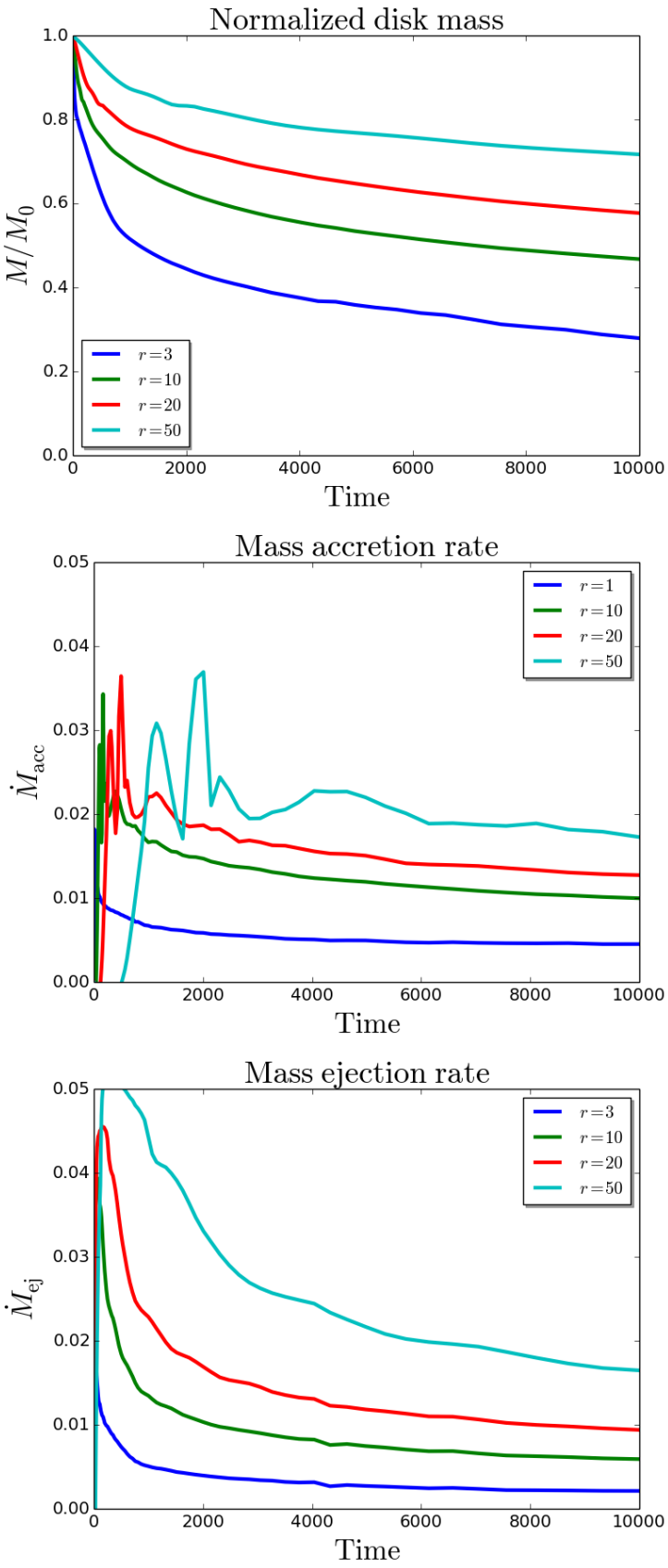


**Figure 4.5:** Time evolution of the disk mass (left), the mass accretion rate (middle), and the mass ejection rate (right) of the reference simulation at different radii.

the disk mass. The behavior and actual values of the mass fluxes are typical in the literature. One should note two distinct features of the mass fluxes. First, the higher integration volume, the higher the mass ejection rate. Second, in jet-launching disks the mass accretion rate must increase with the radius. These plots also indicate that the evolution of the system can be seen as a consecutive evolution through a series of quasi-steady states.

### 4.3.6 Magnetic Field Bending Parameter Study

Here the simulations investigating the influence of the initial magnetic field bending parameter $m$ are discussed. The bending parameter $m$ was varied from 0.2 (strongly inclined) to 0.9 (almost vertical).

The main result is that although the simulations initially evolve slightly differently, in the long-term they are almost indistinguishable.

Figure 4.6 shows the time evolution of the ejection to accretion mass flux ratio. The fluxes are again computed for the control volume extending to $R = 10$. It seems to take a few 1000 dynamical time steps for the simulation to lose the memory of the initial magnetic field configuration, but at $T = 10,000$ convergence has obviously been reached. This is also true for the fluxes of angular momentum and energy, and holds as well for the corresponding flux ratios.

The reason why the simulations convergence into a single, specific, configuration is the fact that it is mainly the diffusivity model that governs the evolution of the magnetic field evolution. When the simulations start with the same initial magnetic field strength at the midplane, this results in exactly the same magnetic diffusivity profile. Since rather weak magnetic fields (weaker than the equipartition field) are explored, the underlying disk structure cannot be changed substantially by the Lorentz force. On the contrary, the magnetic field distribution adjusts itself in accordance with the diffusivity model, which has the same vertical profile ab initio.

The convergence that is observed for these simulations, starting from an initial magnetic field with different bending, again confirms the reliability of the presented model in general.

### 4.3.7 Resolution Study

In this section the results of the resolution study are presented. Simulations with a grid resolution of (0.5, 0.75, 1.0, 1.5, 2.0) times the standard resolution of 128 cells per quadrant were performed. It corresponds to (64, 96, 128, 192, 256) cells per quadrant, or approximately (8, 12, 16, 24, 32) cells per disk height $2\epsilon$. Note that once the resolution in the $\theta$ direction and the

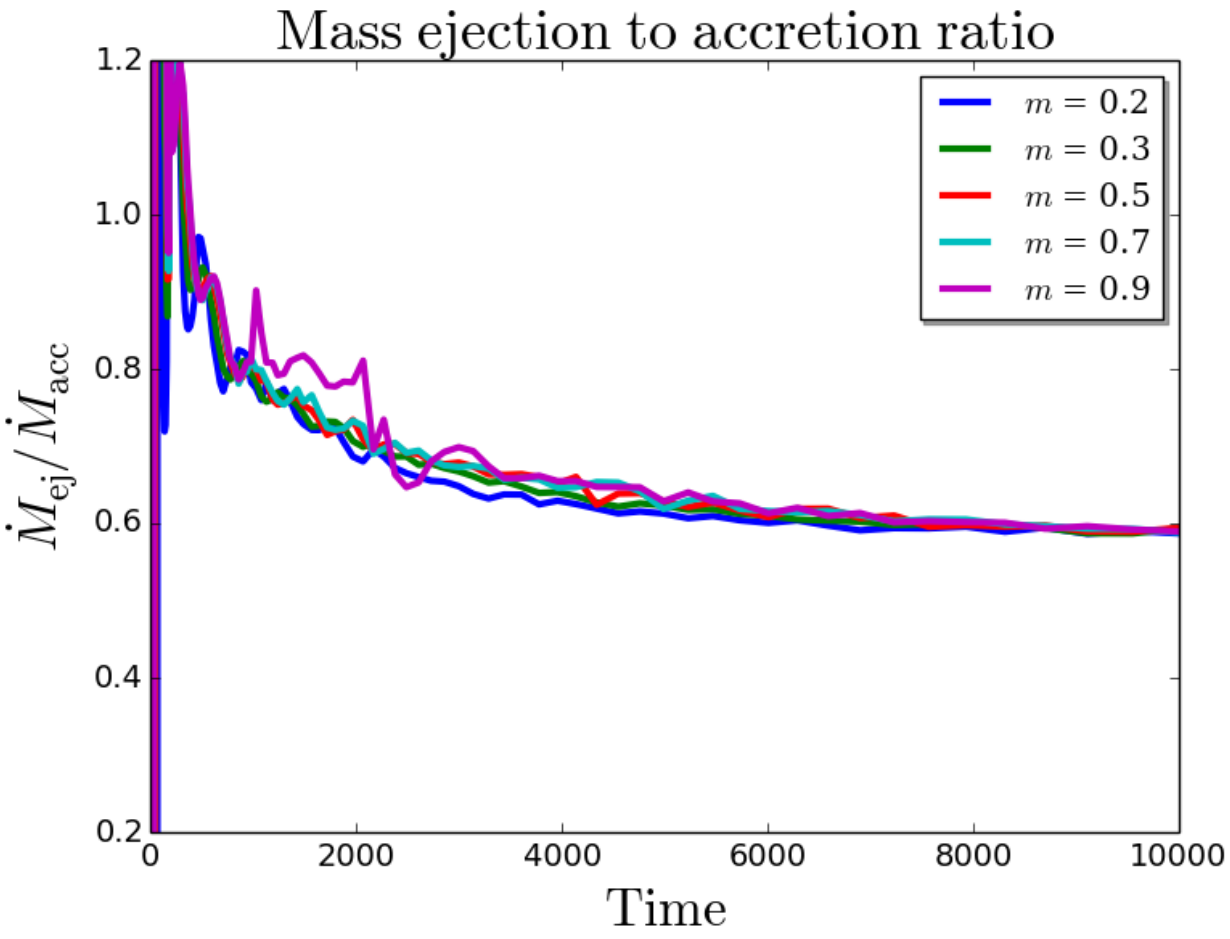


**Figure 4.6:** Time evolution of the mass ejection to accretion ratio for simulations evolving from an initial magnetic field distribution with a different initial bending parameter $m$.

radial extent of the disk is chosen, the resolution in the $R$ direction is uniquely determined (see Section 3.3).

For the resolution study, all simulations were performed up to typically 10,000 time units. Figure 4.7 shows snapshots of some of these simulations. Essentially, these disk-outflow structures are almost identical, indicating that numerical convergence is indeed reached.

Figure 4.8 shows the time evolution of the mass ejection to accretion ratio, again integrated throughout the control volume $R < 10$, for simulations of a different resolution. Note two particular issues. First, all curves bunch together at a mass ejection to accretion ratio of about 0.6, indicating convergence of the simulations (this is also true for other flux ratios). Second, the simulation with the highest resolution shows some intermittent behavior (see Figure 4.7). This might be related to the spatial reconstruction in non-Cartesian coordinates close to the symmetry axis or to the ability to resolve more detailed structures. The simulations have converged for the launching region for the resolution chosen.

Note that although the spherical grid is beneficial for the disk and outflow-launching studies, mainly due to the higher resolution of the inner disk, its application to the jet propagation further away from the jet source is limited because of the lack of resolution at larger radii.

## 4.4 MAGNETIZATION ANALYSIS

This section investigates a number of physical processes of jet launching by comparing different simulations similar to the reference simulation.

As mentioned above, the evolution of the reference simulation can be seen as a sequence of quasi-steady states. The slow, but constant, decrease of the disk mass eventually leads to a change of the disk magnetization. This is more prominent in the inner part of the disk, whereas the magnetization of the outer disk does not change much. This feature provides the opportunity of studying the disk and jet quantities with respect to the actual disk magnetization.

In this section, a set of simulations similar to the reference simulation is presented, however, applying a slightly different choice of parameters. The reference simulation was chosen such that diffusive processes are in balance with advective processes. Now, by choosing a slightly different diffusivity parameter $\alpha_{\rm m}$, these processes now are out of balance. This leads either to further faster advection or diffusion of the magnetic field. Naturally, in the case of lower $\alpha_{\rm m}$, advection dominates, and, thus, magnetization grows, leading to even faster advection. In the opposite case, the disk magnetization decreases.

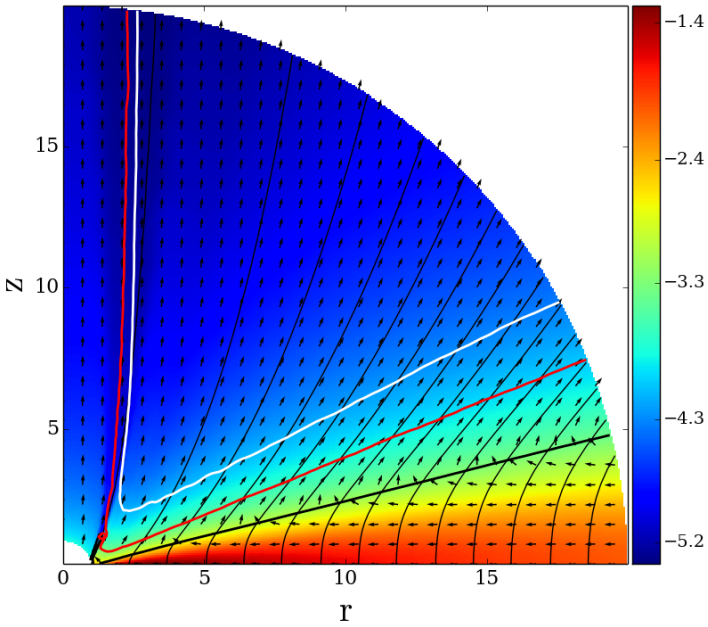
z
r
0
5
10
15
−1.4
−2.4
−3.3
−4.3
−5.2

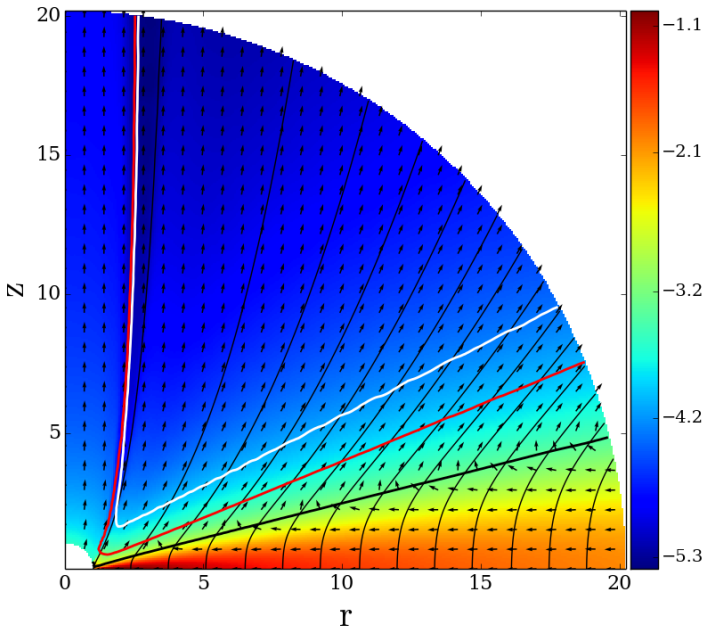
z
r
0
5
10
15
20
−1.1
−2.1
−3.2
−4.2
−5.3

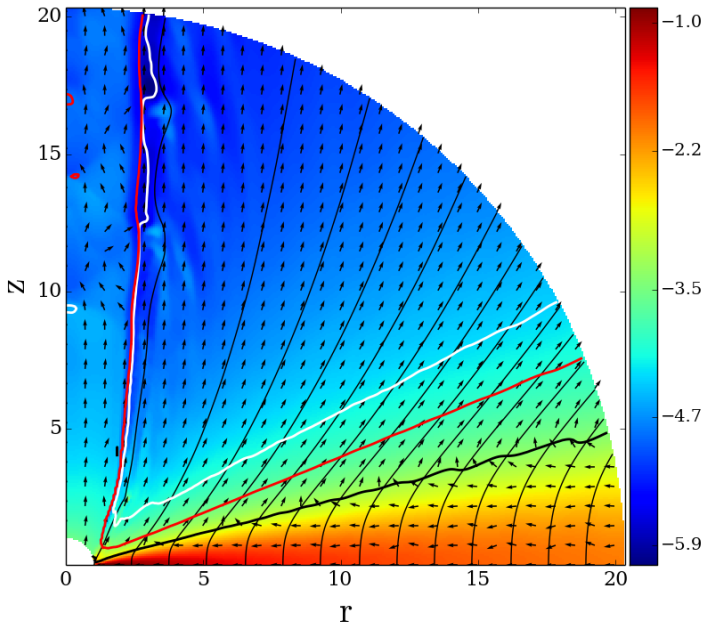
z
r
0
5
10
15
20
−1.0
−2.2
−3.5
−4.7
−5.9

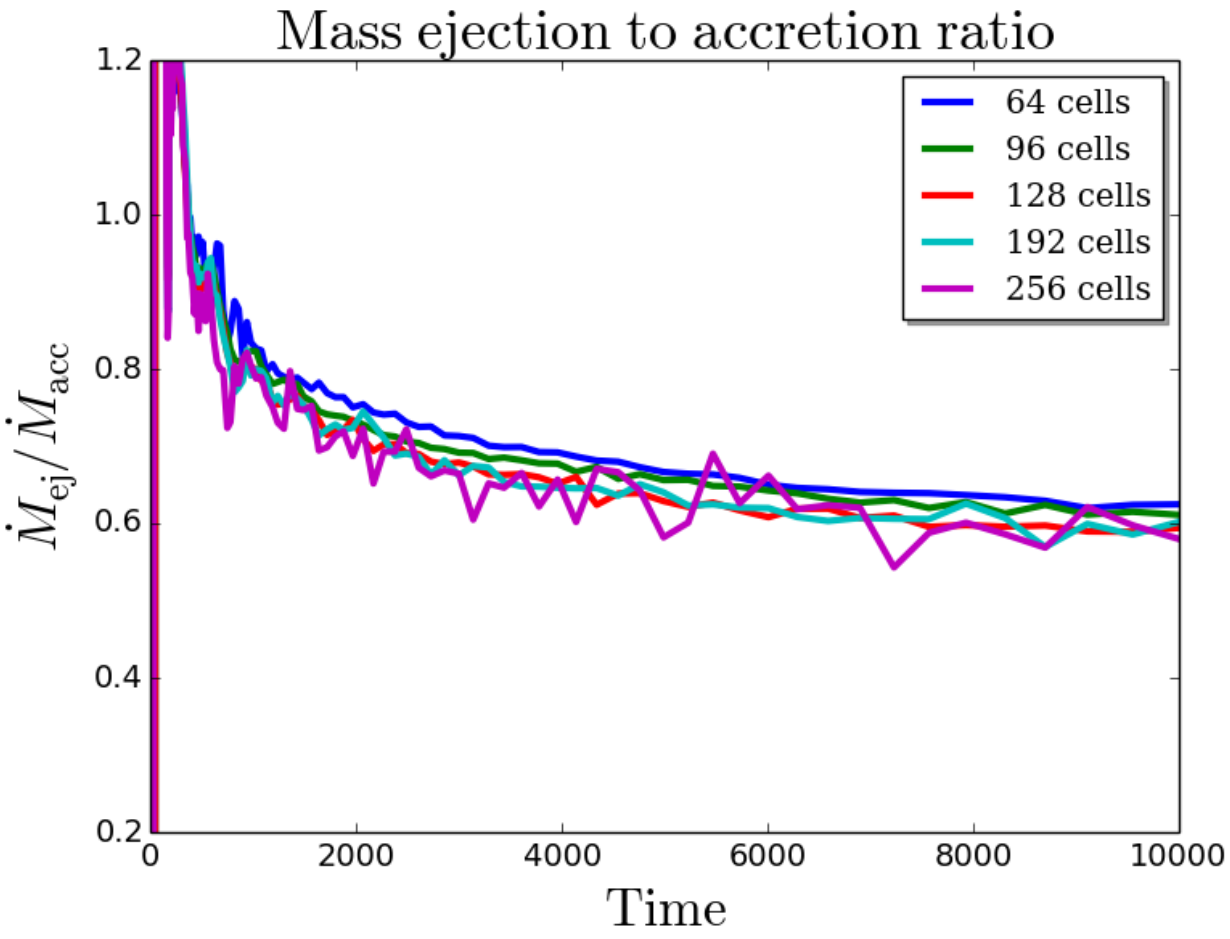


**Figure 4.8:** Evolution of the ejection to accretion ratio at $R = 10$ for the reference simulation with different resolutions.

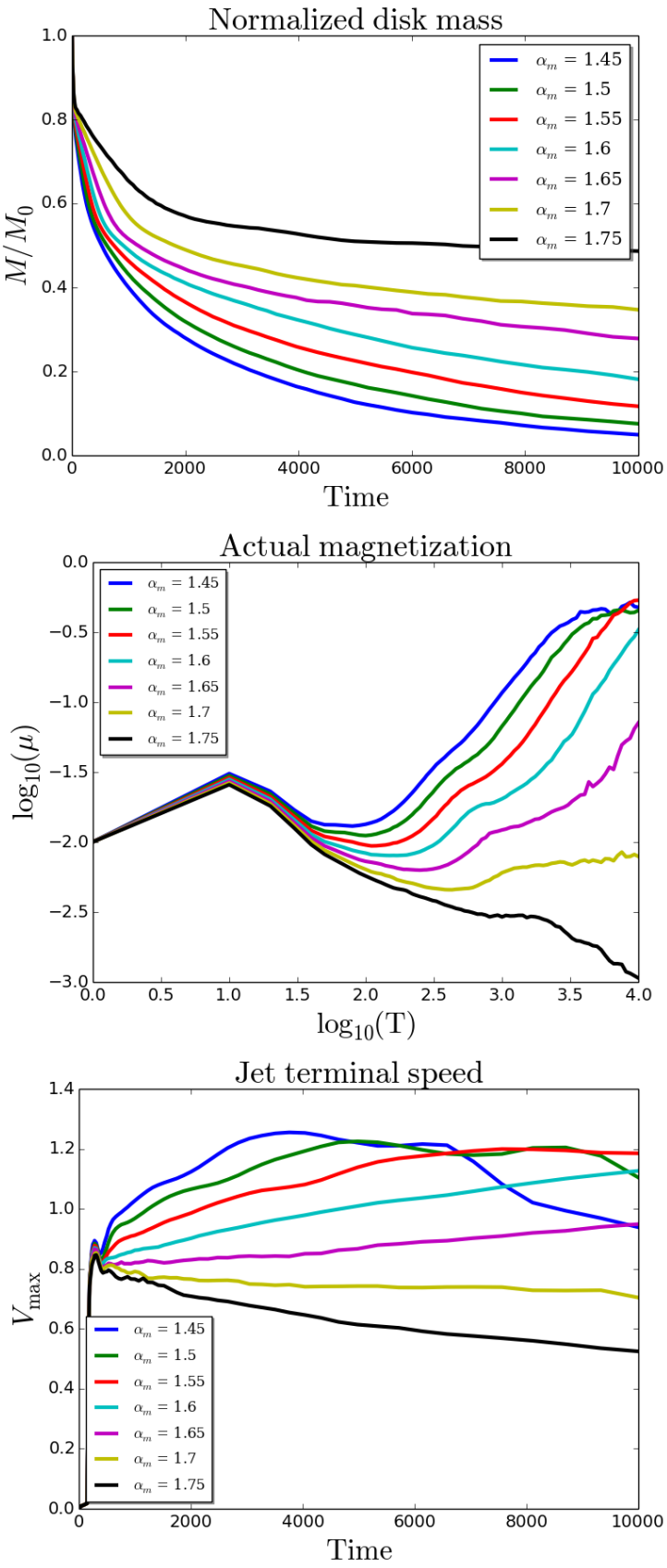


**Figure 4.9:** Time evolution of the normalized disk mass (left), the actual magnetization of the disk (middle), and the jet terminal speed (right) for different diffusivity ($\alpha_{\rm m}$) strength.

This approach allows to study the evolution of the accretion–ejection in a very general way. Each of the simulations applied has started from the same initial conditions, however, it now follows a different evolutionary track and finally evolves into a quite different state of the system.

Figure 4.9 shows the time evolution of the disk mass, the average magnetization of the inner disk (averaged between $R = 1.1$ and $R = 1.5$), and the jet speed defined here as

$$V_{\mathrm{jet,act}} \equiv \max(V_{\mathrm{P}})|_{R=100}, \tag{4.11}$$

the maximum jet speed obtained at $R = 100$, considering only those magnetic field lines rooted in the disk.

Note that the jet speed as computed here is only an extrapolation of the terminal jet speed (at infinity). The general behavior of the disk is as follows. First, the different simulations behave rather similarly. After some time, they begin to differ from each other. At later stages the disks and their outflows arrive at definitely different dynamical states. The exact times at which this happens depends, of course, on the radius for which the disk properties are examined. From Figure 4.9 shows that the time when the simulations begin to differ considerably is fairly small, about a few hundred dynamical time steps.

Since the simulation start with no accretion, diffusion is not initially in balance. However, electric currents are induced quickly within the disk, and subsequent angular momentum transport results in accretion. Depending on the value of the diffusivity parameter $\alpha_{\mathrm{m}}$, the system results either in an advection-dominated regime (for $\alpha_{\mathrm{m}} < 1.65$), or a diffusion dominated regime ($\alpha_{\mathrm{m}} > 1.65$). In principle, an equilibrium situation is possible in which these two processes are in balance. In the case of $\mu_0 = 0.01$, the diffusivity parameter for an equilibrium situation is around $\alpha_{\mathrm{m}} = 1.65$. The critial diffusivity parameter $\alpha_{\mathrm{cr}}$ is referred to as the one corresponding to the equilibrium state when advection and diffusion are balanced. Generally, the lower the diffusivity, the stronger the advection and thus the resulting magnetization.

The simulations confirm the finding of Tzeferacos et al. (2009) that in case of a strong magnetic field with $\mu \sim 0.3$, the disk structure changes substantially – the disk becomes much thinner in the inner region of the disk. A stronger magnetic field exerts a stronger torque on the disk, leading to a faster accretion rate. Thus, at some point in time, the accretion velocity becomes supersonic, $M_{\mathrm{R,act}} > 1$. This is considered as the limit for applying the magnetic diffusivity model.

As clearly visible from the figures discussed above, for the present setup the current diffusivity model (Equation 2.14) is only marginally stable – all deviations from the critical diffusivity will be further amplified. If magnetic diffusion dominates the disk, the magnetic field becomes increasingly weaker unless at about $\mu \sim 0.001$, where the jet outflow can no longer be sustained.

On the other hand, a weaker diffusivity leads to a faster accretion that also results in a runaway process. One way to circumvent this problem is to apply a different model for the diffusivity, namely $\alpha_{\rm ssm}(\mu)$ (see Section 4.5).

As might be easily seen from Figure 4.9, ongoing disk mass depletion in most cases leads to a higher degree of disk magnetization, a process that happens faster for less diffusive, thus higher advective simulations. A change in magnetization may substantially change the dynamics of the disk. Stronger magnetization, for example, leads to a higher jet speed.

One might notice the deviation in the behavior of the jet terminal speed for a low value of $\alpha_{\rm m}$. This results from the position where the terminal speed is calculated – for this case the jet accelerates even further out and the asymptotic velocity is not reached at $R = 100$ for the low $\alpha_{\rm m}$ (or highly magnetized) case and is still in the process of transforming the magnetic energy into kinetic. In a next chapter, the terminal jet speed will be discussed in much more detail, demonstrating that for a moderately weak magnetic field, $\mu \approx 0.05$, the terminal jet speed already reaches unity.

In summary, it is the actual magnetization in the disk that governs ejection and accretion and that is directly linked to various disk–jet quantities.

### 4.4.1 TRANSPORT OF ANGULAR MOMENTUM AND ENERGY

Here the analysis of the angular momentum and energy transport in the simulations is presented. It is common to explore the angular momentum and energy transport by means of their fluxes through a control volume (Section 4.3.4). The accretion angular momentum flux $\dot{J}_{\rm acc} = \dot{J}_{\rm acc,kin} + \dot{J}_{\rm acc,mag}$ is defined as the sum of the kinetic and magnetic parts,

$$\dot{J}_{\rm acc,kin} = -2\int_{S_1}^{S_R} r\rho V_\phi \boldsymbol{V}_p \cdot d\boldsymbol{S}, \qquad \dot{J}_{\rm acc,mag} = 2\int_{S_1}^{S_R} rB_\phi \boldsymbol{B}_p \cdot d\boldsymbol{S}. \tag{4.12}$$

The jet angular momentum flux is defined as $\dot{J}_{\rm jet} = \dot{J}_{\rm jet,kin} + \dot{J}_{\rm jet,mag}$ with

$$\dot{J}_{\rm jet,kin} = -2\int_{S_S} r\rho V_\phi \boldsymbol{V}_p \cdot d\boldsymbol{S}, \qquad \dot{J}_{\rm jet,mag} = 2\int_{S_S} rB_\phi \boldsymbol{B} \cdot d\boldsymbol{S}. \tag{4.13}$$

Figure 4.10 shows the time evolution of the jet angular momentum flux for a number of simulations. They can be divided into three different groups distinguished by their initial magnetization, $\mu_0 = 0.003, 0.01, 0.03$. Different lines within each group represent simulations with different diffusivity parameters $\alpha_{\rm m}$. The jet angular momentum flux is calculated through the upper part of the control volume, thus, up to R = 10.

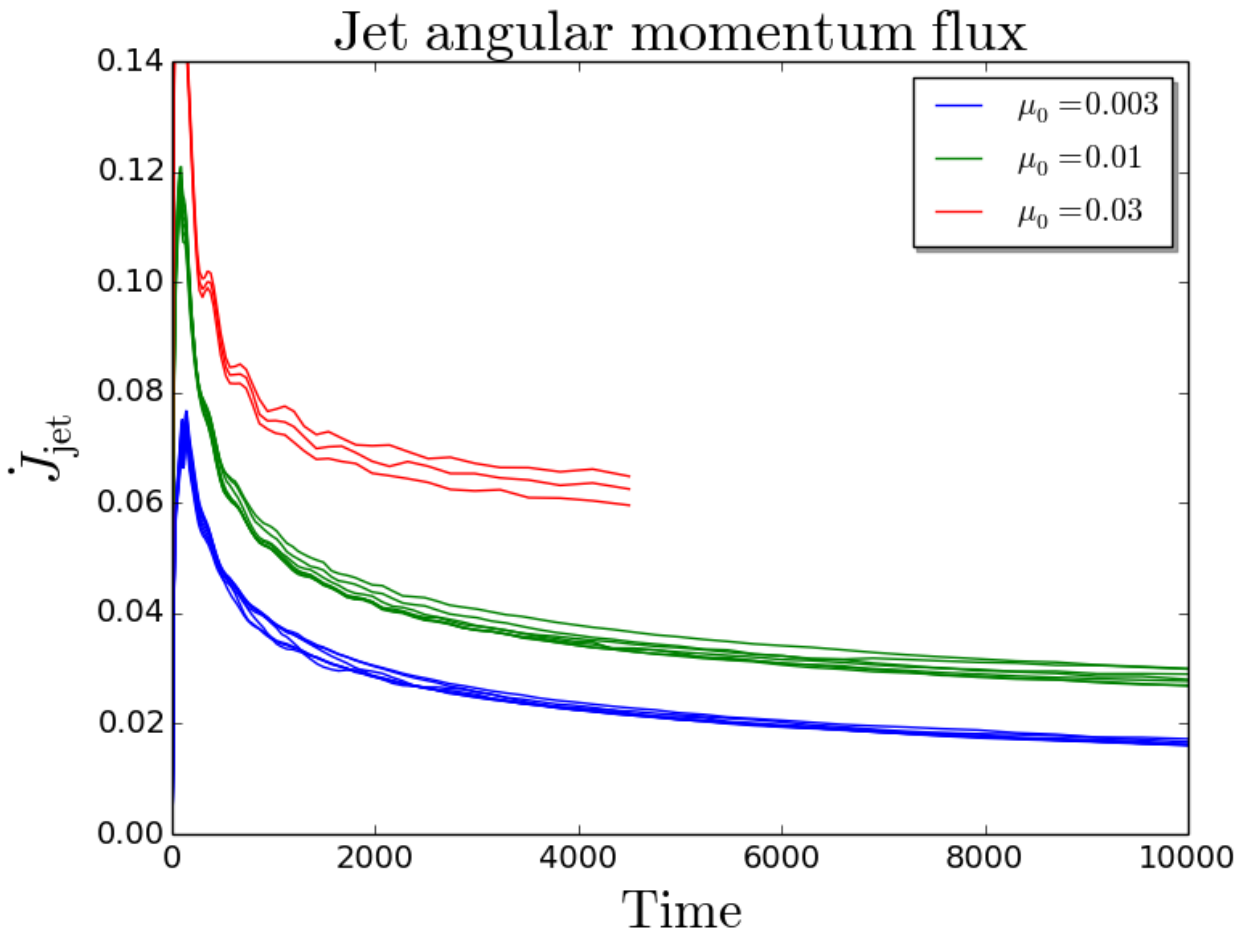


**Figure 4.10:** Time evolution of the jet angular momentum flux for the reference simulation at radius 10. Simulations with different initial magnetic fields form three distinct groups corresponding to $\mu_0 = (0.003, 0.01, 0.03)$ (from bottom to top)

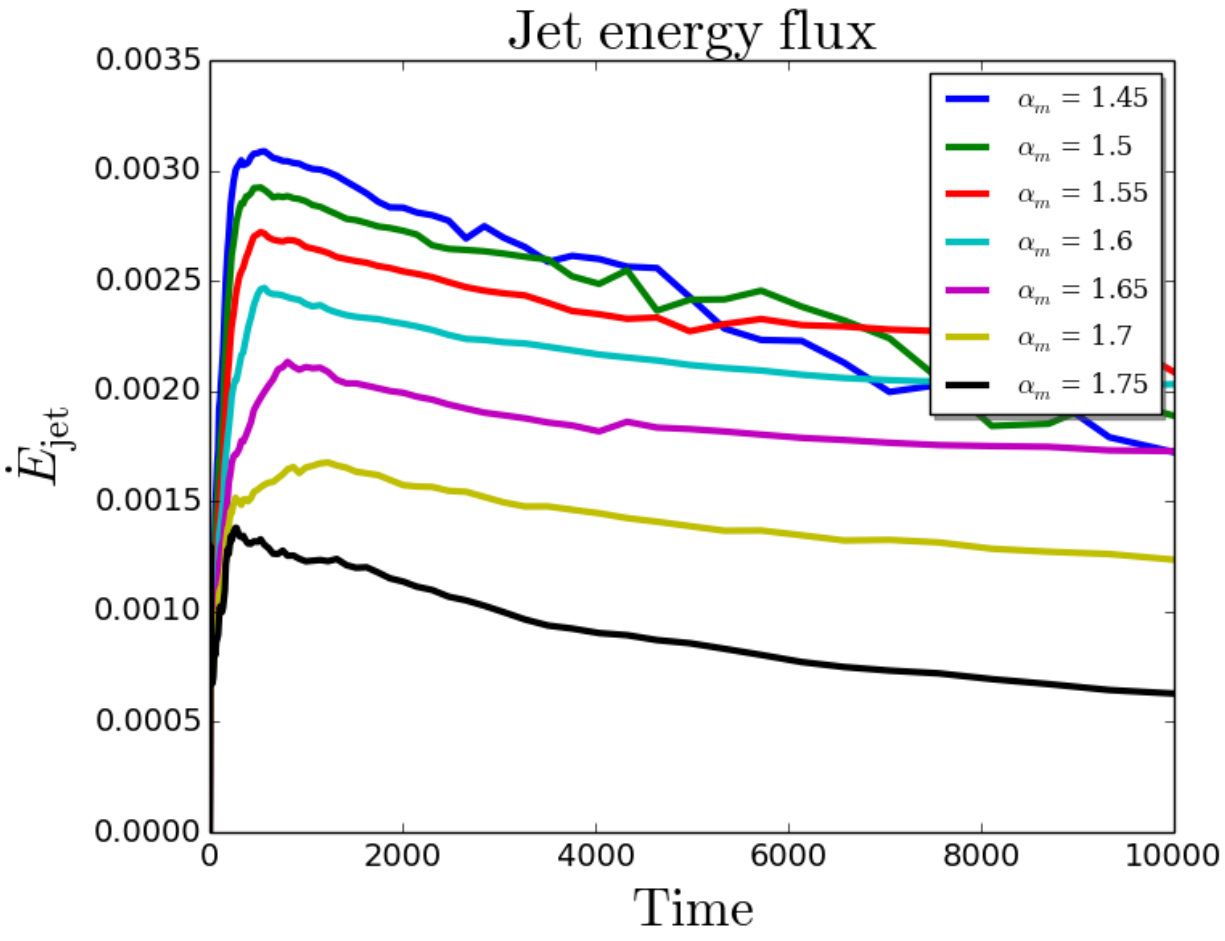


**Figure 4.11:** Time evolution of the jet energy flux for the reference simulations at radius 10.

As expected, the stronger the overall magnetic field strength is in the disk, the stronger torque it exerts, and thus the higher angular momentum fluxes are presented.

Although the magnetic diffusivity parameter $\alpha_{\rm m}$ differs within each group of lines (marked by different colors), the total torque measured for the corresponding simulations is about the same. This comes from the fact that the total torque is set by the global magnetic field. Thus, the evolution of the total torque is mainly set by the initial conditions.

Note that the simulations applying a strong initial magnetic field (represented by the upper bundle of curves in Figure 4.10) have been interrupted earlier compared to usual evolution times. For these cases, the inner part of the disk became highly magnetized. The strong magnetic field changes the inner disk structure such that the model for the magnetic diffusivity can no longer be applied. This is simply because the actual scale height of the disk significantly decreases and no longer coincides with the initial disk surface. The case of strong magnetic fields is considered as being beyond the scope of this study. The underlying turbulence might be significantly suppressed as well.

In accordance with previous works (see, e.g., Zanni et al. 2007), the ratio of angular momentum extracted by the jet to that provided by the disk accretion is always close to, but slightly larger than, unity, $\dot{J}_{\rm jet}/\dot{J}_{\rm acc} \gtrsim 1$. The main reason is that the accretion rate in the outer part of the disk is too low to compete with a strong mass loss by the disk wind at these radii.

The accretion energy flux (accretion power) $\dot{E}_{\rm acc} = \dot{E}_{\rm acc,mec} + \dot{E}_{\rm acc,mag} + \dot{E}_{\rm acc,thm}$ is defined as the sum of the mechanical (kinetic and gravitational), magnetic, and thermal energy fluxes,

$$\dot{E}_{\rm acc,mec} = -2\int_{S_1}^{S_R}\left(\frac{\boldsymbol{V}^2}{2}+\Phi_{\rm g}\right)\rho\boldsymbol{V}_p\cdot d\boldsymbol{S}, \quad \dot{E}_{\rm acc,mag} = -2\int_{S_1}^{S_R}\boldsymbol{E}\times\boldsymbol{B}\cdot d\boldsymbol{S}, \quad \dot{E}_{\rm acc,thm} = -2\int_{S_1}^{S_R}\frac{\gamma}{\gamma-1}P\boldsymbol{V}_p\cdot d\boldsymbol{S}, \tag{4.14}$$

and, similarly, the jet energy flux (jet power) $\dot{E}_{\rm jet} = \dot{E}_{\rm jet,kin} + \dot{E}_{\rm jet,grv} + \dot{E}_{\rm jet,mag} + \dot{E}_{\rm jet,thm}$ is defined by

$$\dot{E}_{\rm jet,kin} = -2\int_{S_S}\frac{\boldsymbol{V}^2}{2}\rho\boldsymbol{V}_p\cdot d\boldsymbol{S}, \quad \dot{E}_{\rm jet,grv} = -2\int_{S_S}\Phi_{\rm g}\rho\boldsymbol{V}_p\cdot d\boldsymbol{S}, \tag{4.15}$$

$$\dot{E}_{\rm jet,mag} = -2\int_{S_S}\boldsymbol{E}\times\boldsymbol{B}\cdot d\boldsymbol{S}, \quad \dot{E}_{\rm jet,thm} = -2\int_{S_S}\frac{\gamma}{\gamma-1}P\boldsymbol{V}_p\cdot d\boldsymbol{S}. \tag{4.16}$$

In contrast to the angular momentum flux, most of the energy flux is being released from the inner part of the disk. This makes the energy flux very sensitive to the conditions in the inner disk. Indeed, Figure 4.11 shows that the power liberated by the jet strongly depends on the

diffusivity parameter, which is the main agent for governing the magnetic field strength. A weaker diffusivity parameter $\alpha_{\rm m}$ leads to a higher magnetization, and thus a higher jet power. The same is true for the accretion power.

Moreover, he ratio of energy fluxes, namely the ratio of the jet to the accretion energy flux, is always close to, but slightly lower than, unity. This is also in accordance with Zanni et al. (2007).

In this section, some evidence is provided that it is the actual magnetization in the disk that governs the fluxes of mass, energy, and angular momentum. In the next section, it is shown how exactly these fluxes are connected to magnetization.

### 4.4.2 ANALYSIS OF MAGNETIZATION, DIFFUSIVITY AND FLUXES

In a steady state, diffusion and advection balance. Advection of the magnetic flux in principle increases the magnetic field strength, predominantly in the inner disk. On the contrary, the diffusion smooths out the magnetic field gradient. Therefore, the diffusivity model applied is a key ingredient for these processes, directly influencing the disk structure and evolution.

Following analysis will not focus on the profile or the magnitude of the magnetic diffusivity, but concentrate on the resulting magnetization and its time evolution. As discussed above, by changing the magnetic diffusivity parameter $\alpha_{\rm m}$, it is possible to explore how the actual disk magnetization influences various properties of the disk–jet system.

For each parameter run performed, the actual physical variables in the disk–jet system are measured, such as the *time-dependent* mean magnetization, accretion fluxes, jet fluxes, or the accretion Mach number. Naturally, the actual value of a certain property has evolved from the initial value during the simulation. A mean value denotes the values averaged over a small area of the inner disk,

$$X \equiv < X(r, z = 0) > . \tag{4.17}$$

All mean quantities discussed are averaged over the inner disk midplane from $R = 1.1$ to $R = 1.5$. The choice of the averaging area is motivated as follows. First, in order to avoid any influence of the inner accretion boundary the inner integration radius is moved about 10 grid cells away from it. Second, only the inner part of the disk is examined , since it is the region where the magnetization is changing predominantly and it is the launching area for the most energetic part of the jet. Third, it is desirable to avoid large magnetic gradients affecting the averaging area. Although most of jet energy is launched from regions broader than this small area, the area is seen as representative. Note that the profiles of the jet power along the disk surface are similar for all simulations. In all cases, the general behavior of the physical outflow or disk quantities

with respect to underlying disk magnetization does not depend on the area where the averaging is performed (on neither the location nor the size).

Keeping all other parameters the same, simulations varying the initial magnetization $\mu_0$ and the strength of the magnetic diffusivity $\alpha_{\rm m}$ were carried out. For all the simulations, starting with different initial magnetization, $\mu_0 = 0.003$, $\mu_0 = 0.01$, and $\mu_0 = 0.03$, the interrelation between the different jet or disk quantities and the disk magnetization is essentially the same. Therefore only one group of simulations, namely that with $\mu_0 = 0.01$, is presented. Although the initial magnetic field strength differs, It can be already suspected at this point that it is the actual rather than the initial strength of the magnetic field in the disk that governs the disk accretion and ejection of the jet, and, thus plays a major role in the launching process. This has not yet been discussed in the literature, as most publications parameterize their simulations by the initial parameters. An exception might be Sheikhnezami et al. (2012), who pointed out substantial changes in the disk plasma beta during the time evolution.

An interesting representation of the evolution of the main disk–jet quantities are $(\mu, X)$ plots, where X stands for the examining variable. Note that in these plots the time evolution is hidden.

#### 4.4.2.1 ACCRETION MACH NUMBER

As was shown by Königl & Salmeron (2011), there is a link between the mean accretion Mach number and the disk magnetization. In currently used terms, this relation can be expressed as

$$M_{\rm R,act} = \frac{2}{\sqrt{\gamma}} q \mu_{\rm act}, \tag{4.18}$$

where $q$ is the magnetic shear,

$$q = \frac{H J_R}{B_{\rm P}} = -\frac{B_\phi^+}{B_{\rm P}}, \tag{4.19}$$

and where the plus sign denotes a variable estimated on the disk surface. Note that in current case there is no viscous contribution and the factor $1/\sqrt{\gamma}$ appears in the relation since the accretion Mach number is calculated using adiabatic sound speed.

Figure 4.12 shows that setting $q$ to constant $q = 2\sqrt{\gamma}$ (thus $M_R = 4\mu$) is a good first approximation, especially for the strong magnetization cases. As it will be shown in the next section, in the case of a weak magnetic field the magnetic shear $q$ behaves far from being constant. Closer examination of the magnetic shear $q$ reveals a presence of two different jet launching regimes.

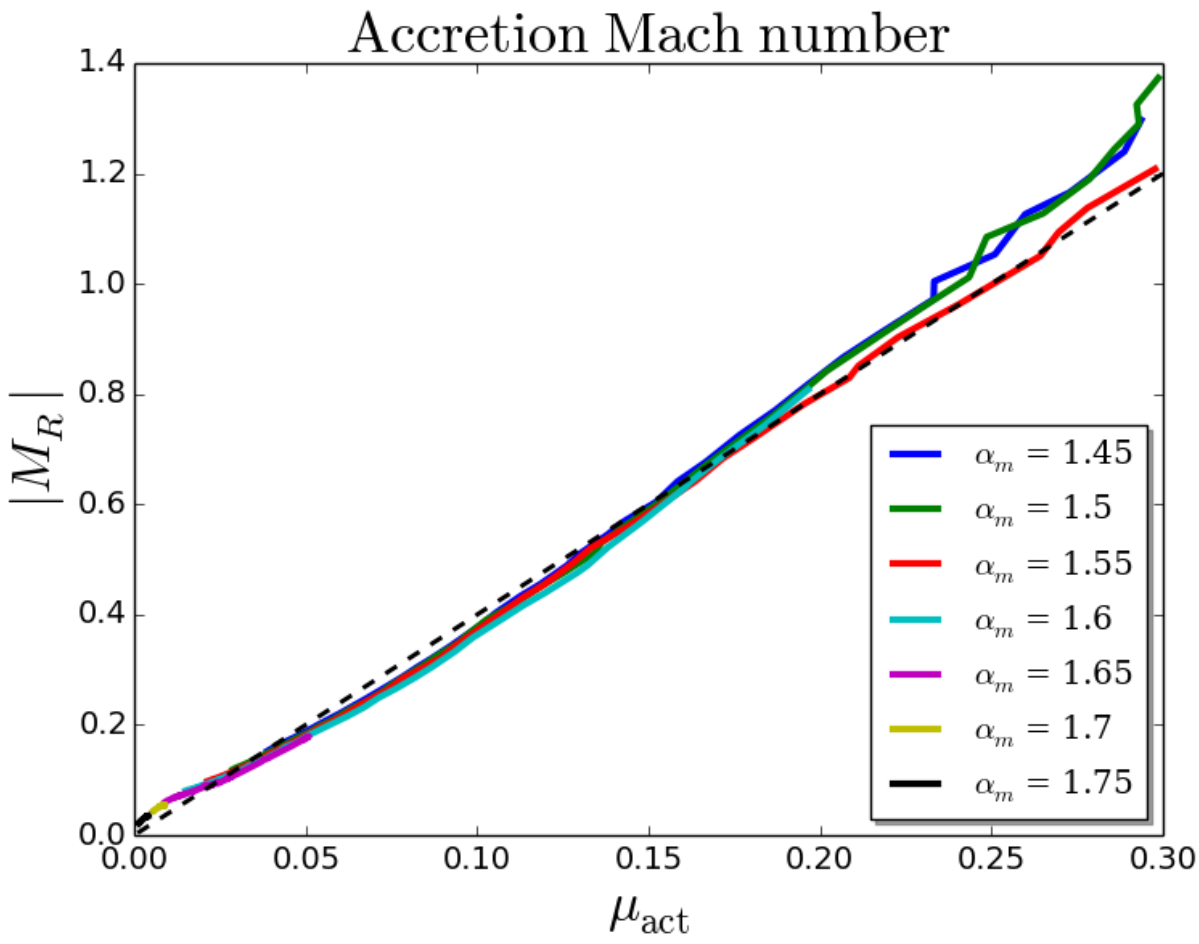


**Figure 4.12:** Relation of the accretion Mach number to the actual magnetization for the initial magnetization $\mu_0 = 0.01$. The linear approximation $M_R = 4\mu$ is shown by the dashed black line.

#### 4.4.2.2 MAGNETIC SHEAR

A tight relation exists between the magnetic shear $q$ and the ratio between the toroidal and poloidal magnetic field components. The magnetic shear $q$ is defined by the radial electric current at the disk midplane, since it does not require to apply the notation of the disk surface, which, in case of a strong magnetic field, might change by up to 40%. Note, that the magnetic shear is the first derivative of the accretion Mach number with respect to the magnetization. Therefore, it shows the growth rate of the local Mach number or steepness of the curve.

Figure 4.13 shows the magnetic shear with respect to the underlying inner disk magnetization. The magnetic shear behaves in two different ways – in the case of low magnetization, $\mu \leq 0.03 - 0.05$, the magnetic shear is substantially higher in comparison to the case of high magnetization, $\mu \geq 0.03 - 0.05$. The explanation is straightforward: there is a turning point concerning the generation of the toroidal magnetic field versus flux losses through the disk surface (by the outflow). To understand this, one needs to set apart the generation processes of the toroidal magnetic field from the loss processes. The rate of the generation of the magnetic field in Keplerian disks is primarily set by the structure of the magnetic field and is rather constant in the case of a quasi-steady state On the other hand, the outflow speed (through the disk surface) is highly dependent on the actual disk magnetization. In the case of a weak magnetization the outflow speed is rather small, which makes it possible to sustain a stronger magnetic shear. A strong disk magnetization results in a fast outflow, thus setting the maximum limit for the magnetic shear.

#### 4.4.2.3 MASS AND ENERGY FLUX

The magnetic shear has a great impact on outflow launching (Ferreira & Pelletier 1995). The mass and energy ejection and accretion fluxes confirm this finding.

Figure 4.14 shows the ratio of the mass ejection rate, $\dot{M}_{\rm ej}(1.5) - \dot{M}_{\rm ej}(1.1)$, to the accretion rate, both averaged over the same area. Obviously, the ejection efficiency is higher for weaker magnetized disks.

This is easy to understand considering Equation 4.6. In the case of a weak magnetic field, the strong magnetic shear (the high toroidal to poloidal magnetic field ratio) leads to faster poloidal acceleration, which is caused by the force component parallel to the magnetic field. This force also extracts the matter from the disk. In the case of a strong disk magnetization, the acceleration of matter is primarily supported by the centrifugal force.

Note that studying the ejection index (calculated within an area $R = 2 \ldots 10$) with respect to

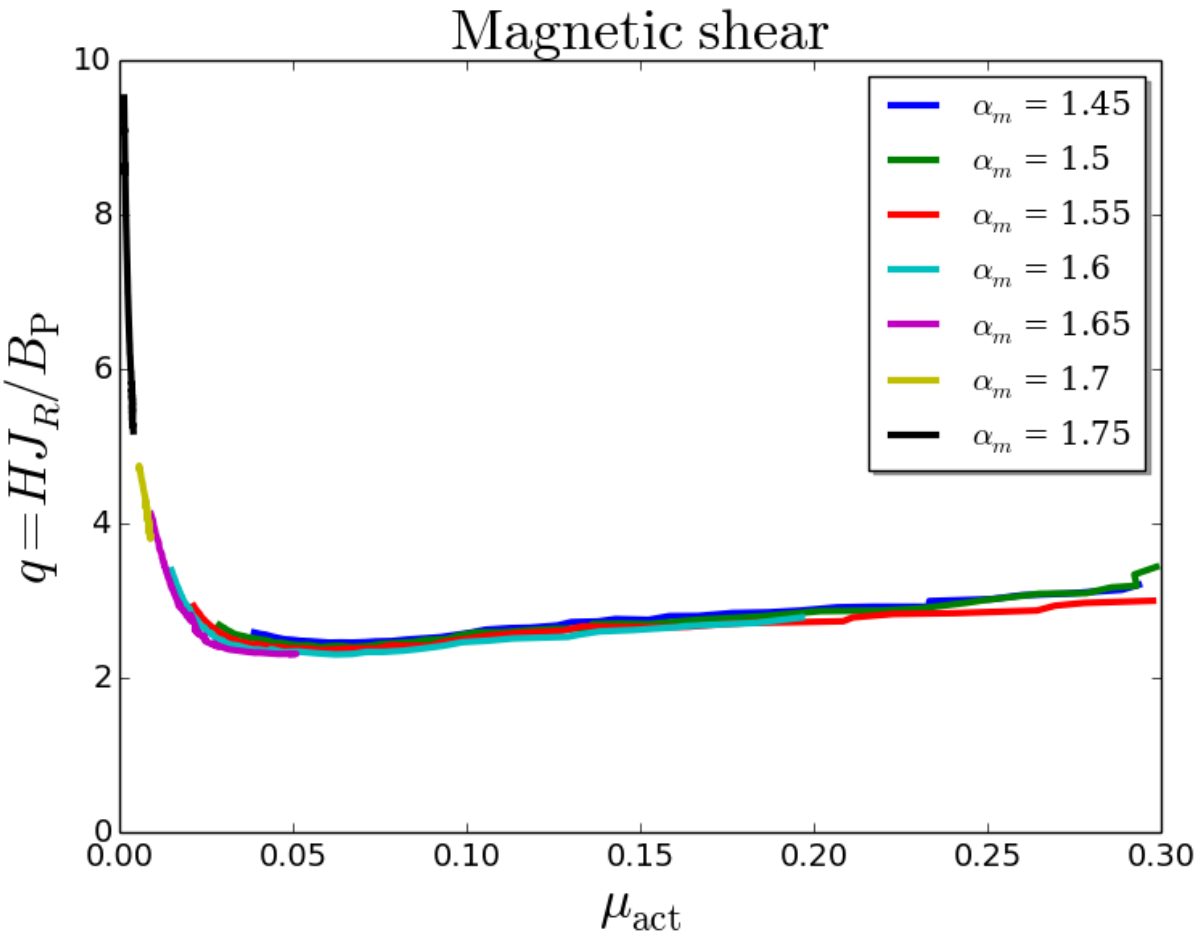


**Figure 4.13:** Relation of the magnetic shear with respect to the actual magnetization.

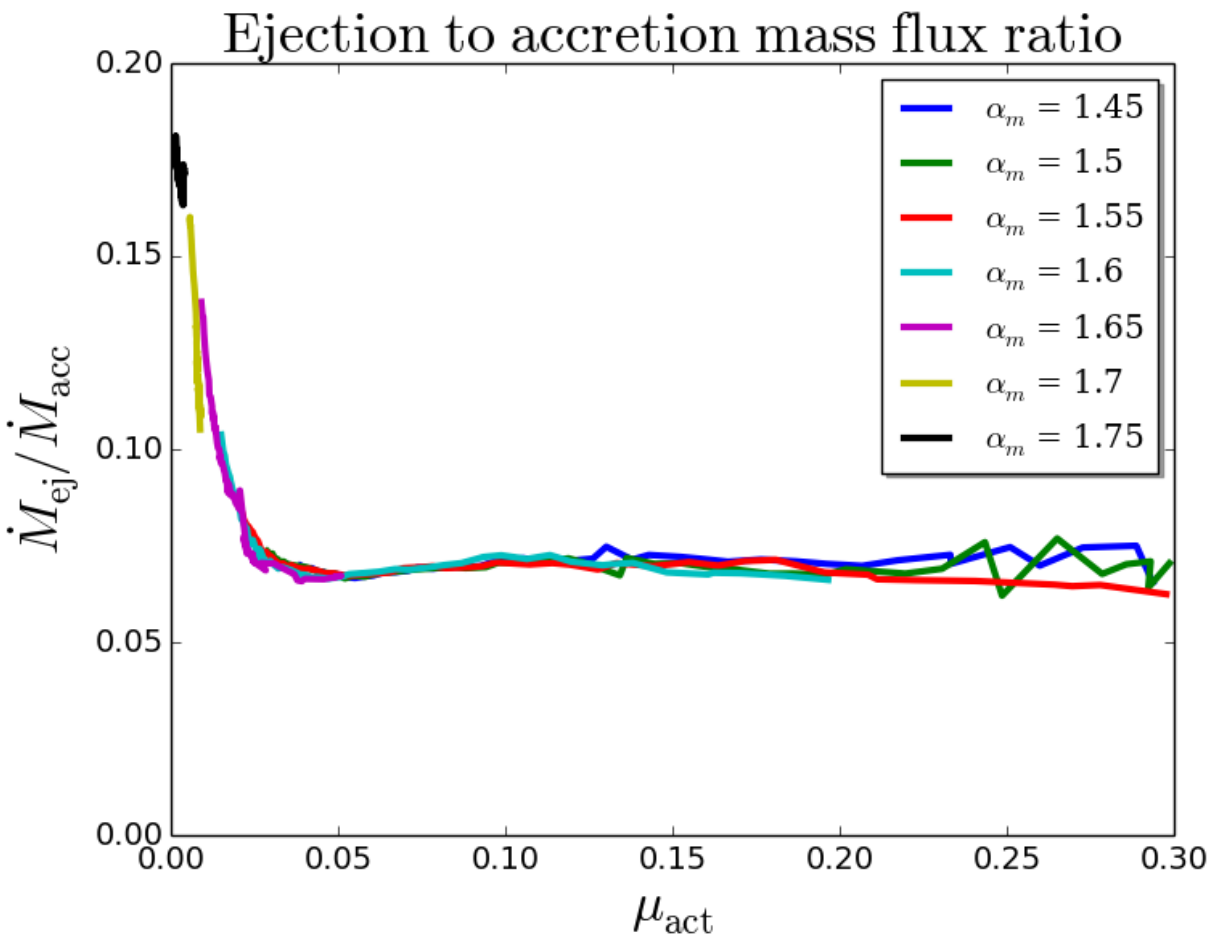


**Figure 4.14:** Relation of the mass ejection to accretion ratio with respect to the actual magnetization.

the mean disk magnetization leads to very similar results, that is a saturation to values of about 0.35–0.40 in the case of a high magnetization and a significant increase in the case of a low magnetization.

Figure 4.15 shows the ratio of the energy ejection density to the average accretion energy, computed in the same way as for the mass fluxes. Compared to the mass fluxes, the energies show opposite behavior – the ejection to accretion power is an increasing function with magnetization. This is a highly important relation, since it relates two observables. Note that there is not a fixed value for the ratio between the jet and accretion power. This should be considered when comparing observational results to theory.

Essentially, this result shows the general importance of the magnetic energy flux compared to the mechanical energy. The mechanical energy flux is always negative, while the magnetic energy flux is positive. In the case of a strong magnetic field, the results are similar to Zanni et al. (2007),

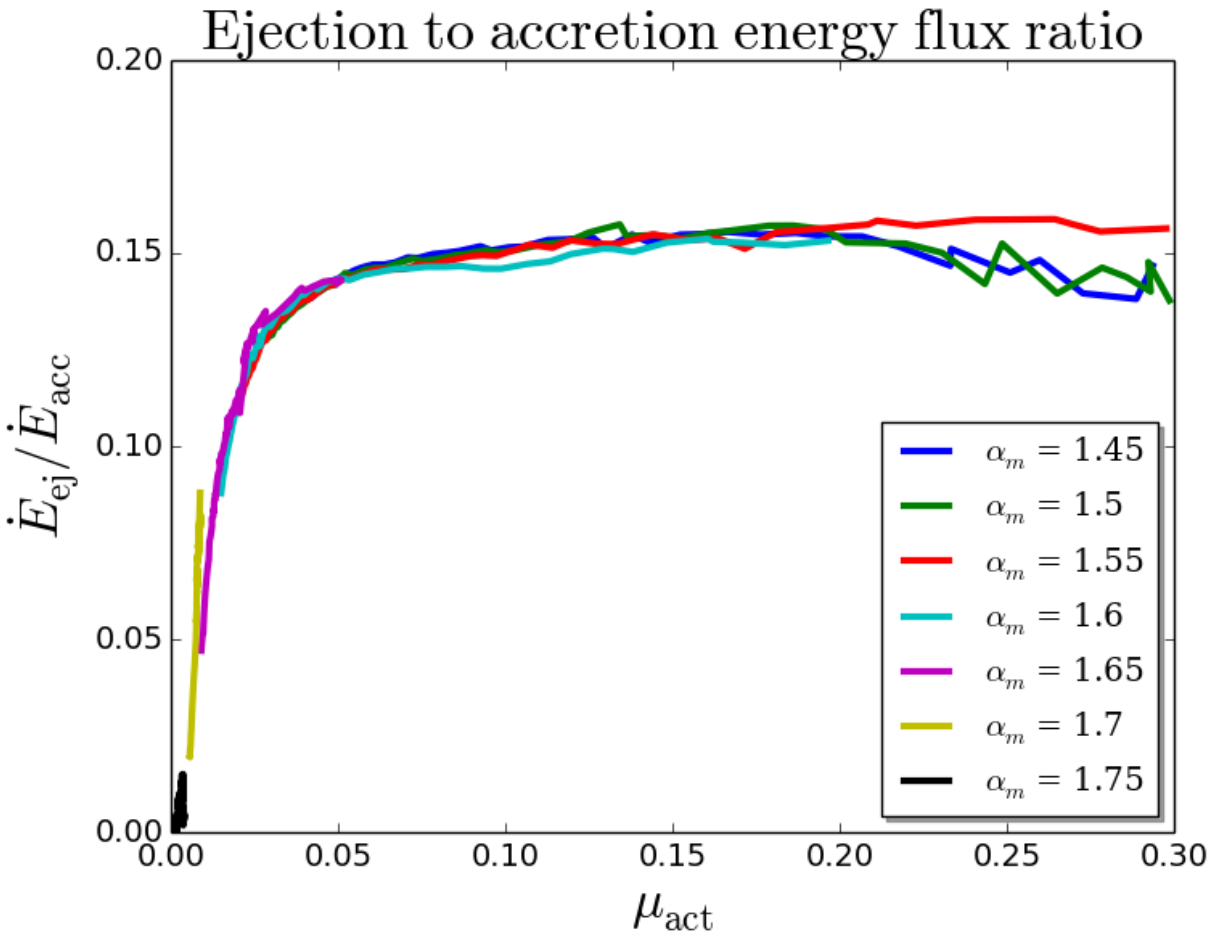


**Figure 4.15:** The relation of the energy ejection to accretion with respect to the actual magnetization.

namely, that magnetic energy flux dominates the mechanical flux. A saturation of the flux ratio in the case of a moderately strong magnetization is also seen. In a weak magnetization case the energy flux ratio can be very small.

The ejection Mach number, Equation 4.4, increases almost linearly with magnetization.

Essentially, the general behavior of the mass and energy flux ratios does depend on the averaging area or its position.

The accretion power is mainly determined by the accretion rate at the inner disk radius. Assuming a typical scale height for the mass accretion as $\epsilon r$, the accretion power can be estimated considering the magnetic shear and the actual magnetization of the disk,

$$\dot{E}_{\rm acc} \simeq 0.06\, q\, \mu_{\rm act} \dot{E}_0, \tag{4.20}$$

where $\dot{E}_0$ is the unit power (see Chapter 3).

In the case of strongly magnetized disks one can assume that the magnetic shear is approximately constant $q \approx 3$, and this relation transforms into $\dot{E}_{\rm acc} \simeq 0.2\mu_{\rm act}\dot{E}_0$. Note that this result connects two essential quantities – the accretion power, which manifests itself by the accretion luminosity, to the disk magnetization, which is intrinsically hidden from the observations.

## 4.5 A Stable Long-term Evolution

This section discusses the commonly used diffusivity model and the reasons why it fails in the case of very long-term simulations, in particular when treating weakly magnetized disks. In order to overcome this problem – the accretion instability – another magnetic diffusivity model is proposed. This new model enables to simulate the evolution of the disk–jet system for much longer times.

### 4.5.1 Constraints on the Diffusivity Parameters

The simple idea that the induction of the magnetic flux in steady state is compensated by the flux losses, both by diffusion and magnetic flux escape through the disk surface, becomes barely applicable in the case of a weak magnetic field. As discussed previously (see Section 4.2.1), in order to keep the magnetic field distribution properly bent, the magnetic diffusivity parameter $\alpha_{\rm m}$ must be linked to the anisotropy parameter $\chi$. Equation 4.5 was obtained considering the standard magnetic diffusivity model. A more general relation can be derived assuming a curvature of the

magnetic field of about 0.5, which is the mean curvature of the initial field distribution (see Equation 3.3),

$$(\alpha_{\rm ssm}\chi - M_\theta)\,\alpha_{\rm ssm} \leq \mu. \tag{4.21}$$

Solving this inequality for $\alpha_{\rm ssm}$ and assuming $M_\theta \propto \beta\mu$, one finds

$$\alpha_{\rm ssm} \leq \alpha_0 = \frac{\beta}{2}\mu_\chi + \sqrt{\left(\frac{\beta}{2}\right)^2 \mu_\chi^2 + \mu_\chi}, \tag{4.22}$$

where $\mu_\chi = \mu/\chi$, and $\beta \approx 6$ in the simulations. This relation shows that in order to keep the disk magnetic field properly bent, the $\alpha_{\rm ssm}$ should behave differently in the two limits of magnetization: a linear relation to the magnetization in the case of a strong magnetic field, and proportional to the square root of magnetization in the case of a weak field. In the case of a strong deviation from this relation, the magnetic field structure will be substantially affected, resulting in a high field inclination (for $\alpha_{\rm ssm} \ll \alpha_0$), or a strong outward bending (for $\alpha_{\rm ssm} \gg \alpha_0$).

For Equation 4.22, it is implicitly assumed a linear relation between the ejection Mach number (at the disk surface) and the magnetization. In fact, the simulations approve such an interrelation. Figure 4.16 shows that for a moderately strong magnetic field, there is a linear relation between the ejection Mach number and the underlying disk magnetization. This behavior is also consistent with the ejection to accretion mass flux ratio as discussed above.

As a consequence of Equation 4.1, the $\alpha_{\rm ssm}$ plays a direct role in determining the strength of the poloidal electric current with respect to the toroidal current. In order to sustain jets, the ratio of the poloidal to the toroidal current should be sufficiently high (about 15).

The difficulty in performing simulations of weakly magnetized outflows is that the specific torques may increase toward the disk surface area due to the low densities in that area. This will lead to a layered accretion along the disk surface, and thus, much lower accretion along the midplane. Although this might be a relevant process in reality, the currently used numerical setup is not suited for the treatment of such a configuration.

The standard, commonly used magnetic diffusivity model is parameterized by two constants, $\alpha_{\rm m}$ and $\chi$. In general, choosing a high anisotropy parameter $\chi$ implies a low diffusivity parameter $\alpha_{\rm m}$. Together, this will lead to a decrease in the poloidal electric current and an increase in the toroidal current (see Equation 4.1). Thus, the resulting torque will not be sufficient to brake the dense matter along the midplane, and will lead to layered accretion. An anisotropy parameter lower than unity has proven to lead to a smoother time evolution, since it allows for stronger poloidal currents at the midplane, and thus a mass accretion that is developed over the full disk height. Another option to have $\chi > 1$ would be to modify the vertical diffusivity profile such that it reaches the maximum not at the disk midplane, but at the disk surface. This would also help to develop a strong electric current in the disk midplane.

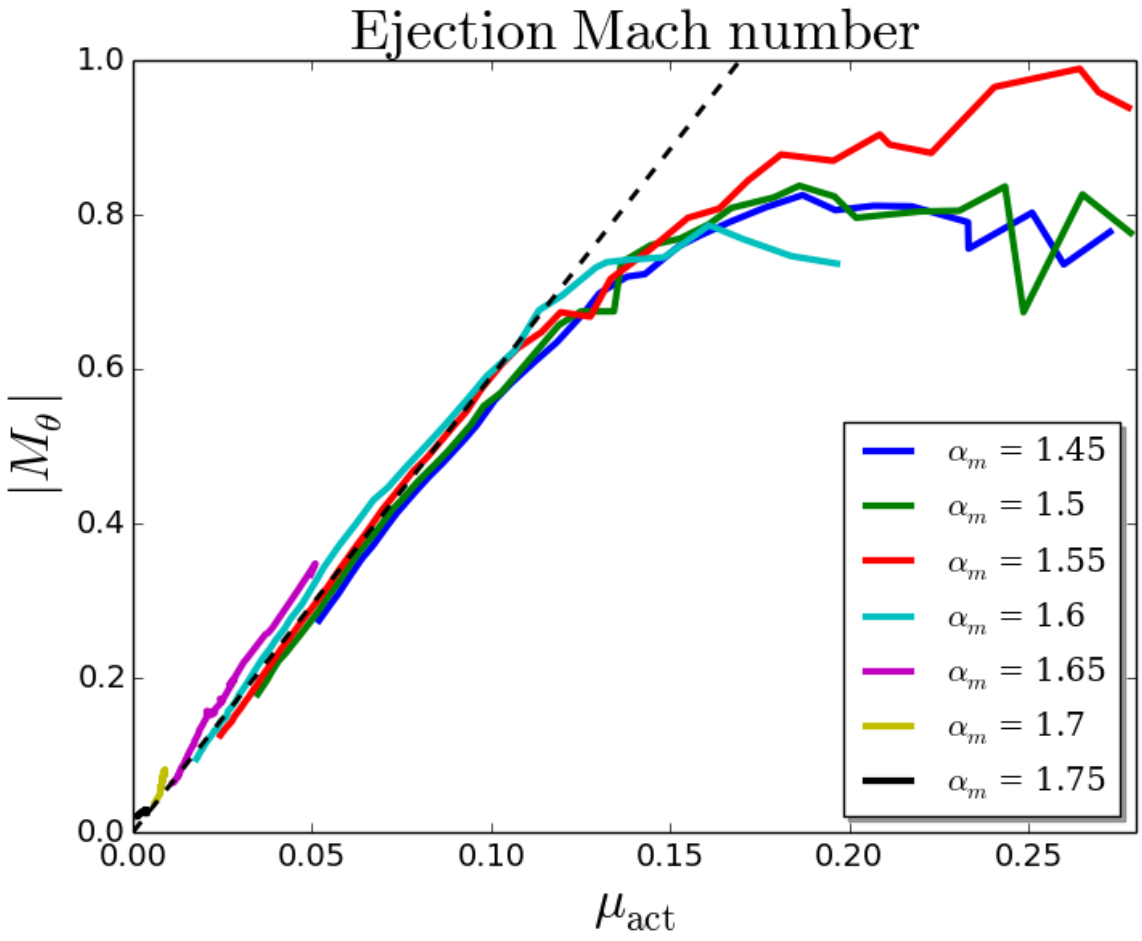


**Figure 4.16:** Relation of the ejection Mach number with respect to actual magnetization. The slope of the dashed line is $\beta = 5.9$.

### 4.5.2 THE ACCRETION INSTABILITY

This section discusses another problem, which is common in the standard diffusivity model. As previously shown, most of the simulations suffer from the mass loss from the disk, leading to the increase of magnetization. However, the increase of magnetization further amplifies the mass loss. This is known as the accretion instability, first studied by Lubow et al. (1994), and later confirmed for more general cases (Campbell 2009). If, on the other hand, the diffusivity is too high (chosen by a high $\alpha_{\rm m}$ parameter), the inevitable diffusion of the magnetic field will lead to the situation where a jet can no longer be sustained.

The main reason for the increase in magnetization is the mass loss, but not the actual magnetic field amplification. This is a direct consequence of the accretion instability, namely, a lack of sufficient feedback that could bring the accretion system back to a stable state. In other words, in order to run long-term simulations, one needs to apply a diffusivity model that provides a stronger feedback to the diffusivity profile than the standard choice $\propto \sqrt{2\mu}$.

### 4.5.3 A PROPER MAGNETIZATION PROFILE

The direct consequence of the accretion instability is that the magnetization increases toward the center. It is easy to show that the behavior of the magnetization has to be opposite. In accretion disks producing outflows, the mass accretion rate must naturally increase with radius. Assuming a radial self-similarity of the disk and taking into account that the accretion Mach number is linearly related to the magnetization and that $\rho \propto C_{\rm s}^3$, one derives

$$\beta_\mu = \xi - 2 - 4\beta_{C_{\rm s}}, \tag{4.23}$$

where $\xi$ is the ejection index and $\beta_X$ represent the power-law index of a physical quantity $X$. Considering that magnetized disks are very efficient in producing outflows, $\xi \approx 0.2 - 0.4$, one may expect $\beta_\mu$ to be positive (if $\beta_{C_{\rm s}} \approx -1/2$), thus, an increasing function with radius. However, the disk structure itself can be re-arranged such that $|\beta_{C_{\rm s}}| \leq 1/2$, which eventually will satisfy the relation 4.23. This is indeed what is found.

One should, however, keep in mind that this equation is a rough estimate and might be subject to the different disk physics involved. If the magnetic torque is not the only supporter of the accretion, as in the case of the viscous simulations of Murphy et al. (2010), the above presented relation might be relaxed. However, similar analysis can be performed to set the limit of the magnetization with respect to other quantities.

### 4.5.4 A Modified Diffusivity Model

This section presents a diffusivity model, which does not suffer from the accretion instability. Although the standard diffusivity model provided the opportunity to probe a wider parameter space, it is not applicable for very long-term studies.

Note that the transition from the a direct simulation of turbulence to the mean field approach, which lacks the small scales by design, is indeed subtle. So far, in the literature, the jet launching problem is addressed without considering the origin of the magnetic field by a dynamo. Therefore, the only way of amplifying the magnetic field is by advection (or stretching in case of a toroidal field). There is also no intrinsic angular momentum transport by the turbulence itself. The only term needed to be modeled when applying a small-scale turbulence, is the effective magnetic diffusivity. This might have surprising consequences. In order to suppress the turbulence, one should rather amplify the effective diffusivity – leading to a stronger decay of the magnetic field and resembling the quenching of diffusivity (or dynamo) – rather than decrease it, leading to stronger advection and thus an amplification of the magnetic field. The main motivation of a new model for the diffusivity is to consider stronger feedback by the disk magnetization. The accretion instability is overcomed by assuming a stronger dependence of $\alpha_{\rm ssm}$ on the magnetization,

$$\alpha_{\rm ssm} = \alpha_{\rm m} \sqrt{2\mu_0} \left( \frac{\mu}{\mu_0} \right)^2 , \tag{4.24}$$

where $\alpha_{\rm m} = 1.55$ and $\mu_0 = 0.01$. Here the previous overall form and constants are preserved, indicating that both models are the same at the magnetization $\mu_0$. A quadratic dependence on $\mu$ was chosen in order to amplify the feedback. Choosing a power lower than two might have revealed other complications, for example, feedback too weak to work fast enough, and keep $\alpha_{\rm ssm}$ under the constraint of Equation 4.22. This diffusivity model is referred as the strong diffusivity model.

### 4.5.5 The Long-term Disk-outflow Evolution

The strong diffusivity model allows to overcome the accretion instability. As a result, it is possible to perform the simulations for much longer times, reaching evolutionary time steps of $t > 150,000$ which corresponds to approximately 25,000 revolutions at the inner disk orbit.

Figure 4.17 shows the typical computation domain and the initial dynamics of the system. As usual, the evolution starts with the propagation of the toroidal Alfvén wave, resulting in a propagating cocoon. At this point, the innermost area ($R \leq 10$) has reached a quasi-steady state, while the outer part has not even slightly moved from the initial state. Figure 4.18 presents the

same simulation at a later state when a strong outflow has been developed. Notice the difference between the inner part, $r \leq 200$, and the outer part, $r \geq 200$. The inner part has already relaxed to a steady state, while the outer region shows rapid accretion and ejection patterns. This is a direct consequence of the new diffusivity model. The logic behind implementing the enhanced feedback is valid only when the accumulation of the flux is possible. The initial imbalance between advection and diffusion in the outer part leads to a rapid advection of the magnetic flux to the inner disk. As a result, the rapid accretion further leads to higher inclination angles of the magnetic field (smaller angle with respect to the disk surface). This results in a higher efficiency for the toroidal magnetic field induction, thus leading to even more rapid accretion and ejection.

Figure 4.19 shows the long-term evolution on a small sub-grid of the simulation with the strong diffusivity model. As can be seen, until time $t = 10,000$ only a small fraction of the disk has dynamically evolved (up to $R \approx 50$), while at later times the outer parts of the disk also reach a new dynamic state. A steady outflow is established from the whole disk surface (shown on this sub-grid) and reaches a super-fast magnetosonic speed. Note that the positions of the critical MHD surfaces are constant in time, which is a further signature of a steady state.

The outflow reaches maximum velocities typically of the order of 100 km s$^{-1}$ for YSOs, or 70,000 km s$^{-1}$ in case of AGNs. Concerning observationally relevant scales, the simulations compare to the following numbers. The numerical grid is comparable to 150 AU for YSOs, and 0.14 pc in the case of AGNs Physically more meaningful is the grid size where the simulation has reached a steady state. This is a size comparable to 25 AU for YSOs, and 5000 AU in the case of AGNs, but can be extended by running the simulations longer. The dynamical timescale of 150,000 time units (or 25,000 disk orbits) corresponds to about 550 yr in the case of YSOs and about 200 yr in the case of AGNs. Typical accretion rates of the simulations are $3 \times 10^{-7} M_\odot\,\mathrm{yr}^{-1}$ for YSOs and $0.1 M_\odot\,\mathrm{yr}^{-1}$ in the case of AGNs, but one has to keep in mind that these values depend not only on the intrinsic scaling of the central mass and inner disk radius, but also on the scaling of density. Therefore, the most extended and longest MHD simulations of jet launching obtained is presented so far–connecting the jet launching area close to the central object with the asymptotic domain which is accessible by observations.

Although a spherical grid is computationally very efficient and may allow to extend the computational domain to almost any radius, in reality its application for the jet-launching simulations is somewhat limited. There are two reasons for that. First, it takes obviously much longer time for the outer disk areas to evolve into a new dynamical steady state. Thus, the outer disk will remain close to the initial state of the simulation for quite some time. Second, a more severe drawback is the lack of resolution for the asymptotic jet. For example, for distances $R > 500 R_0$ along the rotational axis, a jet radius of about $r_{\mathrm{jet}} \approx 25$ can be resolved only by about five grid cells (applying a typical resolution). Therefore the computational domain for such grid size is restricted to about $R_{\mathrm{out}} \simeq 1000 - 2000 R_0$. The above-mentioned resolution issue is in fact one of

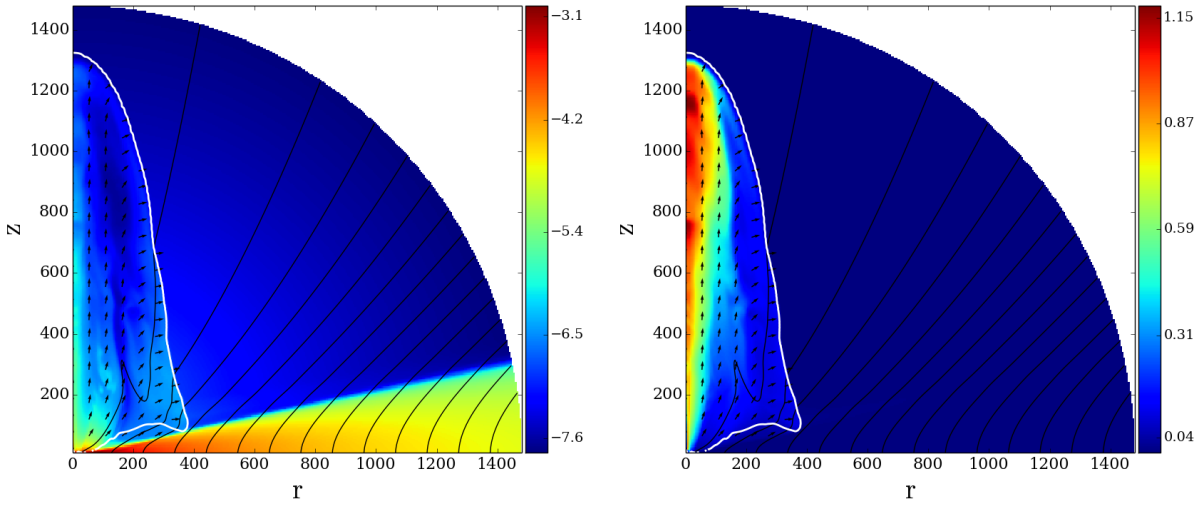


**Figure 4.17:** Initial evolution of the strong diffusivity setup at $T = 1500$. The colors represent the logarithm of density (left) and speed (right), the black lines denote the magnetic field, the arrows the normalized velocity, and the white line shows the Alfvén surface. Arrows show normalized velocity vectors.

the advantages for using cylindrical coordinates for jet formation simulations.

### 4.5.6 Results of the Strong Diffusivity Model

By design, the purpose of the strong diffusivity model was to avoid the accretion instability. As a consequence of this application, the magnetization profile does not decrease with radius (see Figure 4.20) Although both simulations (with standard and strong diffusivity model) start from the same initial disk magnetization, the disk evolution results in a quite different magnetization distribution. The standard diffusivity model (the reference simulation from above) results in a magnetization profile decreasing with radius. In contrast, for the strong diffusivity model a rather flat magnetization profile emerges. In non-viscous simulations, assuming radial self-similarity, a flat (or not decreasing with radius) profile is essential for sustaining a continuous accretion flow at any given radius.

As soon as a steady state is reached, the evolutionary track for this simulation is represented by a simple dot in all $(\mu, X)$ diagrams (at least from 1000 to 150,000 time units). The mean inner disk magnetization is $\mu \approx 0.012$. This simulation fits to every relation presented above, such as mass and energy flux ratios, or magnetic shear, that were derived, applying a standard diffusivity model. In other words, the aforementioned dots belong to the curves drawn in the $(\mu, X)$ diagrams.

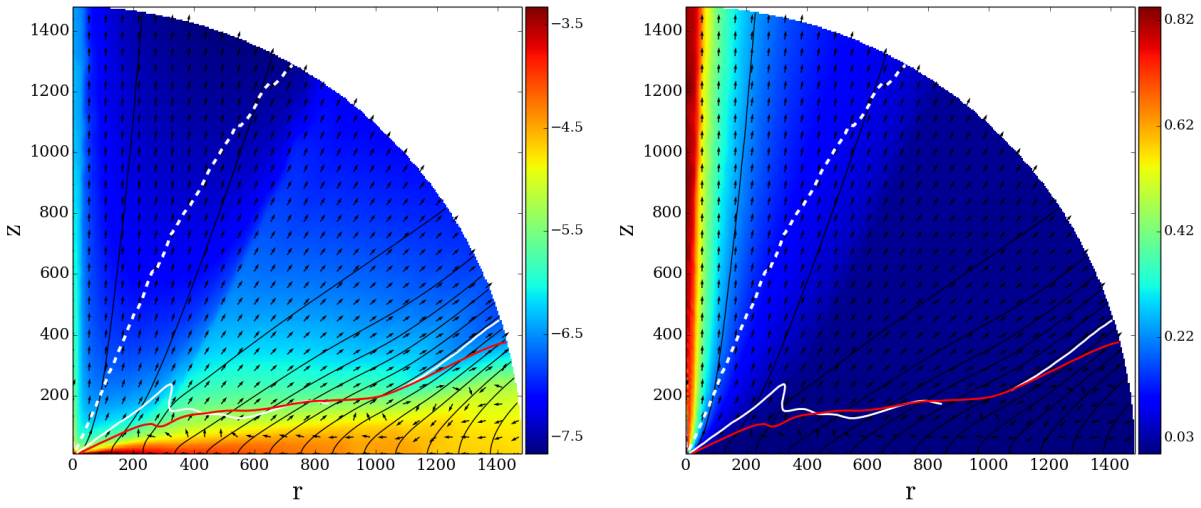


**Figure 4.18:** Time snapshot of the strong diffusivity setup at $T = 150,000$. Shown are the density (colors, in logarithmic scale), the poloidal magnetic flux (thin black lines), the sonic (red line), the Alfvén (white line), and the fast magnetosonic (white dashed line) surfaces. Arrows show normalized velocity vectors.

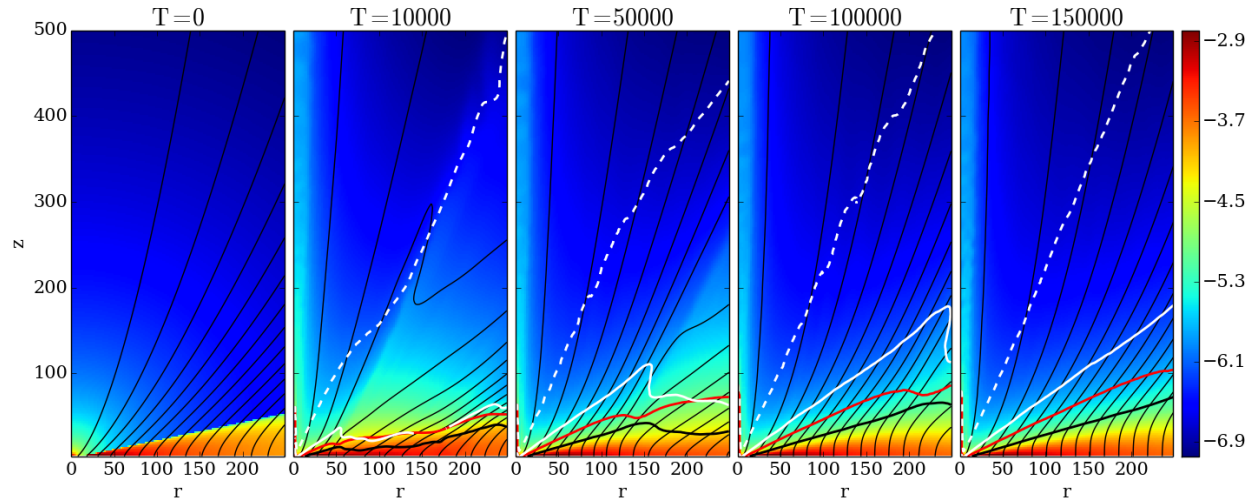


**Figure 4.19:** Time evolution of the disk–jet structure for the strong diffusivity simulation. Shown is the evolution of density (colors, in logarithmic scale), the poloidal magnetic flux (thin black lines), the disk surface (thick black line) the sonic (red line), the Alfvén (white line), and the fast magnetosonic (white dashed line) surfaces.

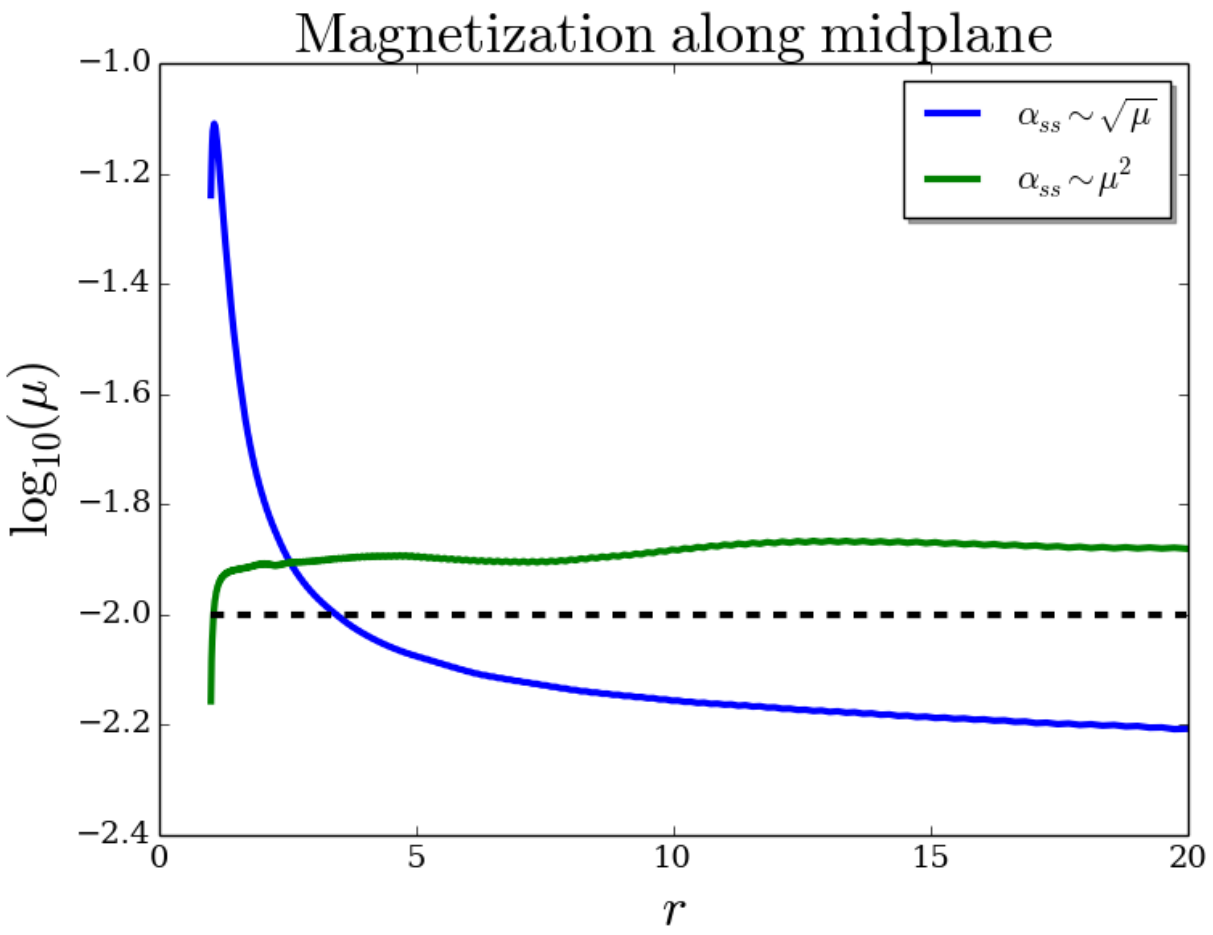


**Figure 4.20:** Magnetization distribution throughout the disk for reference and the strong diffusivity model at $T = 10,000$. The dashed line marks the initial magnetization.

There are several distinct features one can derive from the resulting magnetic field structure. Figure 4.21 shows the toroidal to poloidal magnetic field component ratio. Taking into account that the disk magnetization (calculated from poloidal component only) is uniform, three different regions can be distinguished. The first region is between the midplane and the disk surface where the toroidal magnetic field reaches its maximum and the torques change sign. The second region is between the disk surface and the Alfvén surface where the ratio of the field components is quite constant. The third region is beyond the Alfvén surface when the poloidal component of the magnetic field becomes weak enough to keep a rigid magnetic field structure and the toroidal component starts to dominate the poloidal one.

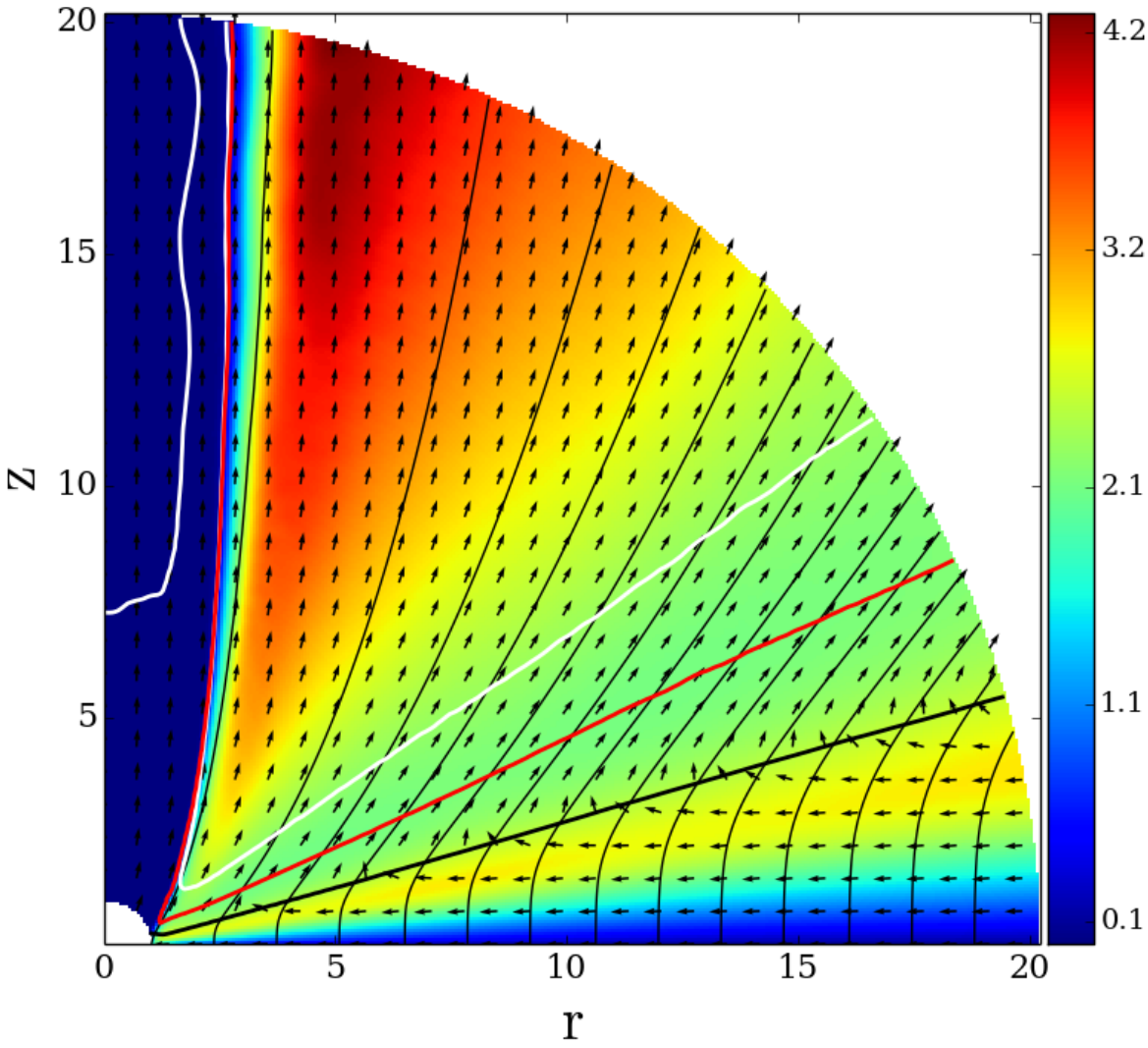


**Figure 4.21:** Ratio of the toroidal to poloidal magnetic field for the strong diffusivity model at $T = 10,000$. The lines represent the disk (thick black line), the sonic (red line), and the Alfvén (white line) surfaces. Arrows show normalized velocity vectors.

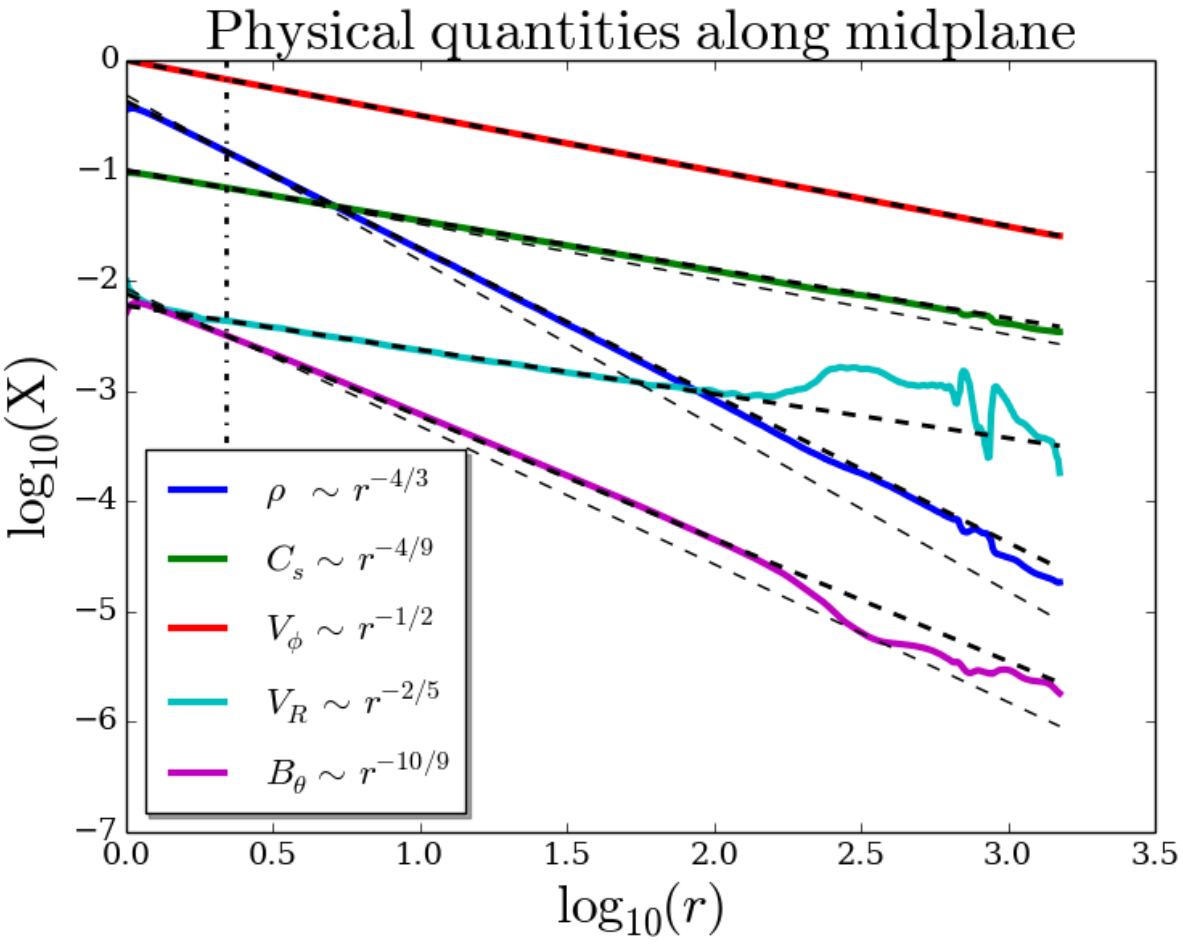


**Figure 4.22:** Physical quantities along the midplane for the strong diffusivity model. The colors show different variable profiles, the thick dashed lines correspond to certain power laws, and the mismatched thin dashed lines correspond to the initial distributions of variables. The vertical dashed line marks $r$ = 200.

### 4.5.7 DYNAMICAL PROFILES OF A STEADY STATE ACCRETION DISK

In this subsection, the disk structure in a steady state is further explored. Figure 4.22 presents the radial profiles of certain magnetohydrodynamical variables along the midplane. The profiles derived from the numerical simulations with their approximations by power laws are shown and compared to the initial distribution. These radial profiles are obtained along the disk midplane, however, they also hold for at least one disk semi-height. The thetoidal profiles that normalized to the corresponding midplane value (not shown here) almost coincide with each other, indicating that the assumption of a self-similar disk is in fact reasonable, though different power indexes should be used.

In particular, Figure 4.22 shows how the disk structure evolves from a certain initial power-law distribution into another power-law profile. Distinct power-law profiles are present for radii up to $R \leq 250$. This corresponds to the area where the disk evolution has reached a steady state. For very small radii, $R \leq 1.1$, a deviation from a power-law profile are also seen, which is considered as a boundary effect.

At time $t = 150,000$, the following numerical values for the power-law coefficients $\beta_X$ for the different variables at the midplane $X(r, \theta = \pi/2) \sim r^{\beta_X}$ are found. The disk rotation remains Keplerian throughout the entire evolution, thus $\beta_{V_\phi} = -1/2$. The radial profiles for density and gas pressure slightly change from their initial distribution. The density power-low index changes from $\beta_\rho = -3/2$ to $\beta_\rho = -4/3$, while the pressure changes from $\beta_{\rm P} = -5/2$ to $\beta_{\rm P} = -20/9$. For the accretion velocity, a profile of $\beta_{V_R} = -2/5$ is found, and $\beta_{B_\theta} = -10/9$ for the magnetic field. As a consequence, the profile for the magnetization remains about constant $\beta_\mu \sim 2\beta_{B_\theta}/\beta_{\rm P} = (-20/9)/(20/9)$. The accretion velocity remains subsonic over the whole disk with an accretion Mach number of $V_R/C_{\rm s} \simeq 0.1$.

Following Ferreira & Pelletier (1995) and considering the mass accretion $\dot{M}_{\rm acc} \sim R^2 \rho V_R$, it is easy to get the ejection index $\xi = 0.26$. This is in accordance with previous work Sheikhnezami et al. (2012).

### 4.5.8 DISCUSSION OF THE NEW DIFFUSIVITY MODEL

The strong diffusivity model, Equation 4.24, does not necessarily lead to a flat magnetization profile. The model does not directly force the magnetization to be uniformly distributed – in contrast, the profile is expected to be outwardly increasing. As previously showed, the magnetization profile is linked to the ejection index and it has to be positive if the sound speed remains as initially distributed. The disk hydrodynamics changes such that the magnetization of the disk remains flat, thus satisfying Equation 4.23.

Another way of reasoning is the following. In the case of a flat magnetization profile the result of the simulation is no longer sensitive to the diffusivity model. In other words, it is possible to switch back from the new diffusivity model to the standard model when the radial magnetization profile is uniform (along the midplane). However, the diffusivity parameter $\alpha_{\rm m}$ has to be correspondingly re-normalized. The only substantial deviation from a uniform profile is in the innermost disk, which might be influenced by the boundary condition. In fact, such a test simulation is performed, switching back from a strong diffusivity to a standard diffusivity model. As expected, the accretion instability begins to manifest itself similarly as before, leading to the typical magnetization profile (increasing toward the center). However, it takes a much longer time to substantially affect the outer parts of the disk.

The steady state solution achieved when using the strong diffusivity model, perfectly fits the results obtained by the standard model (shown previously as a dot in the plots). This actually approves that the main agent in driving outflows is the actual magnetization, and that the magnetic diffusivity is only the mediator through which the magnetic field structure is being governed. A self-consistent treatment of turbulence is not yet feasible in the context of outflow launching. Therefore, what should be considered first, is the resulting magnetic field strength and distribution, but not the diffusivity model itself.

## 4.6 CONCLUSIONS

The results of MHD simulations were presented, investigating the launching of jets and outflows from a magnetically diffusive accretion disk. The time evolution of the disk structure is self-consistently taken into account. The simulations are performed in axisymmetry applying the MHD code PLUTO 4.0. In contrast to previous work, a spherical coordinate system and numerical grid were applied, which implies substantial benefits concerning the numerical resolution and the stability (in time evolution) of the simulations.

In particular, the following results were obtained.

(1) The numerical setup in spherical coordinates for disk–jet-related problems is very robust. The use of spherical geometry in the context of the outflow launching cannot be underestimated. It allows to study the launching of outflows for very long time (more than 150,000 time units) on highly resolved (up to 24 cells per disk height) and at the same time very large (1500 $r_0$) domains. On the other hand, a spherical grid somewhat limits the study of jet propagation, since the resolution far from the origin becomes low. The rather low resolution in the outer disk region, where the dynamical timescales are long, helps to smooth out small-scale disturbances, thus helping to establish a steady state.

(2) The study has approved a robust disk-outflow structure: however, for the highest resolution, the evolution is prone to have some more fluctuations. The ability to evolve the disk for a very long time disentangles the complex interrelations between the essential quantities for the jet launching. Those are the disk actual magnetization ( at a certain time and averaged for a certain location), the mass, energy and angular momentum fluxes, and the jet terminal velocity.

(3) The main result is that it is the actual rather than the initial disk magnetization that plays a key role for the jet formation and directly affects the accretion power. The value of the initial magnetization can fail to properly characterize the disk–jet properties, but sets the overall jet torque and the disk's magnetic reservoir. This becomes obvious for very weakly magnetized disks ($\mu_0 = 0.003$). In this case, when choosing a low magnetic diffusivity, the magnetic flux can still be accumulated to a high magnetization in the inner disk. The actual magnetization necessary for sustaining a stable jet is of the order of $10^{-3}$, that is in accordance with Murphy et al. (2010).

(4) The ejection Mach number in the case of a moderately strong magnetization ($\mu < 0.15$) is linearly related with respect to the disk magnetization. This is indeed consistent with the linear to the magnetization the mass ejection to accretion relation. The mass ejection index (the ratio between ejection and accretion) is about 0.3 and thus is similar to the literature values.

(5) In case of uniform magnetization, the MHD disk quantities show a self-similar structure, i.e., resulting in approximately the same vertical profile, and a radial power-law distribution. In the case of the strong diffusivity model, the corresponding power-law indices for all MHD quantities were presented, although these power-law indices may directly depend on the actual strength of the magnetization. This would be a natural consequence of the ejection index being a function of magnetization as well.

(6) There are two principally different regimes for outflow launching, which are complementary to each other. In the case of weak magnetic fields (below $\mu \approx 0.03$), the signatures of a strong magnetic shear are present, which results in less powerful, but more efficient (higher ejection index), outflows. In the case of a higher magnetization, the magnetic shear, the ejection efficiency, and the energy ejection to accretion flux ratio do not strongly depend on magnetization

(7) The upper theoretical limit for the parameter specifying the anisotropy $\chi$ in the magnetic diffusivity in case of the standard diffusivity model is found, essentially depending on the actual magnetization in the disk. In the limit of low magnetization the anisotropy parameter must satisfy $\chi \leq 1/\alpha_{\rm m}^2$.

(8) In the non-viscous steady state, assuming radial self-similarity, the magnetization profile should be non-decreasing function of radius. In a steady state, jet-launching disks must have a radially increasing profile of the mass accretion rate. This is a requirement of a positive ejection

index. Taking into account that (i) the accretion Mach number is proportional to the magnetization and (ii) assuming that the radial profile of the sound speed does not strongly deviate from Keplerian, it was shown that the index of the magnetization profile is non-negative.

This chapter studied the long-term evolution of outflow-generating disks. In the following chapters, the connection of the jet properties (the potential observables) with the underlying disk quantities (Chapter 5), and the extended setup for treating self-generated magnetic field by a mean-field dynamo (Chapter 6), will be discussed.

# 5

# Connecting Jet to the Disk: what jets are launched from what disks*

This chapter investigates what kind of jets are launched by what kind of disks. This chapter further studies the great importance of the disk magnetization, moving from the disk to the jet space. A striking interrelation between the jet properties, in terms of the jet integrals, and the degree of the underlying disk magnetization has been firmly established. This chapter also discusses how from the jet observables the magnetization of the underlying disk can be inferred. The corresponding example is also provided.

## 5.1 Introduction

Astrophysical jets as highly collimated beams of high velocity material and outflows of less degree of collimation and lower speed are an ubiquitous phenomenon in a variety of astrophysical

*This chapter is based on a paper submitted to the Astrophysical Journal by Deniss Stepanovs and Christian Fendt; titled: Modeling MHD Accretion-Ejection – disk Magnetization and Asymptotic Jet (Stepanovs & Fendt 2014b). All the simulations, the figures and most of the scientific discussion and interpretation presented in this chapter were done by the author of the thesis.

sources. These outflows are launched from a magnetized accretion disk surrounding the central object. A number of studies have been devoted to understand the launching process, i.e. the transition from ejection, treating steady-state MHD (Wardle & Königl 1993; Li 1995; Ferreira & Pelletier 1995; Königl et al. 2010; Salmeron et al. 2011) or time-dependent numerical simulations (Casse & Keppens 2002, 2004; Meliani et al. 2006; Zanni et al. 2007; Murphy et al. 2010). However, despite all efforts in recent years, it is still unclear, what kind of disk drive jets and what kind of disks do not. In this chapter, the interrelation between essential disk parameters and the disk jet is further investigated. The main question is: what are the disk properties that govern the shape and propagation of the jet?

In Chapter 4 was shown that it is essential to relate the actual jet properties resulting from a simulation to the actual disk properties. This implies that initial simulation parameters such as the initial plasma beta or magnetization do not necessarily govern the jet evolution, as they are substantially changing during the disk evolution. This has been suggested earlier by Sheikhnezami et al. (2012); Fendt & Sheikhnezami (2013), who report a variation of the disk Alfvén speed by a factor ten during the simulation. As usual models for the disk magnetic diffusivity parameterize the diffusivity with the Alfvén speed, the disk diffusivity is substantially modified that severely affects the disk evolution and also the mass loading from disk to outflow. The magnetic diffusivity generally defines the trend for the disk magnetization - field amplification by advection versus field decline by diffusion. The resulting magnetization - at a certain time - determines the actual launching conditions.

On the other hand, due to the constant mass loss of the disk, the disk magnetization is slowly changing in time. This gives the opportunity to investigate the jet-launching conditions in a quasi-steady state over a wide parameter range. This compares to the classical approach of running a few parameter runs characterized by a difference in the initial choice of say plasma beta or maximum magnetic diffusivity.

While Chapter 4 essentially demonstrated that disk accretion and ejection and the accretion-to-ejection ratio of the mass and energy fluxes strongly depend on the actual disk magnetization, the current Chapter proceeds a step further and provide relations between a number of jet observables and the underlying disk quantities.

The sample of simulations is mainly the same, but extended. It allows to probe a broader parameter space concerning the accretion disk magnetization. The steady-state jet MHD integrals are discussed that later are linked to the disk magnetization. The assumptions under which these integrals, derived from simulation results, can be referred to the jet observables are further discussed. Finally, it is demonstrated how the disk quantities such as magnetization can be linked to the jet integrals, applying in particular parameters of a protostellar jet.

This chapter is organized as follows. Section 2 briefly comments on the model setup, namely

the choice of parameters. Section 3 presents the general evolution of the jet-disk system. It also explains how the jet characteristics are estimated from the simulations. Section 4 discusses and tests the steady-state MHD integrals of the simulations. It also discusses the jet terminal speed, energy and angular momentum. Section 5 finally connects the disk properties, mainly the disk magnetization, to the jet parameters, presenting general relations between these properties. It also investigates the jet-launching mechanism from the jet perspective. Section 6 provides an example in which the disk properties are derived from the observables. Finally, Section 7 summarizes the chapter.

## 5.2 MODEL SETUP

As stated in Introduction, the model presented in Chapter 4 is used for current studies. However, the parameter space of the model is further enlarged. The parameters for the model are selected as follows. The initial magnetization for the parameter runs covers a broad range $\mu_0 = 0.001, 0.002, 0.003, 0.005, 0.01, 0.02, 0.03$. The magnetization is defined as in Chapter 4, as the ratio of the poloidal magnetic field to thermal pressure $\mu \equiv B_{\rm p}^2/2P$, measured at the disk midplane.

The magnetic diffusivity parameter $\alpha_{\rm m}$ is chosen to be about the critical value, for which diffusive and advective processes are balanced. A slight deviation from the critical value for diffusivity brings the simulation in a state that is either slightly dominated by diffusion or advection. Essentially, as simulations progress this allows to probe of a wide range of actual disk magnetization $\mu = 2 \times 10^{-4} - 3 \times 10^{-1}$, as the magnetic flux is then either advected into a larger value, or diffused out to a lower value. When the actual disk magnetization is in the above-mentioned range, all simulations show a robust behavior over long timescales and smoothly evolve for more than 10,000 time units when the simulation is stopped.

Table 5.1 summarizes all the simulations discussed in this chapter. The simulations are labelled alphabetically according to the strength of the initial magnetization. The plus and minus signs indicate a slightly higher or lower diffusivity parameter $\alpha_{\rm m}$, respectively. Note, that a *lower* diffusivity parameter leads to *stronger* actual disk magnetization.

As usual, all variables are normalized to their values at the inner disk radius $R_0$.

**Table 5.1:** Parameter runs of the simulations, alphabetically labelled according to the initial disk magnetization $\mu_0$. The plus and minus signs indicate a slightly higher or lower diffusivity parameter $\alpha_m$, respectively.

| | A | B+ | B | C+ | C- | D+ | D- | E+ | E- | G | H |
|---|---|---|---|---|---|---|---|---|---|---|---|
| $\mu_0$ | 0.001 | 0.002 | 0.002 | 0.003 | 0.003 | 0.005 | 0.005 | 0.01 | 0.01 | 0.02 | 0.03 |
| $\alpha_m$ | 1.6 | 1.6 | 1.5 | 1.65 | 1.6 | 1.6 | 1.55 | 1.65 | 1.6 | 1.8 | 1.65 |

## 5.3 GENERAL DISK-JET EVOLUTION

Chapter 4 presented the approach that allowed to study a vast parameter space of the disk-jet structure. It was mainly concentrated on the disk physics. In the present study the same model as in Chapter 4 is applied, however, the main emphasis is on the jet dynamics and how it is linked to the disk properties.

When the simulation is started from the initial conditions, the disk will evolve into a new dynamic equilibrium. Accretion starts as soon as the disk wind is able to remove sufficient angular momentum from the disk. A new dynamic state of the disk is defined by the balance between advection of mass and magnetic flux and diffusion of magnetic flux. Accreted disk material is lifted onto the outgoing magnetic field lines of jet and outflow. This is essentially a *diffusive MHD* process. The material that is loaded on the field lines is mainly accelerated by magneto-centrifugal effects (Blandford-Payne mechanism) for sufficiently strong poloidal field strength. When the outflow strengthens, the angular momentum removal increases, supporting further accretion. Finally, a steady state is reached. This state as well as the balance between accretion and ejection, and also the mass loading from disk onto jet is strongly governed by the magnetization, which depends on the diffusivity.

### 5.3.1 DISK AND JET CHARACTERISTIC QUANTITIES

Chapter 4 explored in detail the general structure of the simulations, putting an emphasis on the disk variables, namely accretion and ejection efficiencies of the mass and energy fluxes. In this chapter, the main concern is the jet quantities, especially the jet integrals that can be compared to steady-state MHD theory.

Figure 5.1 shows a subset of a large grid of a typical result of the simulations for the structure of the disk-jet system at a very evolved stage, $T = 10,000$. The location of typical surfaces,

namely the disk surface and the magneto-sonic surfaces have become stationary, indicating that the disk-outflow structure in this volume has reached a steady state.

For further comparison, a certain sheet of the jet is considered, i.e. that part of the outflow that is most energetic and that is confined between the magnetic flux surfaces rooted at $r = 1.1$ and $r = 1.5$. The jet quantities are referred as the averages over this jet layer at a certain height $z$,

$$X(z) = \text{mean}(X)|_z = \frac{1}{N}\sum_i^N X(r_i, z). \tag{5.1}$$

Thus, the averaging is performed over $N$ grid cells between two close magnetic flux surfaces. This choice of the averaging region is guided by two reasons. First, in order to avoid any direct influence of the accretion boundary, the inner radius is chosen to be slightly larger than unity. In order to average the physical quantities over a certain height, a sufficient number of cells needed to be considered. However, not to many cell should be considered as it is desirable to have a typical number for this flux surface and not a broad average over parts of the whole outflow.

$X_\mathrm{D} = X(0)$ is referred as the root or disk quantities of the jet and $X_\mathrm{A} = X(z_\mathrm{A})$ as to jet quantities at the Alfvén point, where the poloidal flow reaches the Alfvén speed $V_\mathrm{A} = B_\mathrm{P}/\sqrt{\rho}$. The detailed interrelation between the disk magnetization and all jet quantities will be discussed below.

This approach is similar to the classical steady-state MHD analysis of jet quantities along a given magnetic flux surface. However, when investigating simulation results, the average over a bundle of flux surfaces (a jet sheet) provides a more robust measure. That measure taken at the innermost sheet of the jet can be seen as representative of the whole jet. This is easy to demonstrate by exploring the profiles of different quantities along the disk surface. For example Figure 5.2 shows the normalized profiles of jet power density along the disk surface $\rho_\mathrm{\dot{E}} = \rho E V_\mathrm{P}$. Although these profiles were taken at the same time $T = 10,000$, the underlying disk properties are completely different. Nevertheless, these profiles show a very similar shape, approving that the average measure is representative for the whole jet.

## 5.4 STEADY-STATE JET MHD INTEGRALS

In Chapter 2, the jet integrals along the magnetic flux surface $\Psi \equiv \int \vec{B}_\mathrm{p} \cdot d\vec{A}$ were introduced. In order to explore the interrelation of these integrals, characterizing the jet properties, to the actual quantities describing the disk (mainly disk magnetization), the integrals are normalized to their midplane values. In this chapter, all jet integrals are presented in non-dimensional units, namely

$$k \equiv \frac{K}{\sqrt{\rho_\mathrm{D}}},\ w \equiv \frac{\Omega_\mathrm{F}}{\Omega_{\mathrm{F}_0}},\ l \equiv \frac{L}{L_0},\ e \equiv \frac{E}{E_0},\ v_\mathrm{inf} \equiv \sqrt{e},\ j \equiv \frac{J}{J_0} \tag{5.2}$$

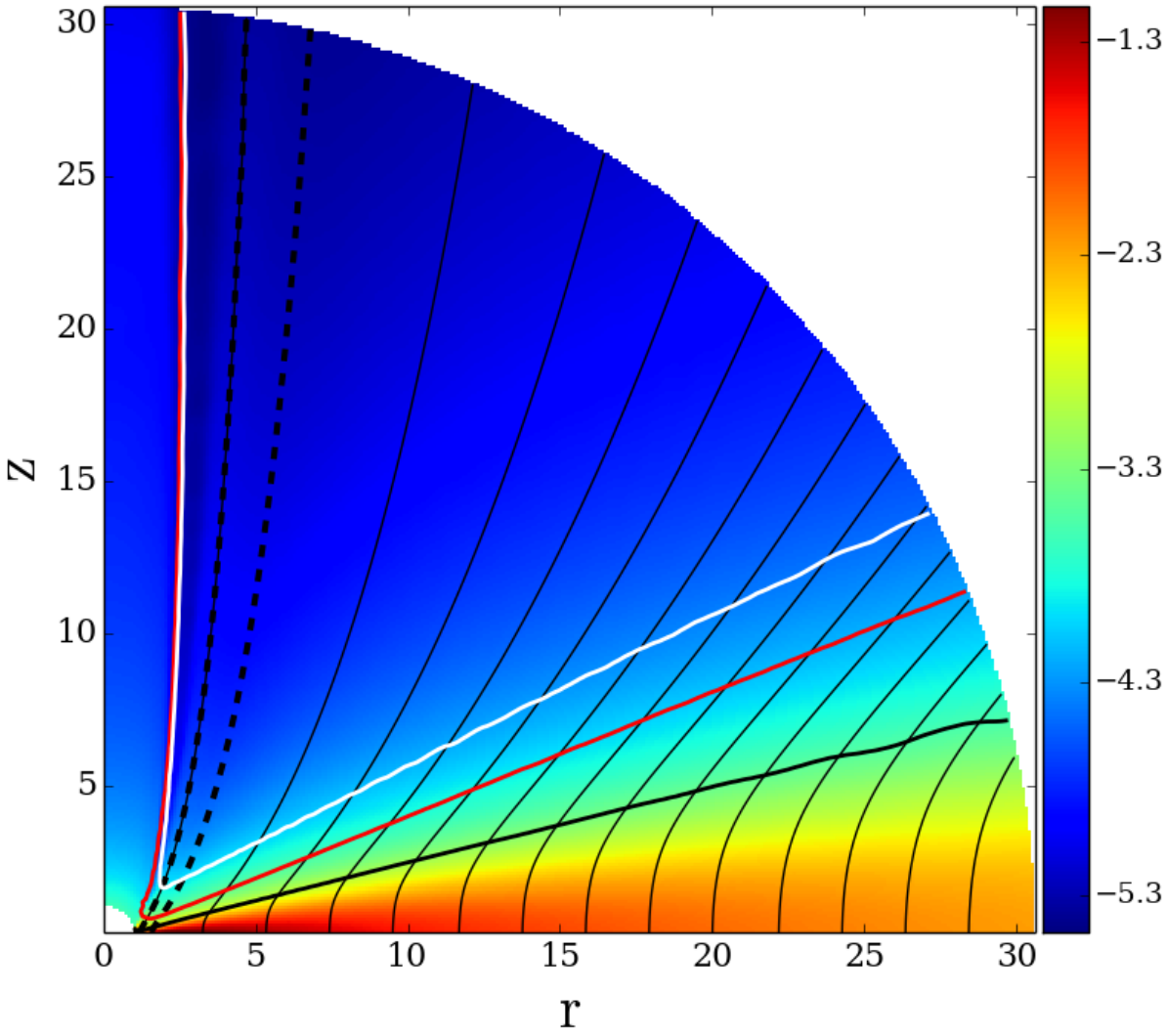


**Figure 5.1:** Typical structure of the disk-jet system at $T = 10,000$. Colors show logarithmic density. Thin black lines show the magnetic field line. Thick dashed lines, rooted at $r = 1.1$ and $r = 1.5$, mark the jet region, investigated in this chapter. White, red and black lines mark the Alfvén, the sonic and the disk surface, respectively.

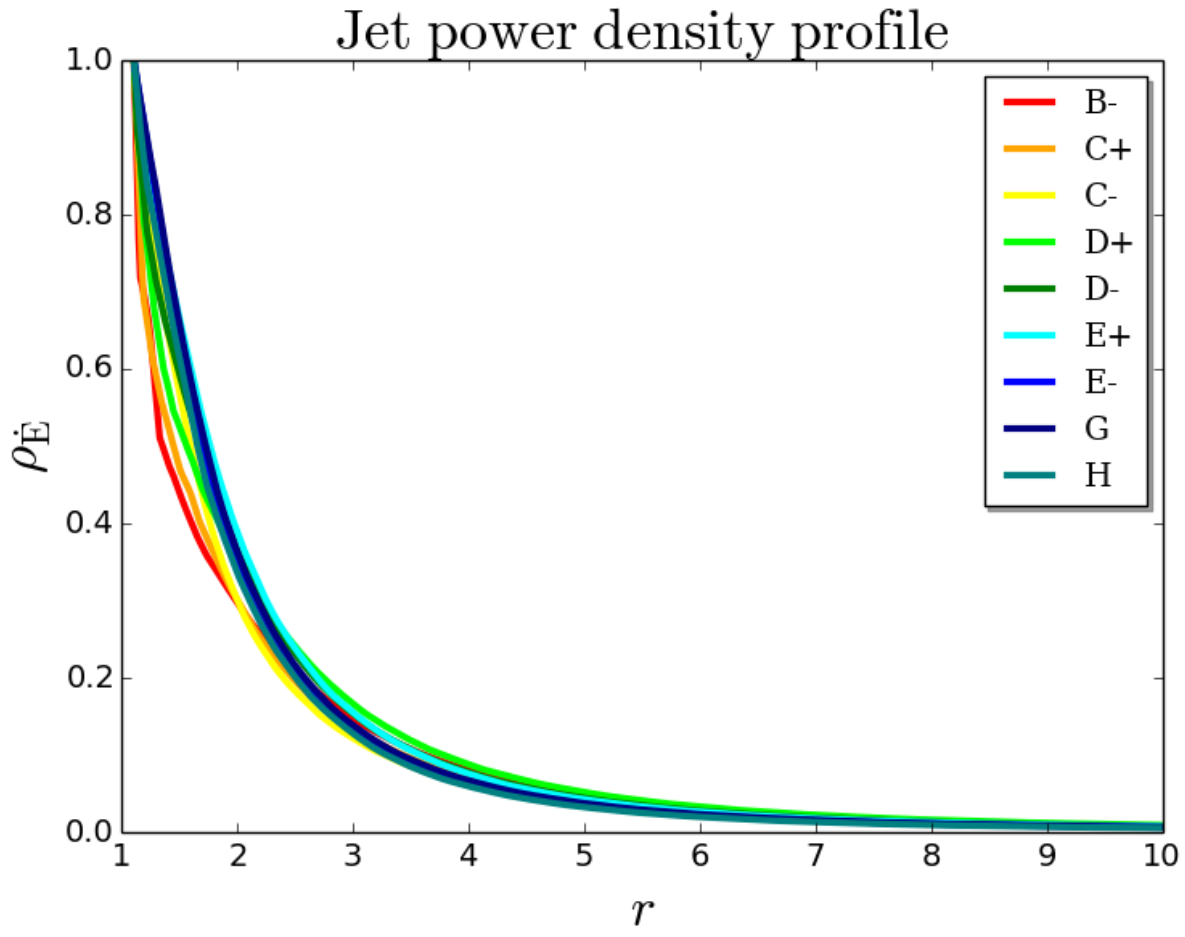


**Figure 5.2:** Normalized profile of the jet power density $\rho_{\dot{E}}$ along the surface $z = Hr + 1$ (parallel to the disk surface) for a range of parameter runs (see Tab. 5.1 for the notation).

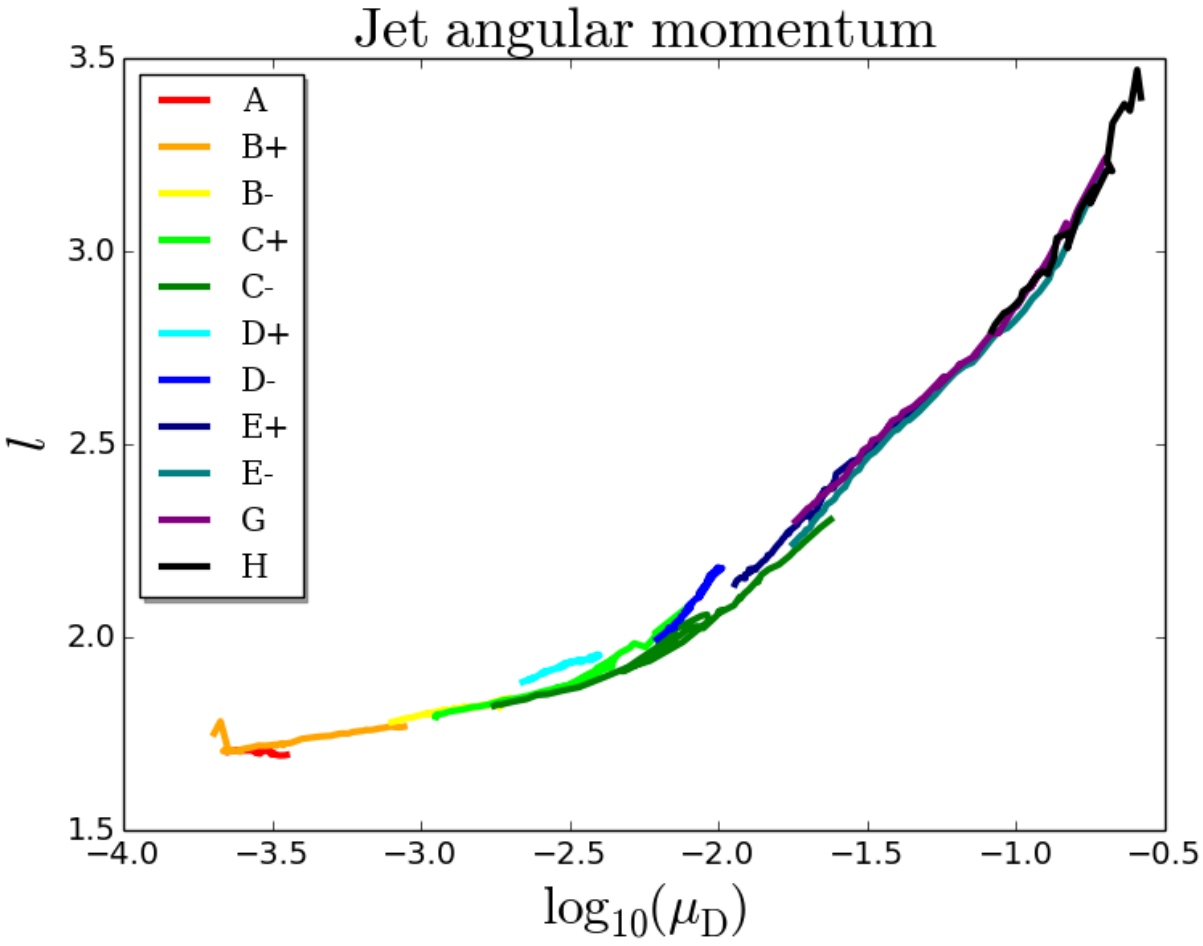


**Figure 5.3:** Jet specific angular momentum $l$ with respect to the disk magnetization $\mu_{\rm D}$. Each line represents the evolution of a single simulation (see Table 5.1) from 700 to 10,000 time units.

Note that since the underlying disk is only slightly sub-Keplerian, $\Omega_{\rm F,0}, L_0, E_0, J_0$ are constants that can be determined solely by the their midplane value, averaged over the area $r = 1.1 - 1.5$. The jet integrals are obtained numerically by averaging over an area along the outflow sheet across the Alfvén surface, $z = [z_{\rm A}...(z_{\rm A} + 2.0)]$. For each integral, the conservation along the magnetic field line is checked.

One of the main result of this study is the strong interrelation between the jet physical properties and the disk magnetization. Such a relation is illustrated in Figure 5.3. The relation between the disk magnetization and the jet angular momentum as measured at the Alfvén surface is shown. Each of the lines shown in the plot is the result of a long time evolution of a certain simulation. The simulations have started from a different initial disk magnetization and evolve in time. As the actual disk magnetization changes with time, the corresponding jet angular momentum changes as well. It is clearly seen that all simulations follow the same general trend. The main point to learn from this figure is that there is a clear interrelation between the disk magnetization and the jet angular momentum. The higher the disk magnetization the more angular momentum is extracted by the outflow. Note that the interrelation between the jet integrals is of course expected from steady-state MHD jet theory (Okamoto 1975; Sauty & Tsinganos 1994; Contopoulos & Lovelace 1994; Fendt & Camenzind 1996; Ferreira 1997). In that approach the motion along the magnetic flux surfaces is described by the so-called wind equation or Bernoulli equation. For cold jets the critical solution of the wind equation relies on the prescription of the magnetization at the foot point of the field line, sometimes denoted by the parameter $\sigma_\star$. If gas pressure is considered, the flow magnetization is defined by the critical condition at the slow magnetosonic point that is usually seen as the foot point of the outflow. In this approach, it is the underlying disk (magnetization) that defines the jet integrals. In order to make this distinction, the different jet physical properties will be subsequently interrelated not only with the disk magnetization, but also with respect to the jet angular momentum.

### 5.4.1 CONSERVED QUANTITIES ALONG THE JET

This section discusses how the physical jet properties vary along the outflow. The outflow is followed from its origin to the asymptotic domain.

Figure 5.4 shows the profiles along the jet for the different jet energy components. It can be seen that although the variables along different field lines are averaged, the total energy is well conserved along the jet. This approves the averaging approach. The same is true for all jet integrals studied here. The thermal energy is negligible everywhere in the jet. The gravitational energy is negligible only far from the disk, when the jet has passed the escape surface $V_{\rm P}(R,\theta) \gg V_{\rm escape}(R,\theta)$, at about $Z = 20$ One also sees how the magnetic energy is being spent for the exit

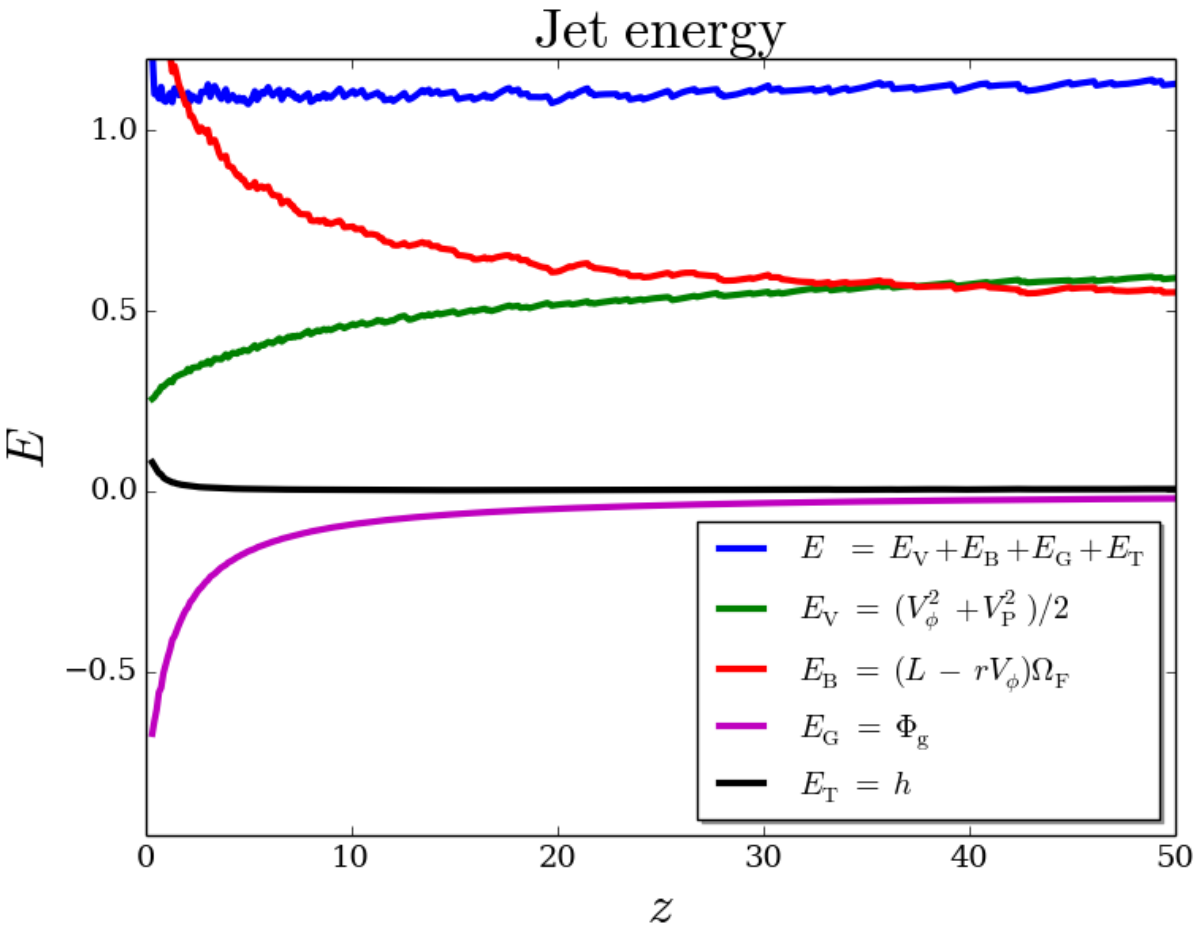


**Figure 5.4:** Jet energy $E$ along the jet $\mathcal{Z}$ for the $B$- simulation at time $T = 10,000$. Different energy components are indicated by colors: total (blue), kinetic (green), magnetic (red), gravitational (magenta), and thermal (black) energy.

from the potential well and being transferred into kinetic energy of propagation. Note that the transformation of magnetic into kinetic energy far from the disk becomes slow.

Figure 5.5 shows how the magnetic angular momentum is being transferred into kinetic one. The magnetic angular momentum of the jet is transferred slower into the kinetic angular momentum at later stages of the disk-jet evolution of about $T = 10.000$. What is actually happening is that the disk magnetization substantially changes from $\mu_{\rm D} \approx 0.02$ at $T = 1.000$ to $\mu_{\rm D} \approx 0.2$ at $T = 10.000$. The stronger the magnetic field in the disk, the more angular momentum is being extracted by the outflow (Figure 5.3). Note that for the strong magnetic field it is more difficult to reach the state where all magnetic energy has been transformed into kinetic jet energy.

The next section continues the analysis of the asymptotic jet velocity.

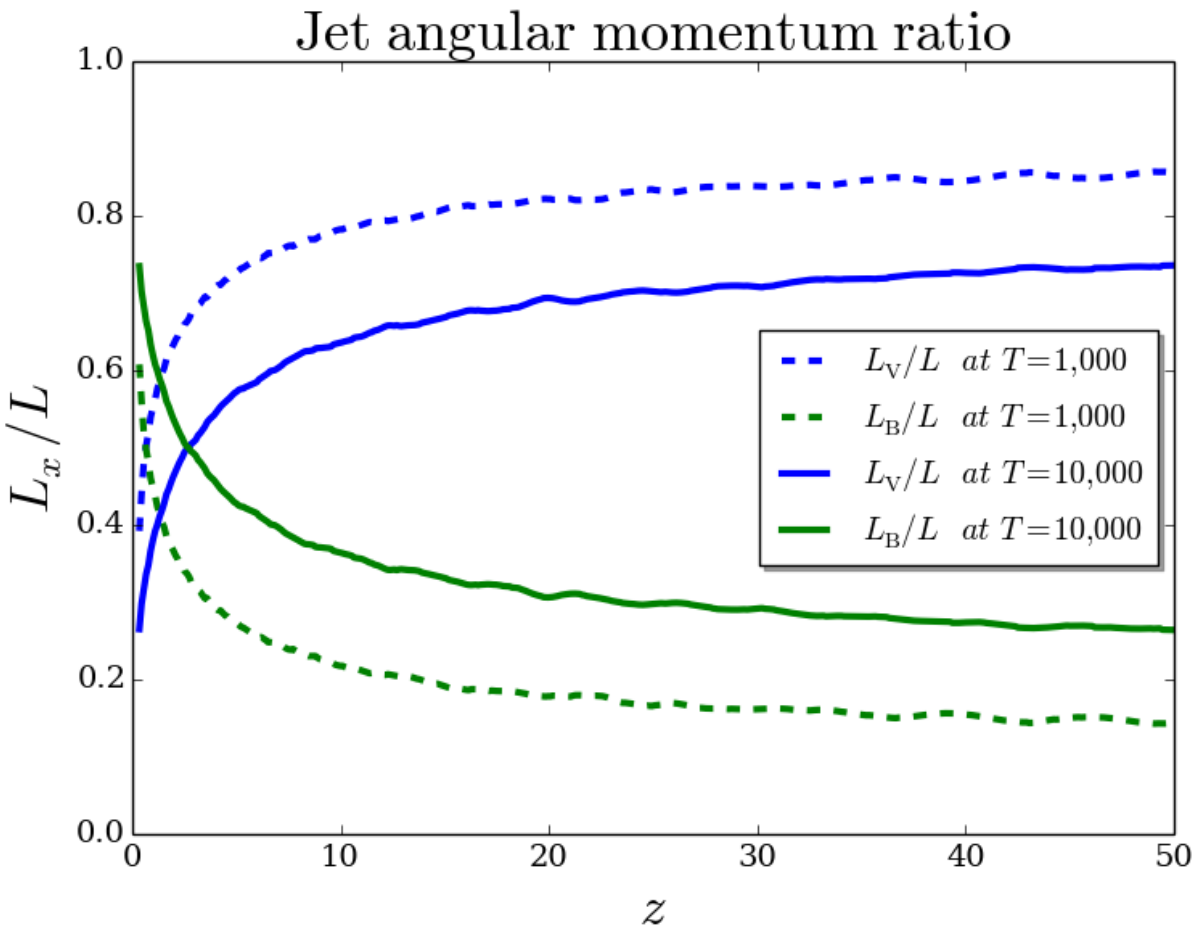


**Figure 5.5:** Jet angular momentum components along the jet, derived for the *B*- simulation. Kinetic (blue lines) and magnetic (green lines) to total jet angular momentum ratios are plotted at $T = 1000$ (dashed lines) and T=10.000 (solid lines).

### 5.4.2 ASYMPTOTIC JET VELOCITY

Applying the steady-state MHD conservation laws in principle allows to connect the observed jet quantities far from the source to the conditions of the launching area, and for example derive the size of this area (Anderson et al. 2003)[1]. The essential assumption is that far from the disk the magnetic component of the jet angular momentum is negligible with respect to the kinetic one.

Most of the literature on this question considers steady state MHD jets, starting with Blandford & Payne (1982) who already provided analytical expressions for the energy and angular momentum partition for self-similar cold jets. Far from the source they find a ratio of Poynting flux to kinetic energy flux of $2/(M_{\rm FM}^2 - 2)$ for flows with a fast magnetosonic Mach number $M_{\rm FM} > 1$. Applied to protostellar jets with typically $M_{\rm FM} \simeq 3$, this corresponds to kinematically dominated jets by a factor four. Similarly, the angular momentum flux is typically dominated by the kinematic part. Also relativistic jets can be dominated by the kinetic energy flux (Chiueh et al. 1991; Li et al. 1992; Begelman & Li 1994) as they typically extend beyond the fast surface (where the flow energies are in equipartition. Numerical simulations of the relativistic MHD jet formation (Porth & Fendt 2010; Porth et al. 2011) agree with these results, however, it is numerically difficult to reach the asymptotic domain far from the source. In particular if additional Poynting flux is provided from the jet-launching accretion disk, the computational domain may not be large enough to allow to transfer all magnetic energy to kinetic energy. Collimated jets are different in this respect from radial (monopole-type) stellar wind that have their fast surface at infinity and only reach equipartition (Michel 1969).

Although there are no evidence in the simulations that the jet can in principle transfer all its energy into kinetic one, several issues have to be taken into account. First, the terminal jet speed is very sensitive to the magnetic to total angular momentum ratio. Figure 5.6 shows the jet speed at infinity (defined through Equation 5.2) over the jet angular momentum parameter for different fixed values of the magnetic to total angular momentum ratio. The upper curves represent the limiting case of vanishing magnetic angular momentum in the asymptotic regime and therefore define an upper limit for the jet speed. The bottom curve corresponds to the case when the magnetic angular momentum is 0.15 of the total angular momentum. Notice that in the case of the small angular momentum $l$, corresponding to the low magnetization, the jet speed is significantly reduced.

Second, the asymptotic value for the jet velocity that can be observed has to be measured far from the disk, since it will take a long time to transform the magnetic angular momentum and energy into the kinetic component. Figure 5.7 shows the jet distance from the origin at which the magnetic to total angular momentum ratio reaches certain value. Notice that the magnetic

[1] Note that a direct interrelation is maybe as internal shocks will affect the jet angular momentum balance and jet rotation (Fendt 2011).

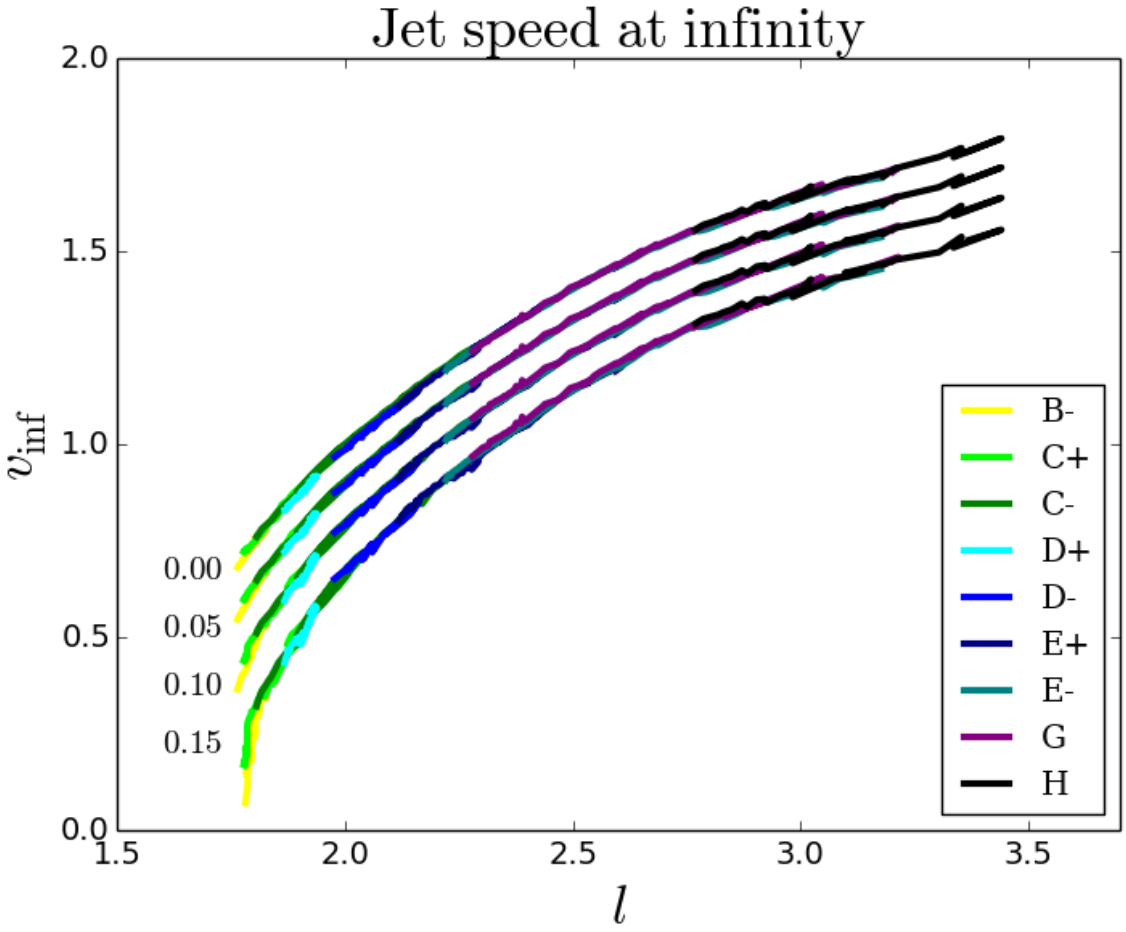


**Figure 5.6:** Asymptotic jet velocity $v_{\rm inf}$ with respect to the specific angular momentum $l$ for different magnetic to total angular momentum ratios [0.0, 0.05, 0.1, 0.15] (from top to bottom)

and kinetic angular momenta become equal (thus the ratio is 0.5) rather close to the disk surface, while other branches (for higher ratio) clearly levels up. Thus, the two upper branches corresponding to the close values of 0.80 and 0.82, significantly differ, especially for the high total angular momentum case.

Figure 5.8 shows the maximum speed of the jet $v_{\rm max} = \max_z V_{\rm P}$ in the computational domain with respect to the theoretical limit of the jet speed. This speed is measured as the maximum speed of the jet region of the whole domain, thus along the $z$-axis. The simulations are only considered after 3000 time units, when the initial Alfvén wave leaves the domain. The theoretical limit is never realized, and that the jet maximum speed is 75% of this limit. Note, however, that the increase of resolution leads to a higher jet maximum speed in the domain. Thus, in order disentangle the final jet speed, a further investigation is needed.

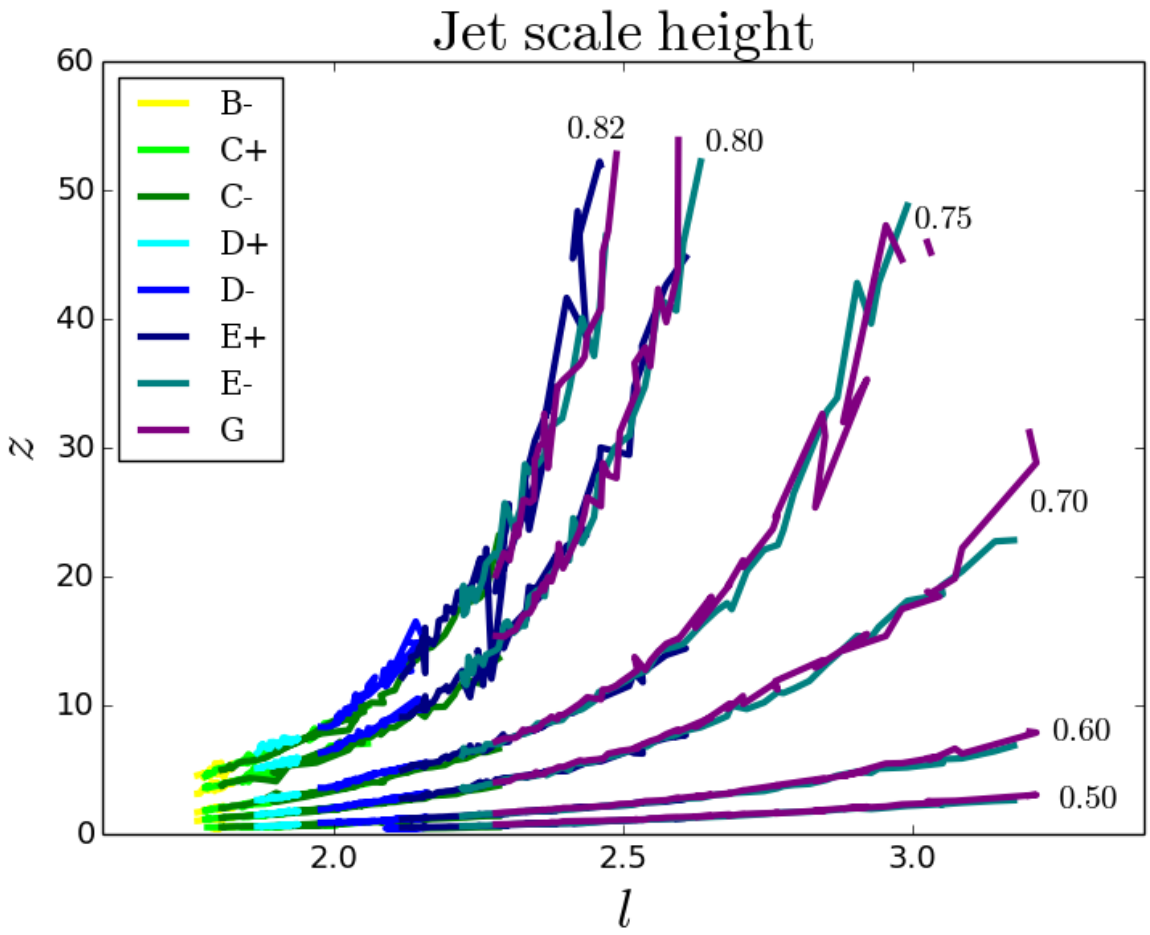


**Figure 5.7:** Jet scale heights $z$ with respect to the jet angular momentum $l$. Different groups of lines show the heights at which the jet kinetic angular momentum is [0.5, 0.6, 0.7, 0.75, 0.8, 0.82] (from bottom to the top) of the jet total angular momentum.

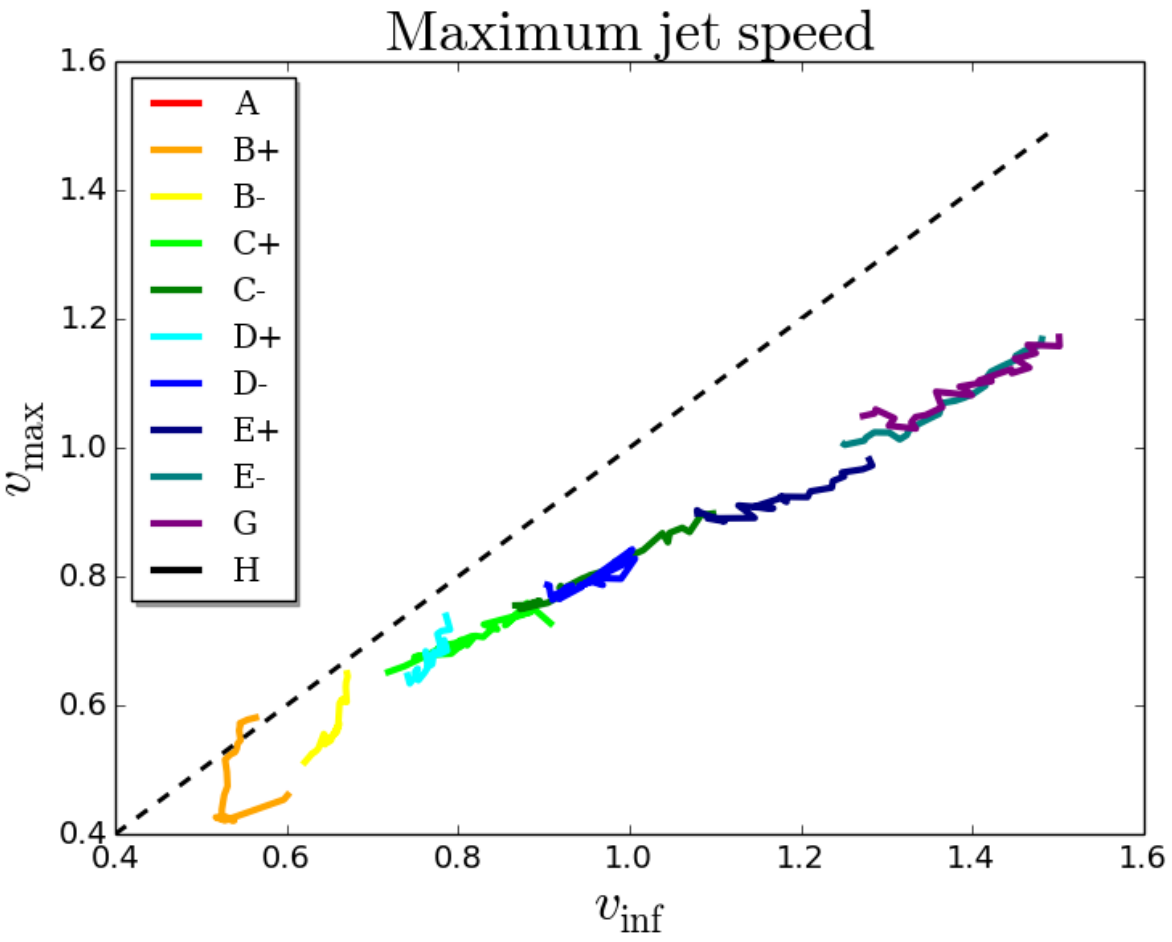


**Figure 5.8:** Jet maximum speed $v_{\mathrm{max}}$ as measured in the domain with respect to the estimated jet speed at infinity $v_{\mathrm{inf}}$. Each line represents the evolution of a single simulation (see Table 5.1) from 3,000 to 10,000 time units.

## 5.5 THE DISK-JET CONNECTION

This section discusses the interrelation between the jet physical properties and the accretion disk properties. The main question considered is *what kind of disks drive what kind of jets?*. Consequently, applying such an interrelation would allow to derive from the observed jet parameters conclusions about the underlying jet-driving disk.

### 5.5.1 "STABILITY" CHECK

In order to connect the jet to the underlying disk, the conservation of jet quantities along the field lines is being used. The conservation of integrals hold only in a steady state case (also axisymmetry required). Although it is found that in the case of low disk magnetization ($\mu_{\rm D} \leq 0.001$) jet becomes unstable after the Alfvén surface, it shows a steady behavior before the Alfvén surface. Therefore all derived relations hold for even smaller disk magnetizations ($\mu_{\rm D} < 0.001$).

Nevertheless, the presented logic and derived formulas are valid even for estimated jet observables even for lower magnetizations, since the unsteadiness of the jet is presumably caused by the interaction between artificial inflow of the coronal region of the boundary.

### 5.5.2 JET ENERGY AND ANGULAR MOMENTUM RELATION

One way to translate the jet kinetic properties to the underlying Keplerian disk properties is to assume that the energy and angular momentum on the disk surface are predominantly of the kinetic origin (Anderson et al. 2003). As a consequence the $j$ and $\omega$ integrals do not depend on the underlying disk properties. In other words the relation between the jet energy and jet angular momentum is linear (see Equation 2.19). This is not no longer true if the underlying disk is strongly magnetized. Figure 5.9 shows the jet angular velocity $\omega$ with respect the disk magnetization. As can be clearly seen, this variable is not constant and does depend on the underlying disk magnetization (this is also true for the $j$).

Although $\omega$ and $j$ are not constant there is still a tight relation between the jet energy and the jet angular momentum (see Figure 5.10 ). For small angular momentum the relation is almost linear, when in the case of high angular momentum the relation shows significant deviation from linearity.

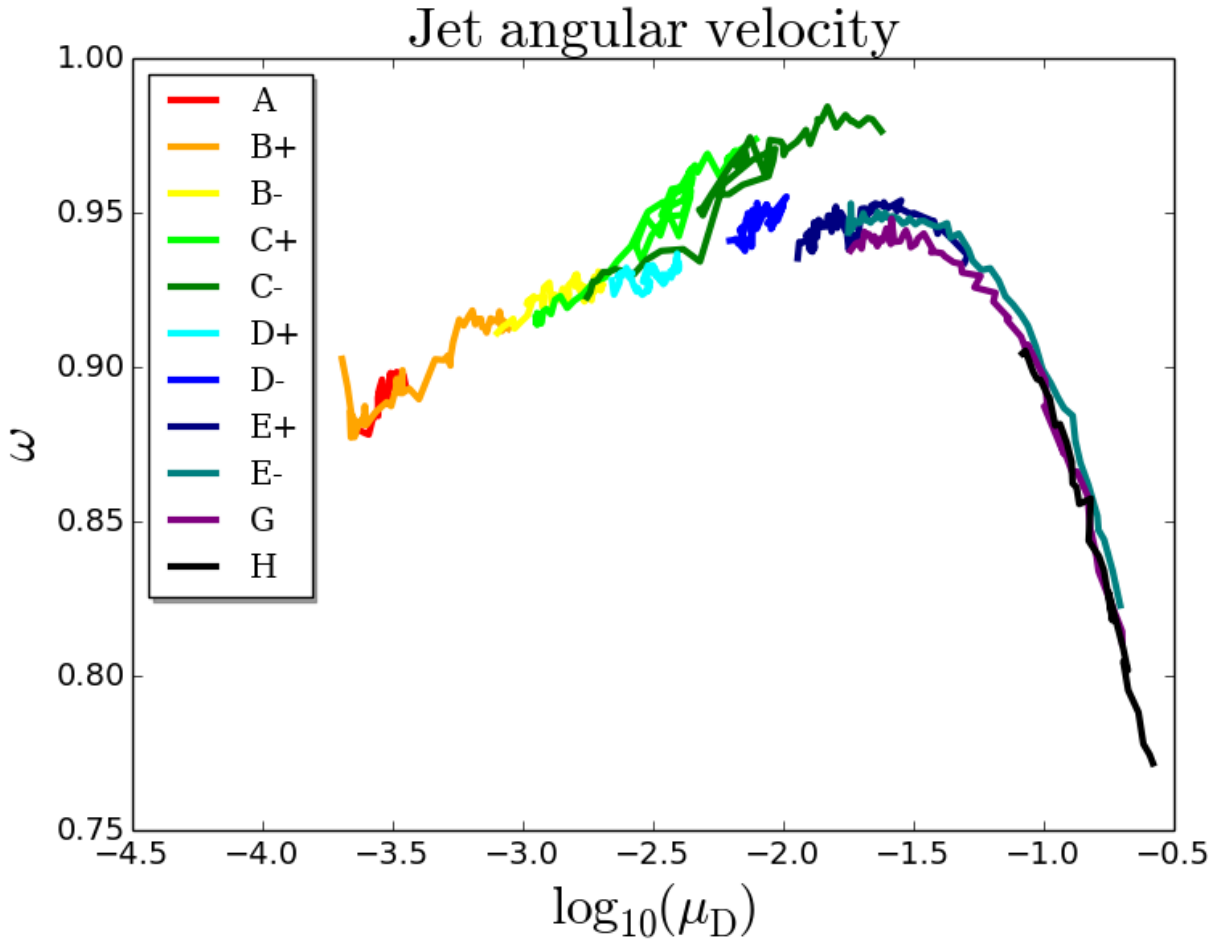


**Figure 5.9:** Jet angular velocity $\omega$ with respect to the disk magnetization $\mu_{\rm D}$. Each line represents the evolution of a single simulation (see Table 5.1) from 700 to 10,000 time units.

This relation can be approximated by formula

$$e = a/l^4 + b/l^2 + c \tag{5.3}$$

Later this approximation will be used to translate the jet observables into the underlying disk properties such as launching radius, disk magnetization and other jet quantities. For now on it is assumed that the jet-launching radius is obtained. Using the jet-launching radius the observables (energy and angular momentum) can be translated by simple normalization to the jet quantities $(e, l)$

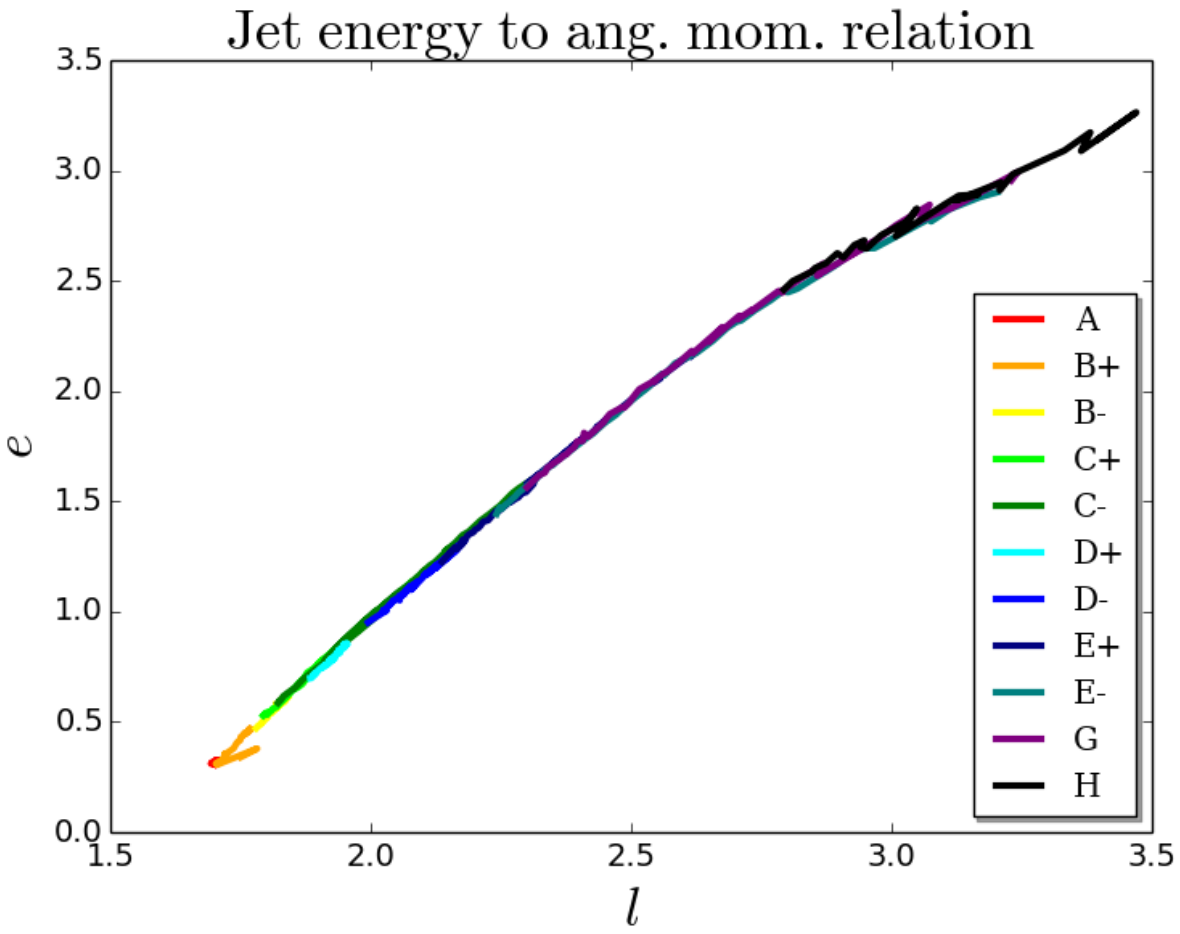


**Figure 5.10:** Jet specific energy $e$ and jet specific angular momentum $l$ relation. Each line represents the evolution of single a simulation (see Table 5.1) from 700 to 10,000 time units.

### 5.5.3 JET ENERGY AND DISK MAGNETIZATION

This subsection presents how the jet energy is related to the disk magnetization. Figure 5.11 indeed present the strong relation between the jet energy and the underlying disk magnetization. Two different regions, corresponding to different slopes, can be distinguished before and after a $\mu \approx 0.03 - 0.05$. This magnetization is referred to as a critical one $\mu_{\rm crit}$ Before the critical magnetization (as was shown in Chapter 4), the magnetic forces play a great role in the outflow launching. For magnetization higher than critical, the centrifugal forces strongly dominate the magnetic ones.

Note that knowing the jet energy automatically gives the information of the actual magnetization in the disk. Later it will be shown how other jet variables at the Alfvén point are related to the disk magnetization.

### 5.5.4 ALFVÉN LEVER ARM

Another very useful quantity, which directly links the mass ejection and accretion rates is so-called Alfvén lever arm (Pelletier & Pudritz 1992).

$$\lambda = r_{\rm A}/r_0. \tag{5.4}$$

The mass accretion rate can be obtained from the mass ejection rate by simple approximation $\dot{M}_{\rm acc} \sim \lambda^2 \dot{M}_{\rm ej}$. Note, that the jet angular momentum is related to the jet angular velocity through the Alfvén lever arm $l = \lambda^2 \omega$. Figure 5.12 shows the square of lever arm. As for the jet energy and angular momentum, a strong relation of the Alfvén lever arm with respect to the disk magnetization is presented. For stronger disk magnetization, the Alfvén lever increases. The reason is twofold. First, the stronger the magnetization of the disk, the higher the Alfvén surface is located from the disk. Second, the higher the disk magnetization, the stronger the extraction of the angular momentum in the disk. The higher angular momentum extracted from this material allows the material to reach locations further away from the axis. In principle, these processes are what the Blandford-Payne magneto-centrifugal acceleration is referring to.

### 5.5.5 THE ACCRETION-EJECTION PROCESS

In order to compute the mass, energy and angular momentum fluxes, respectively, one needs to interrelate the accretion and ejection densities and velocities. Therefore a ratio

$$\zeta = \frac{\rho_{\rm A} V_{\rm P,A}}{\rho_{\rm D} V_{\rm P,D}}. \tag{5.5}$$

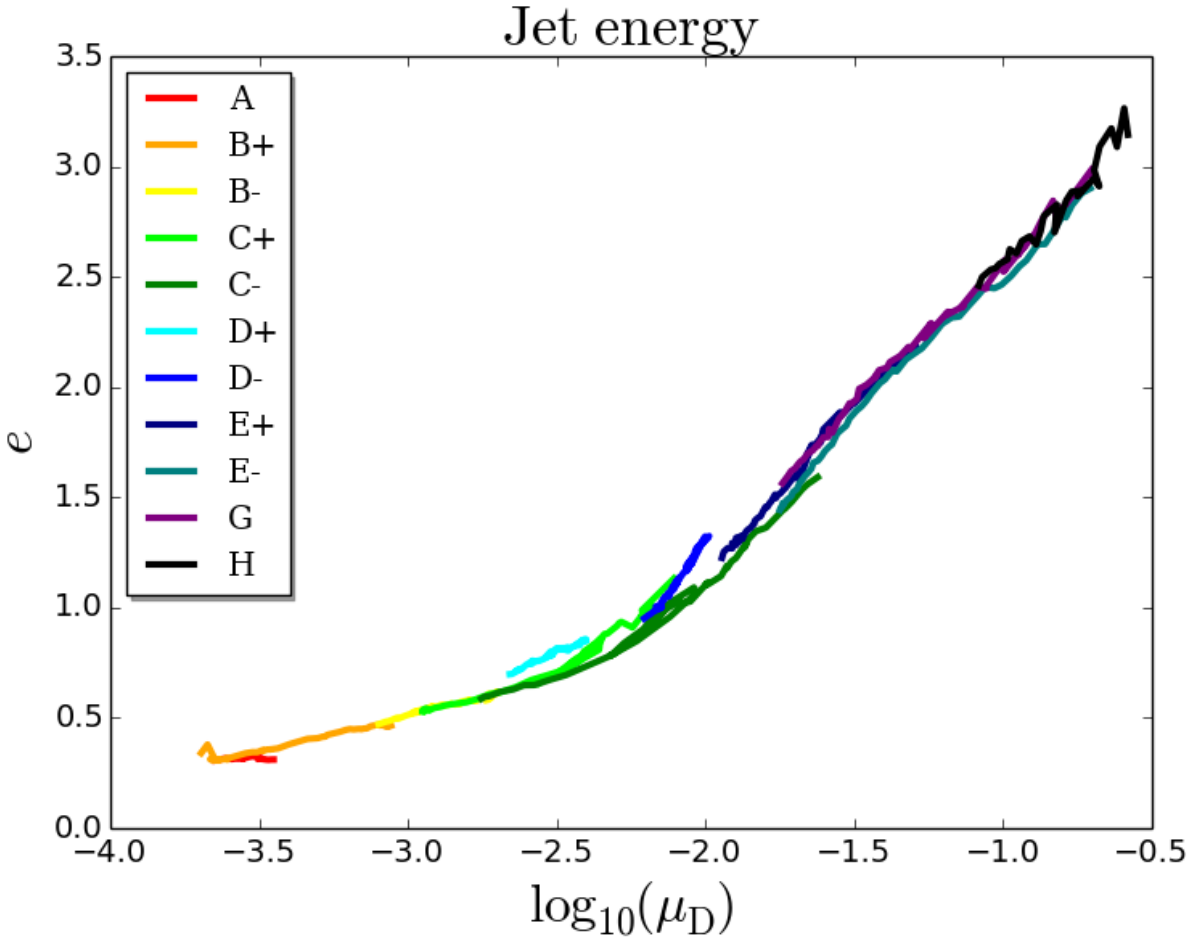


**Figure 5.11:** Jet energy $e$ with respect to the disk magnetization $\mu_{\rm D}$. Each line represents the evolution of a single simulation (see Table 5.1) from 700 to 10,000 time units.

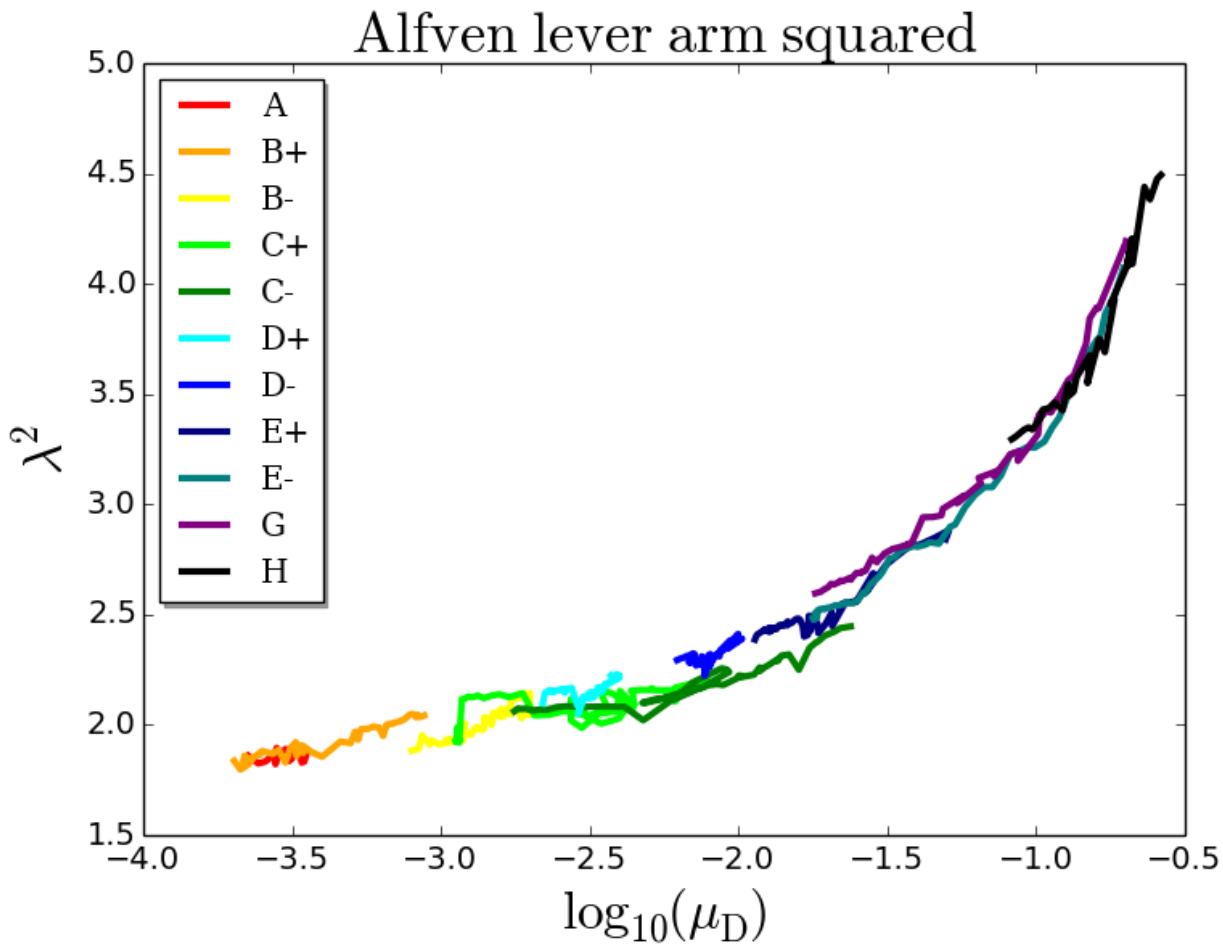


**Figure 5.12:** Squared Alfvén lever arm $\lambda^2$ with respect to the disk magnetization $\mu_D$. Each line represents the evolution of a single simulation (see Table 5.1) from 700 to 10,000 time units.

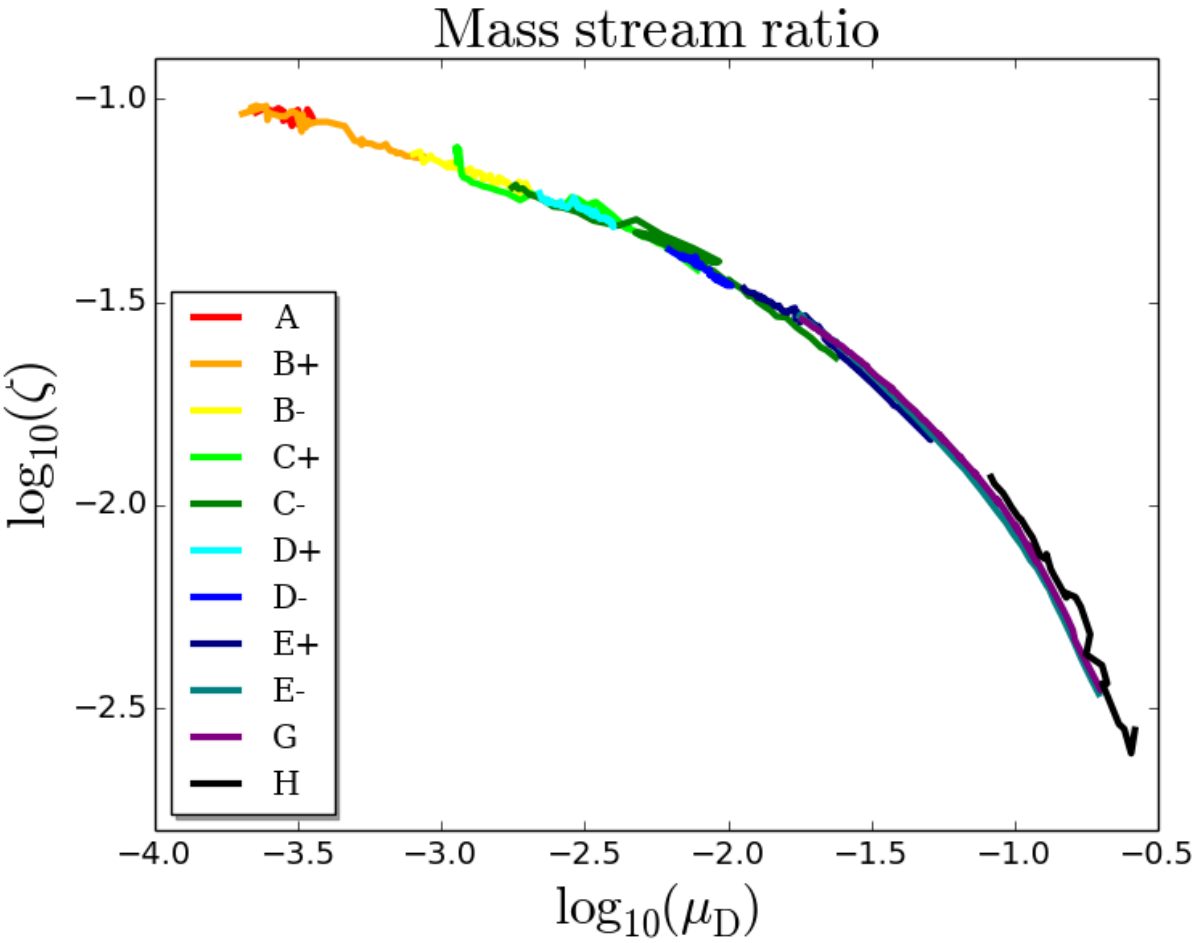


**Figure 5.13:** Mass stream ratio $\zeta$ with respect to the disk magnetization $\mu_{\rm D}$. Each line represents the evolution of a single simulation (see Table 5.1) from 700 to 10,000 time units.

is introduced. It compares the property of the ejected gas (the stream of the mass along the flux surface) at the Alfvén point to the value measured in the underlying disk This is analogue to the ejection index introduced by (Ferreira & Pelletier 1995). Figure 5.13 shows this mass stream ratio with respect to the disk magnetization. It is clearly seen that the mass stream ratio is much smaller for the strong disk magnetization. In the case of not very strong magnetization ($\mu_{\rm D} < 0.1$) the relation between $\zeta$ and *logarithm* of the disk magnetization can be linearly approximated.

There is also a tight correlation between the disk magnetization and the mean accretion Mach number (Königl & Salmeron 2011, Chapter 4). Figure 5.14 presents this relation for a wider range of the disk magnetization. First, a tight relation is seen also for very low disk magnetization. There is also an indication for different rates at which the accretion Mach number grows as the disk magnetization increases.

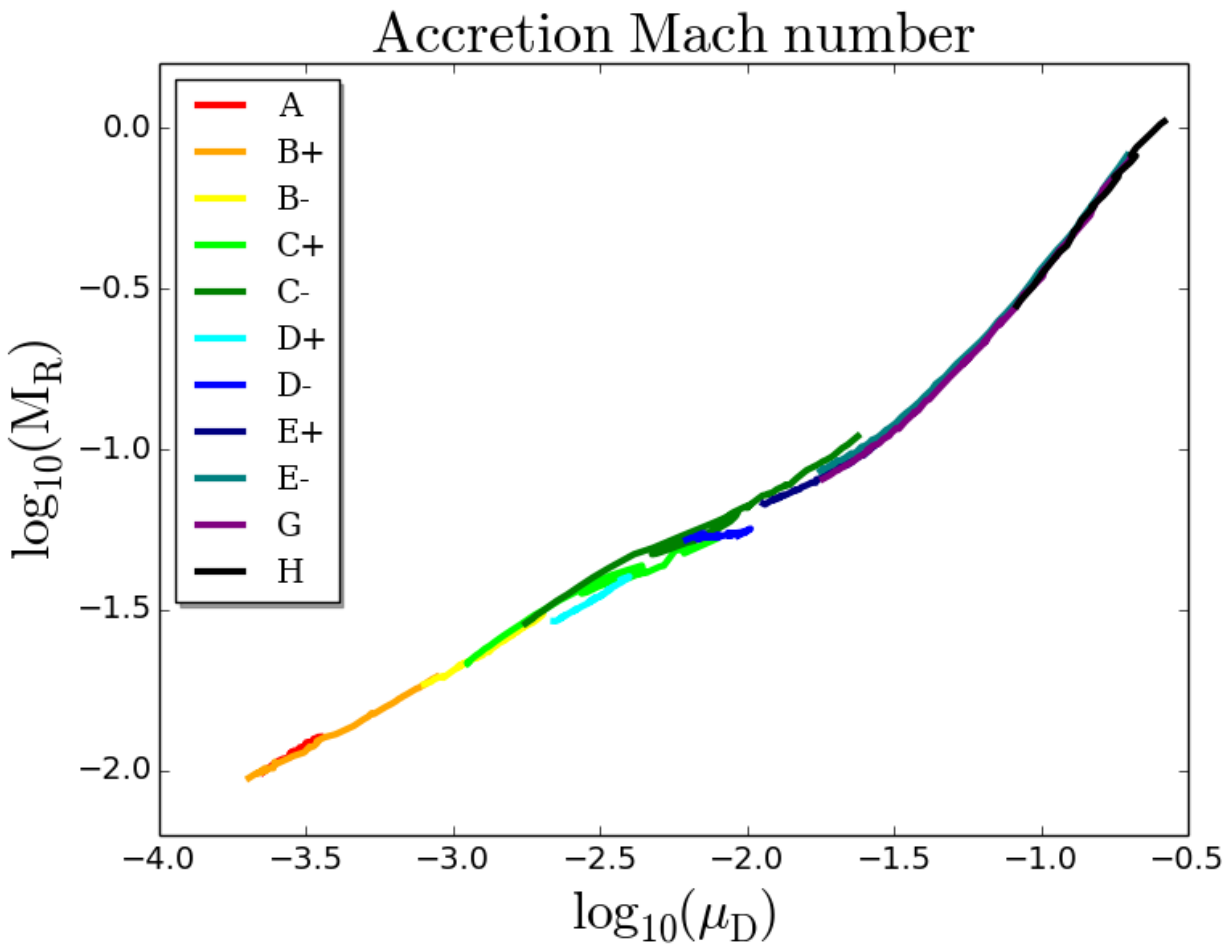


**Figure 5.14:** Accretion Mach number $M_R$ with respect to the disk magnetization $\mu_{\rm D}$. Each line represents the evolution of a single simulation (see Table 5.1) from 700 to 10,000 time units.

A further jet MHD integral is the mass loading parameter $k$ Figure 5.15 and Figure 5.16. For this integral the different simulations converge slightly less than compared to the integrals discussed before. Essentially, this is a result of the *gas density* being present in the calculation of the integral (Equation 5.2). Since the plotted lines show the continuous evolution of the disk-jet system, disk (and thus outflow) densities are in principle different.

As it was pointed out by Ferreira (1997), since cold jets carry away the whole disc angular momentum, one expects to find a systematic relation between mass loading and lever arm. In fact, the existence of such relation is confirmed, though being stronger than previously thought (Ferreira 1997; Ouyed & Pudritz 1997). For the disk magnetization lower than $\mu_{\rm D} < \mu_{\rm crit}$, the Alfvén lever arm is $\lambda \propto k^{-5.8}$ and for $\mu_{\rm D} > \mu_{\rm crit}$ it is $\lambda \propto k^{-2.3}$.

In order to disentangle the different mechanisms affecting ejection, The mass loading parameter is derived by means of the above-mentioned quantities.

$$k = \frac{\sqrt{\gamma} M_R \zeta \lambda^2}{\sqrt{2\mu}}, \tag{5.6}$$

using $B_{\rm P,A} = B_{\rm P,D}/\lambda^2$.

As the accretion Mach number increases linearly with the disk magnetization (Königl & Salmeron 2011; Chapter 4) the $M_R/\sqrt{\mu}$ is also an increasing function with respect to the disk magnetization.

From Figure 5.12 it becomes obvious that also the Alfvén lever arm increases with the disk magnetization. The mass loading parameter decreases with disk magnetization because the ejection to accretion ratio for a stream also decreases with magnetization. In other words, when the disk magnetization increases, relatively more disk material is being accreted than ejected with the outflow.

Note that while Figure 5.15 shows the interrelation between two jet properties (as expected already from the steady MHD theory), Figure 5.16 essentially *connects jet properties to disk properties* as a result of treating the launching process. Note, however, that implicitly the disk magnetization is also present in Figure 5.16 as it connects the ejection process (mass loading) with the disk (angular momentum removal).

Finally, it is worth to mention how the flux ratios, namely ejection to accretion mass, energy and angular momentum, can be computed. In general, any flux ratio are defined using the mass stream ratio.

$$\xi_X = \frac{X_{ej}}{X_{acc}} = \frac{X_A}{X_D}\frac{S_A}{S_D}\zeta \tag{5.7}$$

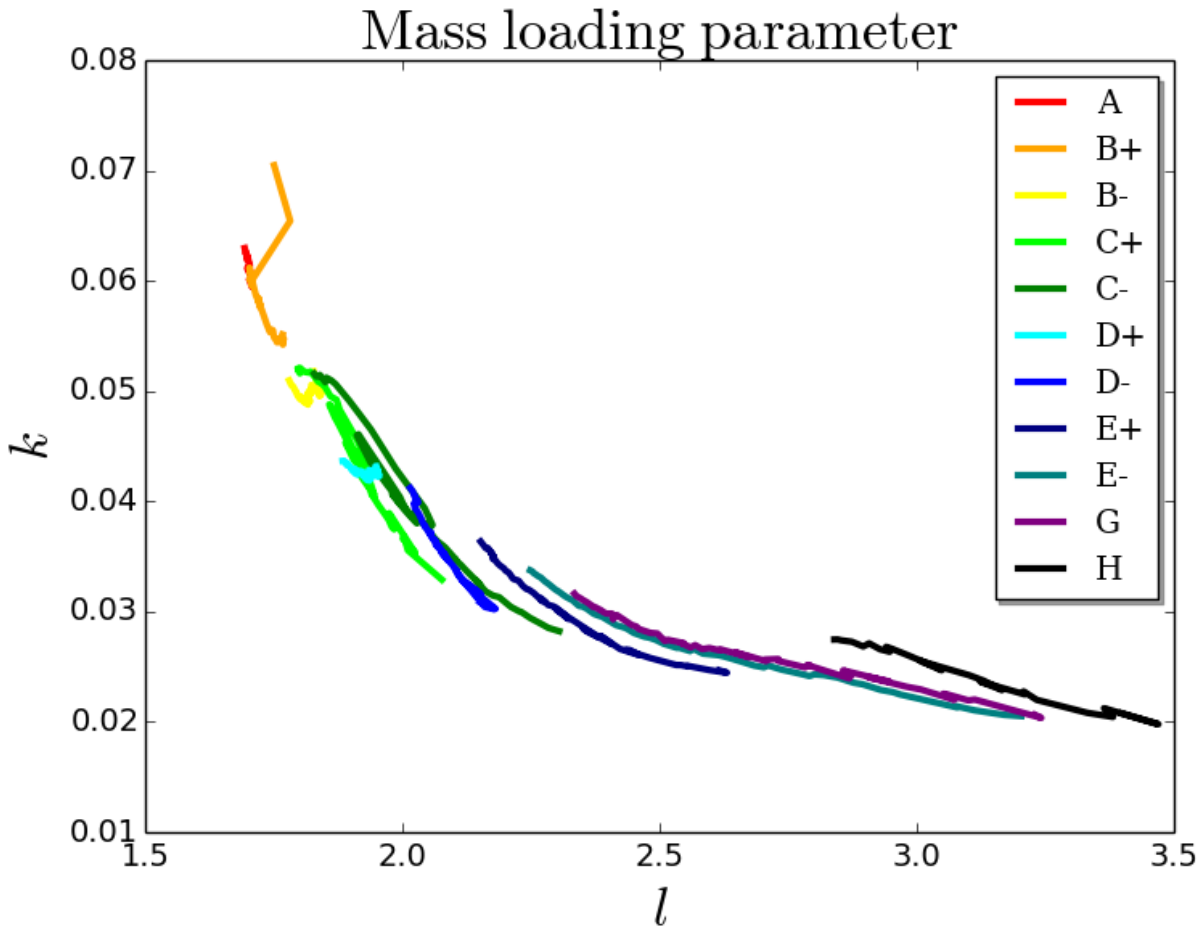


**Figure 5.15:** Mass loading parameter $k$ with respect to the disk specific angular momentum $l$. Each line represents the evolution of a single simulation (see Table 5.1) from 700 to 10,000 time units.

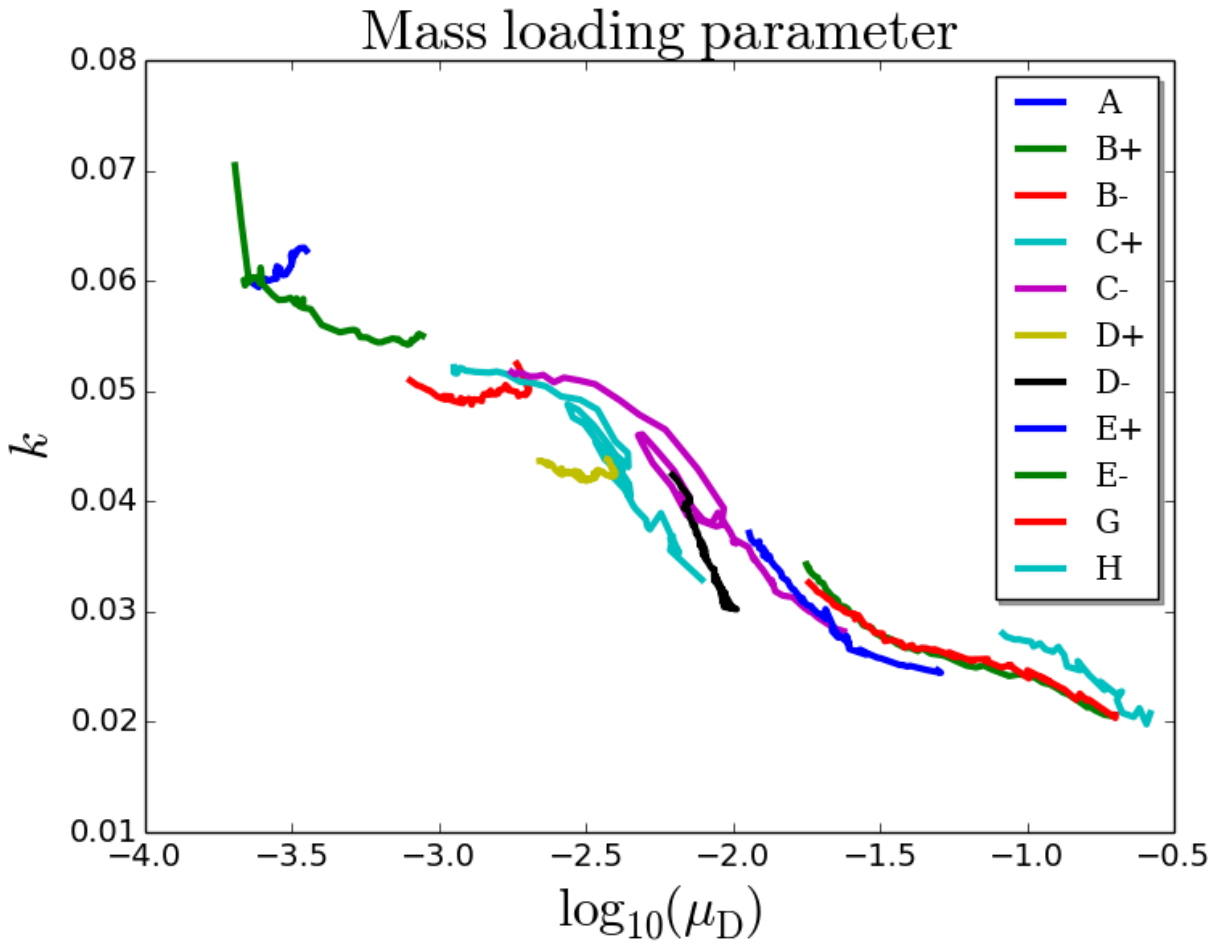


**Figure 5.16:** Mass loading parameter $k$ with respect to the disk magnetization $\mu_{\rm D}$. Each line represents the evolution of a single simulation (see Table 5.1) from 700 to 10,000 time units.

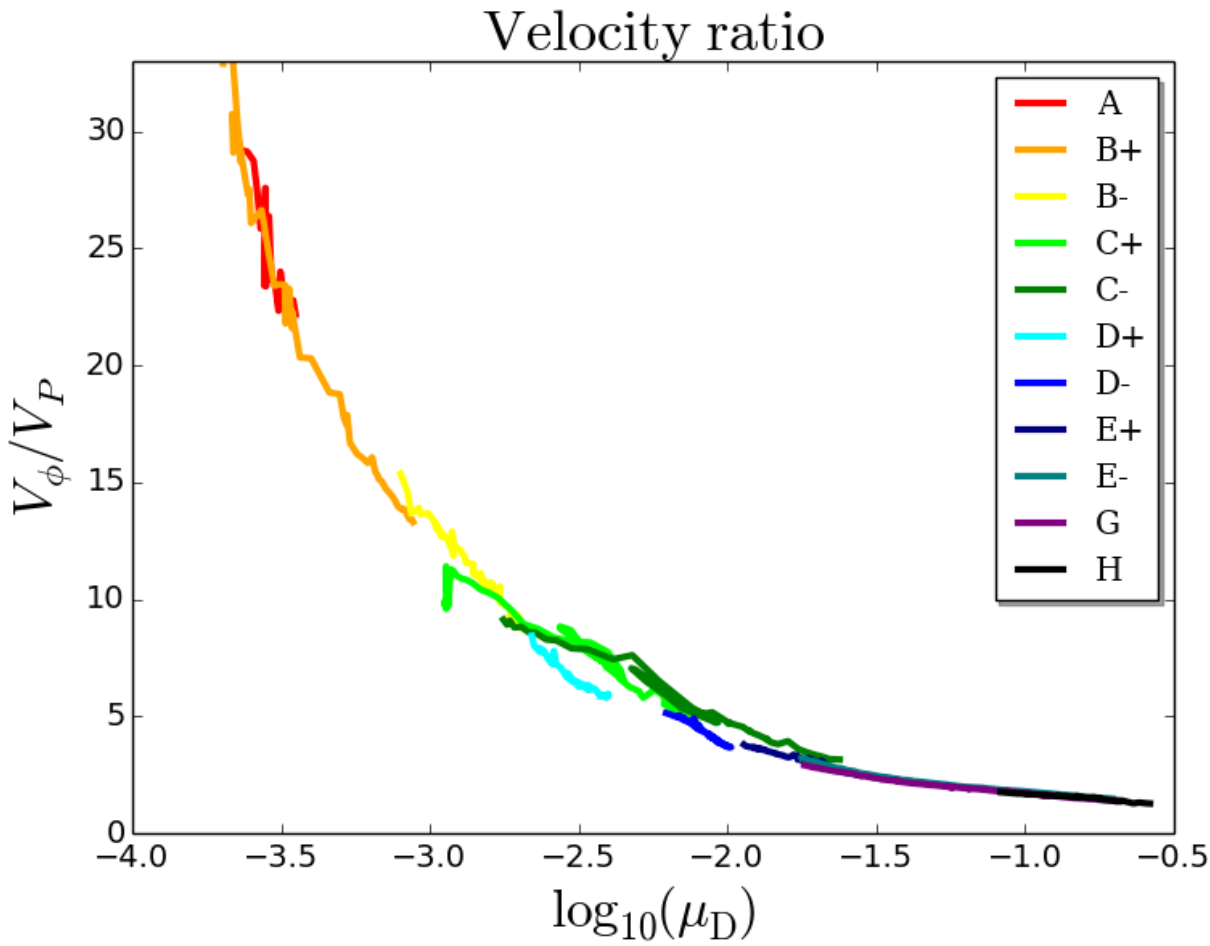


**Figure 5.17:** Poloidal to toroidal velocity ratio with respect to the disk magnetization $\mu_D$. Each line represents the evolution of a single simulation (see Table 5.1) from 700 to 10,000 time units.

where $S_A$ and $S_D$ are the areas through the fluxes are computed at the Alfvén point and the disk region.

Since $X_D$ is a quantity computed at the disk midplane, $S_D$ represents the effective disk height, such that the flux through this area is a product of $S_D$ and $X_D$. The effective disk height is $H_D = 0.15R_0$, resulting in $S_D = 0.3\pi R_0^2$. Note that the flux ratio in principle depends on the area of jet $S_A$ through which the flux ratio is computed.

### 5.5.6 DIFFERENT LAUNCHING MECHANISMS

Following Chapter 4, two different, but complementary regimes of the jet-launching can be distinguished. They result in a different efficiency of the mass, angular momentum and energy

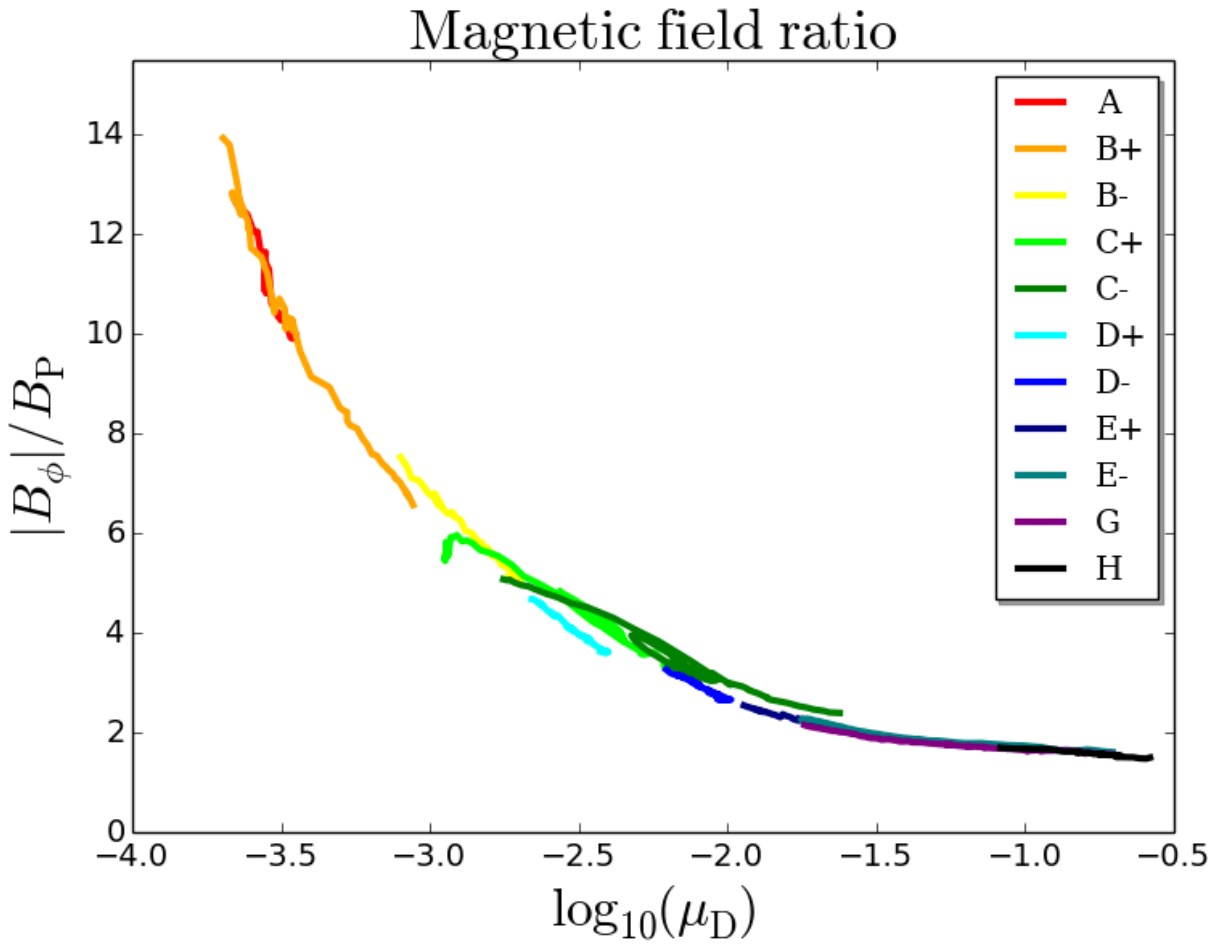


**Figure 5.18:** Toroidal to poloidal magnetic field ratio with respect to the disk magnetization $\mu_\mathrm{D}$. Each line represents the evolution of a single simulation (see Table 5.1) from 700 to 10,000 time units.

extraction from the disk. They can be referred as centrifugally and magnetically dominated regimes. As shown throughout this chapter, the demarcation line between these regimes can be drawn around the disk magnetization $\mu_{\rm D} \sim 0.03 - 0.05$. In order to better understand what is the difference between these regimes, some jet quantities computed at the Alfvén point are presented.

Figure 5.17 and Figure 5.18 show the toroidal to poloidal velocity and the magnetic field ratios computed at the Alfvén point. As the disk magnetization decreases, the poloidal velocity decreases as well, which causes the increase of the toroidal to poloidal velocity ratio. For the low disk magnetization the Alfvén surface is located very low, close to the disk surface. Because of the small poloidal velocity, the winding of the toroidal magnetic field is rather efficient, what leads to a high toroidal to poloidal magnetic field ratio.

The excess magnetic energy stored in the toroidal magnetic field component together with the lower angular momentum loss rate results in an outflow that is magnetically rather then centrifugally driven. On the other hand if the disk magnetization is rather strong, then the toroidal to poloidal magnetic field ratio is small, while the disk angular momentum extraction from the disk rate is high. As a consequence, the Alfvén lever arm is larger, and the mass loading is lower. This regime is denoted as centrifugally dominated. The transition between these two regimes seems to be rather smooth. Further details may depend on the diffusivity model applied.

## 5.6 FROM JET OBSERVABLES TO DISK PROPERTIES

This section presents how the jet observables can be translated into the properties of the jet driving accretion disk applying time-dependent MHD simulations. A crucial point for doing this is to apply a proper scaling of the simulations. Although a proper scaling requires *all* three scaling parameters to be known, namely $R_0$, $V_0$, and $\rho_0$, there are the inner disk radius $R_0$ and $V_0$ (set by the mass of the central object) that are essential for a proper scaling between jet observables and the underlying disk. Therefore the first step is to obtain the disk inner radius, or the foot point of the jet.

First, the method of Anderson et al. (2003) is further extended using the accretion-ejection simulations. Note that approach presented in this stude interrelates the observable jet quantities and the inferred disk quantities goes beyond the approach by Anderson et al. Essentially, not only the size of the launching area can be provided, but also the properties of the underlying jet-launching disk such as the disk magnetization. The tight relation between the jet energy and the jet angular momentum $e(l)$ was obtained (see Figure 5.10). This relation implies that in order to carry away more energy, the jet material is required to carry away also more angular momen-

tum. This relation is almost linear for a weak magnetization, but deviates from linearity for a stronger magnetization. Knowing the observed jet energy and angular momentum, the relation $e(l) = E(L/L_0)/E_0$ can be used to solve for the foot point radius $R_0$ of the jet. Here the relation between energy and angular momentum is approximated by $e(l) = 26.45/l^4 - 22.2/l^2 + 4.85$. The resulting quadratic equation for the disk root point $R_0$ can be analytically solved.

Note that in order to estimate the jet energy and angular momentum, certain assumptions have been made. For example, it was assumed that the jet energy and angular momentum at infinity are predominantly kinetic. However, as previously discussed, the asymptotic jet magnetic to kinetic angular momentum ratio is not really known. To measure the jet angular momentum by the low jet rotational velocity is one of the major observational goals (Davis et al. 2000; Bacciotti et al. 2002). However, the jet rotation could also be changed / caused by magnetohydrodynamic shocks in a helical magnetic field (Fendt 2011). Still, as pointed out by White et al. (2014) it is not yet clear how to distinguish between jet rotation and other intrinsic jet physics (turbulence) that produces differential radial jet motion. Note that in order to derive from the jet observables the underlying disk parameters, only one observable is needed if the jet foot point is known, namely the jet propagation speed. The inner disk radius, however, can be estimated by another independent method. The study of the magnetic field of the classical T-Tauri stars by Johnstone et al. (2014) suggests that the dipole component of the magnetic field of the star provides an adequate approximation of the disk truncation radius.

Knowing the foot point of the jet allows to obtain the exact values of the jet angular momentum (or energy), thus in non-dimensional units. As a consequence, one derives the jet angular momentum (or jet energy), namely how many times more angular momentum (or energy) with respect the underlying Keplerian disk $(E_0, L_0)$ is carried away by the jet particle. From these quantities ($l$ and $e$), one can derive the underlying disk magnetization (at the midplane).

Taking the DG Tau system as an example and assuming a central star of one solar mass, a jet radius of 10 AU, a jet speed of $V_P = 58.2\,\mathrm{kms}^{-1}$, and a jet rotational speed $V_\phi = 7.3\,\mathrm{kms}^{-1}$, a jet foot point radius of $R_0 = 0.69$ AU and $l = 2.94$, $e = 2.6$ is obtained. These values for angular momentum and energy indicate a magnetization of the underlying disk of $\mu = 0.1$, suggesting a rather strong disk magnetic field and a magneto-centrifugally launched jet.

## 5.7 CONCLUSIONS

This chapter presented the results of MHD simulations investigating the launching of jets from a magnetically diffusive accretion disk. While Chapter 4 demonstrated that disk accretion, ejection and the accretion-to-ejection ratio of the mass and energy fluxes strongly depend on the actual

disk magnetization, the present study applies a novel approach and have studied the relation between the jet properties and the underlying disk properties. It was shown that the main parameter that governs the jet properties is in fact the underlying disk magnetization.

This result agrees with long-standing understanding of steady-state MHD jet theory, however, here *these relations were derived from time-dependent simulations that include the disk evolution in the treatment.* The classical $\sigma$-parameter of the jet foot point magnetization that is a free parameter in steady-state jet theory, is here derived from time-dependent disk dynamics. The interrelation between the actual values of all jet integrals and a broad range in the disk magnetization was presented for the first time.

Although the number values of the physical quantities presented in current study are supposed to be subject to the various model prescriptions, such as magnetic diffusivity, a non-viscous disk, all relations obtained are likely to be solid at least qualitatively. In particular, the following results were obtained.

(1) The various interrelations between the properties of the jet and the underlying accretion disk were established. It was shown how the four jet MHD integrals are connected to the underlying disk magnetization. With these relations, knowing the jet observables in principle allows to infer from them the magnetization of the jet driving accretion disk. These relations were applied as an example to the jet of DG Tau system.

(2) It was shown that by knowing the disk magnetization, that can be estimated for example from the accretion power, a limit for the jet propagation speed can be set. This allows to connect two - in principle observable - properties together.

(3) In agreement with Ferreira & Pelletier (1995), two different, but complimentary launching mechanism can be distinguished – launching predominantly by Lorentz forces or by centrifugal support.

(4) In particular, a higher disk magnetization yields

i) a larger Alfvén lever arm of the jet, leading to a broader jet,

ii) a larger jet specific angular momentum and energy,

iii) a lower mass loading parameter,

iv) a lower jet angular velocity,

v) a lower mass ejection to accretion stream ratio,

vi) a higher the accretion Mach number,

vii) a lower velocity and magnetic toroidal to poloidal component ratio at the Alfvén surface.

viii) a higher asymptotic jet speed.

For a low disk magnetization the opposite of i)-viii) is true, with the exception of the jet angular velocity that also decreases.

(5) In the case of high disk magnetization the transformation of magnetic-to-kinetic jet specific angular momentum and thus jet specific energy may be strongly limited. Essentially, this sets an upper limit on the jet propagation speed.

# 6

# Launching Jets from $\alpha\Omega$-Dynamo Disk*

This chapter presents simulations of the disk-jet system in which the magnetic field is generated by the disk dynamo. Starting by exploring the dynamo setup and its difference with a non-dynamo one, I further introduce a toy-model that is aimed to model the episodic jet events, known as knots. The main objective of this chapter is to explore the structure of the generated by the dynamo magnetic field.

## 6.1 Introduction

Astrophysical jets as highly collimated beams of high velocity material and outflows of less degree of collimation and lower speed are an ubiquitous phenomenon in astrophysical sources of rather different ranges in energy output and a physical extension. Previous calculations have shown that jets and winds could be produced by the interplay of large scale magnetic fields with the accretion disk (Blandford & Payne 1982; Pelletier & Pudritz 1992; Ferreira 1997).

*This chapter is based on a paper submitted to the Astrophysical Journal by Deniss Stepanovs, Christian Fendt, and Somayeh Sheikhnezami; titled: Modelling MHD Accretion-ejection - Episodic Ejections of Jets Triggered by a Mean-field Disk Dynamo (Stepanovs et al. 2014). All the simulations, the figures and most of the scientific discussion and interpretation presented in this chapter were done by the author of the thesis.

The jet-launching and collimation problem is usually being addressed numerically applying a large scale initial poloidal magnetic field. This holds in particular for simulations considering the acceleration and collimation process only and assuming the underlying disk as a boundary condition (Ustyugova et al. 1995; Ouyed & Pudritz 1997; Krasnopolsky et al. 1999; Fendt & Čemeljić 2002; Fendt 2006; Pudritz et al. 2006; Fendt 2009; Vaidya et al. 2009; Porth & Fendt 2010).

Also simulations treating the launching mechanism, i.e. simulations of the accretion-ejection structure that include the time evolution of the disk dynamics, so far have assumed a global large-scale magnetic field as initial condition (Shibata & Uchida 1985; Casse & Keppens 2002, 2004; Meliani et al. 2006; Zanni et al. 2007; Tzeferacos et al. 2009; Murphy et al. 2010; Sheikhnezami et al. 2012; Fendt & Sheikhnezami 2013).

These studies have provided a deep insight in the launching mechanism, i.e. the connection between the outflow and the underlying disk. It is clear today that the magnetic field plays *the* crucial role in lifting the matter out of the disk and accelerating it to high velocity. By knowing the disk magnetization one can refer many details of the launched outflow, namely its energetics and the ejection efficiency (see Zanni et al. 2007; Sheikhnezami et al. 2012, Chapter 4 and Chapter 5).

In addition to magneto-centrifugal acceleration mechanism proposed by Blandford & Payne (1982), jets can be also accelerated predominantly by the gradient of the toroidal magnetic field pressure. If magnetic loop structure is present in the disk, the strong toroidal magnetic field will be generated as a consequence of the differential rotation in the disk. This mechanism has been studied extensively both analytically (Lynden-Bell & Boily 1994; Lovelace et al. 1995; Lynden-Bell 1996) and numerically (Ustyugova et al. 1995), where a particular structure of a magnetic field was initially imposed. A constantly generated toroidal magnetic field will lead to a vertical expansion of the matter - *tower jets*. These jets are also known as Pointing jets, highlighting that energy and angular momentum fluxes of the jet predominantly consist of the magnetic flux. Later, Hayashi et al. (1996); Ustyugova et al. (2000); Kato et al. (2004) numerically showed that such structures naturally emerge as a result of the interaction between the stellar dipole magnetic field initially penetrating the accretion disk.

It is still an open issue what is exact structure and strength of the magnetic field in the disks, and where does it come from. Besides a central stellar magnetic field or advection of magnetic field from the ambient medium, a turbulent dynamo can be a major source of the disk magnetic field (Pudritz 1981b,a; Brandenburg et al. 1995). In order to study the disk dynamo in the context of outflow launching, only a few numerical experiments were performed in which the magnetic field was generated *ab initio* (Bardou et al. 2001; von Rekowski et al. 2003; von Rekowski & Brandenburg 2004). These authors were first to show how accretion disks start producing the

outflow if the magnetic field is amplified by the dynamo to about its equipartition value.

A further motivation for considering a disk dynamo for jet-launching is seemingly the time-dependent ejection of the jet material. For protostellar jets the typical timescales for ejection derived from the observed knot separation and jet velocity are in the range of 10-100 years. The typical timescale of the jet-launching area is, however, about 10-20 days, that is the Keplerian period close to the inner disk radius. A time-variable dynamo may be responsible for changing the jet-launching conditions on longer timescales.

The dynamo cycle of the Solar magnetic field that is longer than the Sun's rotation period[1] can serve as an example.

The main concern in this chapter is structure and time evolution of the dynamo-generated magnetic field, the launching of outflows by such a disk self-generated magnetic field, and the interrelation between the dynamo and the episodic ejection of jets, possibly leading to the co-called jet knots. Such a study has not yet been presented in the literature.

Disk dynamos were discussed in the literature concerning episodic accretion and ejection events in dwarf novae, and also as a possible physical process to generate MHD instabilities and turbulence, allowing for angular momentum transfer and accretion. Armitage et al. (1996) discussed a disk dynamo mechanism in accretion disks as a cause for dwarf novae eruption, similar to what could probably happen in the jet-launching disks. Tout & Pringle (1992) discuss a disk dynamo action in order to physically produce the magnetic disk viscosity. However, Gammie & Menou (1998) showed that for low Reynolds numbers the MHD disk turbulence and angular momentum transport dies out, possibly leading to episodic accretion in dwarf novae.

Rozyczka et al. (1995) discuss a model of a disk dynamo driven by magnetic buoyancy which does not directly involve a disk turbulence. This model was re-visited by Johansen & Levin (2008) finding that accretion could in fact be established by a Parker instability-driven dynamo. According to Johansen & Levin (2008) accretion could be based on the interaction of Parker and magneto-rotational instabilities. In this scenario the vertical component of the magnetic field is generated by Parker instability (PI) and serves as a source for magnetorotational instability (MRI).

Applying a mean-field $\alpha^2\Omega$ dynamo (Krause & Rädler 1980) the step by step evolution of the magnetic field is presented. In this approach turbulence is being addressed in the mean field approach, and is not self-consistently generated (e.g. by the MRI).

The episodic jet-launching scenarios were also studied by means of a simple toy model in which

[1] By coincidence, the difference in the respective time scales - a magnetic cycle of 22 years and a rotational period of 35 days - is comparable to the protostellar jets.

the dynamo action was artificially switch on/off.

It is discussed whether similar processes in which the dynamo does change its strength may lead to episodic jet ejection and the jet knots. It is also discussed in detail, how the magnetic field can be regenerated by re-establishing the dynamo action.

This chapter is organized as follows. Section 2 briefly describes the diffusivity and dynamo models used for the simulations. Section 3 presents the reference dynamo simulation where the jet-launching magnetic field structure is dynamo-generated from a weak seed field. The difference between dynamo and non-dynamo simulations is discussed. Section 4 presents simulations during which the disk dynamo is switched on and off repeatedly, leading to episodic ejection of the disk material into the collimated outflow. Section 5 summarizes the chapter.

## 6.2 MODELLING LARGE SCALE TURBULENCE

As already mentioned, a small-scale turbulence modeling is out of scope of this research. Therefore, both effective diffusivity and dynamo profiles has to be introduced. This is discussed in this chapter.

### 6.2.1 THE MAGNETIC DIFFUSIVITY MODEL

Chapter 4 presented in detail models applying both a *standard diffusivity* and a so-called *strong diffusivity*. It has been numerically shown that the standard diffusivity model is prone to the accretion instability. This chapter studies the dynamo action, performing simulations using both models. These models qualitatively share many similar features. Therefore, the simulations were presented, applying the strong diffusivity model, however, commenting on differences between diffusivity model.

The main mediator in the magnetic diffusivity models is the magnetization of the underlying disk. In the case of simulations with a substantially strong initial magnetic field (Chapter 4), the disk magnetization is set by the magnetic field at the disk midplane.

Since in the dynamo simulations presented here the initial magnetic field does not intersect with the midplane[2], and may also remain low for quite some time, the parametrization of the diffusivity model with the magnetization had to be revised. The same notation as in Chapter 4 for the

[2]The initial field is purely radial or toroidal

strong diffusivity model was preserved,

$$\alpha_{\rm ssm} = \alpha_{\rm m} \sqrt{2\mu_0} \left( \frac{\mu_{\rm D}}{\mu_0} \right)^2, \tag{6.1}$$

where the *disk magnetization*,

$$\mu_{\rm D} = \frac{< B_{\rm D} >^2}{2P}, \tag{6.2}$$

is defined by means of the *average* total magnetic field $< B_{\rm D} >$ for a certain radius within the disk (up to $H$), normalized to the midplane pressure. A non-zero magnetic diffusivity allows for reconnection and diffusion of the magnetic field across the midplane. An assumption that the magnetic diffusivity is dependent on the total magnetic field strength is consistent with the fact that the MRI is excited by both toroidal and poloidal magnetic field components (Fromang 2013).

### 6.2.2 THE DYNAMO MODEL

A standard mean-field $\alpha^2\Omega$ dynamo formalism (Krause & Rädler 1980) was applied, where $\alpha$ represents the dynamo effect by turbulence, and $\Omega$ stands for the differential rotation of the plasma. According to the mean-field dynamo theory, an extra electromotive force term $\overline{\overline{\alpha}}_{\rm dyn}\boldsymbol{B}$ enters the induction equation (Chapter 2) and is responsible for the generation of the magnetic field. In general, $\overline{\overline{\alpha}}_{\rm dyn}$ is a tensor, however non-diagonal components are less relevant for the dynamo process (Brandenburg & Donner 1997; Bardou et al. 2001), in particular when a moderately strong magnetic field is present (Brandenburg et al. 2012). Therefore all non-diagonal components can be neglected and the diagonal values are set equal to one parameter, $\alpha_{\rm dyn}$. The sign of $\alpha_{\rm dyn}$ as well as its number value in real disks has been widely debated (Brandenburg & Campbell 1997; Rekowski et al. 2000; Arlt & Rüdiger 2001). It has been shown that in order to get a dipolar structure of the mean magnetic field (as opposed to a quadrupolar structure) a negative sign of alpha should be chosen (Brandenburg & von Rekowski 2007; Bardou et al. 2001).

Following a dimensional analysis, $\alpha_{\rm dyn}$ is scaled as the Keplerian velocity, thus applying

$$\alpha_{\rm dyn} = \alpha_{\rm D}\, r^{-1/2} F_\alpha(z), \tag{6.3}$$

where the vertical profile of $\alpha$-effect is defined by

$$F_\alpha(z) = \begin{cases} \sin(\pi \frac{z}{H}) & z \le H \\ 0 & z > H \end{cases}$$

Here, $H$ denotes the disk scale height and is approximated as constant in time. The profile $F_\alpha(z)$ restricts the $\alpha$-effect to the disk area.

It is generally believed that in the case of the strong magnetic field the dynamo is quenched (Brandenburg & Subramanian 2005). The main reason is that a strong global magnetic field suppresses the turbulence, and thus the turblulent dynamo. The quenching is commonly applied by multiplying the $\alpha_{\rm dyn}$-term by a quenching function,

$$Q = \frac{1}{1 + 2\mu_{\rm x}}, \tag{6.4}$$

where $\mu_{\rm x}$, in contrast to the $\mu_{\rm D}$ is the *local* magnetization. In order to be consistent with and directly affect the resulting magnetic field, quenching parameter is chosen $\mu_{\rm x} = q_\mu \mu_{\rm D}$. By setting different $q_\mu$ the magnetic field growth can be limited to a certain value. Typically, a rather high $q_\mu$ is chosen, in order to quench the dynamo already for low magnetizations.

However, there is another possibility of limiting the magnetic field strength. Parameter $\mu_0$ in the strong diffusivity model (Equation 6.1) is, in fact, a good measure for the resulting actual disk magnetization. This comes from the functional form of the diffusivity profile - any further growth of the disk magnetization has a strong feedback of the diffusivity (Chapter 4).

Both direct dynamo quenching and indirect limiting the magnetization by applying the strong diffusivity model lead to the saturation of the magnetic field. The difference between this approaches is that in the case of leaving the dynamo working in the disk, the magnetic flux is being continuously generated and the disk is being filled with the magnetic field. If the standard diffusivity model is applied, then the dynamo quenching is the only mechanism to stop further magnetic field amplification. Therefore, since the strong diffusivity model is applied in the simulations presented, these simulations run without dynamo quenching.

The expected dynamo number for accretion disks is given by

$$|D| = |C_\alpha C_\omega| \lesssim \frac{3}{2} {\alpha_{\rm ssm}}^{-2}, \tag{6.5}$$

(von Rekowski et al. 2003) where $C_\alpha = (\alpha_0 H/\eta_0)$ and $C_\omega = (|\Delta\Omega| H^2/\eta_0)$ represent the strength of $\alpha$-effect and shear $d\Omega/dr$, respectively. Since the main concern is the resulting jet-launching magnetic field, the maximum dynamo number is chosen to generate the magnetic field structure as rapid as possible. The maximum dynamo number is provided by $\alpha_{\rm D} = -0.1$. Note, that the dynamo number $D$ is strongly dependent on $\alpha_{\rm ssm}$.

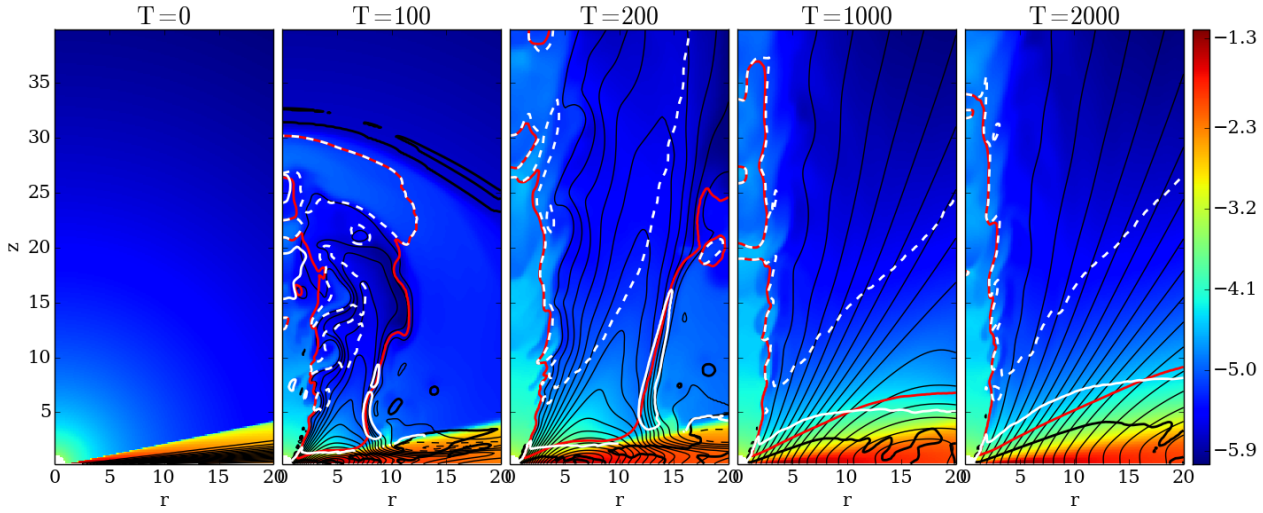


**Figure 6.1:** Time evolution of the disk-jet structure of the reference dynamo simulation. Only a small cylindrical part of the whole spherical domain is presented. Shown is the density (colors, in logarithmic scale); the poloidal magnetic field lines (thin black lines); the disk surface as defined by $V_R = 0$ (thick black line); the sonic (red line), the Alfvén (white line), and the fast magnetosonic (white dashed line) surfaces.

## 6.3 A Reference Dynamo Simulation

This section discusses the dynamo simulations and the resulting configuration of disk-jet system.

The reference dynamo simulation is referred to as the simulation with the parameters $\alpha_{\rm D} = -0.1$, $\alpha_{\rm m} = 1.65$, $\mu_0 = 0.01$. Figure 6.1 shows the time evolution of the reference dynamo simulation, that can be seen as typical for current model setup. The simulation starts from a weak ($\mu_{\rm seed} = 10^{-5}$), purely radial magnetic field, confined within the disk. Once the simulation is started, the toroidal component of the magnetic field is being continuously generated from the radial magnetic field simply by stretching. For the poloidal magnetic field component, the only generation mechanism is the dynamo effect that induces the poloidal component from the toroidal one.

Since the toroidal magnetic field is antisymmetric to equator, the poloidal magnetic field loops that are generated by the dynamo first, do *not* cross the equator. When they evolve in time magnetic reconnection is enforced by the equatorial plane boundary condition and the magnetic diffusivity in the disk. As a consequence the magnetic loops (in the upper and lower hemisphere) merge and do traverse the equatorial plane. Since the diffusivity model depends on the average magnetic field in the disk there is always a substantial diffusivity present in the disk.

As described by Johansen & Levin (2008), the toroidal component of the magnetic field is continuously amplified until it reaches the buoyancy limit and starts moving upwards, away from the disk. The upward motion changes the structure of the magnetic field lines from a predominantly radial into a vertical direction. When the magnetic field is sufficiently inclined, magneto-centrifugal launching (Blandford & Payne 1982) can strongly accelerated the plasma on these field lines. The outflowing gas carries with it the toroidal magnetic field generated in the disk, thus setting a limit for the toroidal magnetic field strength in the disk (Chapter 4).

All dynamo simulations evolve into three distinct domains in the accretion-ejection structure. Starting from the innermost disk, in the first region the magnetic field has the typical structure of field lines inclined with respect to the disk surface. Although magnetic field generation by the dynamo can still take place (if the $\alpha$-effect is not quenched), the magnetization in that region has become sufficiently high in order to operate the standard magneto-centrifugal jet driving. The second region is where the poloidal magnetic field is mostly radial. Here the velocity shear in the disk creates a strong toroidal component of the magnetic field. In this area, the outflow is launched mainly by the buoyancy of the toroidal magnetic field.

The third region is the outer disk, where the magnetic field is rather weak, with somewhat irregular structure. Here, the magnetic flux has originated from the same magnetic loops as the innermost field, but because of longer distance from the inner disk the magnetic field strength has become much lower. Note, that the magnetic field in the outer disk has the opposite polarity.

In summary, the overall structure of the magnetic field has a strong gradient that leads to strong outward diffusion of magnetic flux. Due to this diffusion, the whole disk is filled by a non-zero net magnetic field ($B_{\rm P}|_{\rm midplane} \neq 0$).

### 6.3.1 DYNAMO EFFECT VERSUS MAGNETIC DIFFUSION

As discussed in detail in Chapter 4, the evolution of the disk-jet system is mainly set by the two opposite processes, the diffusion and advection of the magnetic field. It is more complicated to reach this balance. In the case of dynamo simulations a third process contributes to the induction equation, the dynamo, and it is more complex to reach to an equilibrium situation. Nevertheless, the main effects of these processes can be disentangled. The dynamo term in the induction equation manifests itself by generating loops of the poloidal magnetic field. Because of the magnetic flux conservation along the magnetic loops, the magnetization in the inner disk (inner footpoint of the loop) is always higher than in the outer disk (outer footpoint of the loop). Therefore a strong gradient of the magnetic field develops, that evolves primarily following the magnetic diffusivity model.

By smoothing out the gradient of the magnetic field, the diffusivity plays a key role in the overall evolution of the magnetic field - first, it diffuses the magnetic field outwards, thus filling the outer disk with the magnetic flux, second, at the same time the diffusivity destroys some flux within the magnetic loop by reconnection.

In general, if the dynamo is not sufficiently strong (in the case of low dynamo numbers), the generated magnetic field will quickly decay (being diffused) and the magnetization necessary for jet-launching will not be reached.

### 6.3.2 Disk Structure and Disk Surface

Figure 6.2 shows the snapshot of the initial evolution at $T = 1,000$. What can be immediately seen is that the disk structure with the magnetic field is completely different compared to the non-dynamo simulations (Chapter 4). The region around $r = 10$ is the region where the buoyancy force of the toroidal magnetic field is the main force responsible for the lifting the matter into the outflow. Starting from the disk surface ($V_R = 0$), the matter is further accelerated predominantly by the pressure gradient of the toroidal magnetic field. This is, in fact, consistent with the simulations by (Ustyugova et al. 1995). The early evolution of the disk-jet system (Figure 6.1, $T = 200$) clearly show the similarity to the magnetic towers as discussed in Introduction.

Typically, the launching region, defined in Chapter 4 as the region where the velocity of the plasma changes from being perpendicular to the magnetic field to almost parallel to the magnetic field, is broader in dynamo simulations than in the non-dynamo simulations. Also, the disk surface, where the radial velocity changes sign by definition, is located at higher altitudes, although the thermal disk scale height is still about constant in time and about its initial value.

### 6.3.3 Outflow Launching: Accretion-Ejection

The magnetic field of the inner disk that is established in the simulations is similar to the usual structure favoring the magneto-centrifugal launching of the outflow. This type of jet-launching has previously been found and discussed by many authors (Blandford & Payne 1982; Casse & Keppens 2004; Pudritz et al. 2007; Zanni et al. 2007; Murphy et al. 2010) as well in Chapter 4.

Therefore, this section concentrates on the (outer) disk region where the magnetic field has evolved into a structure completely different from the previous simulations. Namely into the structure with the poloidal magnetic field being predominantly radial, and very strong toroidal component. In this part of the disk it is the toroidal magnetic field that plays the key role in the launching (see Fig.6.3).

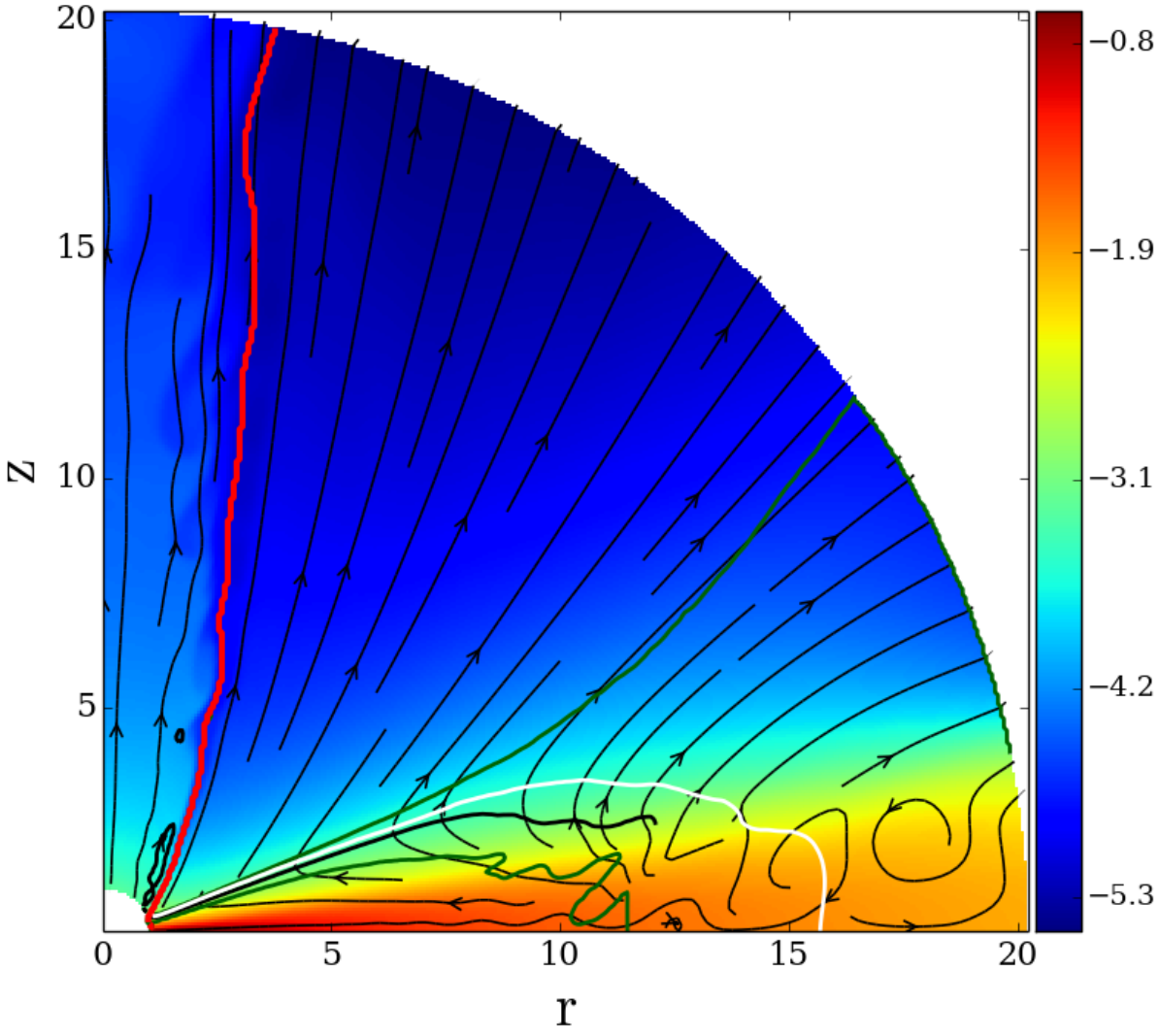


**Figure 6.2:** Snapshot at $T = 1,000$ of physically different regions of the disk-jet structure. Shown is the mass density (in logarithmic scale) and streamlines of the poloidal velocity (black lines with arrows). The red line marks the magnetic field line that is rooted at the innermost disk area along the midplane. The upper green line separates the area where $V_p \| B_p$ from the rest of the disk. The accretion and ejection areas are separated by a white line indicating $V_r = 0$, and a black line indicating $F_\phi = 0$, respectively. The lower green line separates the actual accretion area where $V_r >> V_\theta$ from the rest of the disk.

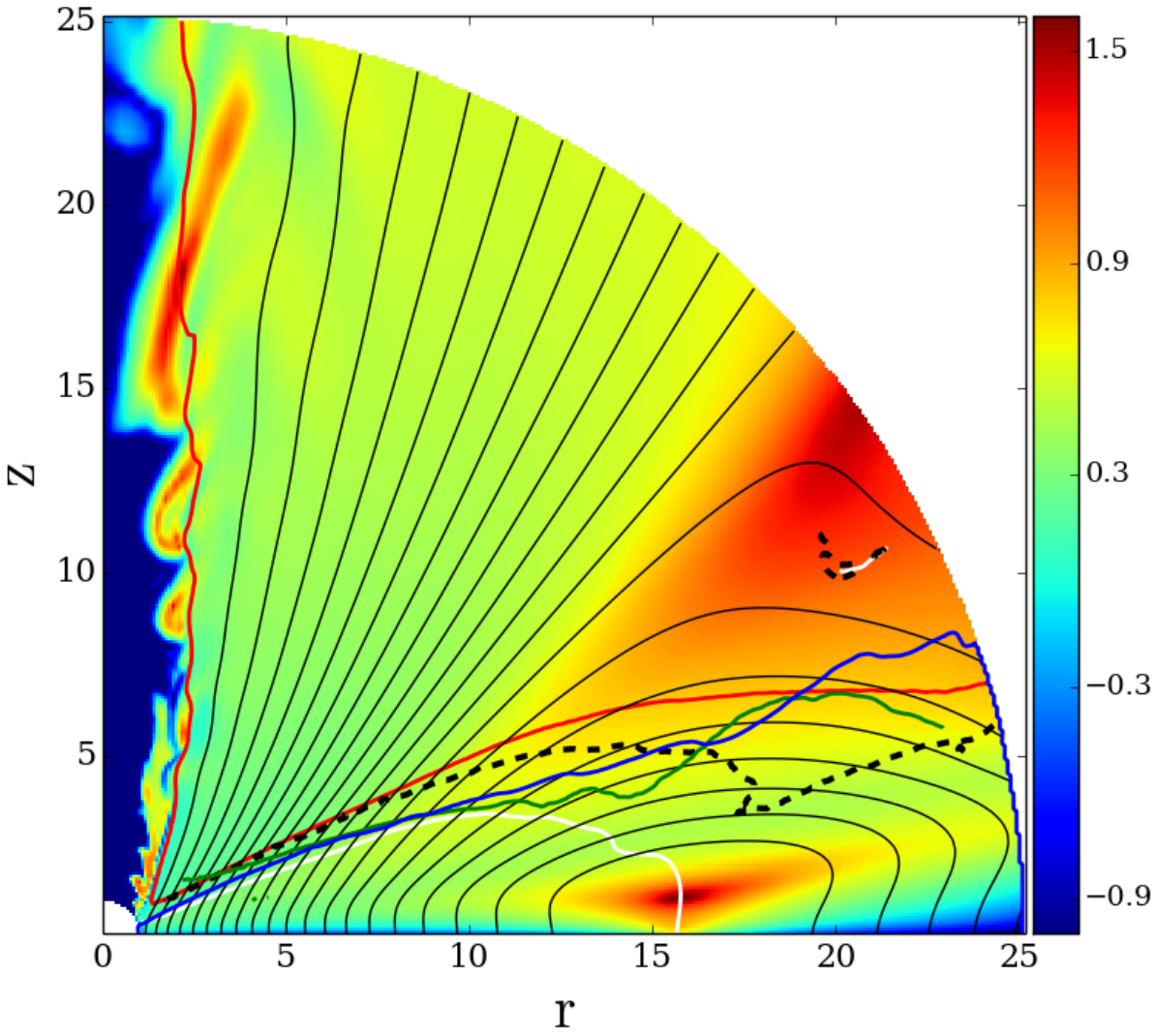


**Figure 6.3:** Distribution of the magnetic field components at $T = 1000$. Shown is the ratio of the toroidal to the poloidal magnetic field (colors, *logarithmic scale*), the poloidal magnetic field lines (thin black lines); the sonic surface (red line); and the locations where the Lorentz force components change sign, $F_\phi = 0$ (white line) and $F_\theta = 0$ (blue line). Further denoted are the locations where i) the gas pressure force is equal to the Lorentz force both projected parallel to the magnetic field (black dashed line), and ii) where the gas pressure force is equal to the Lorentz force both projected parallel to the velocity field (green line).

As the accretion-ejection process is governed by the magnetic torques, these torques need to be discussed in detail. The white line in Figure 6.3 marks the region where the magnetic torque changes sign. The torque is negative in the inner disk (inside the white line), where the angular momentum extraction from disk to outflow takes place, and positive in the disk corona, leading to the acceleration of the outflow material. In the region that is dominated by the magnetic loops at radii of $R \simeq 15$, the torque is purely positive, thus playing a major role in the acceleration of the plasma. The blue line in Figure 6.3 separates two regions, where i) the magnetic forces accelerate the matter in the direction of the outflow ($F_\theta > 0$, above the line), and ii) where the magnetic forces pinch the disk (below the line). In the disk area below this line the main force lifting the matter into the outflow is the thermal pressure. The lines that mark the area where the pressure force is equal to the Lorentz force projected parallel to the magnetic field (black dashed line) and parallel to the velocity field (green line) are also shifted closer towards the disk midplane.

In the area above the loop-like structure the toroidal magnetic field dominates the poloidal field. In this region acceleration is mainly governed by the toroidal magnetic field pressure gradient.

It is worth to note that such a configuration does not reach a steady state. This is already indicated by the misalignment between the magnetic field lines and velocity field. Furthermore, the blue lines in Figure 6.2 denote the launching area, where the velocity field changes from a direction perpendicular to parallel to magnetic field lines. The longer the simulation evolves, the larger the area that reaches a steady state. In other words, the non-steady loop structure is moving outwards along the disk.

### 6.3.4 DYNAMICAL PROFILES OF A DYNAMO DISK DRIVING JETS

Here the overall disk structure of the reference dynamo simulation is discussed. Figure 6.4 presents the radial profiles of a number of MHD variables measured at the disk midplane, and the fits to them by power-laws. The slight deviation between these lines shows how the disk structure changes after a long time evolution. At time $T = 10,000$ the distinct power-laws for the profiles along the disk for radii up to $R \leq 40$ were found. This is the radius that marks a steady state area from the rest of the disk, where the magnetic field is continuously generated. This is most easy to infer from the profile of the poloidal magnetic field profile, that starts deviating from the approximated power-law at $R = 40$.

In order to better compare the analytical fits to the radial profiles resulting from the dynamo simulation to those without the dynamo (Chapter 4), the fits with the same power-law indices are plotted. It can be seen that the actual profiles (for example, the density) show only a tiny deviation.

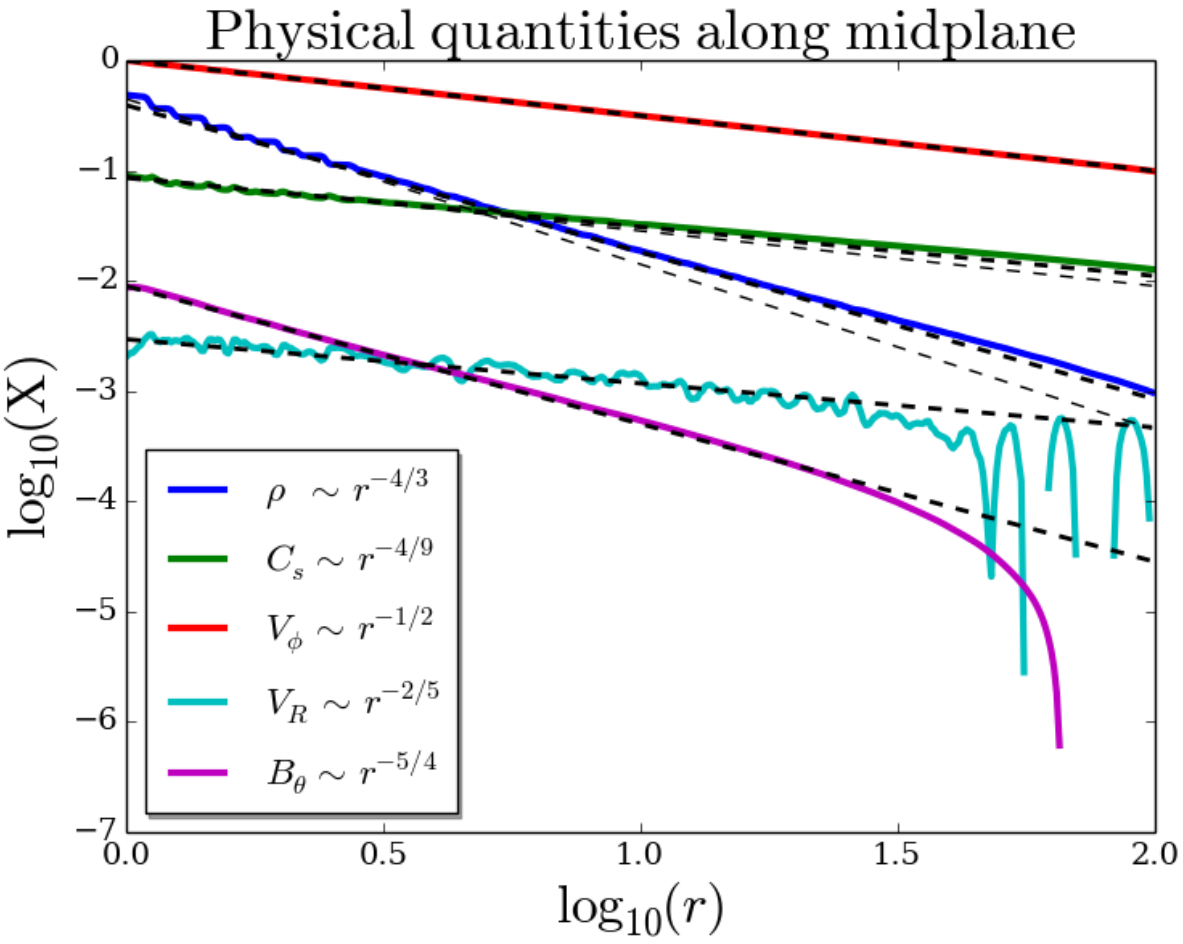


**Figure 6.4:** Physical quantities along the disk midplane for the reference dynamo simulation at $T = 10,000$. Colored lines correspond to different physical quantities, density $\rho$, sound speed $C_s$, rotational velocity $V_\phi$, radial velocity $V_R$, and the magnetic field component $B_\Theta$. The thick dashed lines show the corresponding approximation by a power-law. The thin dashed lines show the initial power-law distribution, slightly offset from the actual distribution at $T = 10,000$.

At time $T = 10,000$, the following numerical values for the power-law coefficients $\beta_X$ were found, for different variables at the midplane $X(r, \theta = \pi/2) \sim r^{\beta_X}$. The disk rotation remains Keplerian over the whole time evolution, therefore $\beta_{V_\phi} = -1/2$. The radial profiles for density and thermal pressure slightly change from their initial distributions. The power-law index of the density changes from $\beta_\rho = -3/2$ to about $\beta_\rho = -4/3$, while for the pressure it changes from $\beta_{\rm P} = -5/2$ to about $\beta_{\rm P} = -20/9$. The following values were found: $\beta_{V_R} = -2/5$ for the accretion velocity, and $\beta_{B_\theta} = -5/4$ for the poloidal magnetic field. The accretion velocity remains subsonic everywhere in the disk with an accretion Mach number of $M_R \equiv V_R/C_{\rm s} \simeq 0.08$. As expected, strong fluctuations were found in the area where the dynamo is active and field magnetic generation is ongoing.

Following Ferreira & Pelletier (1995) and considering the mass accretion rate $\dot{M}_{\rm acc} \sim R^2 \rho V_R$, it is easy to derive the **ejection index $\xi$, that is a measure of the efficiency of the outflow.**. It was $\xi = 0.25$, about the same value as for the non-dynamo simulation (Chapter 4).

This section demonstrates that the radial profiles for disk dynamics along the midplane are very similar for the simulations including dynamo action and those without dynamo. There are several reasons for that. First, in the case of moderately weak magnetic field, the disk dynamics is primarily governed by the hydrodynamical quantities, but not so much the magnetic field. The power-law nature of the Keplerian rotation dominates the dynamics and forces the other hydrodynamical profiles into a power-law distributions as well. Second, the magnetic field strength resulting from the disk evolution is of the same order for both approaches, $\mu \approx 0.01$, that also can lead to profiles with to the same distribution.

### 6.3.5 DYNAMO VERSUS NON-DYNAMO SIMULATIONS

Here the major differences between the simulations with and without the mean-field $\alpha^2\Omega$ dynamo are discussed. As pointed out in the previous sections, the major difference between dynamo and non-dynamo simulations is the structure of the magnetic field and not so much the accretion disk hydrodynamics. The dynamo generates the magnetic field that is continuously spreading over the whole disk. In the early stage of the disk evolution, this makes a substantial difference. Later, when the inner part of the disk has reached a steady state, this part of the disk looks very much the same except a few details. One difference can be found concerning the disk wind close to the disk surface. In dynamo simulation the sonic surface and the Alfvén surface are located 20%-30% further up into the outflow. However, the magnetic lever arm (radius of the Alfvén point) is about the same. This is the result of the vertical component of the magnetic field being stronger, respectively the lower inclination of the magnetic field with respect to the disk surface. (more inclined towards the disk surface). The launching area, namely the area where the velocity field

changes from being almost perpendicular to the magnetic field into a direction parallel to the field, is now wider, while the disk surface stays at about the same level. Note that because of the evolving loop-like structure of the magnetic field, the field inclination with respect to the disk or the sonic surface does change in time and space - except the inner disk where a steady-state has established.

In order to study the jet properties with respect to the actual disk magnetization, several simulations were performed, varying the $\mu_0$ parameter in the definition of the diffusivity (Equation 6.1). This parameter indirectly governs the resulting disk magnetization, as discussed above and also in Chapter 4. By running simulations with different $\mu_0$, it was possible to probe the resulting actual magnetization of the poloidal component in the inner disk over a range $\mu_{\rm act} = 0.01 - 0.05$. As shown in Chapter 4, it is in this range of magnetization where a change in the dominant launching mechanism takes place.

In comparison, in the dynamo simulations the disk and jet properties do not really differ for different actual magnetization, and different launching mechanisms in the dynamo simulations cannot be disentangled. In contrast, the disk quantities as well as the jet integrals behave rather similar in this range of magnetization for both simulations.

In order to disentangle the causes for this similar evolution, two points can be recalled. The main reason why two different mechanisms in the non-dynamo simulation can be distinguished is the ability to generate a strong magnetic shear with sufficiently weak poloidal magnetic field. This is possible because the diffusivity in the standard model depends only on the poloidal magnetic field. Thus, for a weak poloidal field, the diffusivity is also small, that helps to sustain the strong magnetic shear. In contrast, in the current study, the magnetic diffusivity depends on the average *total* magnetic field in the disk. Therefore, a strong magnetic shear (a stronger toroidal magnetic field) directly increases the diffusivity, and, as a consequence, limits the magnetic shear.

This more subtle interrelation between the simulation parameters and physical processes again emphasizes the impact of the magnetic diffusivity model applied.

### 6.3.6 Resolution Study

In this section, the resolution study is shortly discussed. Simulations with a grid resolution of 0.75, and 1.5 times the standard resolution of $N_\theta = 128$ cells per quadrant were performed, corresponding to $N_\theta = 96$ and $N_\theta = 192$ cells per quadrant, or approximately 12 or 24 cells per disk height $2\epsilon$ compared to 16 cells per disk height in the reference run[3].

[3] Note that once the resolution in $\theta$-direction and the radial extent of the disk is chosen, the resolution in $R$-direction is uniquely determined

Figure 6.5 shows the dynamical profiles the three simulations of the resolution study. The radial profiles are plotted along the midplane for various dynamical variables at time $T = 10,000$. As discussed in Section 6.3.4 these profiles can be nicely fitted by power-laws. The same power-law index also provides the same ejection to accretion index. Therefore, the results are not resolution dependent.

However, several differences between these curves can be noticed. The inner part of the disk for the simulation with lower resolution indicates a substantial deviation from the corresponding power-law. In the case of lower resolution the accretion speed increases, and, as a consequence, the overall density in the disk decreases. This highlights the effect of the numerical viscosity that enhances the angular momentum transfer in the disk. On the other hand, the magnetic field is diffused out faster and to a larger distance. This indicates a higher numerical resistivity for the case of lower resolution.

## 6.4 EPISODIC JET EJECTION TRIGGERED BY A TIME-VARIABLE DISK DYNAMO

This section presents simulation results of a toy model applying a time-dependent dynamo action. The motivation is the following. The dynamo is intrinsically a stochastic phenomenon that in real accretion disks can be subject to strong fluctuations. Some accretion disks may exist in which the dynamo action is suppressed, while in other disks if certain conditions are met the dynamo can start to operate. Also, dynamo quenching mechanism can stop an already working dynamo, and thus lead to a reconfiguration of the disk-jet system. The well-known solar cycle can serve as an example. It is believed that a solar dynamo is responsible for the reconfiguration of the magnetic field of the Sun. The strong toroidal field component reveals itself as sunspots with a cyclic appearance. This solar periodicity can be understood as triggered by a constantly operating dynamo (or maybe different types of dynamo). Another interesting feature of the solar activity in this respect is that it exhibits long-term minima (Eddy 1976), during which there were no sunspots observed at all. It is believed that during these minima the dynamo action is either strongly suppressed or completely switched off.

A simple toy model is proposed to explore the impact of such an effect for jet-launching.

The spacial $\alpha$ profile is multiplied with a time-dependent function. A periodic step function (Figure 6.6) is applied, such that the dynamo in the disk is continuously switched on and off. The periodic step function is characterized by its period $T_0$ and time length of a step function $\Delta T$. In other words, $T_0$ is the period of the dynamo cycle and $\Delta T$ the activity cycle of the dynamo. The simulation with $T_0 = 1000$ and $\Delta T = 400$ are presented below.

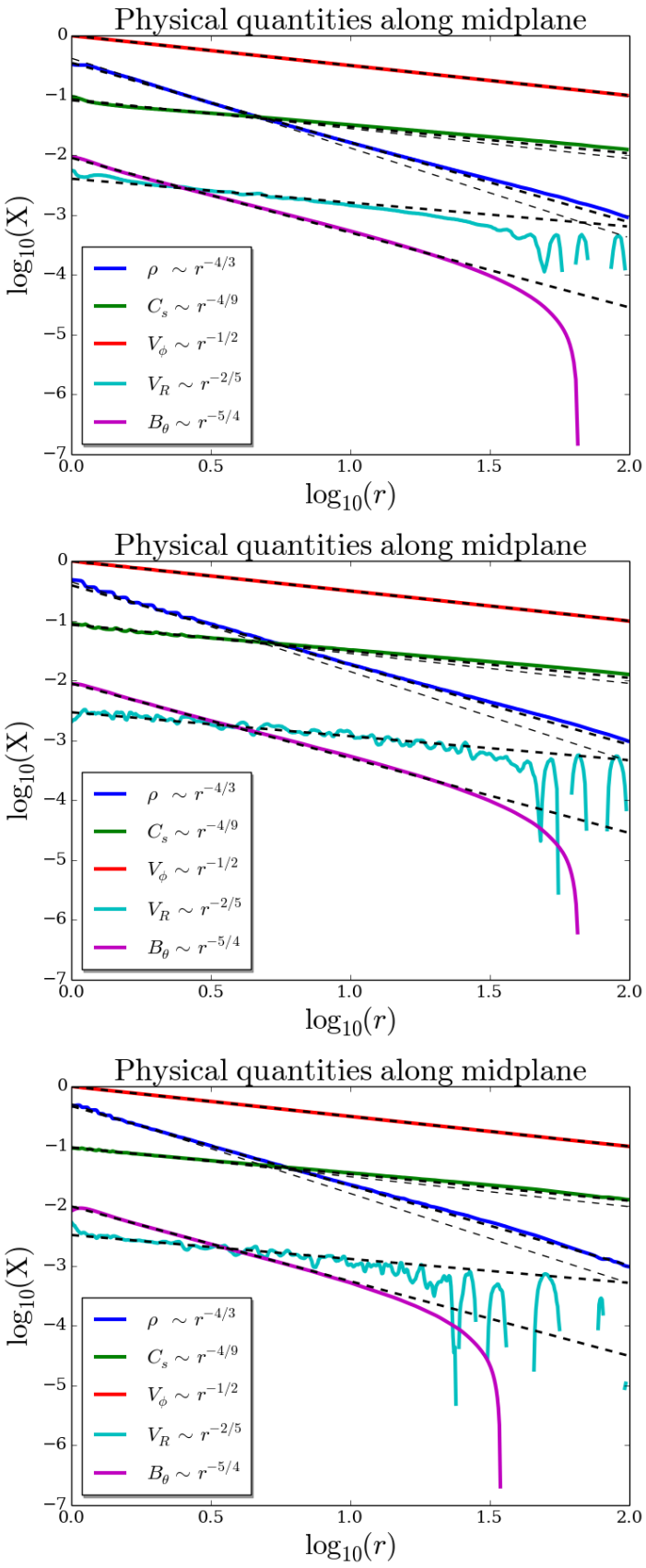


**Figure 6.5:** Resolution study. Physical quantities along the midplane for the simulations with different resolution at $T = 10,000$. From top to bottom the resolution is (12, 16, 24) cells per disk height ($2\epsilon$). Colors show different variable profile, thick dashed lines correspond to certain power-law, the mismatched thin dashed lines correspond to initial distributions of variables.

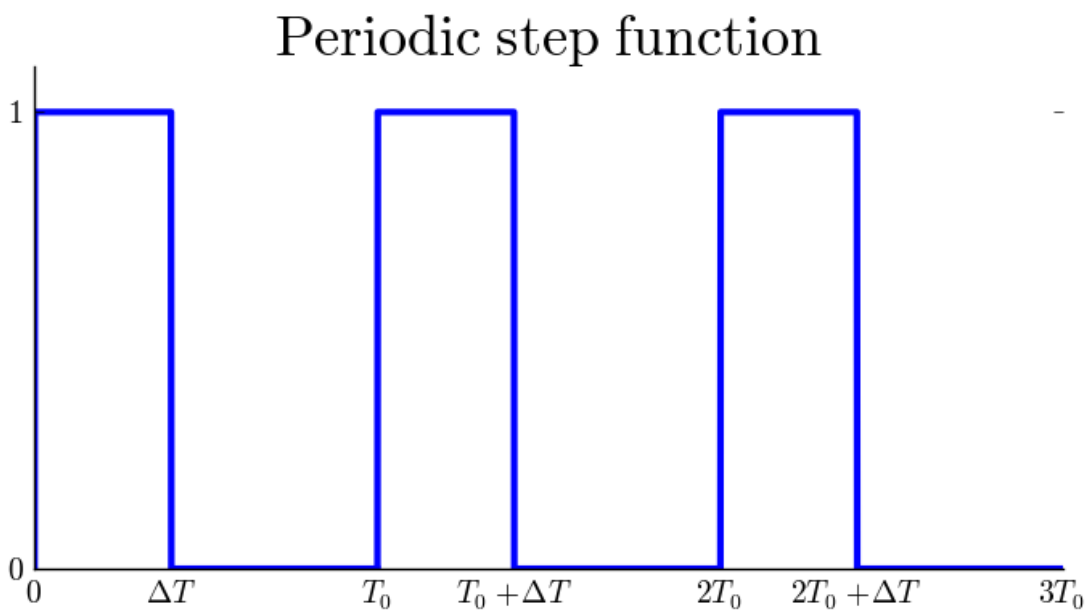


**Figure 6.6:** Periodic step function applied for the toy model of a time-variable disk dynamo. Here the dynamo alpha is simply modulated by the periodic step function. Thus, the dynamo is switched on after periods of $nT_0$ and switched off at $nT_0 + \Delta T$.

Essentially, the modulation of the dynamo-$\alpha$ leads to the variation of the disk magnetization (Figure 6.7) with the same periodicity. The strength of diffusivity is chosen such that without a dynamo working in the disk, the advection of the magnetic flux with the accreted material cannot balance the outward diffusion of the magnetic field. This eventually results in a decrease of the disk magnetization. As previously shown (Chapter 4,5), there exists a limit of the strength of the magnetization below which the disk cannot sustain a jet. When the disk magnetization decays below the level of $\mu \approx 10^{-3}$ the strong jet disappears. On the other hand, if the dynamo action is re-established, the disk magnetization grows again and the outflow is re-launched.

A series of parameter runs were performed, varying both $T_0$ and $\Delta T$. In principle, different scenarios are possible, depending not only on the period of step function, but also on the magnetic diffusivity and the dynamo parameter (and various combinations of those).

In order to generate episodic ejection events, thus in order to re-establish a jet-driving magnetic field structure, several conditions have to be met by the dynamo process. First, the dynamo must be strong enough in order to generate the magnetic field sufficiently fast. Second, in order to suppress the jet ejection during consecutive switch-off periods, $(nT_0 - \Delta T)$, these periods should be sufficiently long, and/or the magnetic diffusivity should be sufficiently high. Only when the inner disk magnetization decreases below $\mu \approx 10^{-3}$, the jet-launching cannot be any longer sustained and the strong outflow disappears. The overall evolution of these processes depends

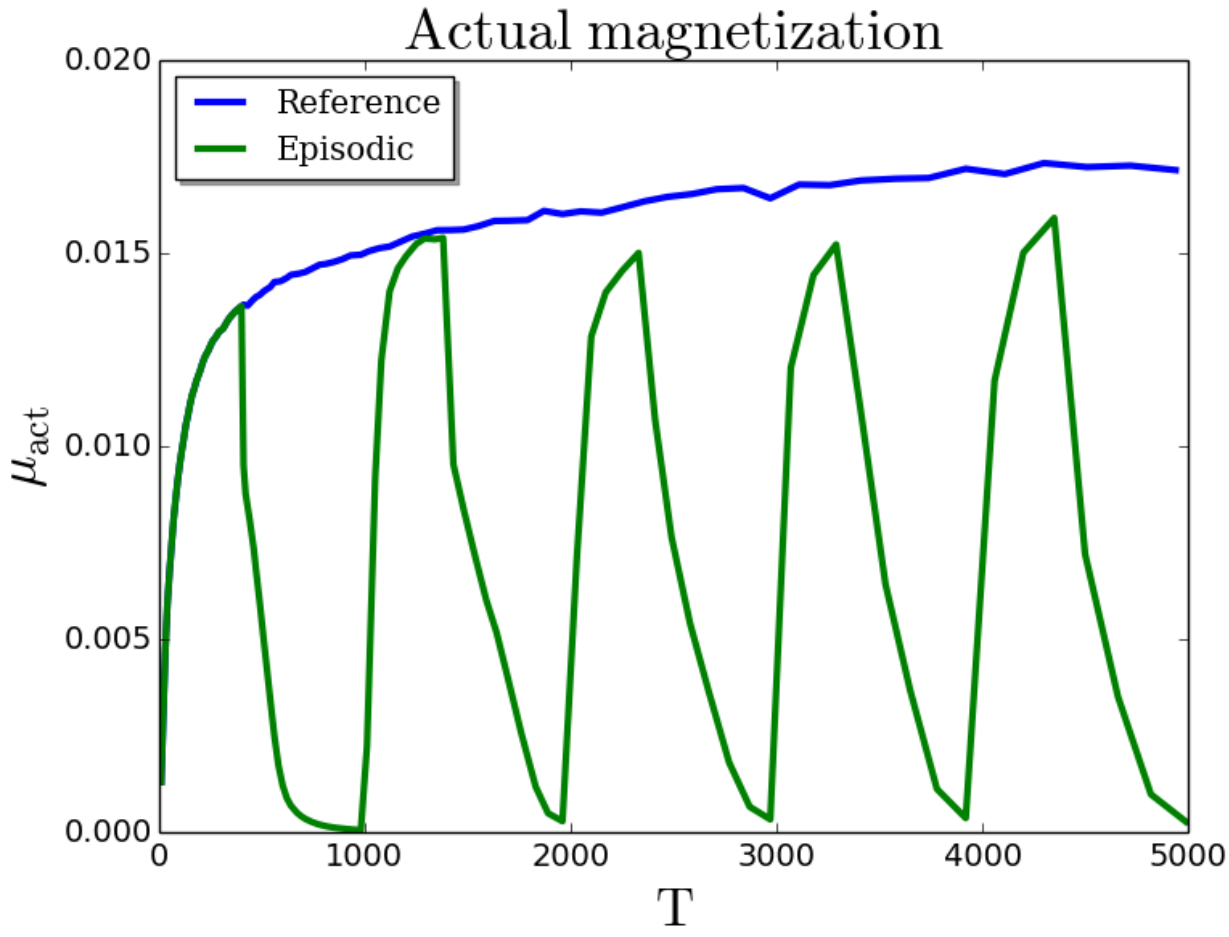


**Figure 6.7:** The time evolution of the actual disk magnetization $\mu_{act}$ of the reference dynamo simulation (blue line) and time-dependent dynamo simulation (green line).

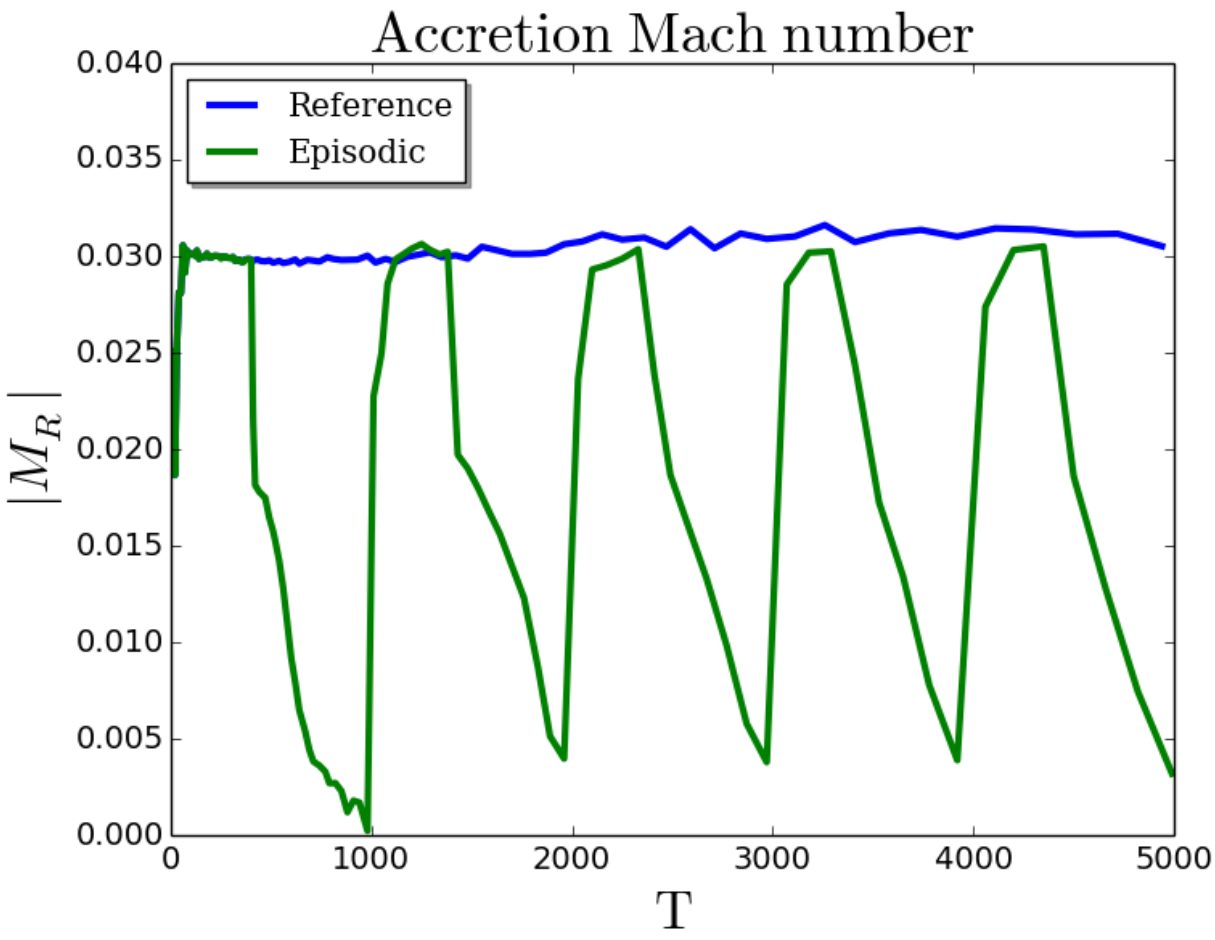


**Figure 6.8:** The time evolution of the accretion Mach number $M_R$ of the reference dynamo simulation (blue line) and time-dependent dynamo simulation (green line).

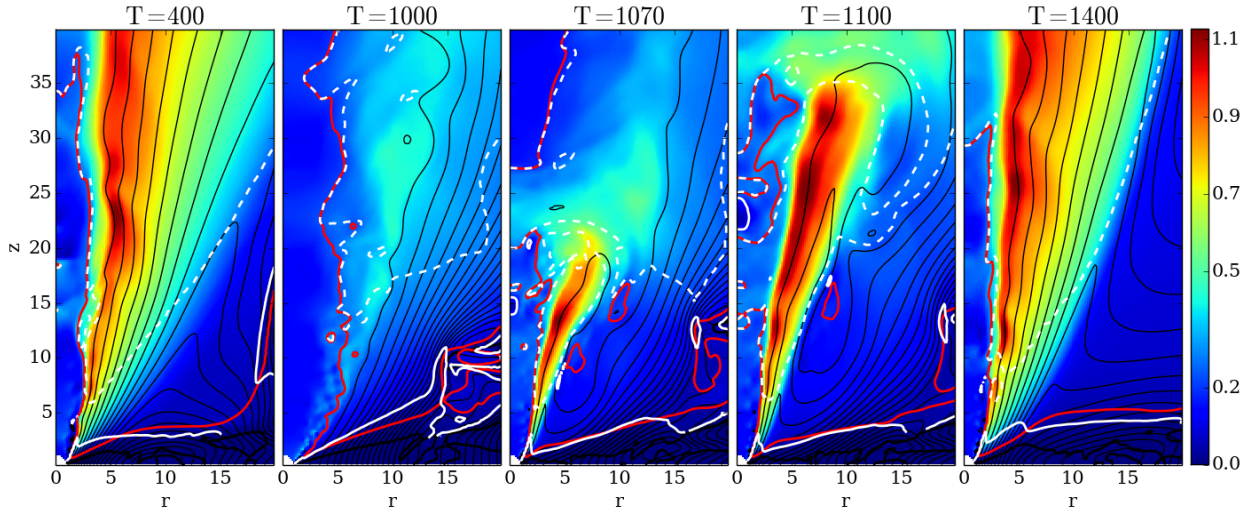


**Figure 6.9:** Time evolution of the disk-jet structure of the simulation with time-dependent dynamo action. Only a small cylindrical part of the whole spherical domain is presented. Shown is the velocity (colors); the poloidal magnetic field lines (thin black lines); the sonic (red line), the Alfvén (white line), and the fast magnetosonic (white dashed line) surfaces.

both on the periods $T_0$ and $\Delta T$ of the step function.

The interplay between dynamo action, accretion and diffusion may lead to different scenarios for the episodic ejection events. If the switch-off period of the the dynamo is shorter than the timescale for the magnetic field to diffuse out, the jet ejection will be constantly sustained, and the jet mass and energy fluxes will be just modulated. If the disk magnetization decays below the value that is necessary to drive a jet, and if the dynamo is weak or works only for a short time, the magnetic field will not be re-established adequately, and, therefore no new jet will be ejected.

Applying such a toy model it is possible to produce *episodic jet events*, during which the jet as well as the disk variables undergo substantial changes. The change of the disk magnetization directly affects both accretion and ejection processes. As the magnetization varies in time, also the other physical quantities vary. As discussed in Chapter 4, the accretion Mach number $M_R = V_R/C_s$ is tightly related to the disk magnetization. Figure 6.8 clearly shows that variations in the disk magnetization triggered by the time-dependent dynamo directly affect the disk accretion.

Figure 6.9 shows the time evolution of a time-dependent dynamo simulation. Again, only a small cylindrical part of the whole spherical domain is presented. All parameters are preserved the same as in the reference dynamo simulation, just folding the dynamo term with the periodic step function. Obviously, compared to the reference dynamo simulation, the overall structure of the disk-jet system changes in time - substantially, and not smoothly as for the case of a

constant dynamo effect. The dynamo is working until $T = 400$ when it is switched off. Therefore before $T = 400$ the evolution of the disk and outflow was identical to previously discussed (see Figure 6.1). Between $T = 400$ and $T = 1,000$ the generation of the magnetic field by the dynamo was switched off. As a consequence, the magnetic field substantially diffuses and the jet velocity decreases. Although the disk magnetization is continuously decreasing, a weak outflow is still present. It is the period when the dynamo is switched off ($T_0 - \Delta T$), that indirectly limits the disk magnetization. The more time is given to diffuse away the magnetic field, the smaller the resulting disk magnetization will be in the period when the dynamo is switched off.

At $T = 1,000$, the dynamo is switched on again, and the generation of the magnetic field is re-established. Because the dynamo-$\alpha$ is rather high and a substantial magnetic flux has remained from the previous cycle, it takes a rather little time to reach again sufficient magnetization for strong outflow launching. Once the substantial magnetization of the disk is reached, $\mu \approx 10^{-3}$, the outflow is re-launched. Starting from the inner part of the disk, the outflow re-establishes to the outward direction. Advection of the magnetic flux, together with the accretion material leads to amplification of the magnetization. At $T = 1,400$ the typical magneto-centrifugal structure of the magnetic field is re-established and a quasi-steady outflow re-appears, thus closing the activity cycle. Essentially, these magnetic cycles and subsequent jet ejection are repetitive. However, they are not necessarily identical, due to the magnetic field structure remaining from the previous cycle.

Note that the dynamo mechanism discussed above is able to regenerate the magnetic field in the disk completely. This is indeed different from the case of a simple modulation by the change in the magnetic diffusivity parameter $\alpha_{\rm ssm}$. As shown in Chapter 4, the diffusivity parameter $\alpha_{\rm ssm}$ is very crucial for determining the *actual* disk magnetization. Without a disk dynamo, it was possible to modulate the outflow simply by varying $\alpha_{\rm ssm}$ parameter, however, it was impossible to drastically affect the structure of the magnetic field, as can now be done by the dynamo.

### 6.4.1 STRUCTURE AND EVOLUTION OF THE EPISODIC JETS

Figure 6.10 presents a time series of snapshots of the high-speed outflow propagating close to the axis. Again, only a small cylindrical part of the whole spherical domain is shown, choosing time and space scales in order to display on the main outflow features. In order to show typical stages of the episodic ejection generation and propagation, the three dynamical time steps times $T = 450, 1,450, 3,450$ of the simulation were chosen. It was lasting lasting, in fact, 10,000 dynamical time units.

First, it can be seen how the outflow is generated initially (thus from the first cycle of dynamo activity) and then propagates throughout the hydrostatic corona. After switching off the dynamo

at $T = 400$, the jet weakens until it almost completely disappears. The dynamo becomes active again at $T = 1,000$. At $T = 1,450$ that first ejection has already reached $R \approx 1,100$, just when another "jet" has been launched. At even later time, $T = 3,450$, this second knot has established an outflow, and a third knot is launched.

The chosen timescales are such that the multiple ejection events can be followed on the grid. The time $T = 1,000$ would correspond to about $T/2\pi$ inner disk rotations, thus about a year if the inner disk radius $R_0 = 0.1\,\mathrm{AU}$ is applied. For comparison, jet observations of young stars suggest the timescales between the knots $\tau_{\mathrm{knot}} \simeq \Delta L/v_{\mathrm{jet}} \sim$ of about 10 years. If the knot generation mechanism is indeed triggered by a disk dynamo, the timescale for the field reversals must be longer.

In the two middle panels of Figure 6.10 it is clearly seen two fast rapidly moving gas ejections. These parcels of ejected material are separated from each other by the typical period of the dynamo $T_0$, corresponding to about $1000r_0$ distance between them. The ejected material rams into the gas which is left from the previous parcel and which moves with lower velocity. Shocks are generated that can be clearly seen in the density map[4]. The repeated ejections can be interpreted as jets knots, however, a more detailed investigation would be necessary to confirm this picture.

The signatures of the inflow from the inner coronal boundary into the domain along the outflow axis for low $z < 200$ can be clearly identified. As discussed above, this axial inflow is essential to provide the gas pressure that balances the collimation forces of the outflow in the vicinity of the disk. In the simulations it is injected artificially by the boundary condition, however, an astrophysical interpretation could be that of a wind driven by the central object.

### 6.4.2 SELF-INDUCED MAGNETIC FIELD REGENERATION

As discussed in the beginning of this section, the dynamo action is a stochastic, highly non-linear process. It can be expected that under certain conditions the non-linear evolution of the dynamo is more pronounced than under other conditions. This section presents preliminary results of simulations evolving in a more stochastic way and, by that, may be considered as a more natural "switch" for the dynamo mechanism. No artificial switch on/off has been applied. These simulations consider a self-induced regeneration of the magnetic field without applying any additional constraints such as a periodic step function in the time-dependent dynamo profile.

In the simulations, very similar self-induced regeneration processes of the magnetic field are observed, however, under different conditions. Thus, there seem to be several ways how a self-

[4]The shock structure is also visible in the pressure distribution and also in the jumps in the velocity profile along the jet (not shown as figure).

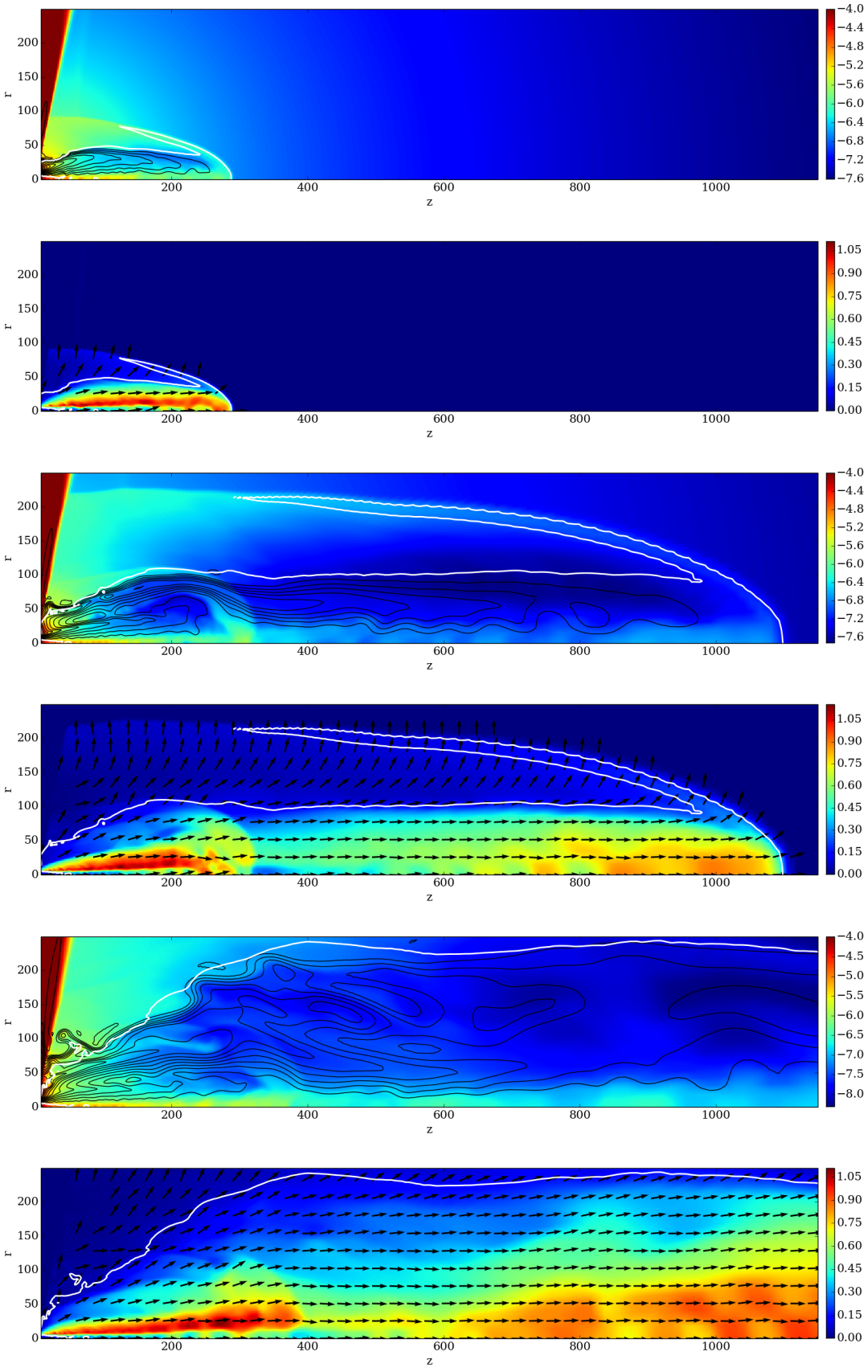


**Figure 6.10:** Structure of the simulation with time-dependent dynamo action shown at $T = (450, 1450, 3450)$, from top to bottom. Plots are grouped by two. Shown by color density logarithm (upper plot) and jet speed (lower plot). Maximum density is set to $10^{-4}$. Black lines show the magnetic field. The white line represents the sonic surface. Arrows show the normalized velocity vectors.

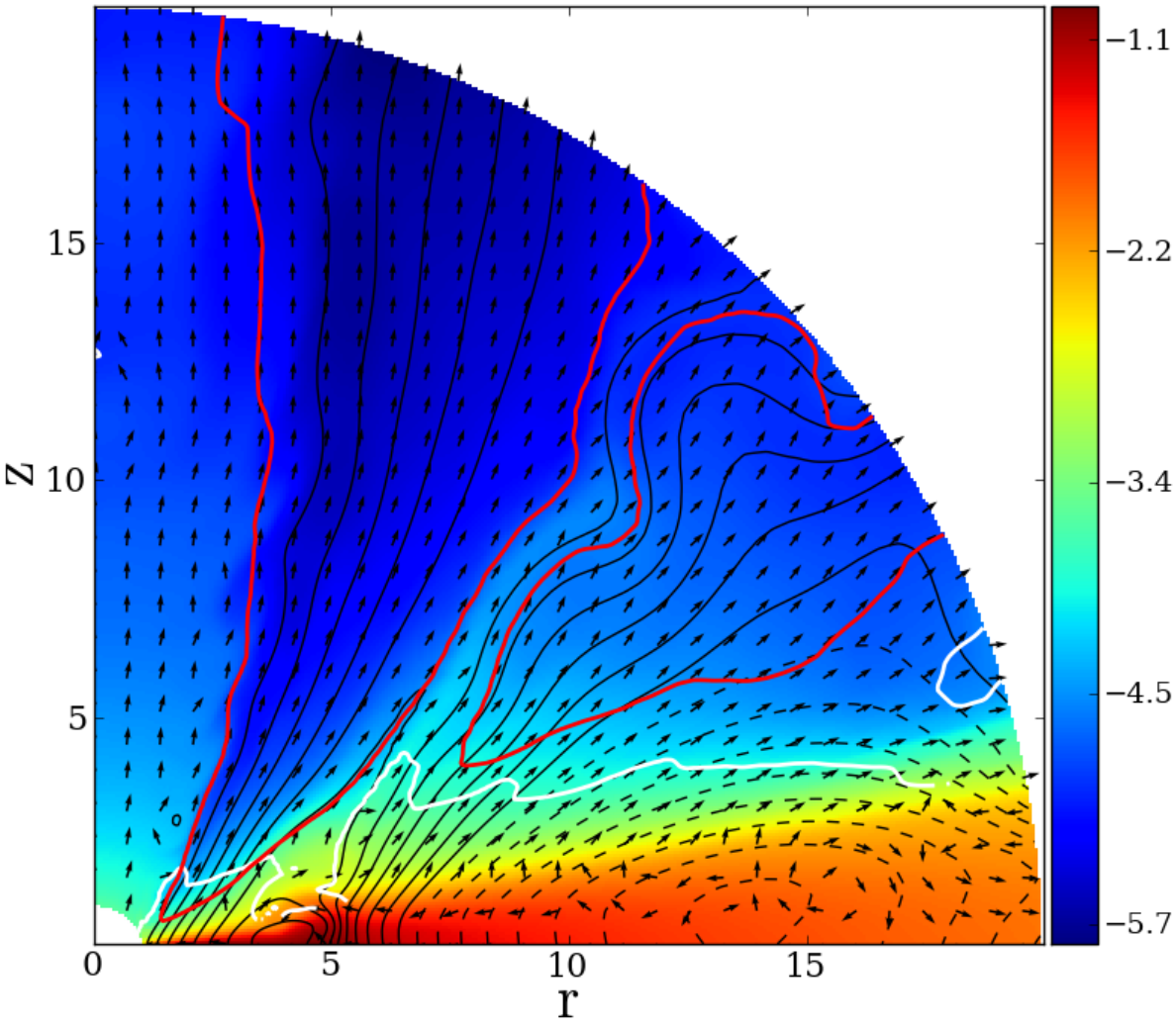


**Figure 6.11:** Example simulation resulting in two opposite magnetic loops generated by dynamo. Shown is the mass density (colors, logarithmic scale), the poloidal magnetic field lines (black lines, dashed lines show opposite magnetic flux), the sonic surface (red line), and the Alfvén surface (white line) at time $T = 1000$. Arrows show normalized velocity vectors.

induced switch of the dynamo regeneration can take place. Some of them require the presence of a quenching mechanism. Without that, the magnetic flux will be contineously generated in the inner disk and will eventually fill the entire disk with magnetic field of one dominant polarity.

One possibility to establish a self-induced switch for the magnetic field, is to initiate the simulation with the disk filled by the toroidal magnetic field of different polarity. Then the poloidal magnetic field that is generated by the dynamo will have different polarities as well. Constant field amplification will lead to the accretion/advection of this magnetic structure. As these structures move towards the center, the generation of the magnetic field in the innermost structure will be quenched, while the magnetic flux in the outer disk will continue to grow. As a consequence these structures merge (by diffusion) and decay, and quiescent period of outflow launching follows.

Another way is to link the dynamo term to the toroidal magnetic field. As discussed above, the poloidal magnetic field in the outer disk has an opposite polarity with respect to the inner disk magnetic field. Thus, in this case an additional feedback channel is provided that - under certain circumstances - can lead to a more fluctuating evolution of the disk-outflow system. The last example that surprisingly showed such self-induced regeneration of the magnetic field is the reference simulation, but with lower dynamo-term $\alpha_{\rm D} = -0.03$. Figure 6.11 shows the magnetic field structure in the disk of one of such simulation. Sometimes, the dynamo generates several magnetic field loops in the disk. While the magnetic field in the inner disk is able to quench the dynamo, in the outer disk the magnetic field is continuously amplified. The magnetic flux generated in the outer disk is of opposite polarity. If advected inwards, it will eventually reconnect with the magnetic flux in the inner disk. During this cancellation (reconnection) process, the disk magnetization in the jet launching region will decrease below a critical level, jet-launching will decay, and the outflow will disappear. At later stages, when the magnetic field remaining from the reconnection process becomes sufficiently amplified by the dynamo, the outflow will be launched again.

The details of the process of magnetic field regeneration in fact depends on many model parameters, in particular the magnetic diffusivity model. Although this might be an interesting mechanism triggering episodic events, the details are not presented here, since it was not possible yet to get it work robustly, and run the simulation longer than for just a few regenerations.

## 6.5 CONCLUSIONS

The results of MHD simulations are presented, investigating the generation of the magnetic field by the accretion disk dynamo in the context of jet and outflows launching. The time evolution

of the disk structure is self-consistently taken into account. The simulations are performed in axisymmetry treating all three field components. The MHD code PLUTO-4.0 was applied, that was modified for the mean-field $\alpha^2\Omega$ dynamo problem in the induction equation.

Present study explored the generation of a large scale, global magnetic field. The simulations were initiated by the purely radial magnetic field with magnetization $\mu_{\rm init} = 10^{-5}$. It was showed in detail how the magnetic field is being generated and through which consecutive stages it evolves, acquiring in the end the ability to launch jet and outflows. In this respect, these simulations can be seen as a continuation of early work by von Rekowski et al. 2003 and von Rekowski & Brandenburg 2004. This study is concentrating more on the jet and outflow generation and propagation.

One advantage of presented simulations is that current model keeps the disk magnetization at a rather low level. Therefore, the magnetic field does not substantially affect the disk hydrodynamics, and allows to evolve the simulations for a very long time. Each simulation was evolved at least up to $T = 10,000$ on a spherical domain with $R = [1, 1500]$.

The following summarizes the main results.

(1) In presented mean-field disk dynamo simulations, two main features in the magnetic field structures can be distinguished. The magnetic field of the inner disk that is similar to the commonly found open field structure, favoring the magneto-centrifugal launching of the outflow. The poloidal magnetic field of the outer part of the disk is highly inclined, and predominantly radial. Differential rotation induces a very strong toroidal component from it. This structure is known as tower or Pointing jet in literature. In this part of the disk it is toroidal magnetic field that plays a key role in outflow launching. First, below the disk surface, where $V_R < 0$, the matter is lifted by the buoyant force of the magnetic field, thus, by the gradient of the thermal pressure. Starting from the disk surface, where $V_R > 0$, the matter is further accelerated predominantly by the pressure gradient of the toroidal magnetic field. The outflows from the outer part of the disk are typically slower and denser, and less collimated, thus corresponding to a higher mass loading.

(2) In principle, the dynamo can fill the entire accretion disk with magnetic flux. Thus, if the dynamo action is not quenched, magnetic flux is continuously generated, diffuses outwards along the disk until it fills the entire disk. This loop-like structure of the magnetic field that is typical for a dynamo, propagates further outwards.

(3) As soon as the disk magnetization reaches a critical limit, $\mu > 10^{-3}$, disk winds are launched and can be accelerated to super-magnetosonic speed. This result is complementary to simulations presented in Chapter 4, that does not consider dynamo, where obtained a critical magnetization just from advection of magnetic flux by accretion. Thus the long-standing belief that the disk magnetization plays the key role in the outflow launching can be again confirmed. In the inner

disk, the rate of generation of magnetic field by the dynamo is higher, leading to a strong gradient of the disk magnetization.

(4) A toy model was further invented, triggering a time-dependent efficiency of the mean-field dynamo. In that model approach, the dynamo is periodically switch on and off. This strongly affects the magnetic field structure. The decay of the magnetic flux by the diffusion can be completely balanced by the dynamo that regenerates the magnetic field. As a consequence, the duty cycles of the dynamo action can lead to episodic jet ejection, just depending on the disk magnetization obtained during dynamo activity. When the dynamo is suppressed and the disk magnetization falls below a critical value, $\mu \approx 10^{-3}$, the generation of outflows as well as the accretion is substantially inhibited. The timescale of the dynamo cycle and the corresponding timescale for the episodic ejections was chosen somehow shorter compared to the observed values - just to follow several events in the same simulation box. However, the main - and general - result is that the episodic ejection and *large-scale jet knots* can be steered by the *disk intrinsic dynamo* that is time-dependent and regenerates the jet-launching magnetic field.

(5) Concerning the disk hydrodynamics, the accretion velocity follows the same power-law $\beta_{V_R} \approx -2/5$ for the simulations with and without dynamo. This interesting also, because slightly different diffusivity model were applied, leading to different magnetic field structure. Nevertheless, the accretion profiles are approximately the same. As a consequence, approximately the same ejection index $\xi \approx 0.25$ was found.

(6) Although the dynamo and non-dynamo simulations are significantly different, launching mechanism of the fast jet is primarily the same. Thus, from a pure observational point of view, one would not yet be able to distinguish whether the jets are launched from a dynamo-generated magnetic field or from a magnetic field advected from the interstellar medium.

# 7

# Summary and Outlook

## 7.1 Summary

Jets and outflows play an indispensable role in star formation. They are a cornerstone of the accretion-ejection processes. Jets not only provide a very efficient mechanism of angular momentum extraction from the disk, but also help to sustain the interstellar turbulence. A better understanding of these phenomena is the major focus of the research.

In this work, the results of MHD simulations are presented, investigating jet and outflow launching from a magnetically diffusive accretion disks with and without a presence of a dynamo action. All simulations are performed in three-dimensional axisymmetry applying the MHD code PLUTO 4.0, that was adapted for the mean-field $\alpha^2\Omega$ dynamo problem.

In contrast to previous works, a spherical coordinate system and numerical grid is applied. Spherical grid provides substantial benefits concerning the numerical resolution and the stability of the simulations. New boundary conditions were specifically designed for treating the disk-jet system.

The study presented in this work is the most extensive in its category. Dozens of simulations presented here were evolved up to 10,000 time units - thus, longer than any known so far in

literature. The longest simulation presented in this work progressed up to more than 150,000 time units, that is one order of magnitude longer than any simulation previously.

To analyse these simulations, a new method of analysis – magnetization analysis – was developed. This method allows to probe online the evolution of both disk and jet, establishing a deep interrelation between these properties.

In Chapter 4, a reference non-dynamo simulation is presented. The main result discussed in this chapter is that it is the actual disk magnetization that plays the major role in the jet formation, setting most of the jet parameters. It directly affects the accretion power and ejection efficiency. During this study, the following theoretical insights were discovered. The upper theoretical limit for the diffusivity anisotropy parameter was found. It was also showed that if the disk is uniformly magnetized, the MHD disk quantities show a self-similar structure. The ejection Mach number in the case of a moderately strong disk magnetization ($\mu < 0.15$) is a linear function of the disk magnetization;

In Chapter 5, the interrelation between the jet and the underlying disk is studied. The simulation ensemble, presented in Chapter 4 was further enlarged. This allowed to consistently probe much broader parameter space of the disk-jet system. The main goal of connecting the jet to the disk properties was successfully achieved. Various interrelations between the jet properties (four jet integrals) and the underlying disk magnetization were established that, in principle, allows to derive the physical parameters of the jet-launching area from the jet observables. Two different but complementary launching mechanisms, magnetically and centrifugally dominated, were introduced.

In Chapter 6, the results of the disk-jet simulations investigating the generation of the magnetic field by the accretion disk dynamo are presented. It was shown in detail how the magnetic field is generated, what is the structure of the generated magnetic field, and what consecutive stages it evolves through, acquiring in the result the ability to launch jet and outflows. Two physically different regions in the disk-jet system can be distinguished: the inner region, where the open magnetic field structure favours a magneto-centrifugal launching, and the outer region in which the outflows are lifted by the buoyancy force of the toroidal magnetic field and later accelerated predominantly by the pressure force of the toroidal magnetic field. In order to study the jet intermittences, a toy model was proposed. Triggering a time-dependent efficiency of the mean-field dynamo, it was shown how a magnetic field in the disk can be regenerated. The main result discussed in this chapter is that the repetitive ejections and large-scale jet knots can be steered by the time-dependent action of the disk dynamo.

## 7.2 OUTLOOK

As a great philosopher, Alfred Korzybski, reminds us, the map is not the territory. In other words, one should always keep in mind that every model can be always improved. Admitting this truth, this section provides a number of ways how the current model can be further improved.

Developed in this work approach of treating the actual disk and jet parameters – the magnetization analysis – is, in fact, very promising. If the simulation is in a quasi-steady state, this approach cannot be overestimated. It allows continuous probe of a large parameter space of the jet-launching problem. Furthermore, the effect of different models of diffusivity, especially anisotropy parameter, can be examined.

A further work in connecting jet observables to the disk parameters is very promising as well. If jet observables such as propagation and rotation velocity, jet power, and jet effective radius are determined to sufficient accuracy, then using the technique developed in Chapter 5, a lot of valuable information of the launching region of the disk can be inferred. As showed in Chapter 5, the jet integrals are tightly connected to the disk magnetization, that allows to probe the degree of magnetization of the launching area. On the other hand, jet integrals, namely jet specific energy and angular momentum, are even more tightly related to each other. If actual jet parameters, namely the jet power and the jet angular momentum are known, the radius of the jet foot point, in other words, corresponding scales of the system, can be inferred. If the relation between jet integrals holds in general case, than it opens an opportunity to probe very distant regions of our Universe, as jets from AGN are the brightest sources ever discovered.

One way is to move the simulations into fully three-dimensional domain, preserving a spherical geometry. This can be done rather easily if keeping the idea of inner boundary prescription, developed in this work. One should, however, keep in mind that axial region of the spherical domain might not be treated well by the numerical scheme. Nevertheless, the disk, the launching area and the lower collimation region should not be affected.

In the direction of dynamo, several studies can consequently follow this work. First, a more natural way of $\alpha$-dynamo term can be prescribed. Preliminary simulations showed that dynamo can be directly linked to the disk magnetization if the dynamo is strongly quenched to the disk region. Second, physically different dynamos such as MRI and Parker dynamos, can operate in the accretion disks and can be modeled by the $\alpha\Omega$-dynamo. This might bring even more complex behavior of the magnetic field and naturally result in episodic events.

# Acknowledgements

I would sincerely like to thank my supervisor Christian Fendt, who supported me throughout my thesis. In fact, I always felt lucky having him as a supervisor. It was always a pleasure to talk to him whether discussing scientific or everyday life questions. Never felt left, always supported, I received only honest, trustful, and respectful treatment. One simply could not wish for a better, friendlier supervisor.

I would especially like to thank Bhargav Vaidya who helped me to set the starting point to my PhD travel. Throughout my PhD, he was always very friendly and helpful. Thanks to Somayeh Sheikhnezami a colleague of mine, who was always open to any discussion and also helped me to dive into the jet topic.

I thank all members of my examination committee: Christian Fendt, Kees Dullemond, Henrik Beuther, and Luca Amendola, who without any hesitation agreed to take part in my final examination. I acknowledge German science foundation DFG, the SFB 881 project, that financed my research.

My special thanks to all my german colleagues who made my life in Germany much easier in many respects. Special thanks to Robert Singh, Kirsten Schuelle, and Maria Lenius.

I thank Christian Fendt as a coordinator of IMPRS, Anahi Caldu and Jan Rybizki as student representatives, who organized so many nice social events during my PhD years.

I would like to thank Alex Buedenbender, Veselina Kalinova, Elena Manjavacas, Sladjana Nikolic, Alberto Rorai, and Akin Yildirim for being nice office-mates.

I would like to acknowledge all the staff of MPIA, without whom such a great environment could not exist.

Many thanks to all my wife, friends and relatives, who made my life in Heidelberg so much enjoyable.

# Bibliography


Akeson, R. L., & Carlstrom, J. E. 1997, ApJ, 491, 254

Anderson, J. M., Li, Z.-Y., Krasnopolsky, R., & Blandford, R. D. 2003, ApJ, 590, L107

Arlt, R., & Rüdiger, G. 2001, A&A, 374, 1035

Armitage, P. J., Livio, M., & Pringle, J. E. 1996, ApJ, 457, 332

Bacciotti, F., Ray, T. P., Mundt, R., Eislöffel, J., & Solf, J. 2002, ApJ, 576, 222

Bai, X.-N., & Stone, J. M. 2013, ApJ, 767, 30

Balbus, S. A., & Hawley, J. F. 1991, ApJ, 376, 214

Bally, J., & Lada, C. J. 1983, ApJ, 265, 824

Banerjee, R., Klessen, R. S., & Fendt, C. 2007, ApJ, 668, 1028

Bardou, A., von Rekowski, B., Dobler, W., Brandenburg, A., & Shukurov, A. 2001, A&A, 370, 635

Beckwith, K., Armitage, P. J., & Simon, J. B. 2011, MNRAS, 416, 361

Begelman, M. C., & Li, Z.-Y. 1994, ApJ, 426, 269

Blandford, R. D., & Payne, D. G. 1982, MNRAS, 199, 883

Brandenburg, A., & Campbell, C. 1997, in Lecture Notes in Physics, Berlin Springer Verlag, Vol. 487, Accretion Disks - New Aspects, ed. E. Meyer-Hofmeister & H. Spruit, 109

Brandenburg, A., & Donner, K. J. 1997, MNRAS, 288, L29

Brandenburg, A., Nordlund, A., Stein, R. F., & Torkelsson, U. 1995, ApJ, 446, 741

Brandenburg, A., Sokoloff, D., & Subramanian, K. 2012, Space Sci. Rev., 169, 123

Brandenburg, A., & Subramanian, K. 2005, Phys. Rep., 417, 1

Brandenburg, A., & von Rekowski, B. 2007, Mem. Soc. Astron. Italiana, 78, 374

Burnham, S. W. 1890, MNRAS, 51, 94

—. 1894, Publications of Lick Observatory, 2, 168

Cabrit, S., & Andre, P. 1991, ApJ, 379, L25

Cabrit, S., Edwards, S., Strom, S. E., & Strom, K. M. 1990, ApJ, 354, 687

Camenzind, M. 1990, in Reviews in Modern Astronomy, Vol. 3, Reviews in Modern Astronomy,

ed. G. Klare, 234–265

Campbell, C. G. 2009, MNRAS, 392, 271

Casse, F., & Ferreira, J. 2000, A&A, 353, 1115

Casse, F., & Keppens, R. 2002, ApJ, 581, 988

—. 2004, ApJ, 601, 90

Chiueh, T., Li, Z.-Y., & Begelman, M. C. 1991, ApJ, 377, 462

Colella, P., & Woodward, P. R. 1984, Journal of Computational Physics, 54, 174

Contopoulos, J., & Lovelace, R. V. E. 1994, ApJ, 429, 139

Curtis, H. D. 1918, Publications of Lick Observatory, 13, 9

Davies, B., Lumsden, S. L., Hoare, M. G., Oudmaijer, R. D., & de Wit, W.-J. 2010, MNRAS, 402, 1504

Davis, C. J., Berndsen, A., Smith, M. D., Chrysostomou, A., & Hobson, J. 2000, MNRAS, 314, 241

Dopita, M. A., Evans, I., & Schwartz, R. D. 1982, ApJ, 263, L73

Eddy, J. A. 1976, Science, 192, 1189

Fendt, C. 2006, ApJ, 651, 272

—. 2009, ApJ, 692, 346

—. 2011, ApJ, 737, 43

Fendt, C., & Camenzind, M. 1996, A&A, 313, 591

Fendt, C., & Sheikhnezami, S. 2013, ApJ, 774, 12

Fendt, C., & Čemeljić, M. 2002, A&A, 395, 1045

Ferreira, J. 1997, A&A, 319, 340

Ferreira, J., & Casse, F. 2013, MNRAS, 428, 307

Ferreira, J., & Pelletier, G. 1993, A&A, 276, 625

—. 1995, A&A, 295, 807

Fromang, S. 2013, in EAS Publications Series, Vol. 62, EAS Publications Series, 95–142

Fukui, Y., Iwata, T., Mizuno, A., Bally, J., & Lane, A. P. 1993, in Protostars and Planets III, ed. E. H. Levy & J. I. Lunine, 603–639

Gaibler, V., Khochfar, S., Krause, M., & Silk, J. 2012, MNRAS, 425, 438

Gammie, C. F., & Menou, K. 1998, ApJ, 492, L75

Goedbloed, J. P., Beliën, A. J. C., Holst, B. V. D., & Keppens, R. 2004, Physics of Plasmas, 11, 4332

Gomez, M., Whitney, B. A., & Kenyon, S. J. 1997, AJ, 114, 1138

Gressel, O. 2010, MNRAS, 405, 41

Haisch, Jr., K. E., Lada, E. A., & Lada, C. J. 2001, ApJ, 553, L153

Haro, G. 1952, ApJ, 115, 572

—. 1953, ApJ, 117, 73

Hawley, J. F., Gammie, C. F., & Balbus, S. A. 1995, ApJ, 440, 742

Hayashi, M. R., Shibata, K., & Matsumoto, R. 1996, ApJ, 468, L37

Herbig, G. H. 1950, ApJ, 111, 11

—. 1951, ApJ, 113, 697

—. 1952, JRASC, 46, 222

Johansen, A., & Levin, Y. 2008, A&A, 490, 501

Johnstone, C. P., Jardine, M., Gregory, S. G., Donati, J.-F., & Hussain, G. 2014, MNRAS, 437, 3202

Kato, Y., Hayashi, M. R., & Matsumoto, R. 2004, ApJ, 600, 338

Keppens, R., Casse, F., & Goedbloed, J. P. 2002, ApJ, 569, L121

King, A. R., Pringle, J. E., & Livio, M. 2007, MNRAS, 376, 1740

Konigl, A., & Pudritz, R. E. 2000, Protostars and Planets IV, 759

Königl, A., & Salmeron, R. 2011, The Effects of Large-Scale Magnetic Fields on Disk Formation and Evolution, ed. Garcia, P. J. V., 283–352

Königl, A., Salmeron, R., & Wardle, M. 2010, MNRAS, 401, 479

Kormendy, J., & Richstone, D. 1995, ARA&A, 33, 581

Krasnopolsky, R., Li, Z., & Blandford, R. 1999, ApJ, 526, 631

Krause, F., & Rädler, K.-H. 1980, Mean-field magnetohydrodynamics and dynamo theory

Lada, C. J. 1985, ARA&A, 23, 267

Lesur, G., & Longaretti, P.-Y. 2009, A&A, 504, 309

Li, Z. 1995, ApJ, 444, 848

Li, Z.-Y., Chiueh, T., & Begelman, M. C. 1992, ApJ, 394, 459

Londrillo, P., & del Zanna, L. 2004, Journal of Computational Physics, 195, 17

Lovelace, R. V. E., Romanova, M. M., & Bisnovatyi-Kogan, G. S. 1995, MNRAS, 275, 244

Lubow, S. H., Papaloizou, J. C. B., & Pringle, J. E. 1994, MNRAS, 268, 1010

Lynden-Bell, D. 1996, MNRAS, 279, 389

Lynden-Bell, D., & Boily, C. 1994, MNRAS, 267, 146

Meliani, Z., Casse, F., & Sauty, C. 2006, A&A, 460, 1

Michel, F. C. 1969, ApJ, 158, 727

Mignone, A., Bodo, G., Massaglia, S., Matsakos, T., Tesileanu, O., Zanni, C., & Ferrari, A. 2007, ApJS, 170, 228

Monin, J.-L., Whelan, E. T., Lefloch, B., Dougados, C., & Alves de Oliveira, C. 2013, A&A, 551, L1

Mundt, R., & Fried, J. W. 1983, ApJ, 274, L83

Murphy, G. C., Ferreira, J., & Zanni, C. 2010, A&A, 512, A82

Okamoto, I. 1975, MNRAS, 173, 357

Ouyed, R., & Pudritz, R. E. 1997, ApJ, 482, 712

Parker, E. N. 1955, ApJ, 122, 293

Parkin, E. R., & Bicknell, G. V. 2013, ApJ, 763, 99

Pelletier, G., & Pudritz, R. E. 1992, ApJ, 394, 117

Pinte, C., Ménard, F., Berger, J. P., Benisty, M., & Malbet, F. 2008, ApJ, 673, L63

Porth, O., & Fendt, C. 2010, ApJ, 709, 1100

Porth, O., Fendt, C., Meliani, Z., & Vaidya, B. 2011, ApJ, 737, 42

Pudritz, R. E. 1981a, MNRAS, 195, 897

—. 1981b, MNRAS, 195, 881

Pudritz, R. E., & Norman, C. A. 1983, ApJ, 274, 677

Pudritz, R. E., Ouyed, R., Fendt, C., & Brandenburg, A. 2007, Protostars and Planets V, 277

Pudritz, R. E., Rogers, C. S., & Ouyed, R. 2006, MNRAS, 365, 1131

Ray, T., Dougados, C., Bacciotti, F., Eislöffel, J., & Chrysostomou, A. 2007, Protostars and Planets V, 231

Rekowski, M. v., Rüdiger, G., & Elstner, D. 2000, A&A, 353, 813

Rozyczka, M., Joung Turner, N., & Bodenheimer, P. 1995, MNRAS, 276, 1179

Salmeron, R., Königl, A., & Wardle, M. 2011, MNRAS, 412, 1162

Sauty, C., & Tsinganos, K. 1994, A&A, 287, 893

Schwartz, R. D. 1975, ApJ, 195, 631

Shakura, N. I., & Sunyaev, R. A. 1973, A&A, 24, 337

Sheikhnezami, S., Fendt, C., Porth, O., Vaidya, B., & Ghanbari, J. 2012, ApJ, 757, 65

Shibata, K., & Uchida, Y. 1985, PASJ, 37, 31

Shu, F. H., & Shang, H. 1997, in IAU Symposium, Vol. 182, Herbig-Haro Flows and the Birth of Stars, ed. B. Reipurth & C. Bertout, 225–239

Simon, J. B., Beckwith, K., & Armitage, P. J. 2012, MNRAS, 422, 2685

Snell, R. L., Loren, R. B., & Plambeck, R. L. 1980, ApJ, 239, L17

Stepanovs, D., & Fendt, C. 2014a, ApJ, 793, 31

—. 2014b, ApJ, submitted, revised

Stepanovs, D., Fendt, C., & Somayeh, S. 2014, ApJ, in press

Stone, J. M., Hawley, J. F., Gammie, C. F., & Balbus, S. A. 1996, ApJ, 463, 656

Takano, T., Fukui, Y., Ogawa, H., Takaba, H., Kawabe, R., Fujimoto, Y., Sugitani, K., & Fujimoto, M. 1984, ApJ, 282, L69

Toro, E. F., Spruce, M., & Speares, W. 1994, Shock Waves, 4, 25

Tout, C. A., & Pringle, J. E. 1992, MNRAS, 259, 604

Tzeferacos, P., Ferrari, A., Mignone, A., Zanni, C., Bodo, G., & Massaglia, S. 2009, MNRAS, 400, 820

—. 2013, MNRAS, 428, 3151

Uchida, Y., & Shibata, K. 1985, PASJ, 37, 515

Ustyugova, G. V., Koldoba, A. V., Romanova, M. M., Chechetkin, V. M., & Lovelace, R. V. E. 1995, ApJ, 439, L39

Ustyugova, G. V., Lovelace, R. V. E., Romanova, M. M., Li, H., & Colgate, S. A. 2000, ApJ, 541, L21

Vaidya, B., Fendt, C., & Beuther, H. 2009, ApJ, 702, 567

Vlemmings, W. H. T., Diamond, P. J., van Langevelde, H. J., & Torrelles, J. M. 2006, A&A, 448, 597

von Rekowski, B., & Brandenburg, A. 2004, A&A, 420, 17

von Rekowski, B., Brandenburg, A., Dobler, W., Dobler, W., & Shukurov, A. 2003, A&A, 398, 825

Wardle, M., & Königl, A. 1993, ApJ, 410, 218

Watson, A. M., Stapelfeldt, K. R., Wood, K., & Ménard, F. 2007, Protostars and Planets V, 523

Whelan, E. T., Bacciotti, F., Ray, T., & Dougados, C. 2011, in IAU Symposium, Vol. 275, IAU Symposium, ed. G. E. Romero, R. A. Sunyaev, & T. Belloni, 396–399

White, M. C., McGregor, P. J., Bicknell, G. V., Salmeron, R., & Beck, T. L. 2014, MNRAS, 441, 1681

Zanni, C., Ferrari, A., Rosner, R., Bodo, G., & Massaglia, S. 2007, A&A, 469, 811